Quasi-static and dynamic granular flows : scaling behavior, microstructure, and particle shape effects

Duc Chung Vu

THÈSE POUR OBTENIR LE GRADE DE DOCTEUR DE L'UNIVERSITÉ DE MONTPELLIER

En Mécanique et Génie Civil ED I2S

École doctorale : Information, Structures, Systèmes

Unité de recherche Laboratoire de Mécanique et Génie Civil (LMGC)

Ecoulements granulaires quasi-statiques et dynamiques: mise à l'échelle, microstructure et effets de la forme des particules

---

Quasi-static and dynamic granular flows: scaling behavior, microstructure, and particle shape effects

Presented by **Duc Chung VU**

Defense date : 28 November 2023

In front of the jury composed of

Jean-Noël Roux	Researcher	Ecole des Ponts ParisTech	President
Catherine O'Sullivan	Professor	Imperial College of London	Rapporteur
Nicolas Vandewalle	Professor	University of Liège	Rapporteur
Vincent Richefeu	Maître de Conférence	University of Grenoble Alpes	Examiner
Rodrigue Largenton	Research Engineer	EDF	Examiner
Farhang Radjai	Director of Research	CNRS, LMGC, University of Montpellier	Thesis Supervisor
Jean-Yves Delenne	Director of Research	IATE, INRAE, University of Montpellier	co-Supervisor
Lhassan Amarsid	Research Engineer	CEA, DES, IRESNE, DEC, SESC, LDOP	co-Supervisor

UNIVERSITÉ DE MONTPELLIER

Acknowledgments

I would like to express my sincere gratitude to Prof. Farhang Radjai who accepted me in his research group and made this research possible. His immense knowledge and plentiful experience have encouraged me in all the time of my academic research and daily life. I would like to thank my co-Director, Dr. Jean-Yves Delenne for his continuous support and invaluable advice with this thesis. I am extremely grateful to my supervisor Dr. Lhassan Amarsid for all his help, advice and patience during my PhD study. Thanks to Dr. Vincent Richefeu who provided the backbone of the code used in this thesis. I would like to thank the president, reviewers, and examiners for accepting being part of this PhD jury, for taking the time to read, for all their commentaries and attention to this work.

I would like to thank all the members of the LDOP in CEA Cadarache and LMGC in University of Montpellier. It is their kind help that have kept my study and life in France running smoothly. I also appreciate all the support of my research team in LMGC. Thanks to Lama Braysh, Kamilia Ayed, Max Sonzogni, Yohann Trivino, and Duy Trieu Tran for time spent together in the laboratory and conferences. A special mention should be made of Sirine Al-Dandachli, Keovathana Run, Assia Gasmi, and Jacintha Naby, whose friendship has been an invaluable asset.

I would like to acknowledge the financial support from SIFCO project (CEA), EDF, and ORANO to this thesis that allowed me to complete my professional formation in France.

QUASI-STATIC AND DYNAMIC GRANULAR FLOWS:
SCALING BEHAVIOR, MICROSTRUCTURE, AND PARTICLE SHAPE EFFECTS

Abstract: Granular processes in nature and industry often involve complex quasistatic or dynamic flows of various particle shapes and frictional properties. Although empirical approaches have been developed for such flows, advanced particle dynamics simulations can be used for detailed sensitivity analysis of their scaling behavior as a function of system parameters or to connect their behavior to the microstructure. In this work, extensive simulations are used in 3D to study the effects of polyhedral particle shape on quasi-static granular flows under fully periodic boundary conditions and dynamic cascading flows in rotating drums. Orthotropic elastic moduli under triaxial compression are expressed as a function of the contact network anisotropy and a constraint number accounting for different types of contacts between polyhedra. In rotating drums, the cascading flow regime is investigated for a broad range of parameter values and shown to be governed by a unique dimensionless scaling parameter that combines all system parameters. Finally, the impact-induced breakage of a single particle is modeled by means of a novel fracture model based exclusively on fracture energy. The fragment shapes and sizes are studied systematically and the distribution of fragment masses is found to be a power-law function with an exponent depending on the fracture energy.
Keywords: Granular Materials, Discrete Element Method, Microstructure, Scaling

ECOULEMENTS GRANULAIRES QUASI-STATIQUES ET DYNAMIQUES: MISE À L'ÉCHELLE, MICROSTRUCTURE ET EFFETS DE LA FORME DES PARTICULES

Resumé: Les processus granulaires naturels et industriels impliquent souvent des écoulements quasi-statiques ou dynamiques complexes de diverses formes de particules. Même si des modèles empiriques de tels écoulements existent, les simulations avancées de dynamique granulaire permettent aujourd'hui de réaliser des analyses de sensibilité détaillée de leur comportement en fonction des paramètres de l'écoulement ou relier leur comportement à la microstructure. Dans ce travail de thèse, des vastes campagnes de simulation ont été menées dans le but d'étudier les effets de la forme polyédrique des particules sur les écoulements granulaires quasi-statiques sous conditions tri-périodiques et sur les écoulements dynamiques dans le régime de cascade dans des tambours rotatifs. Les modules élastiques orthotropes sous compression triaxiale ont été exprimés en fonction de l'anisotropie du réseau de contacts et un nombre de contrainte prenant en compte différents types de contacts entre polyèdres. Dans les tambours rotatifs, le régime d'écoulement en cascade a été étudié pour un large spectre de valeurs des paramètres et il a été montré qu'il est régi par un paramètre d'échelle sans dimension qui combine tous les paramètres du système. Il a été également démontré que la mise à l'échelle proposée est cohérente avec une méthode de coarse-graining. Enfin, la rupture d'une seule particule sous l'effet d'impact avec un plan a été simulée par un nouveau modèle de fracture basé exclusivement sur l'énergie de rupture. Les simulations révèlent une distribution des masses des fragments en loi de puissance avec un exposant qui dépend de l'énergie de rupture.
Mots Clés: Matériaux granulaires, Discrete Element Method, Microstructure, Scaling

Contents

General introduction

The grinding process is one of the most widely used processes in various fields such as mining industry, civil engineering, powder metallurgy, agronomy and pharmacy. In the field of nuclear energy, a great majority (about 90%) of nuclear electricity worldwide is generated in Light Water Reactors (LWR), which uses fuel in the form of cylindrical oxide pellets, either uranium dioxide or mixed oxide (MOX) that is composed of uranium dioxide and plutonium dioxide with a Pu content between 5 and 10%. Grinding is the first step in the process of manufacturing MOX fuels. In terms of particle shape, the uranium and plutonium dioxide powders are basically composed of agglomerates or sub-micron platelets, respectively; see Fig. 0-1. Nevertheless, when the two powders are co-milled, agglomerates similar to uranium dioxide are prone to form.

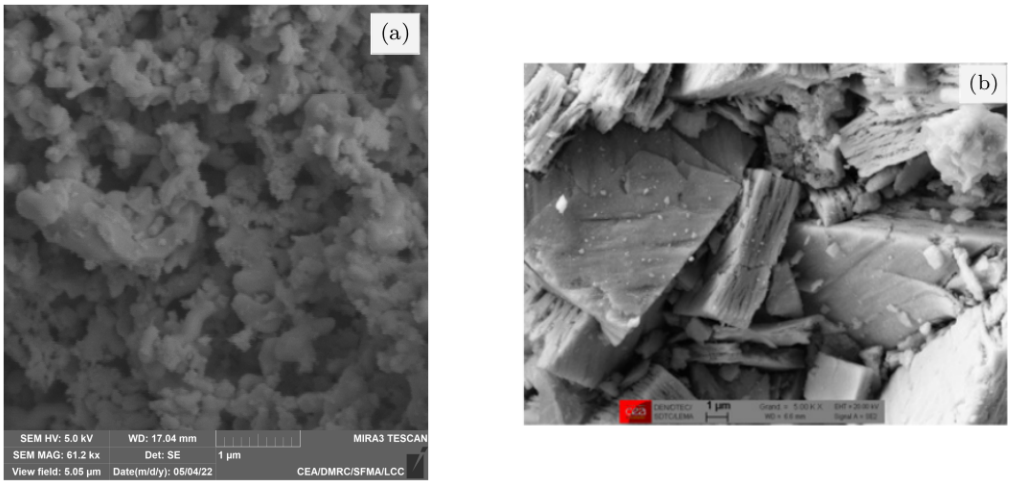

Fig. 0-1. SEM photographs showing granules of (a) uranium dioxide and (b) plutonium dioxide [1].

Mixed oxide pellets for LWR are manufactured by powder metallurgy, but the flow-sheet is more complex because of the use of two different types of powders that need to be mixed. Because of moderate diffusion coefficient of U and Pu at $1700°C$, a simple mixture of UO_2 and PuO_2 powders is not sufficient to achieve a good homogeneity of plutonium distribution. The first stage of fabrication is therefore a simultaneous milling of the UO_2 and PuO_2 powders with a Pu content between 25 and 30 %, much higher than the target Pu content of the pellets ($\sim$ 5 to 10 %). This operation is performed during several hours using a rotating ball mill with low alloy uranium balls. The milling, which produces an intimate homogeneous mixture of both

powders on the scale of a few cubic micrometers, also modifies their characteristics, in particular affecting the flowability of the resulting powder, and causing the formation of agglomerates.

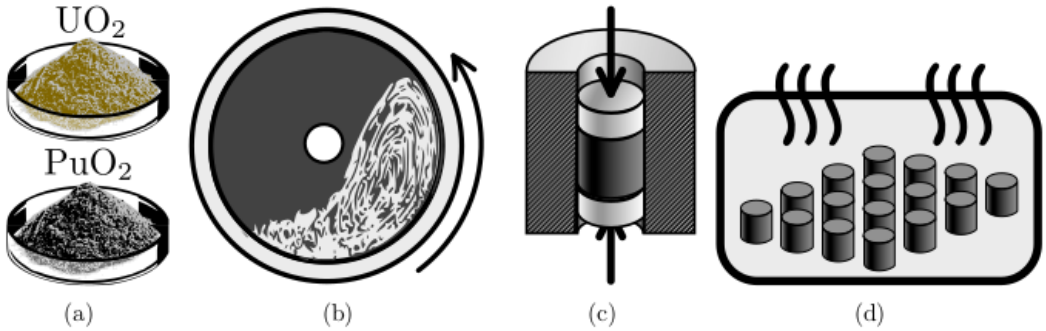

Fig. 0-2. The main steps of MOX pellet fabrication with (a) raw materials, (b) powder blending, (c) pelletizing and (d) sintering.

To improve the performance of milled powders while minimizing the energy cost, the grinding process is a major subject of current research. The complexity of this process in rotating drums has two main sources. The first one concerns the dynamic and inhomogeneous nature of flows in the drum geometry, which depends on various parameters such as rotation speed, filling degree, particle size, drum size, and the number and size of grinding balls. The second factor is the complexity of the material composed of particles of various shapes and sizes and interacting through cohesive-frictional interactions. Previous studies are largely empirical and the phenomena of flow inside the rotating drum and commutation are poorly understood [2–6]. Neither a change of scale, nor an increase in rates by optimizing the parameters is possible. However, as the constraints on the implementation of nuclear materials continues to grow, it becomes very difficult to multiply the experiments. Several constraints must be taken into account. In particular, small amounts of the material can be held under controlled conditions, requiring sealed environment to avoid all kind of contamination and the equipment must be specialized.

Under these conditions, particle dynamics simulations based on the Discrete Element Method (DEM) provide a truly precious tool for a detailed study of the physical mechanisms involved in the milling process. However, it requires high physics-fidelity models of the material and high-performance computations allowing for a meaningful representation of the granular material. In previous numerical studies (thesis L. Orozco 2016-2019 [7]), an approach was developed to model dynamic fragmentation of particles in 3D and single-particle fracture was studied. The numerical method was Contact Dynamics, which is based on nonsmooth modeling of frictional contacts with an implicite integration of the equations of motion. Its use for the simulations of grinding in rotating drums was limited by difficulties of its efficient parallelization. It was, however, shown that the bonded cell method with a rupture criterion based on fracture energy provides realistic and scalable particle breakage. The 3D studies were therefore limited to spherical particles in rotating drums for the scaling of cascading flows. The process of grinding was also studied in 2D with breakable polygonal particles. Several relationships between surface profile, thickness of the active layer, sliding at the walls and variability of the forces were iden-

tified, and a new scaling parameter was proposed for both breakage rate and flow characteristics. These results already put into perspective certain experimental observations which were poorly understood until then. They showed that simulations of granular flows with particle breakage in rotating drums provides a powerful means to investigate the grinding process.

This thesis work represents an extension of the previous work with the goal of developing advanced particle simulations based on DEM to investigate quasistatic and dynamic granular flows of polyhedral-shaped particles and modeling particle breakage for the simulation of the comminution process in rotating drums. To improve computational performance, a different approach to DEM based on the penalty method is necessary to allow for massively parallel simulations. For this reason, new numerical developments are made to reformulate the representation and fragmentation model of particles by accounting for particle shape and fracture energy in the new framework. We use the simulation code called *Rockable*, developed by V. Richefeu in Grenoble and made available within a collaborative project involving four institutions (CNRS, CEA, INRAE, and University of Montpellier). The key components of this code are 1) the representation of arbitrary particle shapes as sphero-polyhedra, 2) a fast contact detection algorithm, and 3) the explicite differentiation between different types of contacts (face-face, face-edge...) between polyhedra. To further reduce computation time, new developments were necessary during this doctoral work to optimize contact detection (between cylindrical walls of the rotating drum and polyhedra, for example) and to implement fully periodic boundary conditions with the possibility of controlling either displacement or pressure in every space direction. Periodic boundary conditions are also used along the rotating drum axis. Furthermore, the code is parallelized and run efficiently on multiple processors.

As in the previous thesis, extensive parametric simulations are performed to identify a general scaling of flow characteristics in the drum geometry. These characteristics are flow thickness in the active layer, the shape of the free surface flow, and inertial number in the flowing layer. As we use for the first time polyhedral particles in this thesis, we also compare the scaling law with those previously proposed for spherical particles in the cascading regime. For that, we use the data of L. Orozco's thesis. Since our simulation method differs from that used in that thesis, this comparison provides also elements of comparison between the two methods. Another novelty of our study is the inclusion of a particle-coarsening argument for the derivation of the scaling law.

Part of this thesis work is devoted to quasistatic deformations granular materials composed of polyhedral particles. We use fully periodic boundary conditions to study the quasi-static behavior for several polyhedral particle shapes (octahedra, dodecahedra, icosahedra) as well as spherical particles. We determine for the first time the five orthotropic elastic moduli of our samples during triaxial compression by applying small strain probes at regular intervals of evolution of the samples. We also analyze the evolution of the microstructure and the correlation between the elastic moduli and the microstructure for four different values of the friction coefficient. Our results clearly evidence the role of coordination number and fabric anisotropy and the effect of particle shape through several parameters involved in the linear correlation between

elastic moduli and microstructure. These results are compared with the predictions of the effective medium theory that we apply to our triaxial configuration. Although quasi-static conditions are not directly related to the problem of grinding in rotating drums, this investigation provides a framework to analyze in the next step particle fragmentation and its effect on the rheology under periodic boundary conditions. The passive state in rotating drum undergoes quasi-static deformations and an aspect of grinding concerns precisely autogenic fragmentation of the particles in this zone. Quasi-static particle fracture can also be used for comparison between simulations and experiments under tomography and used for the validation and/or calibration of the breakage model.

For particle fragmentation, we developed a new model in the framework of the bonded cell method. In this method, the particles are tessellated into irregular convex cells and a fracture model is attributed to the interfaces between cells. The advantage of the bonded cell method is to account for the distribution of stresses inside each particle, but its success crucially depends on the fracture model. The model developed in this thesis is based on fracture energy. Since the face-face links between the cells are modeled as multiple contact points, the total tensile elastic energy stored in the linear springs attributed to each contact point is compared with the fracture energy of the interface. The interface is broken if the elastic energy exceeds the fracture energy. This criterion is equivalent to Griffith's criterion of crack propagation. We perform extensive simulations of single particle breakage and compare the results with those previously obtained by L. Orozco. In particular, the scaling of the effective restitution coefficient and the total energy dissipated by fracture as a function of impact velocity and fracture energy is at the focus of this work.

This PhD dissertation is organized in several chapters. First, a literature review on granular materials as well as the numerical methodology are presented in Chapter 1. We introduce the physical and mechanical properties of granular flows in representative volume element and rotating drums. We also present several important findings of particle fragmentation process from previous research studies that are relevant to the research work presented in this document.

In Chapter 2, the effect of faceted particle shape on the elastic behavior of granular packings will be studied in the framework of particle dynamics simulations based on DEM. By comparing the simulation data with effective medium theory, we propose a general analytical expression that nicely predicts the elastic moduli as a function of two microstructural parameters: 1) a constraint number that accounts for contact types (face-face and face-edge contacts between polyhedra) and is reduced to coordination number for spherical particles, and 2) the contact orientation anisotropy. This expression quantifies both the direct effect of particle shape through our model parameters and indirect effect through microstructure.

In Chapter 3, we study the rheology and scaling of granular flows in a rotating drum partially filled with polyhedral particles. We use the same numerical method presented in Chapter 2 to perform extensive simulations for a wide range of values of drum diameter, particle diameter, rotation speed, and filling degree. We focus on cascading regime due to its important role in industrial processes and the lack of systematic analysis of its variables. We find a dimensionless

scaling parameter that accounts for the effect of all system parameters by a detailed analysis of flow variables such as the average and maximum slopes of free surface, flow thickness, shear rate and inertia number in the flowing layer. This chapter presents the particle-coarsening method and we show that it is consistent with our scaling of flow variables.

In Chapter 4, by means of Bonded Cell Method the impact-induced fracture of a single particle is analyzed. We introduce a breakage model fully based on fracture energy, in which a cell-cell interface breaks only if elastic energy stored in whole interface exceeds the fracture energy of the interface. We analyze the impact process with its distinct regimes, as well as transition between the regimes based on the breakage variables such as restitution coefficient, particle damage, and fracture efficiency. We propose also fitting forms that predict the evolution of breakage variables as a function of impact energy. We study the distribution of fragment masses and their shapes as a function of fracture energy.

The last chapter 5 outlines conclusions, salient results, and perspectives of this PhD work.

Finally, Appendices (A-D) present a detailed analysis of the evolution of the microstructure in simulations used in Chapter 2 for the investigation of elastic behavior.

We also include an extended abstract of the PhD work in French.

Chapter 1

Literature review

Contents

1.1 Granular flows

The behavior of assemblies of grains can be complex even in the simple case of dry cohesionless particles. When grain size is large enough (d $>$ 250 μm) and the surrounding fluid is not too viscous, the particle interactions are dominated by contact interactions. Capillary forces, van der Waals forces or viscous interactions can be neglected and the mechanical properties of the material are only controlled by the momentum transfer during collision or frictional contacts between grains.

However, the flows of these dry granular materials are not easy to describe. They are usually divided into three classes depending on the flow velocity. First, the dense quasi-static regime where the deformations are very slow and the particles interact via frictional contacts. This regime is often described by elasticity and plasticity theories [8]. Secondly, a gas-like regime exits when the medium is strongly agitated and the grains are far apart one from another, in which case particles interact through binary collisions [9]. The intermediate liquid regime, where the granular material is dense but still flows like a liquid, and the particles interact by both collisions and frictional contacts. This is the least understood regime [10, 11]. These different flow regimes can coexist in a single configuration as shown by the flow of beads on a pile in Fig. 1-1.

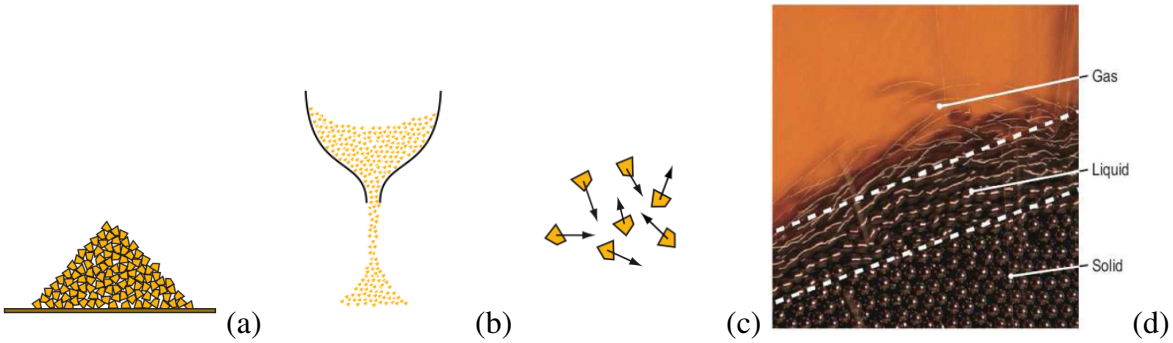

Fig. 1-1. Three phases of granular flows, behaving like (a) a solid, (b) a liquid, (c) a gas. Panel (d) illustrates the pouring of steel beans on a pile, where all three phases can be observed.

It is interesting to mention that the local dynamical properties of flows depend only upon a single dimensionless variable called *inertia number*, which is defined as

$$I = \dot{\gamma} d (\rho / p)^{1/2}, \tag{1.1}$$

where d is mean particle diameter, ρ is material density, p is local pressure and $\dot{\gamma}$ is strain rate. The inertia number measures the local mobility of particles. Small values of I correspond to a quasi-static regime in the sense that macroscopic deformation is slow compared to microscopic rearrangement, whereas large values of I correspond to rapid flow. This inertial number is also equivalent to the square root of the Savage number or Coulomb number introduced by several authors [12, 13]. Importantly, for rigid particles, the shear stress is proportional to the pressure, with the effective friction coefficient and the solid fraction being functions of I, $\tau = p\mu(I)$ and $\Phi = \Phi(I)$.

1.1.1 Quasi-static regime: triaxial compression

In the limit of quasi-static flows $I \to 0$ ($I < 10^{-3}$), the effective friction coefficient μ and solid fraction Φ tend toward a constant value independent of I. In this regime, the behavior under load can be described as a succession of static configurations of particles and stable force networks that slowly evolve with deformation. Here, we briefly introduce an example of quasi-static regime achieved by triaxial shearing and described as elastic and plastic behavior. Macroscopic phenomenological laws have been proposed for this regime in soil mechanics, and more recently the particle-scale variables have been investigated by means of DEM simulations, but the relationship between the macroscopic behavior and grain-level physical phenomena has not yet been fully understood [14–17].

In triaxial experiments in soil mechanics, samples are subjected to axisymmetric states of stress, the axial stress σ_1, or the axial strain ε_1, is controlled via the relative motion of the end platens, while the lateral pressure $p_0 = \sigma_2 = \sigma_3$ is imposed through a flexible membrane by a fluid; see Fig. 1-2(a). In a typical triaxial compression, one starts from a given state, e.g, prepared under isostatic stress. Then, most often ε_1 is increased at a constant slow rate, while lateral pressure p_0 is maintained constant. Axial stress σ_1 or deviator $q = (\sigma_1 - p_0)/3$, and lateral strain $\varepsilon_2 = \varepsilon_3$ or volumetric strain $\varepsilon_v = -tr(\boldsymbol{\varepsilon})$ are measured. Evolution of q and ε_v as ε_1 monotonically increases are schematically represented in Fig. 1-2(b). In a loose sample, the packing fraction and deviator gradually increase, until residual constant values are reached. In a dense sample, the deviator increases more quickly, reaches the peak and then decreases before reaching a constant value coinciding with that of the loose sample, whereas the sample is initially contractant and then dilatant.

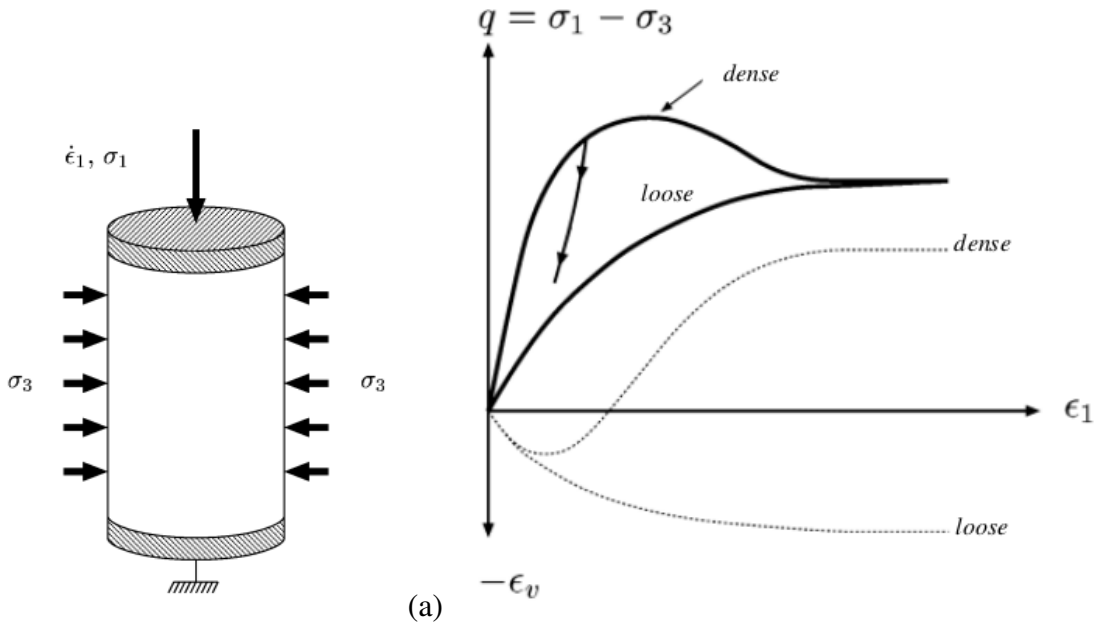

Fig. 1-2. (a) An illustration of triaxial experiment. (b) Variation of deviator q (solid lines) and volumetric strain ε_v (dotted lines) for a dense and a loose sample [8].

For $\varepsilon_1 > 10^{-5}$, the increase of q with ε_1 is not reversible. If the direction of deformation is reserved, the same curved is not retraced back, the decrease of the deviator is steeper, with a slope comparable to that of the tangent at the origin of coordinates in Fig. 1-2(b). As ε_1 increases, the curves approach a plateau, corresponding to an asymptotic state that is called the *critical state*, and is independent of the initial state [8,18]. The stress-strain path depends on the nature of the granular material. For example, the role of inter-particle friction coefficient μ_s in the stress-strain relationship during triaxial loading has been reported by several authors [19,20]. It is found that the maximum stress deviator increases with μ_s up to a value beyond which μ_s has not effect any more.

In parallel to the analysis of stress-strain relationship, microscopic studies have tried to define internal state variables of granular systems and to relate them to stresses and strains. For instance, the density of contacts and some parametrization of the distribution of their orientation called *fabric* or *texture* have been studied. Their evolution can be related to the strain and their values can be correlated to the supported stress orientations [18, 21–24]. Furthermore, the solid fraction Φ, as a geometrical property, is a state variable. When free volume changes are allowed (volume change allowed), the solid fraction evolves with the applied deviatoric strain rate $\dot{\varepsilon}_q$. Reynold's dilatancy refers to the incremental volume change produced by shearing and characterized generally by a dilation angle ψ, $\sin\psi = -(2\dot{\varepsilon}_v + \dot{\varepsilon}_q)/3\dot{\varepsilon}_q$. The negative sign here ensures that negative values of the dilation angle correspond to contraction. The dilation angle ψ is thus a basic plastic flow property of a granular material, and like the internal angle of friction φ, $\sin\varphi = 3q/(2p+q)$, where $p = (\sigma_1 + \sigma_2 + \sigma_3)/3$ is mean stress, it has to be specified as a function of the fabric. While the internal angle of friction φ basically reflects the Coulomb's friction law (at the contact scale), the dilation angle ψ is a purely structural property which has no counterpart at the contact scale for spherical particles [25]. The variation of ψ versus φ, a sort of stress-dilatancy diagram, has been proposed as flow rule for plastic deformations of granular media [26].

1.1.2 Nonaffine displacement field

In granular systems, the physics of deformations at the microscopic level is very different from that of perfect crystals. Under an infinitesimal constant shear, the particles will move and settle into new equilibrium positions. For a crystalline solid, it is natural to suppose that the new positions of the particles are related to the old positions by a simple *affine* transformation that can be calculated from the strain tensor. Nevertheless, in disordered systems, no such affine transformations exists. In fact, there is a net nonzero force acting on each particle in its affine position. An extra (*nonaffine*) displacement away from the affine position is needed in order to maintain the mechanical equilibrium throughout the deformation. The nonaffine displacement provide an additional contribution to the standard displacement field of elasticity theory. The nonaffine part of the displacement field is random and does not possess any particular symmetry [27].

Figure 1-3 displays the rearrangement or displacements of particles upon the application of

an external shear strain. If the deformation is affine, particles which sit exactly on dashed lines in the underformed frame (Fig.1-3(a)) would still sit exactly on the dashed line of deformed frame (Fig.1-3(b)). However, the particles that are sitting on the dashed lines in the underformed frame are no longer sitting on the dashed lines in the deformed frame, but are displaced from them. The distance from the actual positions of the atoms to the dashed line corresponds to the nonaffine displacements.

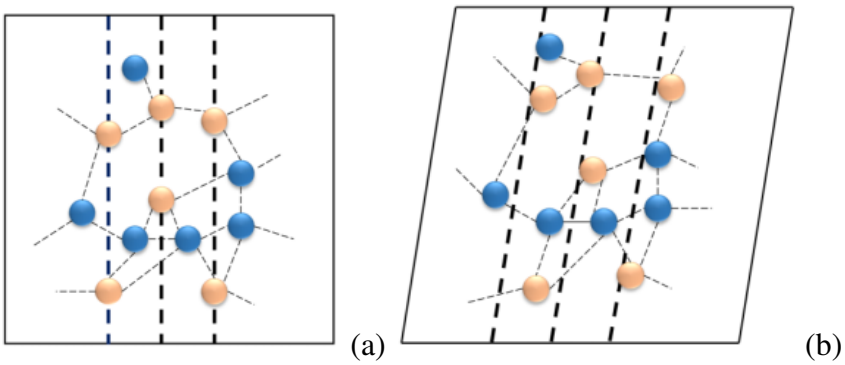

Fig. 1-3. An illustration of nonaffine displacement in disorder systems. Position of particles (a) before shearing and (b) after shearing [27].

One can observe the nonaffine deformation in granular media when the large-scale affine deformation, is subtracted from the displacement field. Some examples of such observations can be found in variety of works. Radjai and Roux showed that the nonaffine granular motions are similar to those observed in fluids undergoing turbulence [28, 29]. Peters and Walizer studied nonaffine displacements in biaxial test, denoted as swirls, consist of rotational motions that satisfy the kinematic boundary conditions. They proved that the sliding motion can be represented as the sum of an affine motion and rotation [30], see Fig. 1-4.

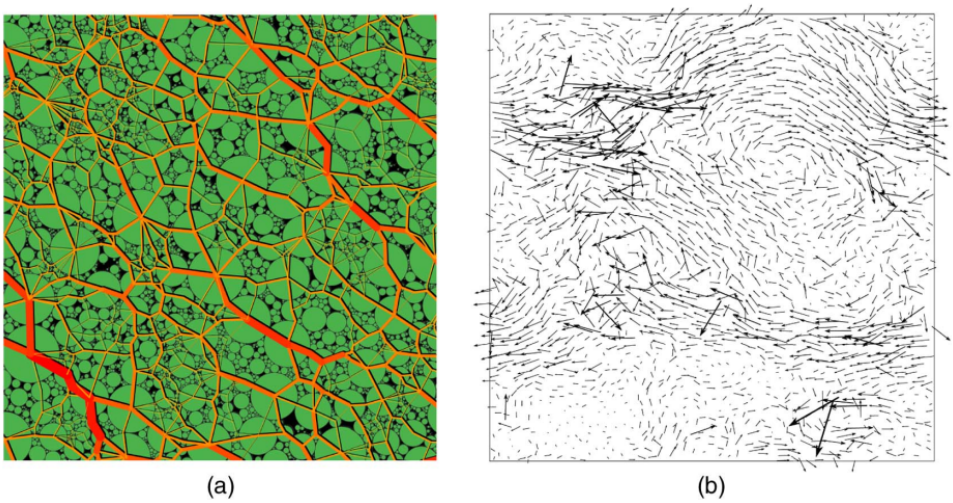

Fig. 1-4. (a) Map of normal forces in a polydisperse packing of disks, line thickness is propotional to normal force; (b) map of nonaffine particle displacement in a sheared packing of disks [29].

1.1.3 Elastic moduli of spherical particle packings

The role of nonaffine displacement in elastic moduli has been discussed in several studies in the vcase of isotropic packings of disks [26, 31], spheres [32–34], and anisotropic packings under oedometric compression (compression along one axis with no lateral strain) [35]. These studies indicate that nonaffine displacements make packings softer, in the sense that the elastic moduli are reduced. The reduction is especially important for shear modulus, while for bulk modulus, the nonaffine effect is less pronounced for geometrical reasons due to the local excluded-volume packing constraints [36–39]. It is worth noting that the elastic moduli are bounded between an upper bound called Voigt approximation based on the uniform strain assumption and a lower bound called Reuss approximation based on uniform stress assumption [40, 41]. The Voigt approximation also refers to *Effective Medium Theory (EMT)*, in which an affine field of particle displacements is assumed, and determined by the macroscopic strain. In the Reuss approximation, the force field is calculated by macroscopic stress, and the elastic energy is written as a function of force increment.

For isotropic assemblies of disks, the upper bounds of the bulk and shear modulus predicted by by EMT are given by [31],

$$\begin{cases} \dfrac{K}{k_n} = \dfrac{n_s \Gamma}{8} \overline{l^2}, \\ \dfrac{G}{k_n} = \dfrac{n_s \Gamma}{16} \left(1 + \dfrac{k_t}{k_n}\right) \overline{l^2}, \end{cases} \tag{1.2}$$

where k_n, k_t are normal and tangential stiffness, respectively, n_s is contact density which is the average number of particles per unit volume, Γ is coordination number which is the average number of contacts per particle, and $\overline{l^2}$ is average over all contacts of the squared length of the branch vector. These predictions can be improved by including the fluctuations from average strain, namely the particle fluctuations and pair fluctuations.

For isotropic spherical particle packings, Zacconne et al [27, 42] proposed an expression for bulk and shear modulus for spherical particles based on the approximate Hessian matrix:

$$\begin{cases} K = \dfrac{1}{18} \dfrac{N}{V} \kappa R_0^2 (Z - 6), \\ G = \dfrac{1}{30} \dfrac{N}{V} \kappa R_0^2 (Z - 6), \end{cases} \tag{1.3}$$

where N is number of particles, V is volume of packing, κ is stiffness of contact, R_0 is branch vector length, and Z is coordination number. Generalizing the result to arbitrary space dimensions gives the scaling for the moduli in d dimensions $G \sim K \sim (Z - 2d)$. The negative term in Eq. (1.3) due to nonaffine displacement makes the moduli vanish at the isostatic state ($Z = 6$). The reason for this might be identified with the fact that in their theory, just like in networks, excluded volume effects are irrelevant while they are important in packings of rigid particles. However, people claimed that by observing in simulations many times Eq. (1.3) is not correct for K, which, unlike G does not vanish as the minimum (isostatic) value of Z is approached.

The bulk modulus K jumps from 0 in the gas phase toward a constant value when the system becomes jammed [43].

The elastic moduli of a packing of elasto-frictional Hertz-Mindlin spherical grains can also be predicted using EMT. The main prediction of the theory is the scaling of bulk and shear modulus with pressure as $G \sim K \sim p^{1/3}$ [32, 44]. For the case of frictionless grains, one finds

$$\begin{cases} K = \dfrac{k_n}{12\pi}(\Phi Z)^{2/3}\left(\dfrac{6\pi p}{k_n}\right)^{1/3}, \\ G = \dfrac{k_n}{20\pi}(\Phi Z)^{2/3}\left(\dfrac{6\pi p}{k_n}\right)^{1/3}. \end{cases} \tag{1.4}$$

For frictional grains, tangential elastic forces are taken into consideration. Note that bulk modulus is not affected by the introduction of tangential forces, but the shear modulus is modified to

$$G = \frac{k_n + (3/2)k_t}{20\pi}(\Phi Z)^{2/3}\left(\frac{6\pi p}{k_n}\right)^{1/3}. \tag{1.5}$$

It is also possible to calculate a lower bound bulk modulus (analogous to the Reuss bound), in the case of Hertzian contacts:

$$K = \frac{1}{2Z(5/3)}\left(\frac{\Phi Z\tilde{E}}{3\pi}\right)^{2/3} p^{1/3}, \tag{1.6}$$

and for linear contact elasticity, the corresponding prediction is

$$K = \frac{\Phi Z k_n}{3\pi a Z(2)}, \tag{1.7}$$

where $Z(5/3)$ and $Z(2)$ are dimensionless quantities given by $Z(\alpha) = \langle N^\alpha \rangle / \langle N \rangle^\alpha$, where N is normal contact force, a is average particle diameter, $\tilde{E} = E/(1-\nu^2)$ with E being the Young modulus of the material, and ν is Poisson's ratio [32, 35, 45]. For shear modulus, no Reuss estimate is available. More elaborate prediction methods for elastic moduli were proposed. Kruyt and Rothenburg consider two-dimensional assemblies of nonrotating particles [41]. Velicky and Caroli studied the case of an imperfect lattice system with contact disorder [46]. Jenkins et al. dealt with frictionless sphere packings [47].

For anisotropic systems, Khalili et al. have studied how the elastic properties reflect the evolution of their internal state under oedometric compression (compression along one axis, with no lateral strain) [35]. It is observed that the elastic moduli, as in isotropic packings, are primarily determined by the coordination number. In addition, the anisotropy of the elastic moduli matrix is related to the anisotropies of both the contact network (the fabric) and the angular force distribution. In order to reach more general conclusions on possible anisotropic states and connections between elasticity, fabric and force anisotropies, it is necessary to explore different states and microstructures, and to vary stresses and fabric independently, by using triaxial loading, for example.

1.1.4 Rheology of particle flow in rotating drums

Rotating drums are widely used to process granular materials in a great variety of industries such as pharmaceutical, food processing, polymer, ceramic, metallurgical, solid waste treatment, etc [48–50]. Due to their facility of using and heat transfer efficiency, as well as their ability to handle heterogeneous feedstock, they are used in a broad range of processes such as size reduction, sintering, mixing, drying, heating, cooling and chemical reactions. However, the dynamics and rheology of granular materials in rotating drums remains challenging because of the complex of particle flow combining the upward rigid-body motion of the particles at the drum wall, downward bulk flow and free surface dynamics. Moreover, in a single rotating drum configuration, different flow regime can be identified. For instance, a solid-like regime that is characterized by dense quasi-static flow can be found in regions located close to drum wall, where the deformations are very slow and the enduring multiparticle contacts are governed by friction. At the free surface, the flows are in gas-like fluidized state that is characterized by very rapid and dilute flows in which the particles interact mainly by collision, while in the intermediate region, a liquid-like state, which is also densely packed but still able to flow like a liquid with particles interacting through both frictional and collisional contacts, can be found. A common classification of flows inside rotating drums includes six different regimes as a function of the *Froude number* :

$$\mathrm{Fr} = \frac{\omega^2 R}{g}, \tag{1.8}$$

where ω is rotation speed, R is drum radius and g is the gravity acceleration [51–57]; Fig. 1-5.

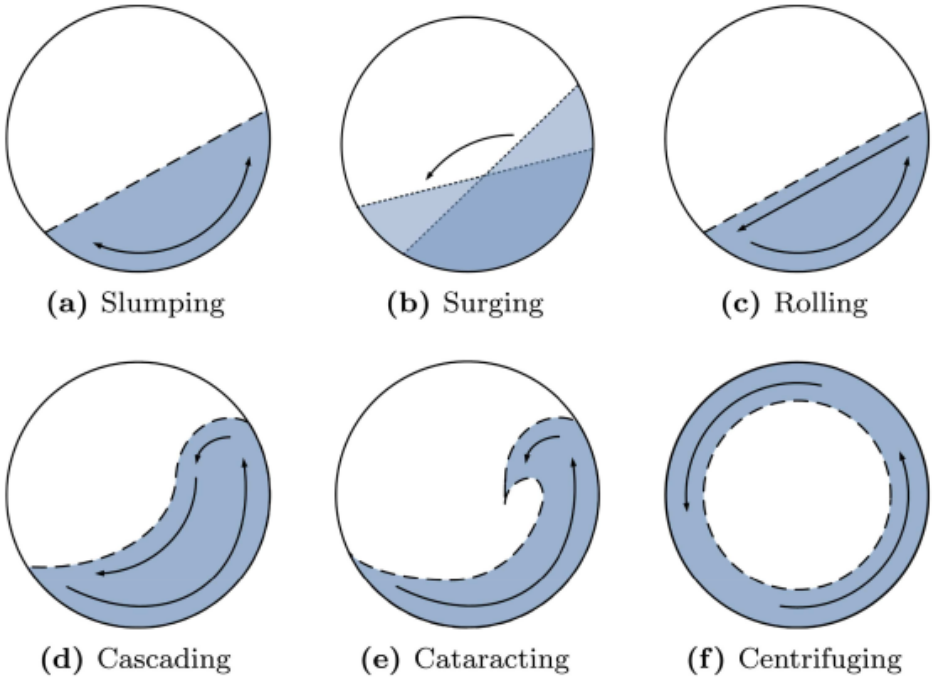

Fig. 1-5. Six flow regimes of granular materials in a rotating drum.

The flow regimes are not only dependent on Fr, but also the filling rate and the friction

coefficient between particles and drum walls. With a small value of Fr and smooth cylinder walls, the *slumping (sliding)* regime can occur. The particles move as a block that slides and oscillates on the drum wall. When the wall friction is increased, the sliding regime turns to *surging* regime, where the granular bed adheres to the rotating wall up to a high angle and subsequently slides back to the lowest position of the drum [58–60]. The first two regimes have no application in industry because the mixing of particles does not take place. With the increase of rotation speed or wall friction, the *rolling* regime can be observed, in which the particles avalanche downward on the free surface due to gravity, while they are transported upward by solid body rotation with the rotation of drum near the drum wall. The free surface is flat with a dynamic slope and the regime can be decomposed into two layer, namely active and passive layers [61–64].

The *cascading* regime is observed for larger values of Froude number. The particles cascade downward and free surface of granular flow has a curved shape [52,65–68]. For further increase of Fr, the flow enters the *cataracting* regime, where the particles undergo ballistic motion and they collide with the downstream part of free surface [69–72]. For even larger value of Fr, the particles begin to adhere to the drum wall and the *centrifuging* regime is observed [73–75]. In granulation process, the particles should be well mixed and undergo fluctuating motions that can trigger the particle collision. Thus, the intermediate state between rolling and cataracting regimes are appropriate geometries for industrial application.

Several studies suggest that the Froude number is insufficient for classifying granular flow in rotating drums as it does not account for finite size effect and filling degree that affect features such as active layer thickness, and surface velocity. Moreover, there is no exact method to predict the transition between the different forms of flow regimes. By using semi-empirical relations, the six modes of bed motion had been represented on a *Bed Behavior Diagram* for different solids rotated in cylinders of different size [56]. This diagram was corrected gradually by Mellmann's work by accounting for more parameters that can influence on the transition of regimes [53]. He indicated that the motion behavior can be represented on a diagram that plots wall friction coefficient and Froude number against the filling degree. He found that in principle, the motion behavior of the bed materials is similar except for the slumping-rolling and rolling-cascading transitions that could differ in shifting to lower Froude number.

The transition to centrifuging granular flow in rotating tumblers was studied by Juarez et al. [74]. They showed that the critical rotational speed for dry systems is not affected by particle diameter unless the fill fraction is above 75%, where endwall friction begins to play a significant role, and it is proportional to fill fraction. Félix et al. [76] worked on the transition from rolling to cascading regime. The free surface shape had been characterized by the parameter $\Delta\theta = \theta_{mean} - \theta_{min}$, as shown in Fig. 1-6. This means that the free surface becomes curved when $\Delta\theta > 0$. They also showed that the transition takes place when the particle accelerations reach a value equal to 6% of the maximal acceleration down an inclined plane $g\sin\theta$. Ding et al. [77] suggested that the transition from slumping to rolling regime occurs when the two turnover times are equal, where the turnover time is defined as the time required to turn the whole particle

bed over once. The Froude number based upon the bed turnover frequency is shown to be more appropriate in constructing the bed behavior diagram than that based on the rotation speed.

The rheology of granular flow has been investigated in both 2D and 3D in rotating drums by means of experiments and simulations for different types of particle shape varying from spherical to aspherical particles. Most of numerical researches conducted with the DEM involve spheres due to their simplicity in terms of contact detection, which results in lowest possible computing time. The drawback of using spherical particles is that most industrial granular materials exhibit a significantly different shape. Recently, aspherical particles have been modeled and used in simulations examples of which are superellipsoids [68, 78], superquadrics [79–81], clumps or glued shepres [82–84], and non-convex polyhedra [82].

A study that compares different particle shapes inside a rotating drum indicated that an increase of particle angularity leads to an increase of the dynamic angle of free surface, see Fig. 1-6. On the other hand, while spheres mix faster than the polyhedral dices, no significant difference in the mixing behaviors of the dices can be observed [85]. It was also found that particle aspect ratio had no significant effect on the thermal conduction properties of the system whereas shape irregularity had the most pronounced effect [86]. Another experimental study was carried out to compare the mixing process in rotating drum of spheres and non-spherical tablets [87]. They found that particles having an aspect ratio larger than two can lead to significant deviations in velocity profile and residence time. In addition, the non-spherical particle higher degree of spatial orientation in the active layer leads to a lower axial dispersion coefficient than the ones obtained with spherical particles. In 2D, the effect of polygonal particles to mixing process was studied [88]. The mixing index indicates higher mixing degree for the square, hexagonal, triangular shapes, and the kinetic energy increases with number of polygonal particles sides. Despite these studies based on DEM, the dynamics and rheology of granular flows of aspherical particles in rotating drums as a function of particle shape has not been investigated on a systematic basis. More generally, it is desirable to understand the scaling behavior for a range system parameters such as Froude number, drum size, particle size, and filling degree for various particle shapes [65].

Another issue concerns segregation and mixing in rotating drums. Particle size is not the only factor responsible for the segregation of materials in rotating drum, but the particle mass plays also an important role [65, 89]. The question of whether density or particle size are the dominant segregation mechanism was answered by Jain et al. [90]. If the core is composed of denser beads, then segregation is dominated by density, if the core is composed of smaller beads, the segregation is dominated by size. It was also found that in order to achieve a correct mixing in system with particles of different sizes and densities, the best strategy is to have larger particles with higher density compared to smaller ones. Moreover, several researches investigated the effect of polydispersity on granular flow, mixing and segregation [91–94]. The results revealed similar velocity profiles and residence times for monodisperse and polydisperse systems, but the small particles tend to remain in the bed core while the bigger ones flow around [94].

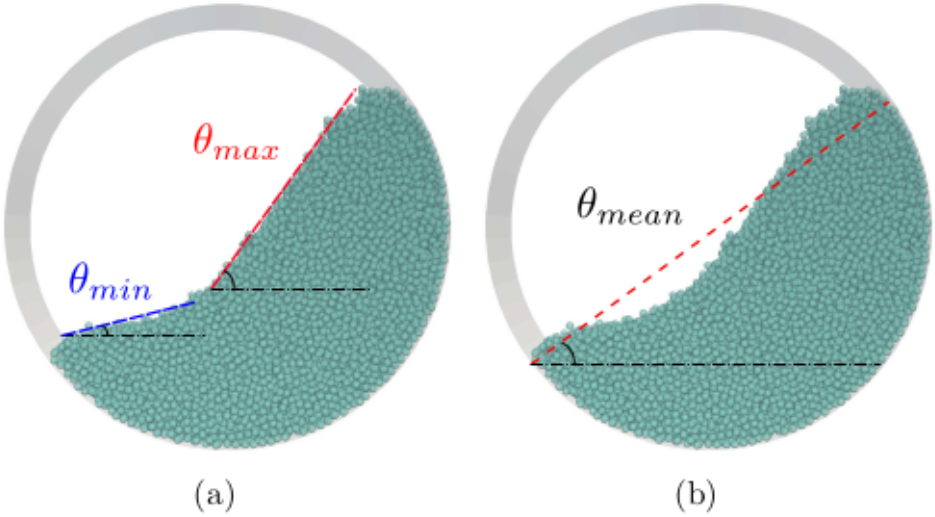

Fig. 1-6. Different dynamic angles of free surface that can be defined in a rotating drum geometry: (a) maximum and minimum, (b) average.

1.1.5 Scaling law in rotating drums

In mixing and/or grinding applications, a key issue is the increase of the linear dimensions from the laboratory to the plant size. This process is called *scale-up*, which is generally defined as a procedure for applying the same process to different output volumes. There are several scale-up issues such as scaling based on wrong unit operation mechanisms, insufficient knowledge of process, or even changes in the product or process during scale-up. In order to eliminate these problems, one needs to understand what makes the processes similar. Dimensional analysis can be used in scale-up process. It is a method for producing dimensionless number that completely characterizes the process. According to the theory of models, two processes may be considered completely similar if they take place in similar geometrical space and if all the dimensionless numbers necessary to describe the process have the same numerical value [95]. Then, the process is expressed by using a complete set of dimensionless numbers, and match them at different scales [96].

Dimensionless numbers, such as Froude number Fr, are frequently used to describe granular flows in rotating drums. However, most scalings based on Fr for scaling purposes do not account for essential parameters like filling degree and particle size. Some of the parameters that should be accounted for in scale-up process are the dynamic angle of repose θ, the active layer thickness, and the total kinetic energy. The relationships between layer thickness, free surface profile, dynamic angle of repose, angular speed, cylinder radius and particle diameter have been considered in several works [97–101]. Other studies were concerned about dimensionless flow rate [11, 102], and impact energy [103].

Taberlet et al. [99] proposed a parameter Λ which includes most relevant parameters: parti-

cle size d, drum length W, and drum radius R, rotation speed, and gravity.

$$\Lambda = \left(\mathrm{Fr}\frac{d}{R}\right)^{1/4}\frac{R}{W}. \tag{1.9}$$

In this study, the shape of the free surfacewas found to changes as a function of the drum length or friction with the end walls. It was shown that the frictional end plates have a major and nontrivial influence on the shape of a granular flow in rotating drum. Pignatel et al. [102] found that the flowing layer thickness and the dynamic angle of repose scale with the dimensionless flow rate Q^*. In the dry case, Q^*_{dry} is given by

$$Q^*_{dry} = \frac{1}{2}\mathrm{Fr}^{1/2}\left(\frac{R}{d}\right)^{3/2}. \tag{1.10}$$

In the case of immersed flows in a viscous liquid, the dimensionless flow rate must be modified

$$Q^*_{dry} = \frac{1}{2}\mathrm{Fr}^{1/2}\left(\frac{R}{d}\right)^{3/2}\left(\frac{\rho_p}{\Delta\rho}\right)^{1/2}\left(1+\frac{1}{St}\right), \tag{1.11}$$

where $\Delta\rho$ is the difference of density between liquid and solid particle (ρ_p), and St is the Stokes number, defined as the ratio of viscous time to flow time.

Orozco et al. [65] introduced the scaling parameter Υ which includes filling degree J, and is given by

$$\Upsilon = \mathrm{Fr}^{1/4}\left(\frac{R}{d}\right)^{1/2}J. \tag{1.12}$$

They proved that the parameter Υ scales well the slope ratio and force variability, and can be used to upscale drum size from laboratory to industrial scale. Note that this study was concerned with the cascading regime, and the width of the drum had no effect due to periodic lateral boundaries.

In spite of multiple efforts to obtain a general scaling law, a full agreement on the scale-up of flow regimes in rotating drums has not been achieved yet. The difficulty of finding a unique general expression valid for all cases resides in the large number of system parameters involved and the system's intrinsic heterogeneity.

1.2 Particle fragmentation

Particle breakage occurs commonly in natural granular flows and industrial processes involving the transport, handling, and compaction of granular materials. Particle size reduction can be undesirable or uncontrolled, and it is referred to as the attrition process like in rock fracture, ballast degradation, etc. In contrast, the fragmentation of particles under controlled conditions is used in comminution processes such as the grinding of mineral materials, and milling of vegetal products. Due to dependence on many factors of the evolution of particle size distribution and energy dissipation, there is not yet a clear quantitative understanding of its origins at the particle scale. For this reason, it is necessary to broaden the horizons in terms of the effects

of various parameters that control fracture-induced phenomena independently of the specific crushing or grinding machines employed in different applications. The fragmentation process in an assembly of particles subjected to shearing or compaction and particles in ball mills can be investigated experimentally [104–108]. However, numerical simulations based on DEM should be used for a better understanding of this process and its impact on the macroscopic behavior.

1.2.1 Single particle crushing

Studying the fracture of a single particle is the first step towards a quantitative description of the complex multi-particle fracture dynamics. The Finite Element Method (FEM) has been used by several authors to study single-particle fracture by incorporating the material behavior and an adequate damage or rupture criterion [109–111]. This method can help us to account for the true nature of the materials and provide an access to the full stress field in a continuum framework. Nevertheless, it requires rather a fine meshing of the particle at its borders or at least around its contact points with other particles and at crack tips. One more drawback is that its application to an assembly of particles requires a proper treatment of frictional contacts and large deformations, which make it computationally inefficient [112].

Another approach to deal with the problem is the method that combines the general framework of the DEM, based on particle dynamics and frictional interactions, with a particle fracture model. The advantage of DEM is to allow for the treatment of frictional contact interactions and provide detailed information about local particle environments and force chains that control the breakup events. This model can be classified at least two main groups. The first method is Bonded Particle Method (BPM), in which the particles are modeled as aggregates of spherical sub-particles bonded together by cohesive forces [113–117]. A major issue of this method is that the total volume of the material is not conserved during the fragmentation process due to the voids between spherical sub-particles. To address the volume loss issue, several authors have used polygonal or polyhedral sub-particles or cells generated by Voronoi tessellation, a method that is called Bonded Cell Method (BCM) [118, 119]. These cells pave the whole volume of the particle so that the volume is conserved during particle fragmentation. However, in such studies the intercell contacts are modeled by a linear force law as that between spherical sub-particles. This is clearly an unphysical approximation since the contacts extend along a line (in 2D) or a surface (in 3D) between cells and thus their treatment needs at least two or three displacement variables, respectively. Later, the issue of contact treatment was addressed in multiple studies by combining BCM with the contact dynamics (CD) method [112, 120, 121].

Another issue is that the rupture criterion should be compatible with fracture mechanics and themodynamics in which the fracture is fully based on energy. Apart from Orozco's work [121] using a fracture law combining material strength and fracture energy, nearly all studies reported in the literature are based on stress thresholds which lead to brittle behavior. Note that the simulations implemented in the framework of the Contact Dynamics Method (CDM) do not account for elastic deflections at contact points due to the fact that the sub-particles are considered as perfectly rigid particles, so the energy stored in elastic deformations is not

accounted. Moreover, it is not obvious that the work performed by external forces is dissipated since in CDM the dissipation is controlled by relative velocities rather than displacements.

In Orozco's work, a cell-cell interface loses its cohesion when it is at a normal or tangential stress threshold and an amount of work equal to the fracture energy is absorbed as a result of the relative cell-cell displacements. She analyzed the damage and fragmentation efficiency defined as the ratio of consumed fracture energy to the impact energy as a function of the impact energy and stress thresholds, and their scaling with fracture energy and impact force. It was shown that the fragmentation efficiency is unmonotonic as a function of the impact energy, and the highest efficiency, which is only 27% of supplied energy, occurs when the impact energy required to fracture the particle into its building cells is 1.81 times the total fracture energy of the particle.

Nguyen et al. [112] showed that the compressive strength scales well with tensile threshold between cells. However, due to the Mohr-Coulomb plastic criterion and interlocking between rigid cells, the strength is also an increasing function of the friction coefficient. the statistical scatter of the data is well described by the Weibull distribution function with a shape parameter varying from 6 to 10 depending on cell shape distribution:

$$\frac{\sigma_p}{\sigma_c} \sim n_v^{-(1-\alpha)/2} \sim d^{-(1-\alpha)}, \tag{1.13}$$

where σ_p and σ_c are the compressible and tensile strengths, respectively, n_v is number of cells, d is average cell diameter, and the exponent α may take a different value depending on the nature of the network. For this reason, the cells should be generated in a fully random way both in sizes and shapes. However, it was also confirmed that for $n_v > 100$ the fracture threshold is nearly independent of n_v, indicating that the number of meshes do not affect the fracture behavior of the particles if the latter is sufficiently high. Note that size effects in single particle fracture suggest that in an assembly of crushable particles the largest particles are most susceptible to break. However, particle size affects the local distribution of contacts forces. In particular, large particles have more contacts and sustain for this reason lower deviatoric stresses. Due to such competing effects, the fragmentation of a granular packing is a complex process that needs further investigation.

In impact fragmentation, a critical velocity that separates the particle response from damage to fragmentation, often referred to as a phase transition, was first identified by Thornton *et al.* [122] and later confirmed by several authors [123–126]. Timár *et al.* [127] performed a finite size scaling analysis to determine the critical exponents of the damage-fragmentation phase transition and deduced scaling relations in terms of radius of spherical solid bodies and impact velocity. They proposed that the total amount of damage D_{tot} has a power law dependence on impact velocity v_0 in the damage phase

$$D_{tot} \sim v_0^{\alpha}, \tag{1.14}$$

while in the fragmentation phase a critical behavior is obtained

$$D_{tot} \sim (v_0 - v_c)^{\alpha}. \tag{1.15}$$

The exponent α gets different values $\alpha_d = 4.45$ and $\alpha_f = 0.22$ in the damage and fragmentation states, respectively, see Fig. 1-7(a).

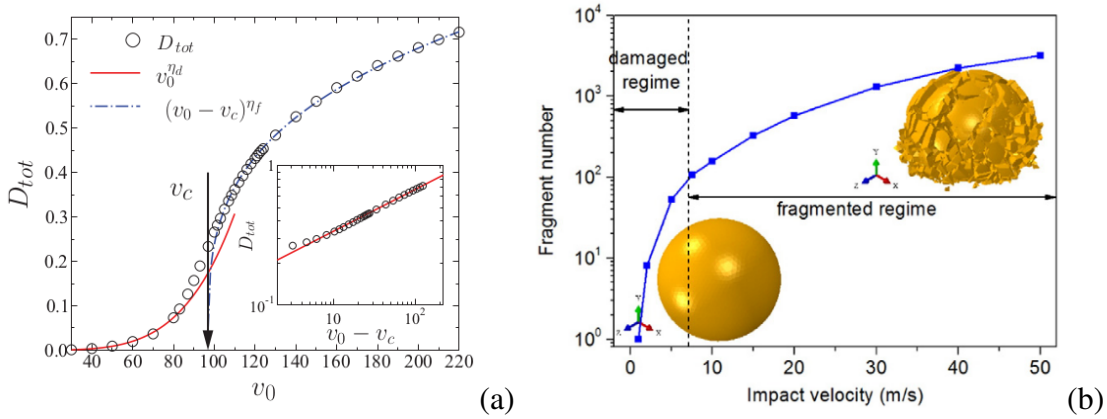

Fig. 1-7. (a) Total amount of damage as a function of the impact velocity. The vertical arrow indicates the critical impact velocity separating the damage and fragmentation states [127]. (b) Number of fragments in two fragmentation regimes [126].

For the effects of impact angle, one observes that the damage ratio (i.e. the number fraction of the broken bonds) depends on the normal component of the impact velocity only, the tangential component has little effect [124, 128]. The effects of material properties such as interface energy [129, 130], agglomerate packing density [131], dominant fracture mechanism [114], and material microstructure [132] on the fracture pattern and fragments mass distribution were also investigated. The impact breakage behavior of aspherical agglomerates as also been studies by DEM approaches [133, 134].

Laboratory impact experiments have found that impact fragments tend to be elongated. The shapes of fragments from catastrophic collisions defined by axes a, b, and c, these being the maximum dimensions of the fragment in three mutually orthogonal planes ($a \geq b \geq c$), are distributed around mean values of the axial ratio $b/a \simeq 0.7$ and $c/a \simeq 0.5$. This corresponds to $a : b : c$ in the simple proportion $2 : \sqrt{2} : 1$ [135, 136]. However, by carrying out the impact experiments, Michikami *et al.* [137] found that the mean value of c/a in each impact decreases with decreasing impact energy per unit target mass Q. For instance, the mean value of c/a in an impact cratering event is nearly 0.2, which is considerably smaller than c/a in catastrophic disruption (~ 0.5). On the other hand the mean b/a ratios seem to be roughly constant with Q, see Fig. 1-8. Matsushima *et al.* [138] describes a procedure used to characterize the three-dimensional grain shape of lunar soil. They indicated that the values of elongation ratio $b/a \simeq 0.723$, and flatness ratio $c/b \simeq 0.694$ implying that $c/a \simeq 0.502$, see Fig. 1-9.

Besides the axial ratio of fragments, one can use the surface to volume ratio $S_f = AR_q/V$ to characterize the shape of objects generated by fragmentation events, where A/V is surface-to-volume ratio, R_g is radius of gyration [139]. Assuming rectangular shape of fragments R_g reads

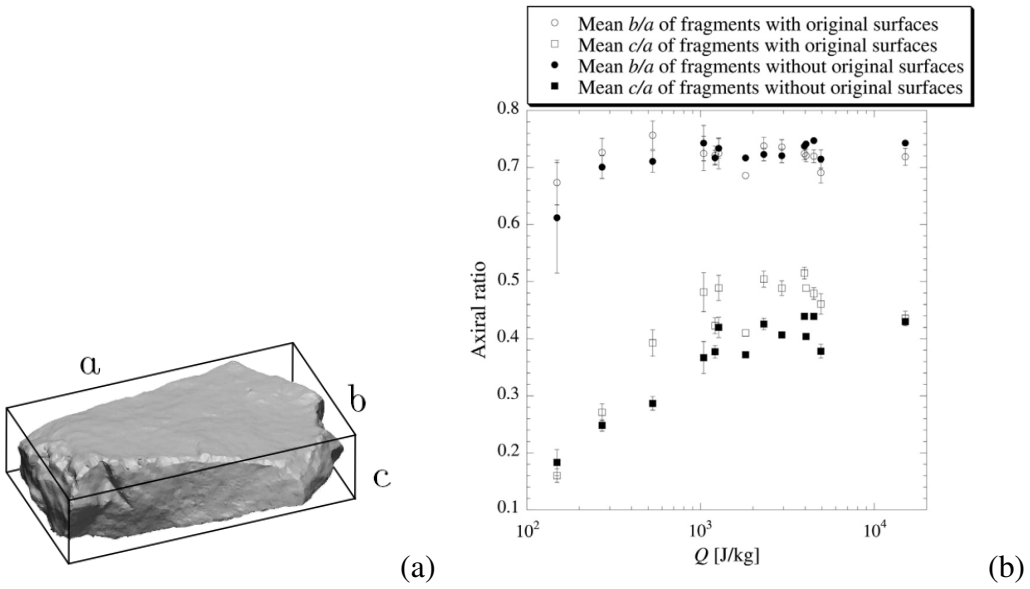

Fig. 1-8. (a) An example of fragment, (b) the mean b/a and c/a ratio versus impact energy per unit target mass Q. Note that the mean c/a ratios decrease with decreasing Q when Q is less than 1000 J/kg [137].

as $R_g = \sqrt{c^2+b^2+a^2}/(2\sqrt{3})$, S_f is given by

$$S_f = \frac{1}{\sqrt{3}}\left(\frac{1}{a}+\frac{1}{b}+\frac{1}{c}\right)\sqrt{c^2+b^2+a^2}. \tag{1.16}$$

For cubic fragments $a \simeq b \simeq c$, the shape parameter simplifies to $S_f = 3$ independent of the size of fragments, while larger values of $S_f > 3$ characterize elongated shapes.

During the past decades research on fragmentation mainly focused on the statistic of fragment masses m which revealed power law distributions

$$p(m) \sim m^{-\tau}. \tag{1.17}$$

The value of the exponent τ is mainly determined by the dimensionality of system and by the brittle and ductile character of the mechanical response on the material involved [114, 140–142]. In Domokos's study the universal exponent $\tau = (2D-1)/D$ depending solely on the dimensionality D of the system [139].

1.2.2 Particle breakage in representative volume element

There are several theoretical [106, 143–146] experimental [105, 107, 108, 147, 148] and numerical [116, 149–153] studies of particle fragmentation of a packing subjected a compression or a deformation. It is obvious that the rupture of particles depends on the contact network and the distribution of force chains in granular packings. Moreover, the initial distribution particle size, particle shape, solid fraction and confining stress play an important role in comminution processes.

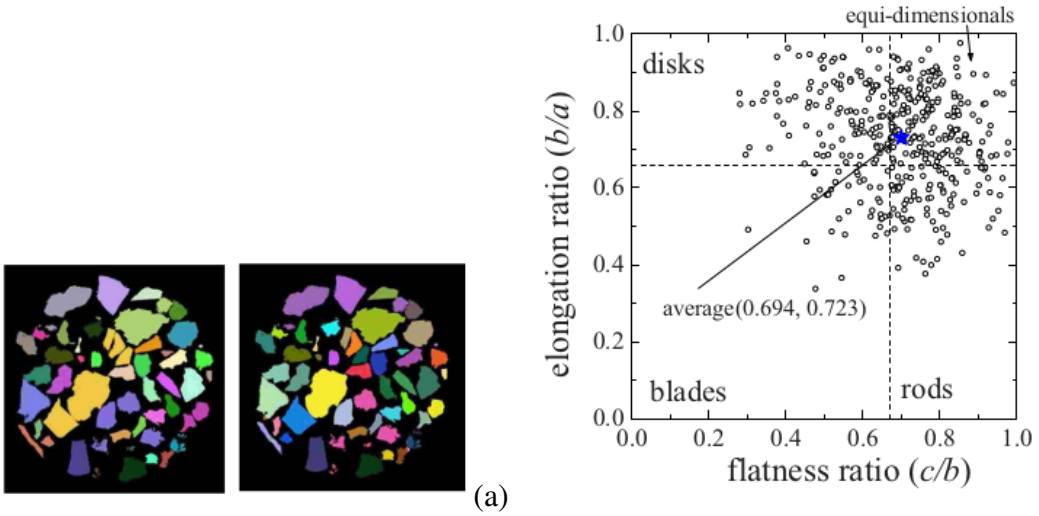

Fig. 1-9. (a) Example of cluster identified following attribution process, (b) Zingg diagram showing grain shape properties [138].

Several experiments seem to indicate that particle fragmentation does not significantly change the size of the largest particles though their number declines [104, 154, 155]. In fact, the larger particles are surrounded by smaller particles, reducing thus the mean shear stress that they support. In this way, the lower shear stress exerted on the large particles outweighs the decreasing strength of individual particles with increasing particle size. For this reason, the resulting size distribution is expected to be dependent on the initial size distribution. In particular, a number of large particles never breaks whereas a large number of particles are fully shattered. As a result, the packing keeps the memory of its initial particle size distribution, whereas a power-law distribution is observed for particles of intermediate size due to consecutive fragmentation events whereby the memory of the initial state is lost [151].

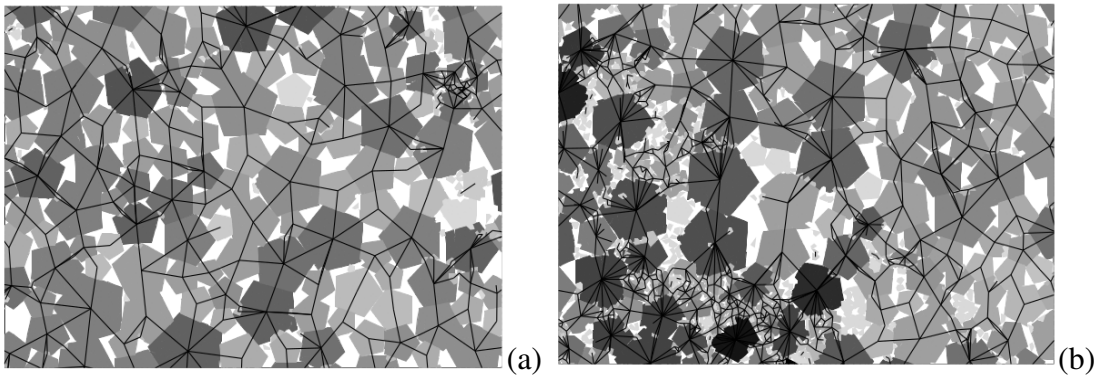

Fig. 1-10. Snapshot of a portion of the contact network at different levels of shear deformation ε_q, (a) $\varepsilon_q = 0.2$, and (b) $\varepsilon_q = 0.6$. The gray level of particles is proportional to the coordination number [151].

Nguyen et al. [151] also confirmed that the usual dilatant behavior of dense granular system is reduced or canceled by effect of particle fragmentation. In some cases, they found that

dilation is counter-balanced by fragments of particles, tending to increase the packing fraction by numerous small particles filling the space between larger particles. Hence, the stress-strain curve no longer passes through a peak stress, and a progressive monotonic evolution towards a pseudo-steady state is observed instead. The shear strength of the packing is well expressed in terms of contact anisotropies and force anisotropies. The stress ratio q/p is independent of the internal cohesion of the particles due to the additive compensation between the increase of normal force anisotropy a_{fn} and the decrease of contact anisotropy a_c. The increase of a_{fn} may be attributed to the production of particle of anisotropic shape by fragmentation whereas the decrease of a_c is a consequence of increasing polydispersity.

The evolution of particle size distribution of crushable particle packings has been studied in 3D during oedometric [156–159], and triaxial compression [117, 160, 161]. In general, the crushing of particles reduces the shear stress ratio peak, and the fragmentation of particles does not have a significant effect on the critical shear stress ratio. Some authors suggested that the fracture characteristics are highly dependent on the particle shape factor [157, 162]. Spherical particles seem to be more likely to undergo major splitting fractures, while realistic particles are more likely to undergo local asperity breakage. Consequently, spherical particles have greater characteristic crushing strength and much higher Weibull modulus than those of realistic particle shape.

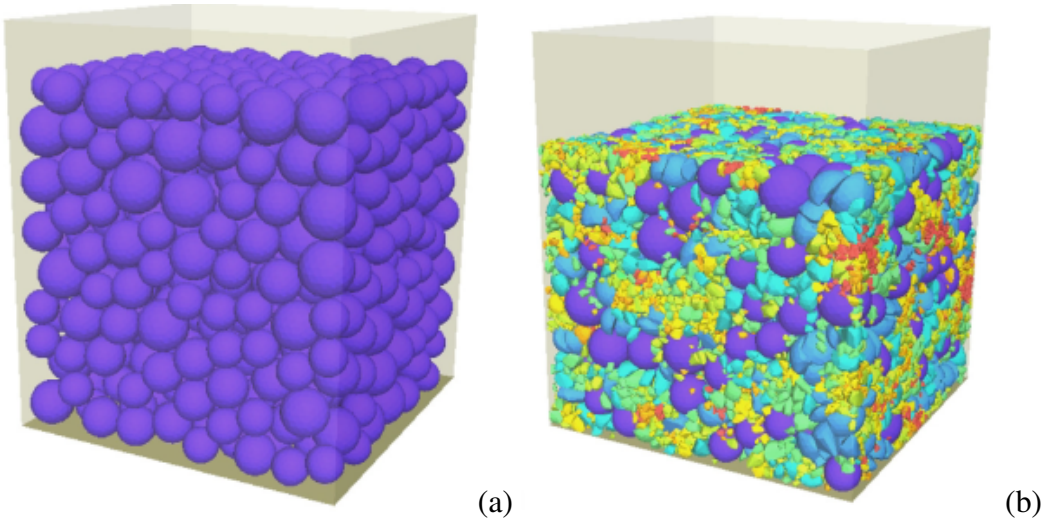

(a) (b)

Fig. 1-11. Sand sample at different vertical pressures: (a) initial condition, (b) stress is 30 MPa. The color indicates the number of crushing events experienced by a particle [158].

1.2.3 Fragmentation Process in Ball Mills

The grinding process in rotating drums is complex and poorly understood from physical and mechanical points of view. The granular flow has an inertial nature and develops a complex geometry with inhomogeneous flow patterns and curved free surface due to the rapid-flow regime in rotating drums, i.e., cascading or cataracting regimes. There are several studies on the grinding process using experimental measurements [103, 163, 164], numerical simulations [65, 165–169],

mechanistic or stochastic models [170–172], and mathematics models [173]. However, the evolution of particle size, powder specific surface, collision energy, and their scaling with operation parameters are open issues.

In the grinding process, particle breakage occurs as a result of frictional and collisional interactions between particles and with the drum walls. Breakage events of different types such as impact, shearing, crushing or compression can take place simultaneously at different locations of flow. Fig. 1-12 describes four different conditions that can make particles to break, for example, (a) colliding with the drum wall, (b) crushing between the wall and an approaching ball, (c) compression of shearing of a particle between tow balls, and (d) the impact and/or weight load of a ball with a bed of particles. In particular, particles can be broken under the particle-particle interactions that carry the forces transmitted from these different events.

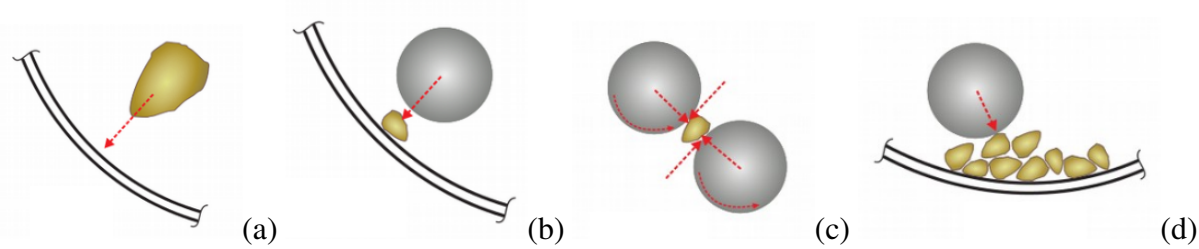

Fig. 1-12. Types of interactions that particles can undergo in rotating drums.

In experiments the range of tested parameters is limited, and therefore conclusive parametric results are difficult to obtain. This gap may be filled by numerical simulations which allow for different particle shapes and values of parameters to be considered and continuous tracking of particles and their mechanical interactions is possible. The numerical studies have, however, their own challenge of reconciling numerical performance with the realism of the underlying physical model. The population balance model (PBM) is a strategy that has been widely used for modeling the rate of change of particle size distribution in materials subjected to comminution processes [173–176]. The PBM combines particle breakage probability, usually obtained from single impact tests, with a mass transfer function to sequentially predict the evolution of particle size distribution during grinding. One disadvantage of this method is the large number of parameters that must be tuned for each specific case. In most cases, the calibration is based on experimental results, and some functions such as the mass transfer are fully empirical as their measurement in experiments is not possible. Moreover, these models do not directly account for the mechanics of particle fracture in multicontact configurations, in which the breakage mechanisms are substantially different from those in a single particle impact test.

Orozco et al. [177, 178] analyzed the evolution of particle breakage in a 2D rotating drum for a broad range of values of rotation speed, drum size, filling degree, and particle size and shape. They were interested in the influence of each system parameter on the evolution of specific surface and mean particle size. They proposed a scaling parameter incorporating all

system parameters:

$$\Gamma = \mathrm{Fr}^{3/4} f^{-1} \left(\frac{R}{d_0}\right)^{1/4} \left(\frac{\rho g d_0}{C_n}\right)^{3/2}, \tag{1.18}$$

where Fr is Froude number, f is filling degree, R is drum radius, d_0 is initial mean particle diameter, C_n is normal stress threshold, and ρ is particle density. This scaling parameter implies an increase of breakage rate with increasing rotation speed, drum size, particle size, density and a decrease of breakage rate with increasing filling degree and internal cohesion of the particles.

The scaling parameter Γ is dimensionless and fully constrained by all the available dimensional parameters of the system. It is shown that the rates of particle breakage for all values of system parameters collapse on a master curve when the times are scaled by the characteristic time defined in the linear regime:

$$\frac{t^*}{\tau} \simeq 0.073 \mathrm{Fr}^{-3/4} f \left(\frac{R}{d_0}\right)^{-1/4} \left(\frac{\rho g d_0}{C_n}\right)^{-3/2}, \tag{1.19}$$

where t^* is characteristic time, $\tau = C_n^{1/2} / \left(g\rho^{1/2}\right)$ is typical time between two breakage events. They also investigated the grinding process in a simulated ball mill geometry, see Fig. 1-13.

When the total volume of grinding balls is kept constant, changing the ball size has little effect on the evolution of grinding, since the total kinetic energy is proportional to the total volume and hence it has nearly the same value. Orozco et al. found that the grinding rate increases with the number of balls of the same size, but this trend is counterbalanced by energy dissipation due to inelastic collisions between balls for a large number of balls. There is therefore an optimal number of balls for which the grinding rate has its largest value. The effect of size and number of the grinding balls on breakage rate parameter is investigated in experiments. For instance, a mathematical equation was proposed to predict the particle size and ball size when maximum breakage occurs [164], providing one way to establish the optimum ball size in grinding process.

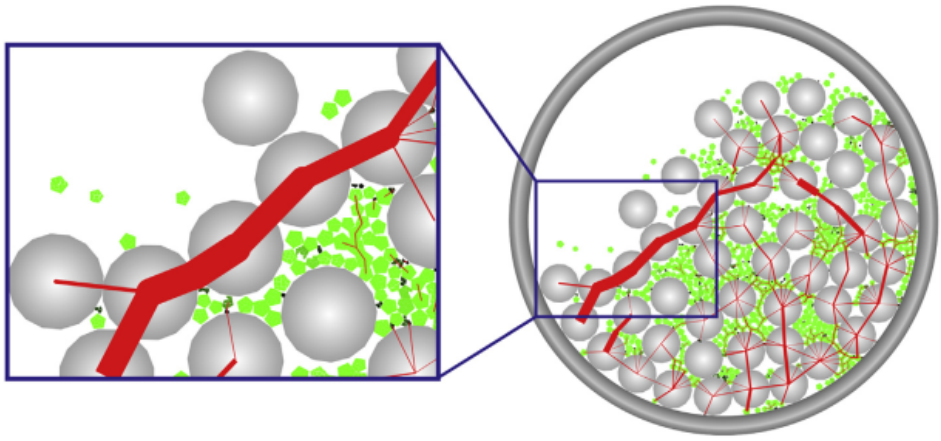

Fig. 1-13. A snapshot of force chains in a simulation with 50 grinding balls. Red lines thickness is proportional to normal force [177].

1.3 Methodology

1.3.1 Discrete Element Method and particle shape strategy

Discrete Element Method (DEM) is a powerful and reliable research tool. This method is based on the integration of equations of motion for all particles, described as rigid elements, by considering contact forces and external forces acting on the particles. Technically, this method requires a time-discretized form of the equations of motion governing particle displacements and rotations and a force law formulated as a force-displacement relation [179]. The equations of motion for each particle are the following:

$$\begin{cases} m_i \dfrac{d^2\vec{x}_i}{dt^2} = \sum_j (f_n\vec{n} + f_t\vec{t}) + m_i\vec{g}, \\ I_i \dfrac{d^2\vec{\varphi}_i}{dt^2} = \sum_j (f_n\vec{n} + f_t\vec{t}) \times \vec{r}, \end{cases} \tag{1.20}$$

where m_i, I_i, $\vec{x}_i$, $\vec{\varphi}_i$ are mass, moment of inertia, position and orientation of particle i, and $\vec{n}$ and $\vec{t}$ are the normal and tangential unit vectors at the contact point between particle i and its neighboring particles j. $\vec{g}$ is the acceleration of gravity and $\vec{r}$ is the vector of minimum distance between contact point and the current rotation axis passing through the mass center of particle i.

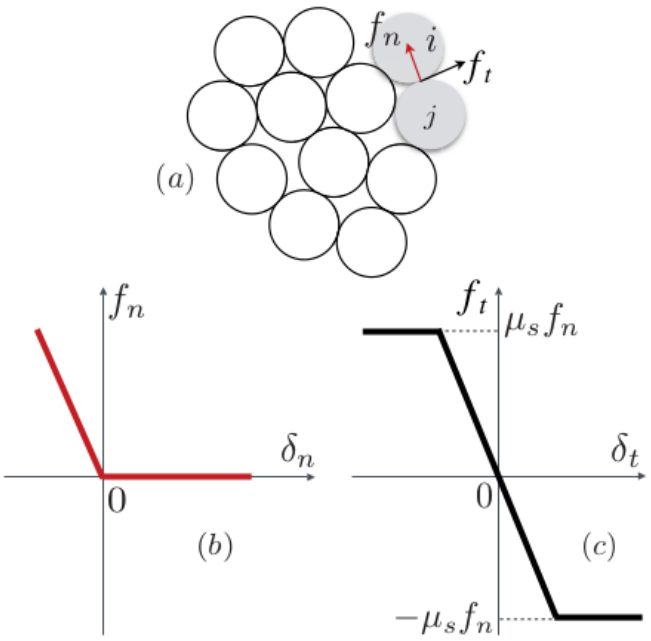

Fig. 1-14. Schematic representation of linear spring contact, (a) contact coordinate, (b) relation between normal force f_n and overlap δ_n, (c) Coulomb's friction law and relation between tangential force f_t and tangential displacement δ_t.

The normal force (f_n) and tangential force (f_t) are calculated from force laws which generally describe frictional contact interactions. An important feature of DEM is to allow the

particles to overlap. This overlap δ_n represents a normal strain localized in the vicinity of the contact point. Generally, a simple linear relation is assumed between f_n and δ_n. This is consistent with the fact that the overlaps allow for a penalty-based explicit formulation of particle motions, i.e. the elastic repulsion force is mobilized to prevent two penalize the overlap. The condition of particle undeformability implies that the overlaps must stay small compared to particle size. In this linear approximation, the normal force is given by

$$f_n = \begin{cases} 0, & \tilde{f}_n \leq 0 \\ \tilde{f}_n, & \tilde{f}_n > 0 \end{cases} \tag{1.21}$$

where $\tilde{f}_n = -k_n\delta_n - \gamma\dot{\delta}_n$ is the candidate normal force, k_n is normal stiffness, δ_n is overlap ($\delta_n < 0$, when two particle overlap), $\dot{\delta}_n$ is relative normal velocity, γ is viscous damping coefficient. The first part of candidate normal force ($k_n\delta_n$) is repulsive force, the second part ($\gamma\dot{\delta}_n$) is a viscous damping force that models the inelasticity of the contact.

Energy dissipation at contacts is an intrinsic characteristic of granular materials and must be considered. The viscous damping coefficient can be related to the normal restitution coefficient e_n:

$$\gamma = \begin{cases} \frac{-2\log e_n\sqrt{mk_n}}{\sqrt{(\log e_n)^2+\pi^2}} & \text{for } 0 < e_n \leq 1, \\ 2\sqrt{mk_n} & \text{for } e_n = 0. \end{cases} \tag{1.22}$$

$e_n = 0$ corresponds to fully inelastic collisions, $e_n = 1$ is for perfectly elastic collisions, m is effective mass of the colliding particles calculated from the masses of the colliding particles: $m = m_i m_j/(m_i + m_j)$.

The tangential force is constrained by Coulomb's law, and it is updated at each time step with the following increment vector [180]

$$\delta\vec{f}_t = \begin{cases} \delta\vec{f}_t = -k_t\vec{\delta}_t & \text{for } |f_t| < \mu f_n, \\ \vec{0} & \text{ortherwise} \end{cases} \tag{1.23}$$

where k_t is tangential stiffness, $\vec{\delta}_t$ is the relative tangential displacement, and μ_s is interparticle friction coefficient. Both the normal and tangential force are shown in Fig. 1-14(b) and 1-14(c), respectively. Note that, here we do not consider the energy dissipation along tangential direction, and granular materials are much more complex than the model that has just been presented. Nevertheless, the linear elastic spring model has several advantages such as simple to increment, its harmonic behavior is well understood that makes it is easier to interpret the results.

The most common nonlinear interaction law is the Hertz law [181]. For smooth spherical particles of diameter a, the normal force is a nonlinear function of overlap as $f_n = (\tilde{E}\sqrt{a}\delta_n^{3/2})/3$, with $\tilde{E} = E/(1-\nu^2)$, where E is the Young modulus, and ν is Poisson's ratio of spheres. The Hertz law implies that normal stiffness k_n is a function of overlap: $k_n = df_n/d\delta_n = (\tilde{E}\sqrt{a}\delta_n^{1/2})/2$. In the same way, the tangential stiffness is within good approximation proportional to normal stiffness: $k_t = (2-2\nu)k_n/(2-\nu)$. The Hertz law has significant influence on the acoustic

properties of simulated granular materials, and on the global elastic moduli of static packings. If we are interested in such questions, Hertzian model should be considered instead of linear law [179].

To solve the equations of motion several methods can be applied, but the velocity-Verlet algorithm is widely used because of its accuracy and numerical robustness. It uses a small number of variables in each time step, so it helps to save the memory of computer and speed up calculations. Let us consider a time discretization of equal intervals h (time step). The state of the system at time t is given by the position $q(t)$ and the velocity $\dot{q}(t)$ of each of its degrees of freedom. The latter can be a scalar or a component of a vector describing a displacement or a rotation. We would like to calculate the position $q(t+h)$ and the velocity $\dot{q}(t+h)$ at the end of the time step (at time $t+h$). The position is calculated by a second-order expansion in time:

$$q(t+h) = q(t) + \dot{q}(t)h + \frac{1}{2}\ddot{q}(t)h^2 \tag{1.24}$$

where $\ddot{q}(t)$ is the acceleration at the beginning of time step calculated in the preceding time step by dividing the resultant force F (or the moment for angular degrees of freedom) by particle mass m (respectively, by the moment of inertia I). This is the *prediction* step.

The velocity is calculated in two steps. First, it is calculated by a first-order expansion at the half-step:

$$\dot{q}(t+h/2) = \dot{q}(t) + \ddot{q}(t)\frac{h}{2} \tag{1.25}$$

and the acceleration $\ddot{q}(t+h)$ is calculated from the forces evaluated at the positions $q(t+h)$ and the velocities $\dot{q}(t+h/2)$:

$$\ddot{q}(t+h) = \frac{F(t+h)}{m} \tag{1.26}$$

This acceleration is then used to correct the velocity for the remaining half step:

$$\dot{q}(t+h) = \dot{q}(t+h/2) + \frac{1}{2}h\ddot{q}(t+h) \tag{1.27}$$

This is the *correction* step. If for a degree of freedom the velocity $\dot{q}$ is imposed, the same scheme can be applied by setting $F(t+h) = 0$ in the direction of the imposed velocity. Fig. 1-15 provides a summary of the particle simulation flow implemented in the software **Rockable** [182].

Particle shape is of primary important because it strongly influences stress transmission and volume change behavior in granular media. Different strategies are possible for the simulation of aspherical particles in DEM such as super-ellipsoids [78], clumps of glued spheres [82] and polyhedra [82]. The code Rockable models the particles as sphero-polyhedra. A sphero-polyhedron is a shape resulting from the sweeping of a sphere onto the surface of a polyhedron. Mathematically, this particle shape is the Minkowski sum of a polyhedron and a sphere. In sphero-polyhedron, vertices are formed of spheres, the cylinders form edges and the planar polygons form faces. This model shape has several advantages including highly simplified contact detection such as finding contact locations and associated local frames. Indeed, all contact configurations between two sphero-polyhedrons can be reduced to a set of only four

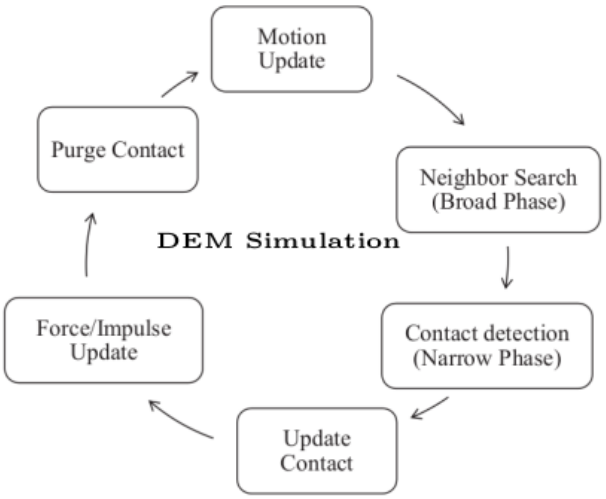

Fig. 1-15. Flow chart of the code Rockable utilized in this work.

types of elementary contact configurations: vertex-vertex, vertex-edge, vertex-face and edge-edge. For example, a face-face intersection test is simply replaced by a set of edge-edge and vertex-face tests [183].

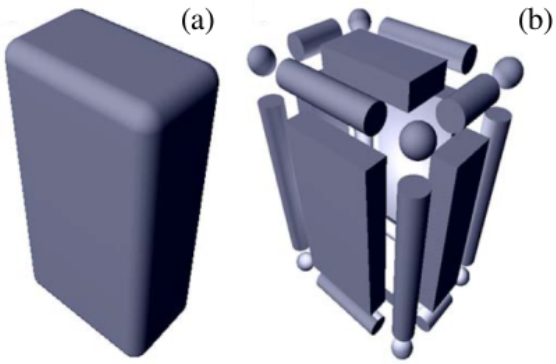

Fig. 1-16. Modeling of complex block shapes by sphero-polyhedra: (a) actual shape introduced in the code, (b) view of the 26 simple elements composing the shape [183].

A clear advantage of polyhedral shape is that arbitrary shapes can be represented as polyhedral particles by simply meshing their surface by polygons. However, polyhedral particle shape makes the computational cost increase significantly due to higher number of contacts which have to be detected. Fig. 1-17 shows that more than 70% of the total simulation time is used for contact detection. Together with neighbor search and contact update, contact-related computation takes more than 90% if the simulation time in DEM [184]. Fig. 1-17 suggests that the effort for parallelizing polyhedral particle simulations should be focused on the contact detection part to maximize the efficiency of the program.

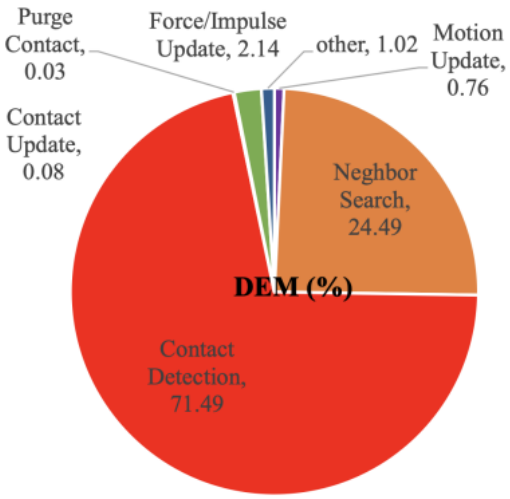

Fig. 1-17. Computational time for each function in DEM [184].

1.3.2 Contact detection strategy and time step

To reduce calculation time, it is necessary to have a suitable strategy of creating neighbor list which avoids calculation of interaction forces of all possible pairs of particles, so that only the interaction forces between two particles that are likely to come into contact need to be computed. In a system of N particles, each involving M edges, the number of operations requires to update the particle positions in each time step is of the order of $O(NM)$ whereas the number of calculations for contact detection is $O(N^2M^2)$. Simulations therefore become very slow when either the number of particles or vertices is large [185].

The first step to speed up simulations is to execute the force calculation only over neighbor particles. With this aim, creating the neighbor list is necessary, which is the collection of pair particles whose distance between them is less than 2δ (the distance between two particles is defined as the minimum of all vertex-edge distances) where the parameter δ is equivalent to the Verlet distance. The Link Cell algorithm is used to allow rapid calculation of this neighbor list: Firstly, the space occupied by the particles is divided in cells, and then the Link Cell List is defined as the list of particles hosted in each cell. Finally, the candidates of neighbor for each particle are searched only in the cell occupied by this grain and its eight neighbor cells. The neighbor list is calculated at the beginning of the simulation, and it is updated when the maximal displacement and rotation of the particles after last neighbor list update are greater than Verlet distance δ. The update condition is checked in each time step.

Increasing the value of δ makes updating of the list less frequent, but increases its size, and hence the memory used in the simulation rises. Therefore, the parameter δ must be chosen by making a compromise between the storage and the computation time. Neighbor list reduces the amount of calculations to $O(NM^2)$. Therefore, the simulations are still very expensive when particles consist of many vertices. Further reduction of the calculation number between neighbor particles can be achieved by identifying which part of particle is neighbor to the other.

This idea is implemented as follows. For each element of the neighbor list, we create a contact list, which consists of those vertex-edge pairs whose distance between is below 2δ. In each time step, only these vertex-edge pairs are involved in the contact force calculations. Overall, neighborhood identification requires a neighbor list with all pairs of neighboring particles, and one contact list for each pair of neighbors. These lists require little memory storage, and they reduce the amount of calculations of contact forces to O(N), which is of the same order as in simulations with spherical particles [185].

An explicit scheme is incremented in the code used in this thesis, so it is important to ensure that the collision dynamics is accurately resolved, which requires a time step much smaller than the typical time of collision [186]. This scheme is only conditionally stable, with the stability determined by the size of time step δt. A small time step can slow down the simulations unnecessarily and thereby increases the computational cost whereas a large time step can lead to numerical instability, as well as excessively large overlaps between particles. Although there are different approaches to estimate the critical time step δt_c, the common approach is the consideration of the critical time step as a function of mass and stiffness, in which δt_c is equal to a half of natural frequency of the system $\delta t_c = \pi\sqrt{m/k_n}$, where m is effective mass of colliding particles, k_n is normal stiffness of contact between particles [187].

Explicit integration method makes its parallelization more efficient by using OpenMP or MPI. MPI (Message Passing Interface) is a common standard for parallel programming on high performance distributed computing systems to take advantage of multi-core processors in different systems. DEM parallelization by MPI adopts a domain decomposition method. In this method, data is sent from one domain to neighboring domains and each core handles their own domains to prevent any race condition. If the user can access a distributed memory system with a large number of cores, domain decomposition may achieve good performance [184]. Another standard for parallel programming on a shared memory multi-core system is OpenMP (Open Multi-Processing). This approach significantly reduces communication costs. However, the number of available processor cores in a shared memory system is smaller than those in a distributed computing environment where MPI can be employed. Shared memory implementation can be done without data transfer, and the effects of these additional tasks related to domain decomposition can be far less pronounced when compared to a distributed memory system.

The performance of OpenMP in our code is displayed in Fig. 1-18. In the first version (V_0), which was not fully optimized, the use of more than 5 threads did not increase the speed of calculation. It even decreased efficiency. The simulations are, however, significantly sped up by using OpenMP in the latest version (V_2). Although the curve is close to the ideal line for the number of threads below 50, increasing the number of threads does not much speed up the simulations.

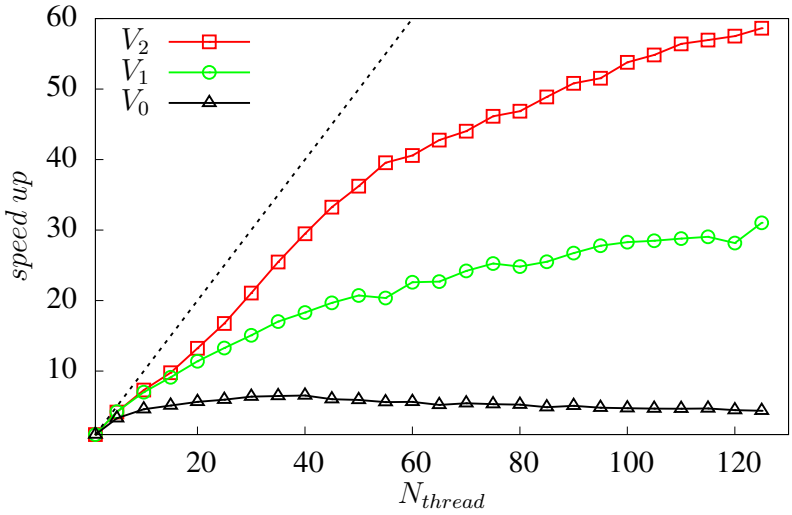

Fig. 1-18. Speed-up in calculation time using OpenMP parallezation method with different versions of the code *Rockable*. The dotted line represents theoretical (ideal) efficiency.

1.3.3 Periodic boundary conditions

In most reported simulations based on DEM both in 2D and 3D, the number of particles is below 10^5, as a result of the restrictions imposed by available computation power and memory. As a consequence, the numerical samples are not always statically representative of the bulk behavior but are also influenced by spurious wall effects. The solid fraction is generally lower in the vicinity of rigid walls and wall-induced ordering can deeply propagate into the bulk. Such effects are real and arise also naturally in experiments on granular materials. However, the number of particles in experiments is generally much higher and hence the wall effects are more critical in numerical simulations [188].

The undesired effects of wall-like boundaries can be removed by means of periodic boundary conditions. In this framework, the simulation domain becomes a unit cell containing the particles with periodic copies paving the whole space. The particles located at the borders of the simulation cell may then interact with the image particles in a neighboring cell. In this way, the periodic boundary condition extend the system boundaries to the infinity so that the simulation cell simply plays the role of a coordinate system to locate particle positions [189].

Let us consider, for example, a dense 3D sample of mono-sized polyhedral particles confined in a cubic box, number of particles is varied from 8^3 to 22^3 (see Fig. 1-19). The solid fraction of packing $\Phi = V_s/V$, where V_s is total volume of particles and V is volume of cubic box, is displayed in Fig. 1-20. We see that Φ in a packing using wall as boundary is generally lower. This effect is due to the fact that the particle close to the wall can settle down in an order that make more void between particles. In addition, the wall effect is dependent on proportion of particle near to the wall, so that this influence is less critical when the number of particles increases. For a packing using tri-periodicity, Φ is stable and reaches homogeneous behavior of representative volume element (RVE) of the material. Such effects arise also in experimental tests on granular materials, but the number of particle in experiments is generally much higher.

As a result, Φ in packings using wall boundaries increases gradually and reaches the value in three-periodic packings.

With wall boundaries, the external stresses or displacement are applied on the simulation box through wall degrees of freedom, which are alternatively kept free or frozen depending on whether a stress of a displacement is monitored in a given space direction. With periodic boundary conditions, this role is played by the collective degrees of freedom carried by the coordinate system, whose basis vector becomes a dynamic variable, and their conjugate stresses are expressed as a state function of the granular configuration. The simulation cell evolves with the particles and change its shape and volume [190].

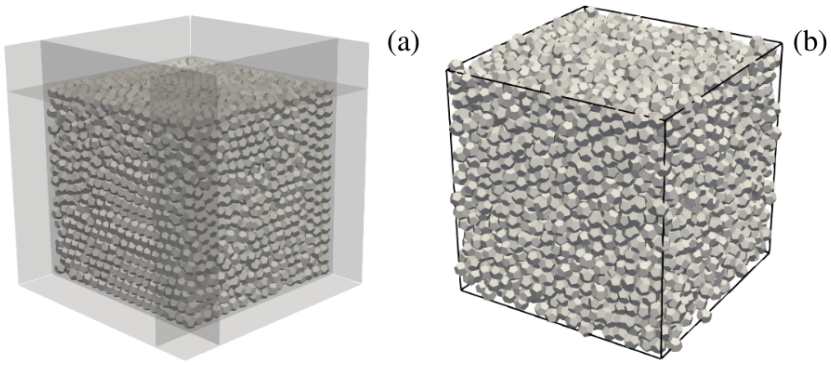

Fig. 1-19. A cubic sample of polyhedral particles using (a) wall as a simplified boundary condition and (b) 3-periodic boundary conditions.

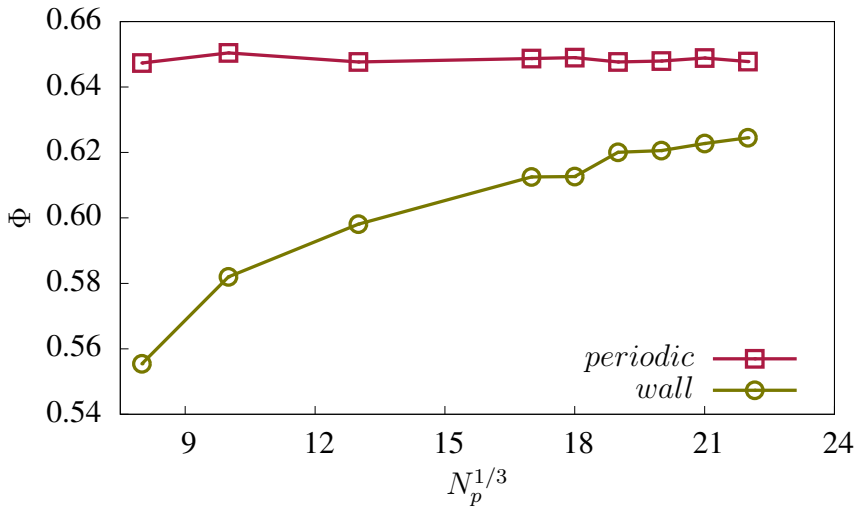

Fig. 1-20. Evolution of solid fraction Φ with the number of particles in an isostatic packing of polyhedral particles using wall boundaries and 3-periodic boundary conditions.

1.3.4 Bonded Cell Method

Particle breakage occurs in natural flows and industrial processes involving granular materials. It can be undesirable or uncontrolled such as rock fracture, ballast degradation, and can also

be a controlled process like grinding of mineral materials and milling of vegetable products. The fragmentation process raises several industrial and scientific challenges that can be listed as follows. First, the distributions of fragment shapes and sizes are difficult to control. We do not know how energy supplied at the process scale is dissipated down to the particle scale. Secondly, we can not mill the particles down to very fine particles (below micrometer). As finer fragments are produced, surface forces (van der Waals, electrostatic, capillary) tend to re-agglomerate the fragments. Hence, part of the power supplied is consumed to break the agglomerates. Finally, we do not know how particle fragmentation depends on the mechanical properties of the particles and their contacts, on the one hand, and on the process operational factors, on the other hand.

Within the framework of DEM, we would like to be able to simulate a granular assembly while allowing the particles to break into smaller particles with the following requirements:

- Cost-effective: we do not use methods such as finite elements that need a fine meshing of the particles. In this method, each particle is discretized into a finite element mesh. The potential fracture paths are represented by pre-inserted cohesive interface elements with a progressive damage model [111], see Fig. 1-21.

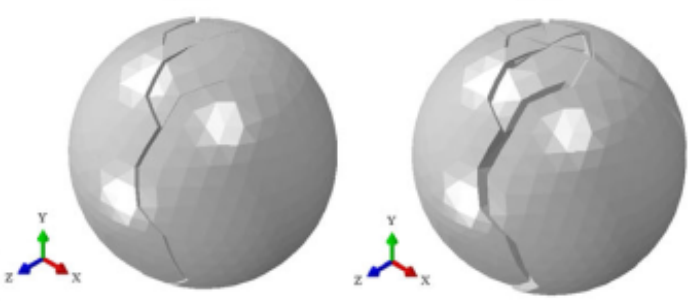

Fig. 1-21. Fracture process of particles in crushing test using finite element method [111].

- Mass and volume conservation: the sum of all fragment volumes should be strictly conserved during fragmentation. Particle fragmentation has been modeled using the Bonded Particle Method (BPM), in which the particles are modeled as agglomerates of glued disks [122] or spheres [114, 131, 191–193]. An issue with this method is that the total volume of the material is not conserved during the fragmentation process, see Fig. 1-22.

- Allowing for arbitrary fragment shapes: the simulation should be able to handle polyhedral particle shapes. Moreover, the generated fragments should be fully random in both size and shape [120, 121], see Fig. 1-23.

- Compatible with fracture mechanics and thermodynamics: Nearly all simulations reported in the literature are based on stress thresholds that leads to brittle behavior. In Orozco's work [7], the fracture involving both a strength and a fracture energy was implemented in the framework of the Contact Dynamics method, which does not account for elastic deflections at the contact points. It can not be implemented in smooth DEM

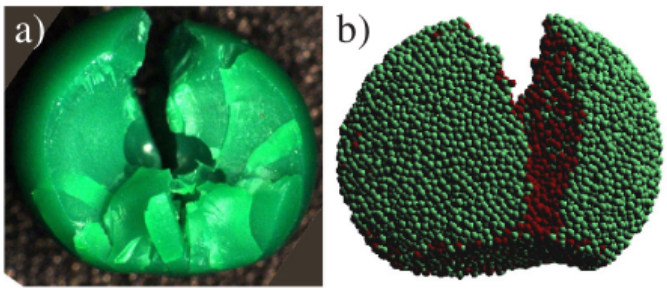

Fig. 1-22. Final states of impact at low impact velocities in the experiment (a) and in the simulation (b). The particle is a cluster of cohesive spheres, up to 40% of volume is lost upon fragmentation [114].

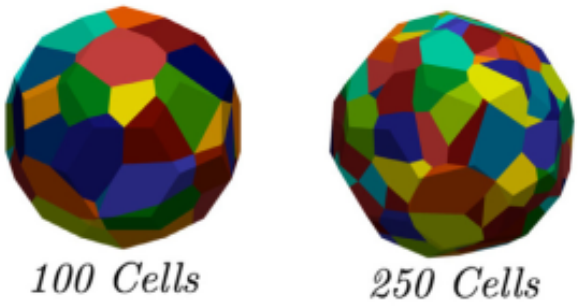

Fig. 1-23. Particles generated with different numbers of polyhedral cells which are represented by different colors [121].

with visco-elastic contacts where energy is stored in elastic deflections. Moreover, it is well known that the fracture mechanics is fully based on energy, so the rupture criterion should involve an energy criterion.

In the Bonded Cell Method (BCM), the particles are modeled as aggregates of potential fragments (cells), whose shapes are polygonal in 2D and polyhedral in 3D [112, 118, 119, 121, 194, 195]. The cells are generated by Voronoi tessellation, and they pave the whole volume of each particle so that the volume is conserved during fragmentation process. They should be generated randomly in their shape and size since the particle strength is influenced by the ordering of the cellular structure of particles [112, 120]. The cells interact through an interface area that needs at least three geometric constraints and a cell-cell contact breaks according to a rupture criterion, which can be reversible or irreversible. When a particle breaks, the fragments generated are smaller particles, each composed of cells, and the smallest fragment is a single cell. The cells are assumed to behave as independent rigid particles, so that their dynamic behavior can be simulated by DEM. A key issue of using DEM with crushable particles is the statistical representation of the particles and their fragments during crushing. In fact, the sizes of the initial particles and cells are, respectively, the upper and lower bounds on the size distribution of fragments in the debris. The statistical representation of particle size distribution in the process of fragmentation is therefore determined by their ratio.

The interface behavior is characterized by a relationship between the normal and tangential components of the cell-cell stress, on the one hand, and the relative cell displacement or velocity, on the other hand. Moreover, a criterion for debonding is required, i.e. the loss of internal cohesion and thus creation of a cohesionless frictional interface between two cells. In our model, the criterion for debonding is governed by an energy propagation condition, in which the propagation of a crack requires that an amount of work per unit area equal to or larger than the fracture energy G_f is supplied; see below.

1.3.5 Voronoi tessellation

From mathematical point of views, given two sets A and B and a distance metric $d(a,b)$ defined for $a \in A$ and $b \in B$, a Voronoi tessellation or diagram is a subdivision of A into subsets, each of which contains the objects in A that are closer, with respect to the distance metric, to one object in B than to any other object in B. Now we are given an open bounded domain $\Omega \in \mathbb{R}^d$ and a set of distinct points $\{\boldsymbol{x}_i\}_{i=1}^n \subset \Omega$. For each point $\boldsymbol{x}_i$, $i = 1,...,n$, the corresponding Voronoi region V_i, $i = 1,...,n$ is defined by

$$V_i = \{\boldsymbol{x} \in \Omega \mid \| \boldsymbol{x} - \boldsymbol{x}_i \| < \| \boldsymbol{x} - \boldsymbol{x}_j \| \text{ for } j = 1,...,n \text{ and } j \neq i\}, \tag{1.28}$$

where $V_i \cap V_j = \emptyset$ for $j \neq i$, and $\cup_{i=1}^n \langle V_i \rangle = \langle \Omega \rangle$, so that $\{V_i\}_{i=1}^n$ as the Voronoi tessellation of Ω associated with the point set $\{\boldsymbol{x}_i\}_{i=1}^n$ [196]. A point $\boldsymbol{x}_i$ is called a generator, a subdomain $V_i \cap \Omega$ is referred to as the Voronoi cell corresponding to the generator $\boldsymbol{x}_i$. Voronoi cells $\{V_i\}_{i=1}^n$ are polygons in two dimensions and polyhedra in three dimensions, see Fig. 1-24.

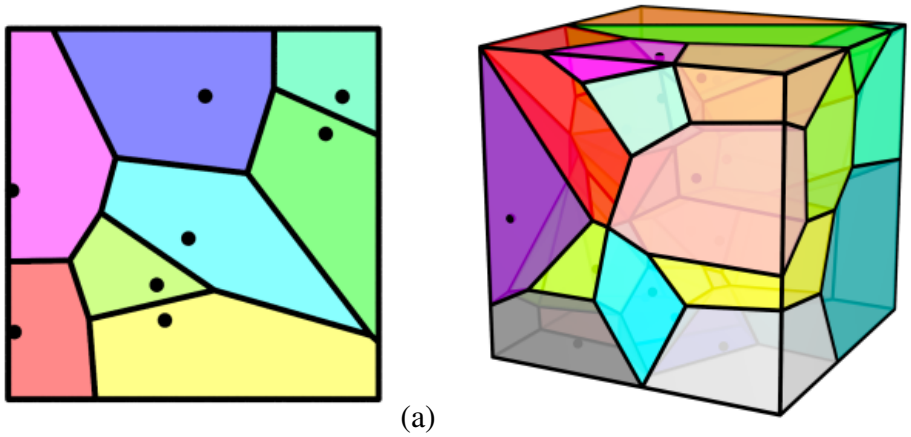

(a) (b)

Fig. 1-24. The Voronoi tessellation in 2D of the square (a), and in 3D of the cubic (b) corresponding to 8 randomly selected generators [197].

Centroidal Voronoi tessellations (CVTs) are special Voronoi tessellations having the property that the generators of the Voronoi tessellation are also the center of mass, with respect to a given density function, of the corresponding Voronoi regions. CVT methodologies produce high quality point distributions in regions and surfaces in $\mathbb{R}^d$ or within sets of discrete data.

Given a density function $\rho(\boldsymbol{x}) \geq 0$ defined on Ω, for any region $V \cap \Omega$, the standard mass center $\boldsymbol{x}^*$ of V is given by

$$\boldsymbol{x}^* = \frac{\int_V \boldsymbol{x}\rho(\boldsymbol{x})d\boldsymbol{x}}{\int_V \rho(\boldsymbol{x})d\boldsymbol{x}}. \tag{1.29}$$

A generic Voronoi tessellation does not in general satisfy the CVT property, see Fig. 1-25 for an illustration as well as for an illustration of CVT. On the other hand, given a density function and the number of generators, the CVT of a domain always exits, although it may not be unique.

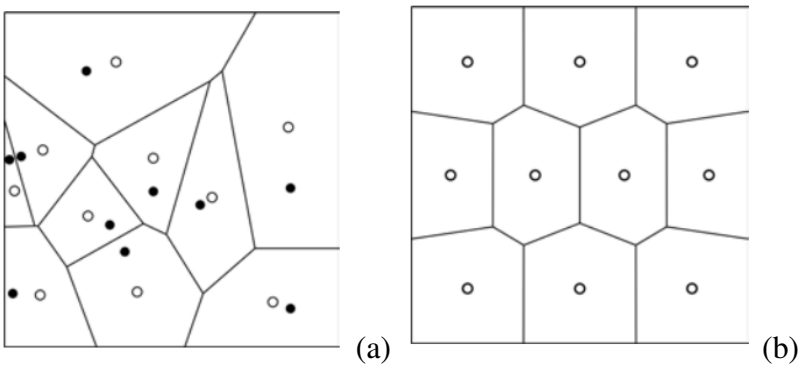

Fig. 1-25. A Voronoi tessellation of the unit square, the open circles denote the centroids of the Voronoi polygons with respect to a uniform density. (a) The centroids do not coincide with the generators. (b) Voronoi tessellation with the generators and centroids coincide [198].

One of the algorithm for constructing CVT is Lloyd's method which simply alternates between constructing Voronoi tessellations and mass centroids [199]. This method may be describe as follows:

1. Select an initial set of n points $\{\boldsymbol{x}_i\}_{i=1}^n$ on Ω.

2. Construct the Voronoi regions $\{V_i\}_{i=1}^n$ of Ω associates with $\{\boldsymbol{x}_i\}_{i=1}^n$.

3. Determine the centroids, with respect to the given density function, of the Voronoi region. These centroids form the new set of points $\{\boldsymbol{x}_i\}_{i=1}^n$.

4. If the new points meet some convergence criterion, return $\{(\boldsymbol{x}_i, V_i)\}_{i=1}^n$ and terminate, otherwise go to step 2.

The convergence criterion that can be used is given by

$$\frac{\sum_{i=1}^n \| \boldsymbol{x} - \boldsymbol{x}^* \|}{\sum_{i=1}^n r_i} \leq \lambda, \tag{1.30}$$

where r_i is the average radius of cell i, and λ is the tolerance. The quantity λ may be interpreted as a measure of disorder of the cell shapes and their distributions.

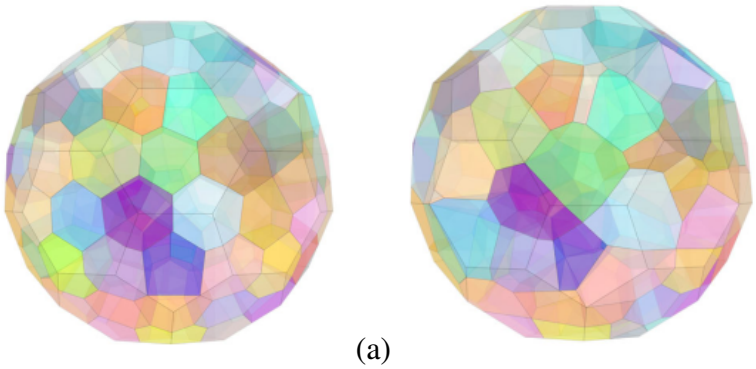

Fig. 1-26. Examples of icosahedral particles composed of 250 Voronoi cells and disorder parameter $\lambda = 0.005$ (a) and $\lambda = 0.5$ (b) [120].

1.3.6 Fracture modes and stress intensity factors

A crack is defined as a surface in 3D or a line in 2D of discontinuity. At the tip, the displacement jump, which is the difference between the displacement of the upper an lower surfaces of the crack, can be decomposed in three directions including normal, in-plane tangential, and out-of-plane tangential displacement discontinuity. This decomposition allows the definition of the three modes of fracture. A crack is said to be loaded in Mode I, if the displacement jump reduces to a normal displacement discontinuity. This mode is often referred to as the *opening* mode; see Fig. 1-27(a). Mode II refers to a loading that leads to an in-plane tangential displacement discontinuity. This mode is referred to as the *sliding* mode; see Fig. 1-27(b). Mode III refers to a loading that leads to an out-of-plane tangential displacement discontinuity. This mode is the *tearing* mode; see Fig. 1-27(c) [200, 201]. Mode I is the most common failure type. For example, fracture in Mode I can take place when a crack is sheared with a kink angle between the initial crack direction and the direction followed under shearing.

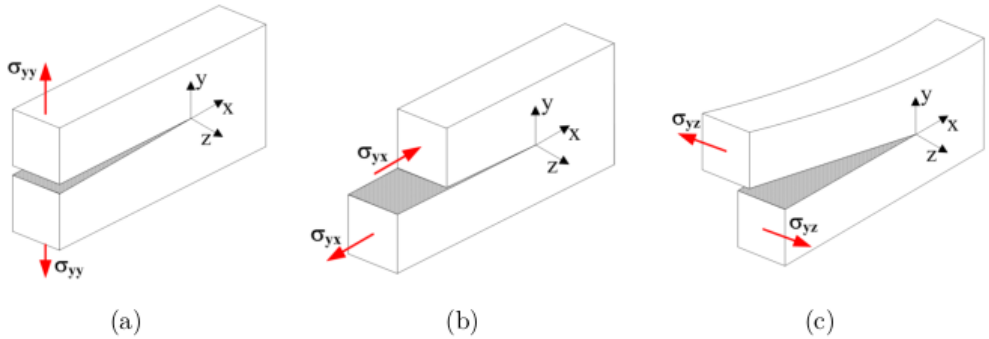

Fig. 1-27. Fracture modes in 3D: (a) Mode I: opening, (b) Mode II: sliding, (c) Mode III: tearing.

Due to the displacement discontinuity that defines a crack, stresses become singular at the crack tip, with a value of the order of $\sigma \propto r^{-1/2}$, where r is the distance to the tip. The stress intensity factors K_I and K_{II} of the Mode I and Mode II quantify the degree of singularity of the

normal and in-plane shear stresses, respectively. If we consider the case of a crack belonging to the z-plane, the stress intensity factors can be defined asymptotically from the stresses:

$$\begin{cases} K_I = \lim_{r\to 0} \sqrt{2\pi r}\sigma_{zz}(r,\theta=0), \\ K_{II} = \lim_{r\to 0} \sqrt{2\pi r}\sigma_{xz}(r,\theta=0), \end{cases} \tag{1.31}$$

where (r,θ) a polar coordinate system with origin at the crack tip.

1.3.7 Crack propagation criteria in solid mechanics

There are two approaches to crack propagation in solids. The first one is said to be *local* in the sense that it focuses on what happens at the crack tip. The relevant quantities are the stress intensity factors. The other one is based on the energy dissipation during the process and therefore is known as the *global* approach.

Irwin's criterion or the local approach

Irwin's criterion applies to cracks in linear elastic brittle solids subjected to purely Mode I loading. A critical stress intensity threshold, named *fracture toughness* K_{Ic} has to be reached in order to allow the crack to propagate [202]. It is commonly considered as a material property, independent of the problem considered. This approach also establishes that the crack opening is irreversible. The drawback of Irwin's criterion is that it accounts only for pure Mode I loading. According to this criterion, an existing crack subjected to a pure Mode II loading would never propagate since $0 = K_I < K_{Ic}$.

Griffith's criterion or the global approach

While Irwin's criterion uses the notation of fracture toughness K_{Ic}, Griffith's criterion makes use of the *fracture energy* G_f which is a material property characterizing a brittle material. When a crack propagates, surfaces are created and energy is dissipated. This energy is proportional to the area of the surfaces created, the proportionality factor being the fracture energy G_f. If any other dissipative phenomenon (such as plasticity) is ignored, this energy should be equal to $2\gamma_s$, where γ_s is the surface energy and the factor two accounts for upper and lower surfaces associated with surface created during propagation. A crack propagates if the rate of energy release (reduction of elastic energy) by surface created s is above the fracture energy, which is second law of thermodynamics.

$$G(s) = -\frac{\partial E_{pot}}{\partial s}, \tag{1.32}$$

where E_{pot} is the potential elastic energy stored in the whole volume of the material due to external loading.

When Irwin's and Griffith's criteria are put together in the case of a crack opening under pure Mode I, the fracture energy G_f can be related to the fracture toughness K_{Ic} as follows:

$$G_f = \frac{K_{Ic}^2}{E'}, \tag{1.33}$$

where $E^{'}$ is the reduced Young's modulus ($E^{'} = E/(1-\nu^2)$ in 3D and 2D plane-strain and $E^{'} = E$ in 2D plane-stress). This relation can be extended to the case where mixed loading modes takes place using the generalized toughness K_c:

$$K_c = \sqrt{E' G_f}. \tag{1.34}$$

Note that since G_f is mode angle independent (the mode angle Θ is defined as $\tan\Theta = K_{II}/K_I$), the fracture toughness should also be mode angle independent.

1.4 Conclusion

In this brief review, we presented a general description of the scientific context regarding particle dynamics simulations based on the Discrete Element Method (DEM), the granular flow for both quasi-static state in representative volume element and liquid-like state in rotating drums, and the particle fragmentation process. In this thesis, before carrying out the research in terms of rotating drum, we would like to understand the influences of particle shape on both elastic and plastic behavior of granular materials. For that, we need to prepare polyhedral particle packings with 3-periodic boundary conditions, so that either pressure or displacement on the boundaries can be fully controlled. Our literature review reveals that there are multiple studies of spherical particle packings, but realistic particle shapes have been seldom used. Obviously, particle shape plays a vital role for the flow and breakage of particles in various industrial applications. We will therefore consider flow behavior and comminution with polyhedral particle shapes in both representative volume element (RVE) and rotating drums.

In this review we also highlighted the fact that most numerical simulations of the fragmentation process in RVE and ball mills has been studied in 2D. Hence, there is significant room for extending simulations to 3D in order to fill the gaps in our understanding of the complex phenomena related to the flow of breakable particles. This can be achieved only by means of an appropriate optimization of numerical codes. Furthermore, the rupture criteria for particle breakage in most previous researches should be adapted to conform to fracture mechanics and thermodynamics.

Chapter 2

Macro-elasticity of granular materials composed of polyhedral particles

Contents

Particle shape variability is a key to understanding the rich behavior of granular materials. Polyhedra are among the most common particle shapes due to their ubiquitous origins in nature such as rock fragmentation and mineral crystallisation. Because of their faceted shape, polyhedral particles tend to assemble in jammed structures in which face-face and face-edge contacts between particles control the packing-level properties. In this chapter, we use tri-periodic particle dynamics simulations to derive for the first time a generic analytical expression of the elastic moduli of polyhedral and spherical particle packings subjected to triaxial compression as a function of two contact network variables: 1) a "constraint number" that accounts for the face-face and edge-face contacts between polyhedra and is reduced to the coordination number in the case of spherical particles, and 2) the contact orientation anisotropy induced by compression. This expression accurately predicts the simulated evolution of elastic moduli during compression, revealing thereby the origins of the higher elastic moduli of polyhedral particle packings. We show that particle shape affects the elastic moduli through its impact on the contact network and the level of nonaffine particle displacements is the same for the simulated shapes. Its nearly constant value during compression underlies the constant values of our model parameters. By connecting the elastic moduli to the contact network through parameters that depend on particle shape, our model makes it possible to extract both the connectivity and anisotropy of granular materials from the knowledge of particle shape and measurements of elastic moduli.

2.1 Introduction

Granular materials have been at the focus of extensive research for their rich and complex properties rooted in dissipative particle interactions, disordered microstructure, and particle characteristics such as shape and size distribution [29, 203, 204]. Although hard-sphere packing has often been used as a model of granular materials, aspherical particle shape is omnipresent in nature and industry. The crucial role of realistic particle shape for quantitative prediction of the strength and space-filling properties of granular materials has been clearly evidenced by recent simulations and experiments [21–23, 205–216]. For example, packings composed of particles slightly deviating from spherical shape are more compact than sphere packings whereas larger deviations towards more elongated or platy shapes lead to significantly lower packing fraction [23, 205, 208].

Among diverse particle shapes, regular and irregular polyhedral particles are quite common due to their ubiquitous origins such as rock fragmentation and mineral crystallisation. Their specific feature is to assemble in structures involving face-face and edge-face contacts which, in contrast to simple contact points between spheres, provide a finite support for the contact force. Particle dynamics simulations have shown that such contacts in packings of polyhedral particles are less in number but they capture strong force chains and carry thereby a much higher average force than simple contacts [21, 22]. The microstructure has also been analyzed as a function of the number of facets in relation to shear strength [22, 209, 213]. However, we are aware of no published work on the elastic properties of polyhedral particle packings.

Past work on granular elasticity has essentially focussed on isotropic sphere packings [31, 32,217,218]. The bulk and shear moduli are proportional to k_n/d, where k_n is the normal contact stiffness and d is mean particle diameter. The moduli depend also on the number of contacts per unit volume, and stiffness ratio k_t/k_n, where k_t is the tangential contact stiffness [35, 44, 217–219]. It is well known that, because of its failure to account for the nonaffine nature of particle displacements in granular media, the effective medium theory (EMT) over-estimates the elastic moduli [36, 42]. The origins of elastic moduli in the general case of anisotropic sheared media and the effects of particle shape mediated by microstructure and nonaffine displacements are therefore widely open issues.

We report in this chapter on a detailed investigation of the elastic moduli of dodecahedral (12 faces), icosahedral (20 faces), and spherical particle packings by means of extensive particle dynamics simulations based on the discrete element method (DEM) with a proper treatment of the contact interactions between polyhedral particles. In particular, each face-face interaction is reduced to a set of elastic/frictional contacts between the edges composing the two faces. This allows the geometrical constraints associated with rigid faces to be imposed and the overlaps between the edges are used to compute point forces according to a linear dashpot-spring force law.

Initially isotropic random close packings were prepared by isotropic compaction at zero friction, representing the unique reproducible densest state of each shape. Subjecting then each packing to quasi-static triaxial compression with tri-periodic boundary conditions and a non-zero friction coefficient between particles, we calculated their five orthotropic elastic moduli at regular strain intervals together with contact network variables such as connectivity and contact anisotropy. A key finding is that the elastic moduli can be fully expressed as a function of connectivity and anisotropy with a functional form that does not depend on particle shape, but involve coefficients that depend on particle shape. Accurate determination of these coefficients makes it therefore possible to nicely predict the evolution of elastic moduli with strain. These expressions also reveal how the face-face and face-edge contacts enhance the elastic moduli compared to sphere packings.

In the following, we first introduce numerical procedures. Then, we discuss in Section 2.3 the evolution of sample-level variables during triaxial compression. The evolution of elastic moduli will be presented in Section 2.4. In Section 2.5, we consider the evolution of microstructural variables. In Section 2.6, we introduce our expression of elastic moduli as a function of microstructural variables by a detailed comparison between the predictions of EMT and our numerical data. Finally, we discuss the most salient results of this chapter.

2.2 Numerical procedures

The simulations were carried out by means of an in-house code based on DEM [182, 220, 221]. The interactions between polyhedral particles need a model for face-face and face-edge contacts. The vertex-face and edge-edge interactions involve a single contact point, which can

be treated in the same way as the contacts between spherical or smooth convex particles. Such simple contacts represent a single unilateral constraint, which is treated either by a penalty approach, i.e. introducing a repulsive force depending on the overlap, or by means of Lagrange multipliers as in the Contact Dynamics method [179, 222, 223]. In contrast, in the case of a face-face interaction, there are three steric constraints that must be correctly treated to avoid interpenetration between the two particles as a result of their relative normal displacement or rotations around the two other axes.

For rigid polyhedral particles with their finite faces defined by their contours composed of several edges, a face-face interaction can be reduced to interactions between edges composing the two faces or between a vertex and one of the faces [182]. This means that a face-face interaction is reduced to a set of contact points, as shown in Fig. 2-1(a). If a penalty approach is applied to all contact points, the three constraints will be fully satisfied. It is noteworthy that, the number of contact points can be large depending on the number of edges, but the number of independent constraints is always 3 due to the rigidity of the particles. Similar considerations apply as well to edge-face interactions, which involve two independent steric constraints; see Fig. 2-1(b). We may thus refer to the face-face and face-edge interactions as *triple* and *double* contacts, respectively.

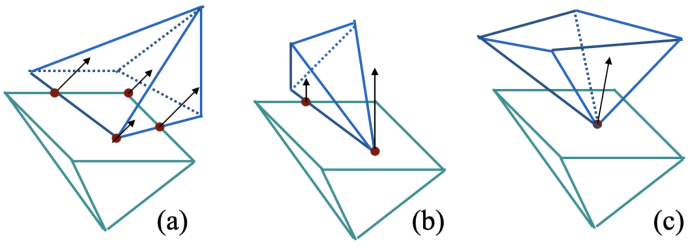

Fig. 2-1. Different types of contacts between two polyhedra: (a) face to face, (b) face to edge, (c) vertex to face.

The contact points between polyhedral particles are detected by considering separately the sub-elements (vertices, edges and faces). At each contact point, either a linear or a nonlinear force law is implemented. As for Hertz contacts, the nonlinear interactions arise from the curvature of the surface at the contact points (e.g. between two edges modeled as cylinders). However, in this paper we are interested in the effects of particle shape and contact network anisotropy, and therefore we used linear contact laws to reduce computational cost. The normal force law is defined as follows [179, 204, 224, 225]:

$$f_n = \begin{cases} 0, & \tilde{f}_n \leq 0, \\ \tilde{f}_n, & \tilde{f}_n > 0, \end{cases} \tag{2.1}$$

where $\tilde{f}_n = -k_n\delta_n - \gamma\dot{\delta}_n$, k_n is normal stiffness, δ_n is overlap (with sign convention that $\delta_n < 0$ when two particle overlap), $\dot{\delta}_n$ is the relative normal velocity, and γ is the viscous damping

coefficient. The tangential force is governed by the Coulomb friction law given by

$$f_t = -min\{k_t\delta_t,\ \mu_s f_n\}sgn(\dot{\delta}_t), \tag{2.2}$$

where k_t is tangential stiffness, δ_t is cumulative tangential displacement, $\dot{\delta}_t$ is relative tangential velocity, and μ_s is the interparticle friction coefficient.

2.3 Triaxial compression

We prepared three samples composed of monodisperse particles of dodecahedral, icosahedral, and spherical shapes enclosed in a 3-periodic cubic cell [45, 188, 226]. They had exactly the same number of particles (8000), values of parameters, and boundary conditions. We first applied an isotropic compression with zero friction between particles, leading to dense isotropic states corresponding to a random closed packing (RCP) of solid fraction $\Phi \simeq 0.648$ for dodecahedral particles, $\Phi \simeq 0.632$ for icosahedral particles, and $\Phi \simeq 0.637$ for spherical particles.

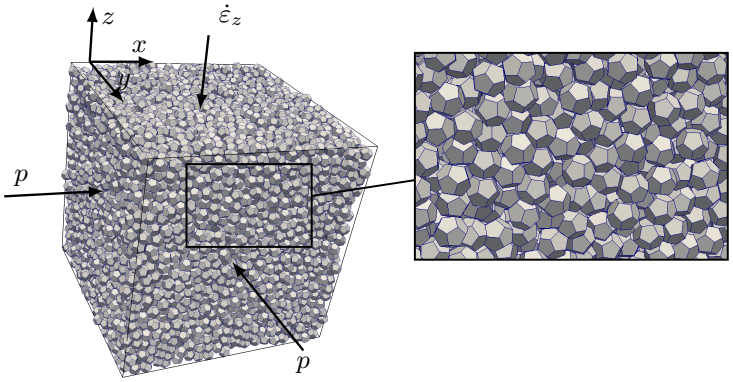

Fig. 2-2. A snapshot of the sample of dodecahedral particles in the isotropic state.

The isotropic samples were sheared by triaxial compression for four values of friction coefficient μ_s = 0.1, 0.2, 0.3, and 0.4 between particles. The compression was applied along the z axis by imposing a constant strain rate $\dot{\varepsilon}_z$ while keeping the same stress p in lateral directions x and y. The simulation box can expand along these directions to accommodate the applied compression. Since the material is in an initially dense state, the packing dilates and the packing fraction declines towards a stead-state value in all simulations. The inertial number $I = \dot{\varepsilon}_z d(\rho/p)^{1/2}$, where ρ is the particle density and d is the mean particle diameter, is low enough ($< 10^{-3}$) to qualify the compression as quasi-static [10, 11, 179]. By symmetry, the principal stresses and strain rates coincide with the three space directions with σ_1 and ε_1 along the z direction, $\sigma_2 = \sigma_3 = p$, and $\varepsilon_2 \simeq \varepsilon_3$.

Figure 2-3 shows the evolution of stress ratio q/p, where $q = (\sigma_1 - \sigma_2)/3$ is stress deviator and $p = (\sigma_1 + \sigma_2 + \sigma_3)/3$ is mean stress, as well as the packing fraction Φ as a function of shear strain $\varepsilon_q = \varepsilon_z - \varepsilon_x$ for dodecahedral and spherical particle packings (the trends being similar for icosahedral particles). Due to the initially high value of packing fraction, the samples yield

only when q/p reaches a threshold where plastic deformation can begin as a result of particle rearrangements and dilation. Beyond this point, q/p continues to increase to a peak value before slowly decreasing towards a residual plateau at $\sim 60\%$ of shear strain. The peak value reflects therefore the initially high packing fraction although no shear bands develop in our system due to three-periodic boundary conditions. The peak value increases with μ_s. In polyhedra packings the peak stress ratio is higher and the effect of friction coefficient is more pronounced as compared to sphere packings. Since the initial packing fraction is high, Φ decreases gradually before reaching a nearly constant value. The reduction of Φ increases when μ_s is larger. This effect is more pronounced in the case of polyhedral particle packing.

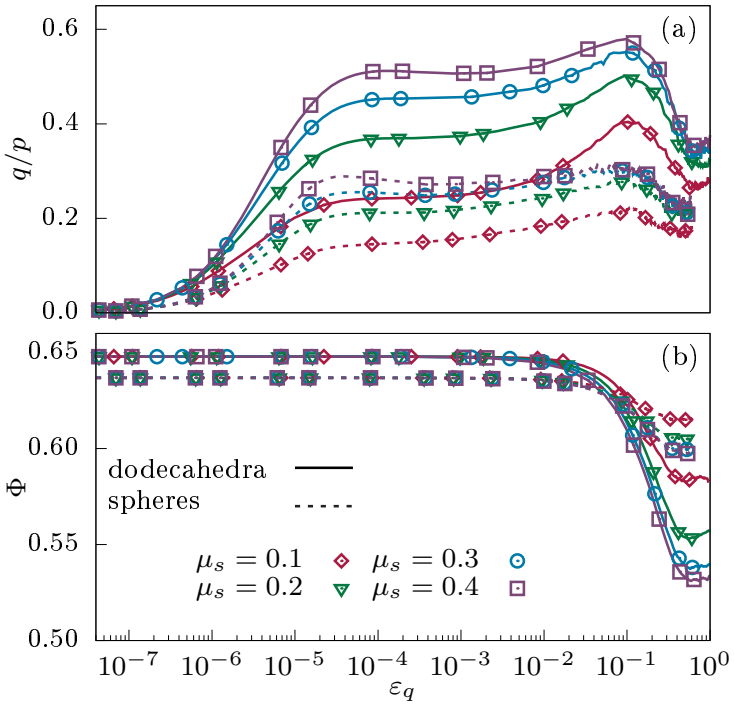

Fig. 2-3. Stress ratio q/p (a), and packing fraction Φ (b) versus shear strain ε_q for packings of spherical and dodecahedral particles with four values of friction coefficient μ_s. The dashed and solid lines join data points for spheres and dodecahedra, respectively. The symbols represent instances where strain probes are applied.

2.4 Evolution of elastic moduli

Due to axial symmetry, there are 5 independent moduli C_{ij}, defined as follows, based on the Voigt notation [227, 228]:

$$\begin{bmatrix} \delta\sigma_{11} \\ \delta\sigma_{22} \\ \delta\sigma_{33} \\ \delta\sigma_{23} \\ \delta\sigma_{31} \\ \delta\sigma_{12} \end{bmatrix} = \begin{bmatrix} C_{11} & C_{12} & C_{12} & 0 & 0 & 0 \\ C_{12} & C_{22} & C_{23} & 0 & 0 & 0 \\ C_{12} & C_{23} & C_{22} & 0 & 0 & 0 \\ 0 & 0 & 0 & 2C_{44} & 0 & 0 \\ 0 & 0 & 0 & 0 & 2C_{55} & 0 \\ 0 & 0 & 0 & 0 & 0 & 2C_{55} \end{bmatrix} \begin{bmatrix} \delta\varepsilon_{11} \\ \delta\varepsilon_{22} \\ \delta\varepsilon_{33} \\ \delta\varepsilon_{23} \\ \delta\varepsilon_{31} \\ \delta\varepsilon_{12} \end{bmatrix} \tag{2.3}$$

The elements C_{11} and C_{22} are the longitudinal moduli, C_{44} and C_{55} are the shear moduli, and C_{12} and C_{23} are the off-diagonal moduli. The bulk modulus K is given by:

$$K = (C_{11} + 4C_{12} + 2C_{22} + 2C_{23})/9. \tag{2.4}$$

To determine the moduli, we applied two distinct strain probes in two different directions.

To compute the elastic moduli, we used the sheared samples at 16 instances of their evolution and applied a small strain increment $\delta\varepsilon_{ij}$ to obtain the corresponding stress response $\delta\sigma_{ij}$, from which the elastic moduli were extracted. The sample was allowed to relax to a fully static state before the application of the strain probe. The response is elastic if there are no particle rearrangements, and, as we shall see below, this is the case when $\delta\varepsilon_{ij} < 10^{-5}$.

To determine all elastic moduli, two distinct strain probes in two different directions were applied at a given stage of evolution of the system. For the first probe, a small strain rate $\dot{\varepsilon}$ was imposed along the z direction while a constant pressure was applied along the directions x and y. Due to axial symmetry, we have $\varepsilon_{22} \simeq \varepsilon_{33}$ and $\delta\sigma_{22} = \delta\sigma_{33} = 0$. Hence, from the general stress-strain relation, we have

$$\begin{cases} C_{11}\varepsilon_{11} + 2C_{12}\varepsilon_{22} = \delta\sigma_{11}, \\ 2C_{55}\varepsilon_{12} = \delta\sigma_{12}, \\ C_{12}\varepsilon_{11} + (C_{22} + C_{23})\varepsilon_{22} = 0. \end{cases} \tag{2.5}$$

For the second probe, $\dot{\varepsilon}$ was imposed along the y direction while keeping a constant pressure along z and x directions. Therefore, we have $\delta\sigma'_{11} = \delta\sigma'_{33} = 0$ and the stress-strain relations are

$$\begin{cases} C_{12}\varepsilon'_{11} + C_{22}\varepsilon'_{22} + C_{23}\varepsilon'_{33} = \delta\sigma'_{22}, \\ 2C_{44}\varepsilon'_{23} = \delta\sigma'_{23}, \\ C_{11}\varepsilon'_{11} + C_{12}\varepsilon'_{22} + C_{12}\varepsilon'_{33} = 0, \\ C_{12}\varepsilon'_{11} + C_{23}\varepsilon'_{22} + C_{22}\varepsilon'_{33} = 0. \end{cases} \tag{2.6}$$

From the applied stress and strain increments, we use Eqs. (2.5) and (2.6) to calculate all elastic moduli. Note that there are only 5 independent moduli while we have 7 equations. The

consistency of the values obtained in this way for the six moduli was verified by checking the following relation imposed by axial symmetry:

$$C_{22} - C_{23} = 2C_{44}. \tag{2.7}$$

In all cases, we find that this relation holds within an error of 1% in the initially fully elastic regime and up to 10% around the stress peak, where the response to the applied strain probe may involve a plastic component due to softening and unstable particle rearrangements.

It is noteworthy that, since the simulations are based on linear contact laws with constant stiffness parameters k_n and k_t, our packings have an inherent stress scale $E^* = k_n/d$ with which all moduli are expected to scale. In the rigid-particle limit, the condition $p/E^* \ll 1$ should be satisfied. In our simulations, we have $p/E^* \simeq 4.10^{-6}$. The normalized elastic moduli depend also on the stiffness ratio $\alpha_t = k_t/k_n$ [31,41,217]. In this work, we set $\alpha_t = 0.8$ in all simulations.

Figures 2-4, 2-5, and 2-6 display the evolution of the longitudinal moduli C_{11} and C_{22}, off-diagonal moduli C_{12} and C_{23}, the shear moduli C_{44} and C_{55}, and the bulk modulus K for packings of spherical and dodecahedral particles together with theoretical predictions that will be discussed in Section 2.6. The moduli of the polyhedral particle packings at each instance of shear are generally above those of spherical particle packings. They are constant and independent of μ_s at very small shear strains ($< 10^{-5}$), but they change significantly at larger strains when slip events at persistent contacts increase in number and intensity; see Fig. 2-7.

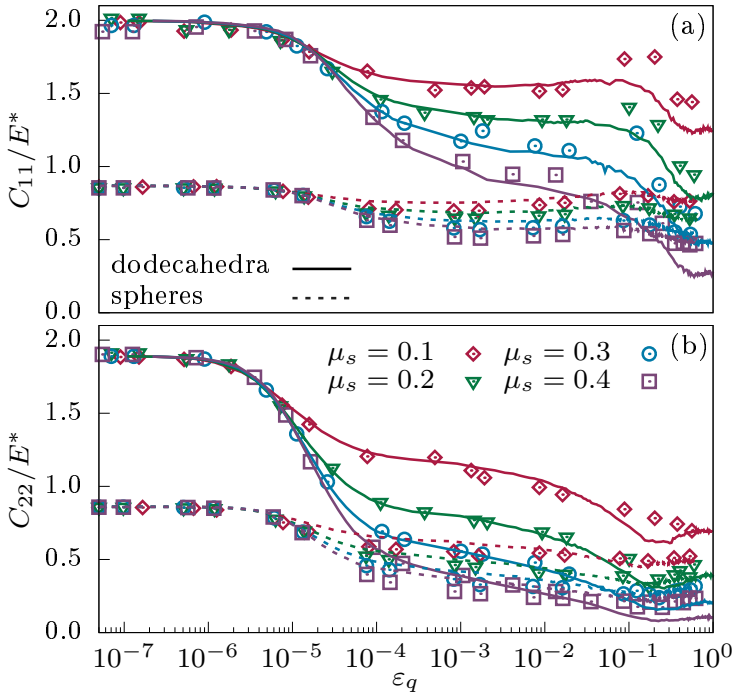

Fig. 2-4. Normalized longitudinal elastic moduli (a) C_{11}/E^* and (b) C_{22}/E^*, as a function of shear strain ε_q for packings of spherical and dodecahedral particles with different values of friction coefficient μ_s. The dashed and solid lines are theoretical predictions (Eq. (2.30)) for packings of spheres and dodecahedra, respectively.

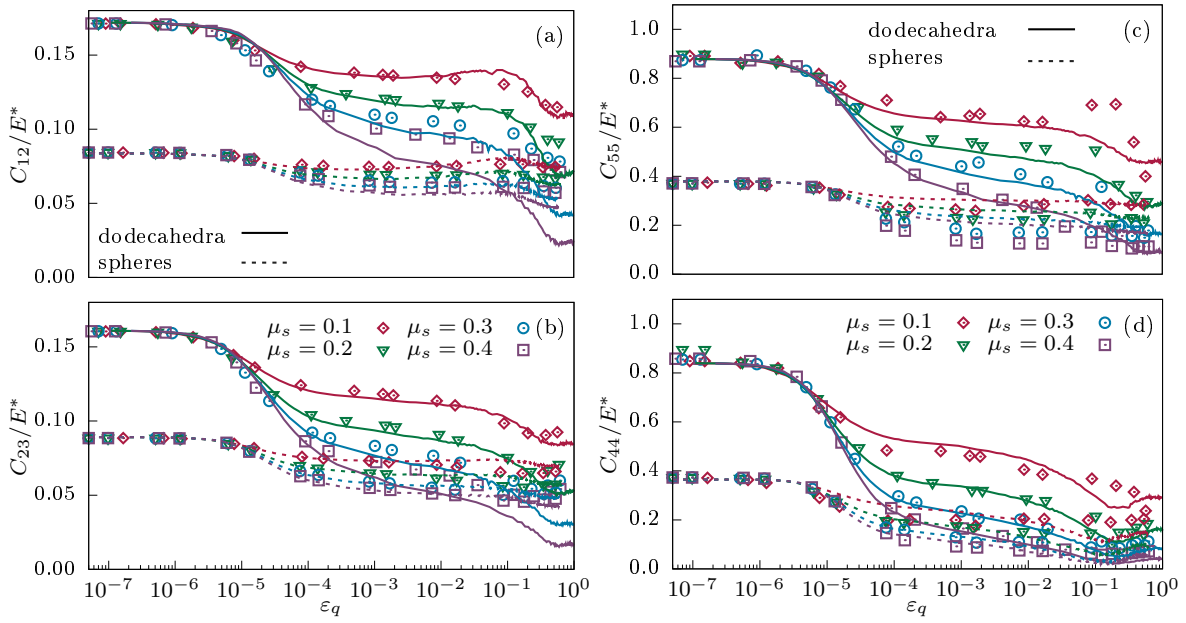

Fig. 2-5. Normalized elastic moduli: off-diagonal moduli, (a) and (b), and shear moduli, (c) and (d), as a function of shear strain ε_q for packings of spherical and dodecahedral particles with different values of friction coefficient μ_s. The lines are predictions by our proposed expression (2.30).

The behavior beyond this elastic limit is rather complex. All moduli first decline to values all the more small that the friction coefficient is large. Then, they increase again or continue to decrease slightly depending on particle shape and μ_s, followed by a slight increase or decrease for $\varepsilon_q > 0.1$. Note that the ratio C_{11}/C_{22} increases to values as large as 4 before decreasing to ~ 2, a value previously reported for dense granular materials with low coordination number [35, 229].

2.5 Evolution of microstructure

The evolution of elastic moduli reflects that of the granular microstructure encoded in the force-bearing contact network. The lowest-order descriptors of granular microstructure are the coordination number Z and contact orientation anisotropy a_c [24, 230]. The latter can be obtained from the *fabric tensor* defined as

$$F_{ij} = \langle n_i n_j \rangle, \tag{2.8}$$

where $\vec{n}$ is the unit contact normal. By definition, we have $tr(\boldsymbol{F}) = 1$, and the largest eigenvalue F_1 occurs along the compression axis. The two other eigenvalues are $F_2 = F_3 = (1 - F_1)/2$. We define the contact anisotropy as [22, 231, 232]

$$a_c = 5(F_1 - F_2)/2. \tag{2.9}$$

The fabric tensor can be evaluated from the probability distribution $P(\vec{n})$ of the unit contact normal $\vec{n}$. In 3D, the contact normal $\vec{n}$ is parametrized by two angles $\theta \in [0;\pi]$ and $\phi \in [0;2\pi]$.

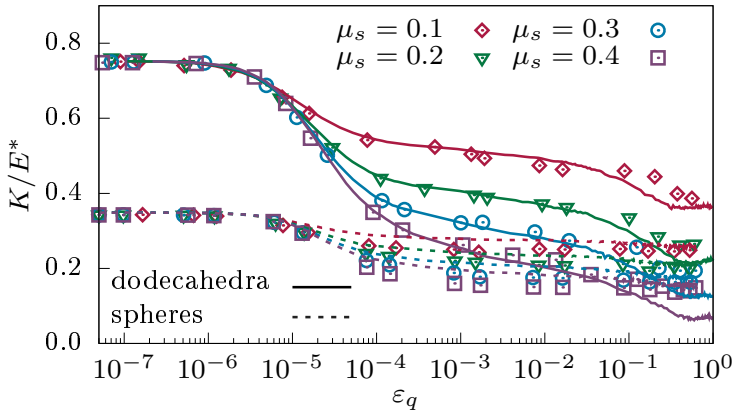

Fig. 2-6. Normalized bulk modulus as a function of shear strain ε_q for packings of spherical and dodecahedral particles with different values of friction coefficient μ_s. The lines are predictions by our proposed expression (2.30).

The probability density function $P(\Omega)$ of contact normals provides a detailed statistical information about the fabric, where $\Omega = (\theta, \phi)$ is the solid angle, with $d\Omega = \sin\theta d\theta d\phi$. The fabric tensor can then be expressed as [22, 230, 233, 234]:

$$F_{ij} = \int_\Omega n_i n_j P(\Omega) d\Omega = \frac{1}{N_c} \sum_{c \in V} n_i^c n_j^c, \tag{2.10}$$

where i and j design the components in a reference frame, and N_c is the total number of contacts in the control volume V. Under axi-symmetric conditions, the probability density function is independent of the azimuth angle ϕ. So, within a second-order harmonic approximation, we have

$$P(\Omega) = \frac{1}{4\pi}\left[1 + a_c(3\cos^2\theta - 1)\right]. \tag{2.11}$$

From Eqs. (2.10) and (2.11), and given the unit contact normal $\vec{n} = (\cos\theta, \sin\theta\cos\phi, \sin\theta\sin\phi)$, the eigenvalues of the fabric tensor are given by

$$F_1 = \int_\Omega n_1^2 P(\Omega) d\Omega = \frac{5 + 4a_c}{15}, \tag{2.12a}$$

$$F_2 = F_3 = \int_\Omega n_2^2 P(\Omega) d\Omega = \frac{5 - 2a_c}{15}. \tag{2.12b}$$

While the definitions of Z and a_c are straightforward in the case of spherical particles, we need to consider the contact types for polyhedral particles, as discussed in Section 2.2. We generalize the coordination number by attributing different weights to different contact types. In particular, we define here a *constraint number* Z_c by weighing each contact type by the number of constraints it represents:

$$Z_c = 2(N_s + 2N_d + 3N_t)/N_p, \tag{2.13}$$

where N_s, N_d, and N_t are the numbers of simple, double, and triple contacts, respectively, and N_p is the total number of particles. The constraint number is reduced to the coordination number in the case of spherical particles.

A packing of frictionless particles is isostatic so that the number of degrees of freedom per particle must be equal to the number of constraints per particle $Z_c/2$. The number of degrees of freedom is 3 per particle in the case of frictionless spheres (the rotations being ineffective), whereas polyhedra have 6 degrees of freedom per particle both with and without friction. Hence, the constraint number for packings of spheres and polyhedra is 6 and 12, respectively. We find $Z_c \simeq 6.03$ for spheres and $Z_c \simeq 12.05$ for polyhedra at the end of isotropic compaction, both remarkably close to the expected values. The small difference is due to the finite stiffness and overlaps between particles. This suggests that Z_c is the relevant connectivity parameter for polyhedral particle packings, in contrast to Z which has a lower value ($\simeq 8$) in the isostatic state. The same remarks apply to the definition of fabric tensor for polyhedra by considering that face-face contacts are equivalent to 3 contact points and edge-face contacts to 2 contact points.

Figure 2-7 displays the evolution of Z_c and a_c during compression. Consistently with the elastic moduli, at small shear strains ($< 10^{-5}$), both Z_c and $a_c \simeq 0$ (initially isotropic state) are constant and independent of μ_s due to the stability of the contact network. With the onset of particle rearrangements, Z_c decreases and tends to a constant value whereas a_c initially increases as a result of the loss of contacts perpendicular to the compression axis [18, 21]. The fabric anisotropy is larger in packings of polyhedral particles compared to spheres, and its peak value increases with μ_s.

The microstructure evolves also in terms of the distribution of different types of contacts. Fig. 2-8 displays a snapshot of force chains in the isotropic (initial) state and near the stress peak with different colors for different contact types. The proportions N_t/N_c of face-face contacts declines from 0.14 in the isotropic state to 0.1 in the peak state although we distinctly observe columnar force chains of face-face contacts along the compression axis in the peak state. In a similar vein, the proportion N_d/N_c of edge-face contacts declines during compression. Hence, the larger proportion of single contacts near the stress peak is the necessary condition for the stability of columnar force chains [232].

2.6 Relation between elastic moduli and microstructure

The central issue that we address here is whether the values of elastic moduli shown in Figs. 2-4, 2-5, and 2-6 can be univocally expressed in terms of Z_c and a_c. The connection between elasticity and granular microstructure has been previously investigated in the case of isotropic packings of spherical particles and compared with the predictions of EMT [31, 35, 36, 41]. We first derive analytical expressions of elastic moduli in the EMT framework for anisotropic media with orthotropic symmetry. Then, we compare our simulation data with its predictions to propose a general expression which correctly predicts the evolution of elastic moduli all along triaxial compression from the isostatic state up to the stress peak state.

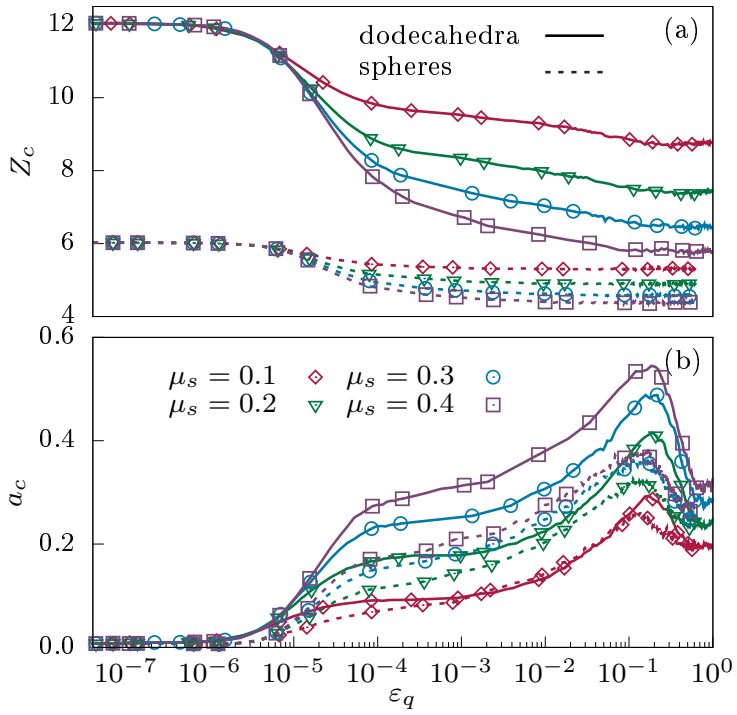

Fig. 2-7. Constraint number Z_c (a) and fabric anisotropy a_c (b) as a function of shear strain ε_q for packings of spherical and dodecahedral particles and different values of friction coefficient μ_s. The dashed and solid lines are for packings of spheres and dodecahedra, respectively. The symbols represent instances where strain probes were applied.

2.6.1 Elastic moduli from EMT

The medium is assumed to behave as a continuum with particle centers moving according to the applied strain field (affine assumption). Hence, in response to an incremental strain $\delta\varepsilon_{ij}$, the normal and tangential displacements at each contact are simply given by

$$\delta_n = \delta\varepsilon_{ij} n_i n_j, \tag{2.14}$$

$$\delta_t = \delta\varepsilon_{ij} n_i t_j, \tag{2.15}$$

where $\vec{t}$ represents a tangential unit vector. The contact forces can therefore be obtained from these displacements and the force laws (2.1) and (2.2).

Let $(\vec{n'},\vec{t'},\vec{s'})$ be a local frame associated with the branch vector $\vec{\ell} = \ell\vec{n'}$ joining the centers of two touching particles. In spherical coordinates, we have

$$\begin{cases} \vec{n'} = (\cos\theta, \sin\theta\cos\phi, \sin\theta\sin\phi), \\ \vec{t'} = (-\sin\theta, \cos\theta\cos\phi, \cos\theta\sin\phi), \\ \vec{s'} = (0, -\sin\phi, \cos\phi), \end{cases} \tag{2.16}$$

where ϕ is the azimuth and θ is the latitude.

By affine assumption, the variation of ℓ is given by

$$\delta\vec{\ell} = \ell\boldsymbol{\varepsilon}\vec{n'}. \tag{2.17}$$

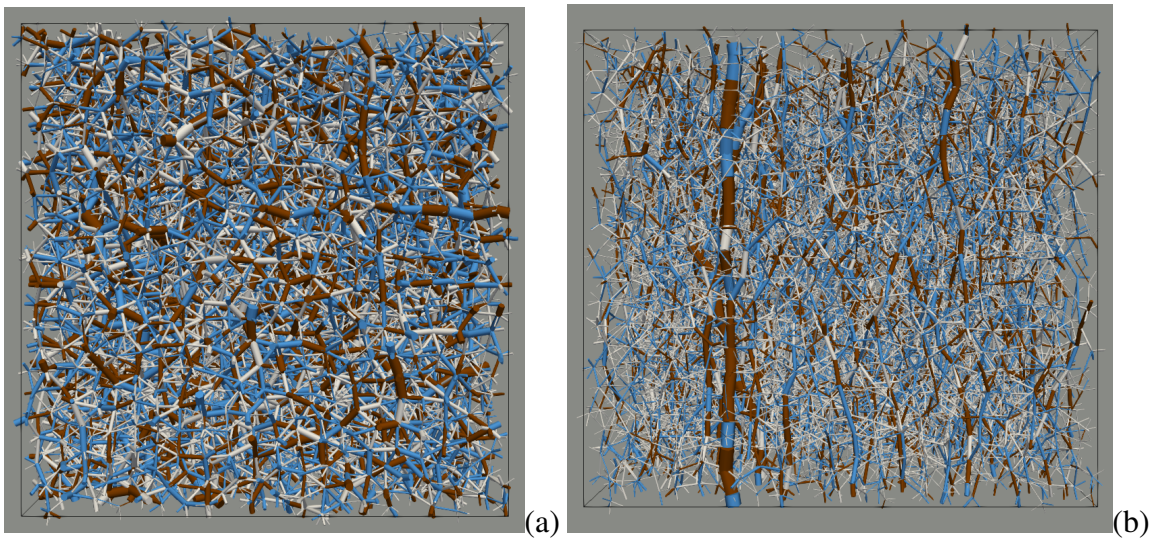

Fig. 2-8. Snapshot of the normal force network of a dodecahedral particle packing at isotropic state (a), and near stress peak (b) with friction coefficient $\mu_s = 0.1$. Line thickness is proportional to normal force. Single contacts are in white, double contacts in blue, and triple contacts in brown. The compression axis is along the vertical direction. At isotropic state, the fractions of single, double and triple contacts are 0.5, 0.36, and 0.14, respectively. At stress peak state, they are 0.59, 0.31, and 0.1, respectively.

This variation leads to relative displacements δ_n, δ_t, and δ_s at any contact point between the two particles with its associated frame $(\vec{n},\vec{t},\vec{s})$, $\vec{n}$ being normal unit vector to the contact plane. For spherical particles, this frame exactly coincides with the frame associated with the branch vector. Due to disorder, this property holds also on average in the case of two convex particles. Indeed, we checked that in our samples, we have $\vec{n}\cdot\vec{n}' \simeq 1$. For this reason, we can use the contact frame together with the branch vector length to approximate the relative displacements at contact points:

$$\begin{cases} \delta_n = \ell \boldsymbol{\varepsilon}\vec{n}\cdot\vec{n}, \\ \delta_t = \ell \boldsymbol{\varepsilon}\vec{n}\cdot\vec{t}, \\ \delta_s = \ell \boldsymbol{\varepsilon}\vec{n}\cdot\vec{s}. \end{cases} \tag{2.18}$$

From the contact displacements, we write down the elastic energy per unit volume ΔW_e as a function of the strain tensor $\boldsymbol{\varepsilon}$. Let k_n and k_t be the normal stiffness and tangential stiffness, respectively, and $n_c = N_c/V$ the contact number density in a volume V containing N_c contacts. Then, we have

$$\begin{aligned} \Delta W_e &= \frac{n_c k_n}{2}\langle\delta_n^2\rangle + \frac{n_c k_t}{2}\langle\delta_t^2\rangle + \frac{n_c k_t}{2}\langle\delta_s^2\rangle \\ &= \frac{n_c}{2}\langle\ell^2\rangle[k_n\langle(\boldsymbol{\varepsilon}\vec{n}\cdot\vec{n})^2\rangle + k_t\langle(\boldsymbol{\varepsilon}\vec{n}\cdot\vec{t})^2\rangle + k_t\langle(\boldsymbol{\varepsilon}\vec{n}\cdot\vec{s})^2\rangle], \end{aligned} \tag{2.19}$$

where it has been assumed that the branch vector length ℓ and contact orientation $\vec{n}$ are not correlated. Indeed, we checked that in our samples, we have $\langle\ell\cos^2\theta\rangle \simeq \langle\ell\rangle\langle\cos^2\theta\rangle$.

In the frame of the principal axes of the strain tensor $\boldsymbol{\varepsilon}$, we have

$$\begin{cases} \boldsymbol{\varepsilon}\vec{n}\cdot\vec{n} = \varepsilon_{11}\cos^2\theta + \varepsilon_{22}\sin^2\theta\cos^2\phi + \varepsilon_{33}\sin^2\theta\sin^2\phi, \\ \boldsymbol{\varepsilon}\vec{n}\cdot\vec{t} = \dfrac{1}{2}\sin 2\theta(-\varepsilon_{11} + \varepsilon_{22}\cos^2\phi + \varepsilon_{33}\sin^2\phi), \\ \boldsymbol{\varepsilon}\vec{n}\cdot\vec{s} = \dfrac{1}{2}\sin\theta\sin 2\phi(\varepsilon_{33} - \varepsilon_{22}). \end{cases} \tag{2.20}$$

The average values $\langle(\boldsymbol{\varepsilon}\vec{n}\cdot\vec{n})^2\rangle$, $\langle(\boldsymbol{\varepsilon}\vec{n}\cdot\vec{t})^2\rangle$, and $\langle(\boldsymbol{\varepsilon}\vec{n}\cdot\vec{s})^2\rangle$ are evaluated by integrating their expressions from Eq. (2.20) over the angles θ and ϕ by using the probability distribution function $P(\theta,\phi)$ given by Eq. (2.11). Once inserted in Eq. (2.19), an expression of the total elastic energy ΔW_e is obtained as a function of n_c, fabric anisotropy a_c, contact parameters, and strain tensor coefficients.

By definition, the elastic moduli C_{ij} are the second derivatives of this energy function with respect to ε_{ij}:

$$\begin{cases} C_{11} = \dfrac{\partial^2\Delta W_e}{\partial\varepsilon_{11}^2} = n_c\langle\ell^2\rangle k_n\left(\dfrac{3+2\alpha_t}{15} + \dfrac{24+4\alpha_t}{105}a_c\right), \\ C_{22} = \dfrac{\partial^2\Delta W_e}{\partial\varepsilon_{22}^2} = n_c\langle\ell^2\rangle k_n\left(\dfrac{3+2\alpha_t}{15} - \dfrac{12+2\alpha_t}{105}a_c\right), \\ C_{12} = \dfrac{\partial^2\Delta W_e}{\partial\varepsilon_{11}\partial\varepsilon_{22}} = n_c\langle\ell^2\rangle k_n(1-\alpha_t)\left(\dfrac{1}{15} + \dfrac{2}{105}a_c\right), \\ C_{23} = \dfrac{\partial^2\Delta W_e}{\partial\varepsilon_{22}\partial\varepsilon_{33}} = n_c\langle\ell^2\rangle k_n(1-\alpha_t)\left(\dfrac{1}{15} - \dfrac{4}{105}a_c\right), \end{cases} \tag{2.21}$$

where $\alpha_t = k_t/k_n$ is the stiffness ratio.

The shear moduli C_{55} and C_{44} are given by the second derivatives of the energy function with respect to the variables $\varepsilon_q = \varepsilon_{11} - \varepsilon_{22}$ and $\varepsilon_{q'} = \varepsilon_{22} - \varepsilon_{33}$:

$$\begin{cases} C_{55} = \dfrac{\partial^2\Delta W_e}{\partial\varepsilon_q^2} = \dfrac{n_c\langle\ell^2\rangle k_n}{30}\left(2+3\alpha_t + \dfrac{4+3\alpha_t}{7}a_c\right), \\ C_{44} = \dfrac{\partial^2\Delta W_e}{\partial\varepsilon_{q'}^2} = \dfrac{n_c\langle\ell^2\rangle k_n}{30}\left(2+3\alpha_t - \dfrac{8+6\alpha_t}{7}a_c\right). \end{cases} \tag{2.22}$$

Finally, the bulk modulus K is the second derivative of the energy function with respect to the volumetric strain $\varepsilon_v = \varepsilon_{11} + \varepsilon_{22} + \varepsilon_{33}$,

$$K = \frac{\partial^2\Delta W_e}{\partial\varepsilon_v^2} = \frac{n_c\langle\ell^2\rangle k_n}{9}. \tag{2.23}$$

Note that, we have $C_{22} - C_{23} = 2C_{44}$, so that the bulk modulus can be expressed as a function of C_{ij}:

$$K = \frac{C_{11} + 4C_{12} + 2C_{22} + 2C_{23}}{9}. \tag{2.24}$$

2.6.2 Comparison with numerical results

The above expressions of elastic moduli based on EMT are proportional to the number density n_c of contacts. It is easy to show that

$$n_c = \frac{Z_c \Phi}{2V_p}, \tag{2.25}$$

where V_p is the average particle volume. Furthermore, the elastic moduli can be normalized by E^*, which defines the reference value of all elastic moduli. Hence, following Eq. (2.23), the bulk modulus K^{EMT} can be expressed as

$$K^{EMT} = mE^* \Phi Z_c, \tag{2.26}$$

where

$$m = \frac{\langle \ell^2 \rangle d}{18V_p}. \tag{2.27}$$

Equation (2.26) suggests that the bulk modulus is proportional to ΦZ_c with a prefactor depending mainly on the mean square distance $\langle \ell^2 \rangle$ between particle centers. This expression of K is the same as the one derived previously for isotropic granular materials composed of spherical particles [31, 35]. Here, it is extended to polyhedral particles by replacing Z by Z_c. Figure 2-9 shows K as a function of ΦZ_c from all our simulation data at different instances of compression. The EMT prediction is also plotted for comparison with the values of $\langle \ell^2 \rangle$ extracted from the simulations. All our data points, independently of friction coefficient, nicely collapse on a straight line for both spherical and polyhedral particle packings, as predicted by EMT, in exception to data points lying slightly above the line at low values of ΦZ_c. These data points represent actually the late stages of compression where the system is in the post-peak softening regime with intense particle rearrangements, leading to an over-estimation of elastic moduli.

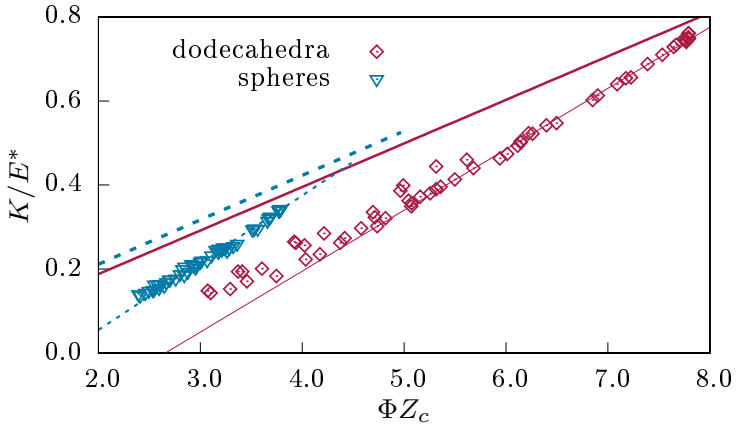

Fig. 2-9. Normalized bulk modulus K/E^* as a function of ΦZ_c from simulations of dodecahedral and spherical particle packings. The thin lines are linear fits to the data. The thick lines represent predictions of EMT for polyhedra (solid line) and spheres (dashed line).

While the predicted linear dependence of elastic moduli on ΦZ_c is in agreement with the simulation results, there are two key differences between the predicted values of bulk modulus

K^{EMT} and the values measured in simulations for both spherical and polyhedral particle packings. First, the prefactor m is higher in the simulations. Secondly, K^{EMT} vanishes only when $Z_c\Phi$ tends to zero whereas in the simulations the bulk modulus vanishes for a finite value of $Z_c\Phi$. This means that the bulk modulus can be approximated as

$$K = E^*(n + m\Phi Z_c), \tag{2.28}$$

where n is a parameter of negative value which depends on particle shape. The fitted values of n and m are given in Table 2-1 for different particle shapes together with the values predicted by EMT. The differences between the EMT prediction and the simulated values of n and m have their origin in the nonaffine relative particle displacements which contradict the EMT assumption of an affine displacement field [31, 217]; see below.

Interestingly, the non-zero value of n in the linear fit to the simulation data implies that K vanishes at $\Phi Z_c = -n/m$. This ratio is $\simeq 2.6$ for polyhedra and $\simeq 1.65$ for spheres. The vanishing of K for a finite value of ΦZ_c is a reminiscent of unjamming transition at a finite value of Z_c. Obviously, unjamming does not occur in our system during compression but Fig. 2-9 shows that the lowest values of ΦZ_c ($\simeq 2.4$ for spheres and $\simeq 3.1$ for polyhedra) occur during post-peak softening and they are close to the values of $-n/m$.

	C_{11}		C_{22}		C_{12}		C_{23}		C_{44}		C_{55}		K	
	r_{11}	s_{11}	r_{22}	s_{22}	r_{12}	s_{12}	r_{23}	s_{23}	r_{44}	s_{44}	r_{55}	s_{55}	n	m
EMT (expression)	$\frac{9+6\alpha_t}{5}$	$\frac{72+12\alpha_t}{35}$	$\frac{9+6\alpha_t}{5}$	$-\frac{36+6\alpha_t}{35}$	$\frac{3-3\alpha_t}{5}$	$\frac{6-6\alpha_t}{35}$	$\frac{3-3\alpha_t}{5}$	$-\frac{12-12\alpha_t}{35}$	$\frac{6+9\alpha_t}{10}$	$-\frac{12+9\alpha_t}{35}$	$\frac{6+9\alpha_t}{10}$	$\frac{12+9\alpha_t}{70}$	0	$\frac{\langle\ell^2\rangle d}{18V_p}$
EMT (value)	2.760	2.332	2.760	-1.166	0.120	0.034	0.120	-0.069	1.320	-0.549	1.320	0.274	0	0.105
Simulation (dodecahedra)	2.617	4.151	2.542	-3.258	0.225	0.387	0.213	0.100	1.132	-1.694	1.234	0.500	-0.378	0.145
Simulation (icosahedra)	2.547	4.565	2.563	-3.482	0.223	0.500	0.215	0.200	1.154	-2.176	1.172	0.932	-0.400	0.150
Simulation (octahedra)	2.486	5.182	2.608	-3.573	0.219	0.420	0.210	0.142	1.227	-1.861	1.215	1.530	-0.360	0.157
Simulation (spheres)	2.490	3.105	2.490	-2.812	0.240	0.255	0.250	0.080	1.065	-2.000	1.087	0.120	-0.265	0.160

Table 2-1. Fitting parameters in Eq. (2.30) for elastic moduli from the effective medium theory (EMT) and DEM simulations of the four particle shapes.

According to Eqs. (2.21) and (2.22), all elastic moduli C_{ij} are proportional to K and their ratio depends linearly on the contact orientation anisotropy a_c:

$$C_{ij} = K(r_{ij} + s_{ij}a_c), \tag{2.29}$$

where the parameters r_{ij} and s_{ij} depend on particle shape. This linear dependence on fabric anisotropy is indeed what we observe in Fig. 2-10 for all elastic moduli and for both polyhedral and spherical particle packings, but with values of r_{ij} and s_{ij} that deviate from those predicted by EMT due to nonaffine displacement field; see Table 2-1.

2.6.3 General expression of elastic moduli

Based on the simulation data and effective medium theory discussed previously, we propose the following analytical expression for the five orthotropic elastic moduli:

$$C_{ij} = E^*(n + m\Phi Z_c)(r_{ij} + s_{ij}a_c). \tag{2.30}$$

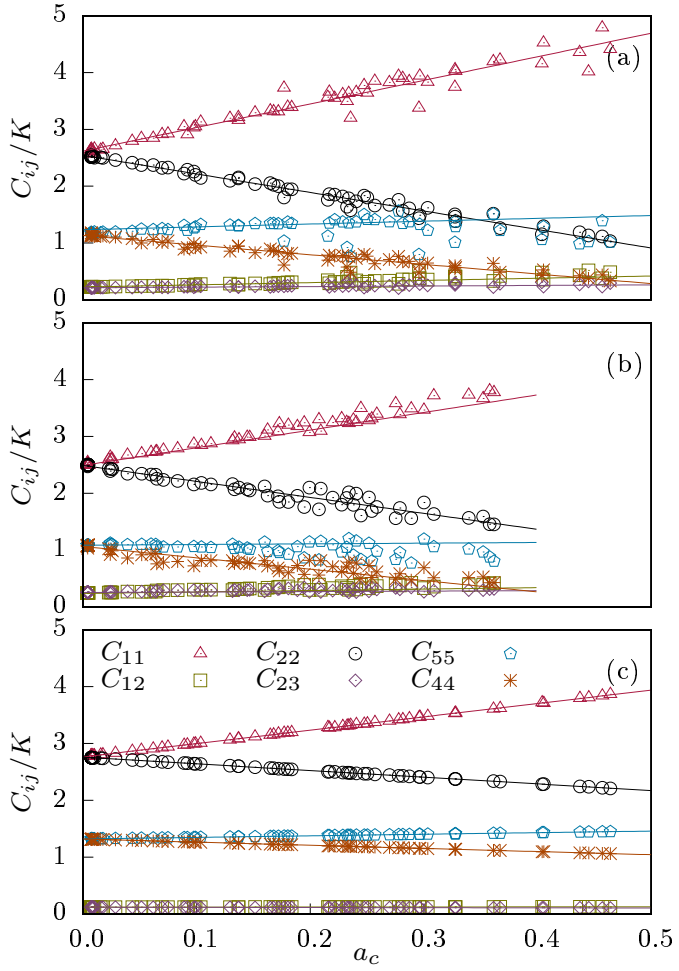

Fig. 2-10. Normalized moduli C_{ij}/K as a function of fabric anisotropy a_c for the dodecahedral (a) and spherical (b) particle packings from simulations with different values of the friction coefficient, together with theoretical prediction (c) based on the EMT. The straight lines are the best linear fits to the data points. The data of icosahedra is shown in Supplemental Material and it follows a similar evolution.

The EMT predictions of n, m, r_{ij}, and s_{ij} are shown in Table 2-1 together with their values measured from our simulations for the three particle shapes. This expression relates in a univocal way the elastic moduli to the microstructure of granular materials under transversely isotropic symmetry. With its parameter values given in Table 2-1, it allows us to predict the evolution of elastic moduli as a function of shear strain ε_q from that of Z_c and a_c extracted from simulations. Figures 2-4, 2-5, and 2-6 show the evolution of the elastic moduli according to this analytical expression together with their measured values from simulations. We see that this expression follows amazingly well the simulation data from the isostatic state up to the stress peak state. The observed "wavy" feature of the evolution of elastic moduli observed in these figures can therefore be explained as a consequence of the multiplicative contributions of the isotropic part $n+m\Phi Z_c$ and the anisotropic part $r_{ij}+s_{ij}a_c$ with decreasing Z_c and increasing a_c during compression.

It is remarkable that the model parameters n, m, r_{ij}, and s_{ij} are independent of friction

coefficient. The differences between elastic moduli for different values of μ_s arise therefore from the effect of the latter on the evolution of Z_c and a_c. The values of parameters in Table 2-1 show also that the higher value of K in the case of polyhedral particle packings compared to that of the sphere packing is mainly due to the higher values of $Z_c\Phi$ rather than the smaller variations of the model parameters. Furthermore, the dodecahedral and icosahedral particle packings have slightly different elastic moduli. A detailed comparison between the elastic moduli of polyhedral particle packings with different numbers of faces will be presented elsewhere.

The observed linear dependence of the elastic moduli on $Z_c\Phi$ and a_c in our simulations suggests that, despite the evolution of the microstructure the level of nonaffine displacements is nearly constant during triaxial compression. To check this point, we investigated the nonaffine displacements in our simulations. Several methods can be used to quantify the level of non-affinity [235–238]. We used a measure of non-affinity from the relative particle displacements. Let $\delta r_z^\alpha = \delta r_z^i - \delta r_z^j$ be the relative displacement at the contact α between particles i and j projected along the z direction and ℓ^α the length of the branch vector joining their centers. Then, the actual strain increment at contact α along the z direction is $\delta\varepsilon_z^\alpha = \delta r_z^\alpha/\ell^\alpha$. We define the nonaffinity ξ along the compression axis as

$$\xi = \frac{\sqrt{\langle(\delta\varepsilon_z)^2\rangle - \langle\delta\varepsilon_z\rangle^2}}{\langle\delta\varepsilon_z\rangle}, \tag{2.31}$$

where the averages run over all contacts inside the packing. Note also that the average $\langle\delta\varepsilon_z\rangle$ is simply equal to the mean affine displacement imposed when probing the elastic response.

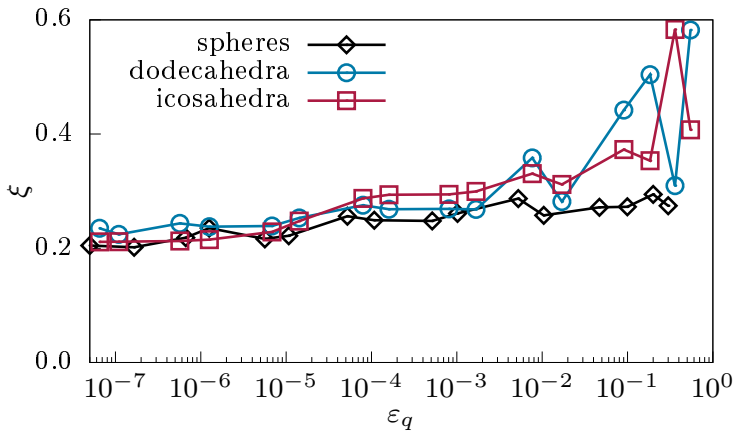

Fig. 2-11. Level of non-affinity ξ (equation (2.31)) as a function of shear strain ε_q for packings of spherical and dodecahedral particles with friction coefficient $\mu_s = 0.1$.

We calculated ξ at all probing instances and Fig. 2-11 displays its evolution for the three particle shapes in the case $\mu_s = 0.1$ (the evolution being similar for other values of μ_s). Interestingly, ξ has nearly the same value for all shapes during compression and increases slowly from $\simeq 0.2$ at low compression until the stress peak at $\varepsilon_q \simeq 5\times10^{-2}$. Beyond this point, it grows rapidly to higher values as a result of softening and unstable particle motions. This is consistent with the evolution of the elastic moduli shown in Fig. 2-9, where the corresponding data points deviate from expression (2.30). The nearly constant level of non-affinity before

stress peak explains the linear dependence of elastic moduli on the microstructural prameters Z_c and a_c and thus the constant values of the parameters n, m, r_{ij}, and s_{ij} in the analytical expression (2.30) implying that their values are almost only functions of particle shape. Obviously, the small second-order effects arising from the dependence of non-affinity on the increasing anisotropy of the packing during compression are not observable within the statistical precision of our simulation data.

2.7 Conclusion

We derived a general expression (2.30) of the orthotropic elastic moduli of granular materials under triaxial boundary conditions as a function of microstructural parameters for three different particle shapes and four different values of the interparticle friction coefficient. This expression reveals three different origins of elastic moduli: a stress scale E^*, an isotropic part, and an anisotropic part. The stress scale E^* depends on the force model. In our linear force model, its value is simply k_n/d, but for a Hertz contact, which is obviously not adapted to faceted particles, it should be multiplied by a ratio $\{p/(\tilde{E}Z_c\Phi)\}^{1/3}$, where $\tilde{E} = E/(1-\nu^2)$ is the reduced elastic modulus [32, 35, 44], and makes depend the moduli on the confining pressure.

The effect of particle shape appears at two levels: on the one hand, through the parameters n, m, r_{ij}, and s_{ij}, which do not depend on friction coefficient and are not neither expected to depend on p for Hertzian contacts, and on the other hand, through the microstructure via the values of Z_c and a_c, which depend on both particle shape and friction coefficient μ_s. While the expression (2.30) provides a powerful model of elastic moduli in the hardening regime (before stress peak) with a clear distinction between the two effects of particle shape, our results indicate that, due to unstable particle rearrangements, the measurement of elastic moduli in the softening regime requires strain probes well below 10^{-5} used in this work throughout triaxial compression.

The expression (2.30) makes it possible to extract the values of Z_c and a_c and the model parameters n, m, r_{ij}, and s_{ij} from experimental measurements of the elastic moduli. This is specially relevant for granular materials composed of aspherical particle shapes whose elastic properties have not yet been a subject of systematic investigation. More work is currently underway to further validate Eq. (2.30) for other particle shapes, different values of the stiffness ratio, and different boundary conditions. A detailed comparison of the elastic moduli of polyhedral particle packings with increasing number of faces will be published in a forthcoming paper.

2.8 Supplementary Information

2.8.1 Evolution of Poisson's ratios of dodecahedral and spherical particle packings

Poisson's ratio can be extracted from two strain probes as follows:

$$\nu_{12} = -\frac{\varepsilon_{22}}{\varepsilon_{11}} = \frac{C_{12}}{C_{22}+C_{23}} \tag{2.32a}$$

$$\nu_{23} = -\frac{\varepsilon'_{33}}{\varepsilon'_{22}} = \frac{C_{11}C_{23}-C_{12}^2}{C_{11}C_{22}-C_{12}^2} \tag{2.32b}$$

It is worth mentioning that although Poisson's ratio for isotropic materials is bounded between -1 and 0.5, those of anisotropic materials can have no bounds [239]. Fig. 2-12 displays the evolution of Poisson's ratios ν_{12} and ν_{23} as a function of shear strain ε_q for dodecahedral and spherical particle packings. Our data show that the initial Poisson's ratios corresponding to isotropic state is 0.1 for spherical particle packings, in agreement with those of Agnolin and Roux [32], and 0.09 for packings of polyhedral particles. This lower value of the Poisson's ratio reflect the lower mobility of the particles. We also find that Poisson's ratios are independent of μ_s at very small shear strain, but they increase significantly at larger strains when slip events at persistent contacts happen. After reaching the peak, which occurs at $\varepsilon_q \sim 0.1$, they decrease considerably or slightly depending on particle shape and μ_s. From the prediction of EMT for elastic moduli in Eqs (2.21) and (2.22), it is clear that the Poisson's ratios are independent of contact density (ΦZ_c), and depend chiefly on the fabric anisotropy a_c.

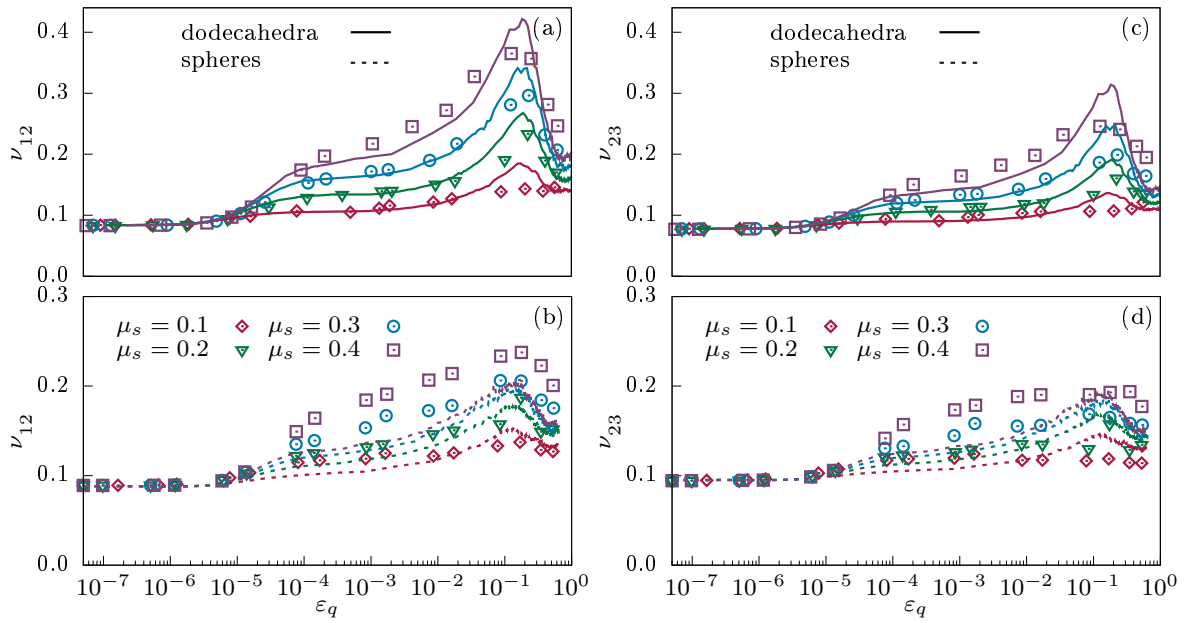

Fig. 2-12. Poisson's ratios as a function of shear strain ε_q for the packings of dodecahedral and spherical particles with different values of friction coefficient μ_s. The lines are predictions by our proposed expression; see main text.

2.8.2 Evolution of microstructure and elastic moduli of icosahedral particle packings

The evolution of stress ratio q/p and microstructures properties for icosahedral particle packings is shown in Fig. 2-13. We see that they change similarly with those of dodecahedral particle packings shown before. Figures 2-14 and 2-15 displays the evolution of elastic moduli for packings of icosahedral particles together with theoretical predictions (2.30) as a function of shear strain ε_q. Fig. 2-16 describes the relation of elastic moduli and microstructures for packings of icosahedral particles.

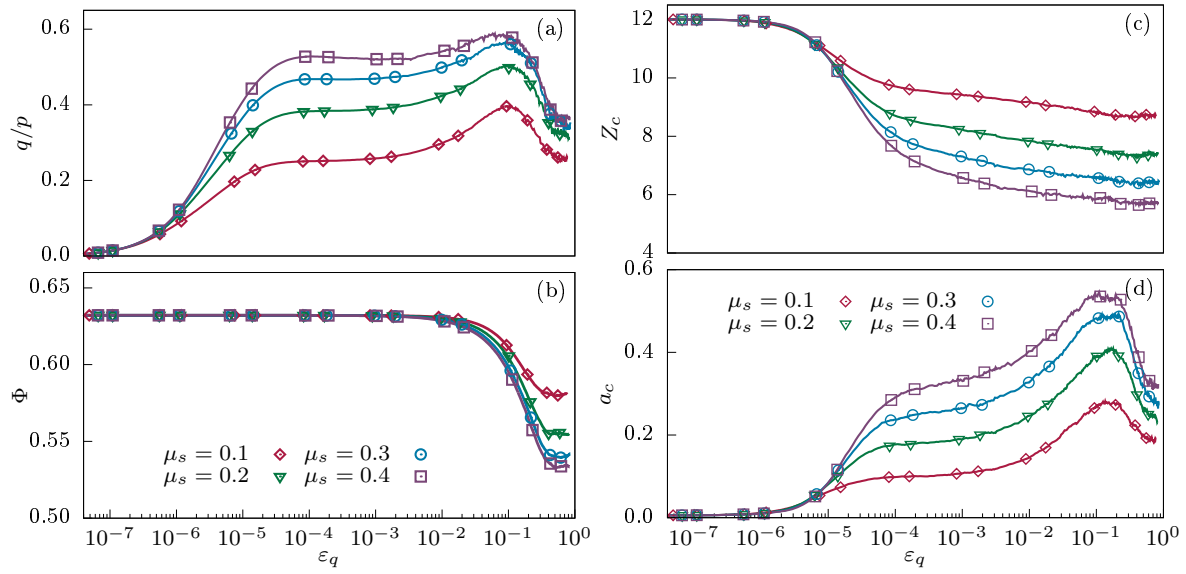

Fig. 2-13. (a) Stress ratio q/p, (b) packing fraction Φ, (c) constraint number Z_c, and (d) fabric anisotropy a_c as a function of shear strain ε_q for packings of icosahedral particles and different values of friction coefficient μ_s. The symbols represent instances where strain probes were applied.

The fractions of each type of contacts is shown in Fig. 2-17(a). The fractions are constant when $\varepsilon_q < 5 \times 10^{-6}$ reflecting the stable of force network. Then the particles start moving, the fraction of single contacts increases whereas those of double and triple contacts reduce. This means a part of double and triple contacts are damaged to become single contacts which are less stable. After that, the number of contacts in whole sample decrease because of the disintegration of not only single contacts but also double and triple contacts. As a consequence, the fraction of double and triple contacts approaches a plateau with $\varepsilon_q > 10^{-3}$. Furthermore, the evolution of average normal force of single, double, and triple contacts is shown in Fig. 2-17(b). We find that average normal force of double and triple contacts are approximate two and three time bigger in those of single contacts, respectively. This means that most of the forces in the sample are carried by more stable contacts (double and triple).

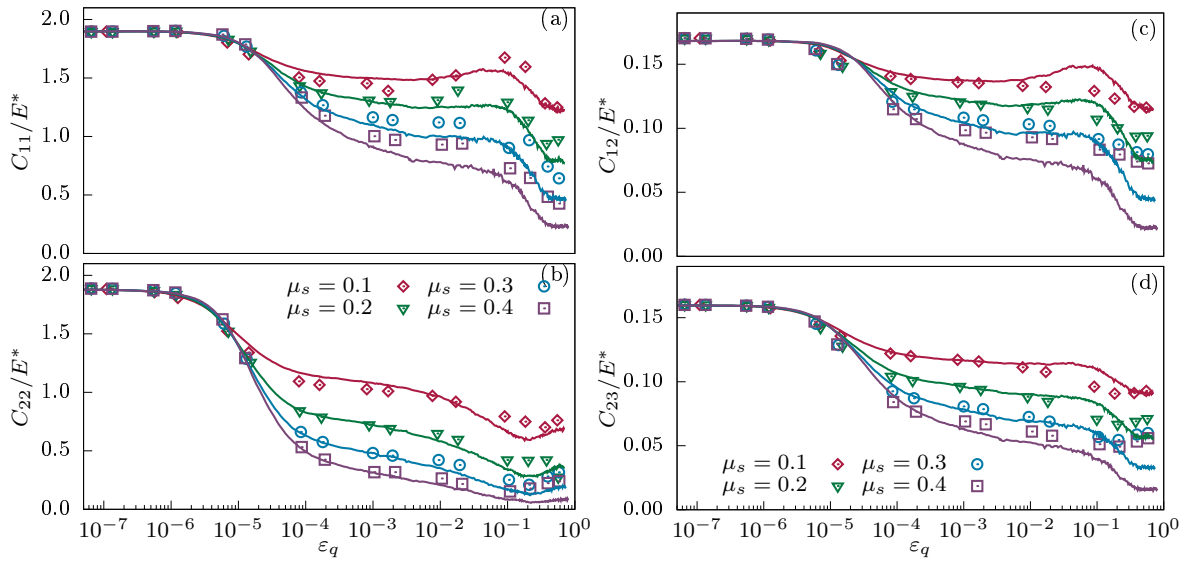

Fig. 2-14. Normalized elastic moduli: longitudinal (a) and (b), off-diagonal (c) and (d) as a function of shear strain ε_q for packings of icosahedral particles with different values of friction coefficient μ_s. The solid lines are predictions by our proposed expression; see main text.

2.8.3 Theoretical model of EMT

Herein, we present more detailed transformation of theoretical model of EMT. The elastic energy per unit volume ΔW_e is given by

$$\Delta W_e = \frac{1}{2}\sum \delta\sigma_{ij}\varepsilon_{ij}, \tag{2.33}$$

where the relation between incremental response stress $\delta\sigma_{ij}$ and incremental applied strain ε_{ij} is extracted from Eq.(2.3). We have

$$\Delta W_e = \frac{1}{2}\left(C_{11}\varepsilon_{11}^2 + C_{22}\varepsilon_{22}^2 + C_{22}\varepsilon_{33}^2\right) + C_{12}(\varepsilon_{11}\varepsilon_{22} + \varepsilon_{11}\varepsilon_{33}) + C_{23}\varepsilon_{22}\varepsilon_{33} + C_{44}(\varepsilon_{12}^2 + \varepsilon_{13}^2) + C_{55}\varepsilon_{23}^2. \tag{2.34}$$

From Eq.(2.34), the elastic moduli C_{ij} are calculated by the second derivatives of the elastic energy function with respect to ε_{ij}, as shown in Eqs. (2.21) and (2.22).

Due to the anisotropy, we have

$$\langle\cos^4\theta\rangle = \int_0^{\pi}\cos^4\theta P(\Omega)\sin\theta d\theta\int_0^{2\pi}d\phi = \frac{1}{5} + \frac{8}{35}a_c. \tag{2.35}$$

In similar vein, we have

$$\langle\sin^4\theta\rangle = \frac{8}{15} - \frac{32}{105}a_c, \langle\sin^2 2\theta\rangle = \frac{8}{15} + \frac{16}{105}a_c, \langle\sin^2\theta\rangle = \frac{2}{3} - \frac{4}{15}a_c$$
$$\langle\sin^2 2\phi\rangle = \frac{1}{2}, \langle\cos^4\phi\rangle = \langle\sin^4\phi\rangle = \frac{3}{8}, \langle\cos^2\phi\rangle = \langle\sin^2\phi\rangle = \frac{1}{2}.$$

From that the average values $\langle(\boldsymbol{\varepsilon}\vec{n}\cdot\vec{n})^2\rangle$, $\langle(\boldsymbol{\varepsilon}\vec{n}\cdot\vec{t})^2\rangle$, and $\langle(\boldsymbol{\varepsilon}\vec{n}\cdot\vec{s})^2\rangle$ in Eq. (2.19) are given by

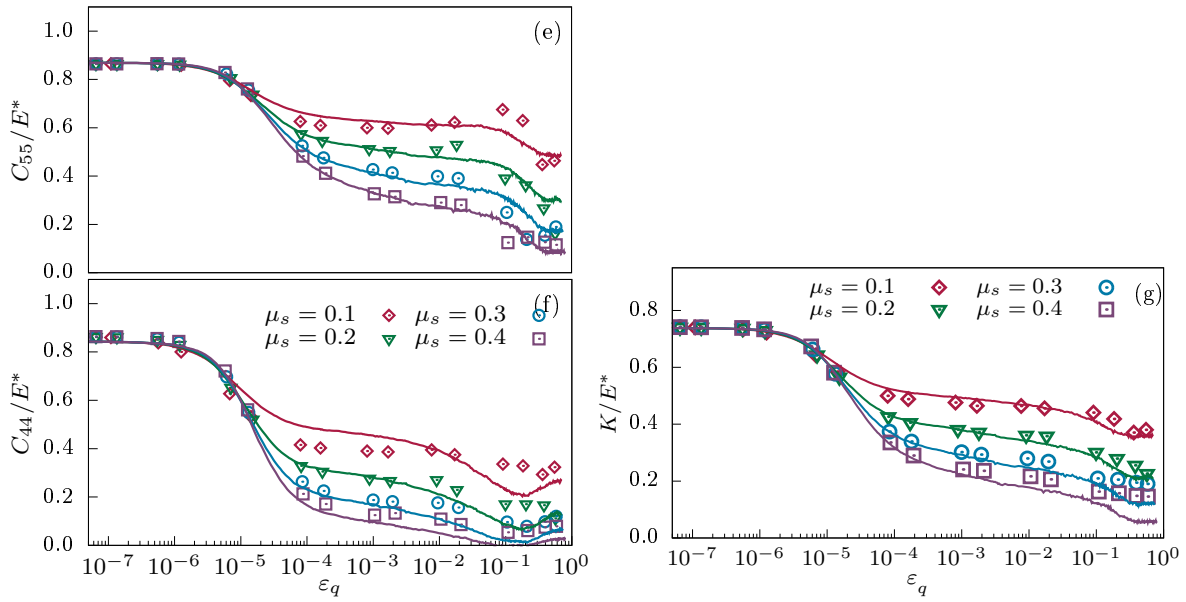

Fig. 2-15. Normalized elastic moduli: shear (e) and (f), bulk (g) as a function of shear strain ε_q for packings of icosahedral particles with different values of friction coefficient μ_s. The solid lines are predictions by our proposed expression; see main text.

$$\begin{cases} \langle(\boldsymbol{\varepsilon}\vec{n}\cdot\vec{n})^2\rangle = \left(\frac{1}{5}+\frac{8}{35}a_c\right)\varepsilon_{11}^2 + \left(\frac{1}{5}-\frac{4}{35}a_c\right)\varepsilon_{22}^2 + \left(\frac{1}{5}-\frac{4}{35}a_c\right)\varepsilon_{33}^2 + \left(\frac{2}{15}+\frac{4}{105}a_c\right)\varepsilon_{11}\varepsilon_{22} \\ \qquad\qquad + \left(\frac{2}{15}+\frac{4}{105}a_c\right)\varepsilon_{11}\varepsilon_{33} + \left(\frac{2}{15}-\frac{8}{105}a_c\right)\varepsilon_{22}\varepsilon_{33} \\ \langle(\boldsymbol{\varepsilon}\vec{n}\cdot\vec{t})^2\rangle = \left(\frac{2}{15}+\frac{4}{105}a_c\right)\left(\varepsilon_{11}^2+\frac{3}{8}\varepsilon_{22}^2+\frac{3}{8}\varepsilon_{33}^2-\varepsilon_{11}\varepsilon_{22}-\varepsilon_{11}\varepsilon_{33}+\frac{1}{4}\varepsilon_{22}\varepsilon_{33}\right) \\ \langle(\boldsymbol{\varepsilon}\vec{n}\cdot\vec{s})^2\rangle = \left(\frac{1}{12}-\frac{1}{30}a_c\right)\left(\varepsilon_{22}^2+\varepsilon_{33}^2-2\varepsilon_{22}\varepsilon_{33}\right). \end{cases} \tag{2.36}$$

$$\begin{cases} C_{11} = \dfrac{\partial^2 W_e}{\partial\varepsilon_{11}^2} = n_c\langle l^2\rangle\left[\frac{1}{5}k_n+\frac{2}{15}k_t+a_c\left(\frac{8}{35}k_n+\frac{4}{105}k_t\right)\right] \\ C_{22} = \dfrac{\partial^2 W_e}{\partial\varepsilon_{22}^2} = n_c\langle l^2\rangle\left[\frac{1}{5}k_n+\frac{2}{15}k_t-a_c\left(\frac{4}{35}k_n+\frac{2}{105}k_t\right)\right] \\ C_{12} = \dfrac{\partial^2 W_e}{\partial\varepsilon_{11}\partial\varepsilon_{22}} = n_c\langle l^2\rangle\left[\frac{1}{15}(k_n-k_t)+\frac{2}{105}a_c(k_n-k_t)\right] \\ C_{23} = \dfrac{\partial^2 W_e}{\partial\varepsilon_{22}\partial\varepsilon_{33}} = n_c\langle l^2\rangle\left[\frac{1}{15}(k_n-k_t)-\frac{4}{105}a_c(k_n-k_t)\right]. \end{cases} \tag{2.37}$$

In order to measure C_{55}, we consider in coordinate $(\varepsilon_v, \varepsilon_q)$ on plane Oxz. Assuming that $\varepsilon_{33} = 0$, we have

$$\begin{cases} \varepsilon_v = \varepsilon_{11}+\varepsilon_{22} \\ \varepsilon_q = \varepsilon_{11}-\varepsilon_{22} \end{cases} \Rightarrow \begin{cases} \varepsilon_{11} = \dfrac{\varepsilon_v+\varepsilon_q}{2} \\ \varepsilon_{22} = \dfrac{\varepsilon_v-\varepsilon_q}{2} \end{cases}$$

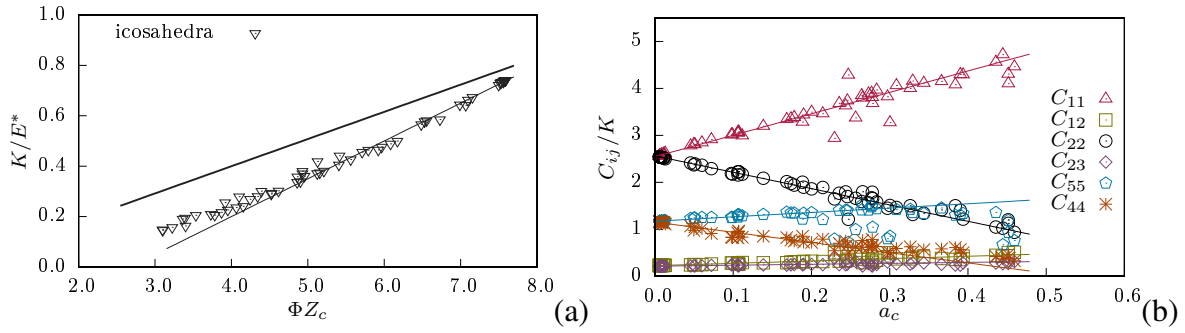

Fig. 2-16. (a) Normalized bulk modulus K/E^* as a function of ΦZ_c from simulations of icosahedral particle packings. The thin line is linear fit to the data. The thick lines represent predictions of EMT for icosahedra. (b) Normalized moduli C_{ij}/K as a function of fabric anisotropy a_c for the icosahedral particle packings from simulations with different values of the friction coefficient. The straight lines are the best linear fits to the data points.

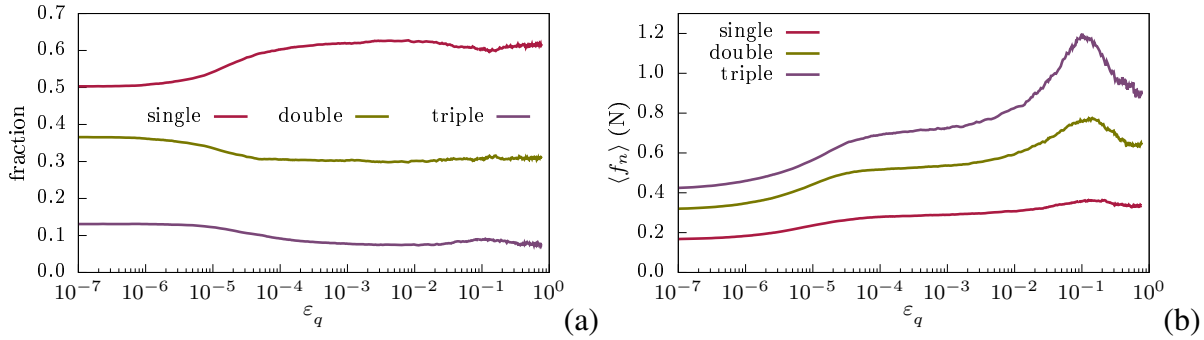

Fig. 2-17. The fraction (a) and the average normal force $\langle f_n \rangle$ (b) of single, double and triple contacts as a function of shear strain ε_q in the packing of icosahedral particles with friction coefficient $\mu_s = 0.1$.

$$\begin{cases} \langle(\boldsymbol{\varepsilon}\vec{n}\cdot\vec{n})^2\rangle = \left(\frac{1}{5}+\frac{8}{35}a_c\right)\left(\frac{\varepsilon_v+\varepsilon_q}{2}\right)^2 + \left(\frac{1}{5}-\frac{4}{35}a_c\right)\left(\frac{\varepsilon_v-\varepsilon_q}{2}\right)^2 + \left(\frac{2}{15}+\frac{4}{105}a_c\right)\left(\frac{\varepsilon_v^2-\varepsilon_q^2}{4}\right) \\ \langle(\boldsymbol{\varepsilon}\vec{n}\cdot\vec{t})^2\rangle = \left(\frac{2}{15}+\frac{4}{105}a_c\right)\left[\left(\frac{\varepsilon_v+\varepsilon_q}{2}\right)^2 + \frac{3}{8}\left(\frac{\varepsilon_v-\varepsilon_q}{2}\right)^2 - \left(\frac{\varepsilon_v^2-\varepsilon_q^2}{4}\right)\right] \\ \langle(\boldsymbol{\varepsilon}\vec{n}\cdot\vec{s})^2\rangle = \left(\frac{1}{12}-\frac{1}{30}a_c\right)\left(\frac{\varepsilon_v-\varepsilon_q}{2}\right)^2. \end{cases} \tag{2.38}$$

Shear modulus on plane Oxz:

$$C_{55} = \frac{\partial^2 W_e}{\partial \varepsilon_q^2} = \frac{n_c\langle l^2\rangle}{2}\left[\frac{2}{15}k_n + \frac{3}{15}k_t + a_c\left(\frac{4}{105}k_n + \frac{3}{105}k_t\right)\right]. \tag{2.39}$$

On plane Oxy, assuming $\varepsilon_{11} = 0$, we have

$$\begin{cases} \varepsilon_v = \varepsilon_{22} + \varepsilon_{33} \\ \varepsilon_q = \varepsilon_{22} - \varepsilon_{33} \end{cases} \Rightarrow \begin{cases} \varepsilon_{22} = \dfrac{\varepsilon_v+\varepsilon_q}{2} \\ \varepsilon_{33} = \dfrac{\varepsilon_v-\varepsilon_q}{2} \end{cases}$$

$$\begin{cases} \langle(\boldsymbol{\varepsilon}\vec{n}\cdot\vec{n})^2\rangle = \left(\frac{8}{15}-\frac{32}{105}a_c\right)\left[\frac{3}{8}\left(\frac{\varepsilon_v+\varepsilon_q}{2}\right)^2+\frac{3}{8}\left(\frac{\varepsilon_v-\varepsilon_q}{2}\right)^2+\frac{1}{4}\left(\frac{\varepsilon_v^2-\varepsilon_q^2}{4}\right)\right] \\ \langle(\boldsymbol{\varepsilon}\vec{n}\cdot\vec{t})^2\rangle = \left(\frac{2}{15}+\frac{4}{105}a_c\right)\left[\frac{3}{8}\left(\frac{\varepsilon_v+\varepsilon_q}{2}\right)^2+\frac{3}{8}\left(\frac{\varepsilon_v-\varepsilon_q}{2}\right)^2+\frac{1}{4}\left(\frac{\varepsilon_v^2-\varepsilon_q^2}{4}\right)\right] \\ \langle(\boldsymbol{\varepsilon}\vec{n}\cdot\vec{s})^2\rangle = \left(\frac{1}{12}-\frac{1}{30}a_c\right)\varepsilon_q^2 \end{cases} \tag{2.40}$$

Shear modulus on isotropic plane Oxy:

$$C_{44} = \frac{\partial^2 W_e}{\partial \varepsilon_q^2} = \frac{n_c\langle l^2\rangle}{2}\left[\frac{2}{15}k_n+\frac{3}{15}k_t-a_c\left(\frac{8}{105}k_n+\frac{6}{105}k_t\right)\right]. \tag{2.41}$$

To evaluate bulk modulus K, we need to consider volumetric strain of whole cubic box, we have

$$\begin{cases} \varepsilon_v = \varepsilon_{11}+\varepsilon_{22}+\varepsilon_{33} \\ \varepsilon_q = \varepsilon_{11}-\varepsilon_{33} \\ \varepsilon_q^{'} = \varepsilon_{22}-\varepsilon_{33} \end{cases} \Rightarrow \begin{cases} \varepsilon_{11} = \dfrac{\varepsilon_v+2\varepsilon_q-\varepsilon_q^{'}}{3} \\ \varepsilon_{22} = \dfrac{\varepsilon_v-\varepsilon_q+2\varepsilon_q^{'}}{3} \\ \varepsilon_{33} = \dfrac{\varepsilon_v-\varepsilon_q-\varepsilon_q^{'}}{3} \end{cases}$$

Bulk modulus K:

$$K = \frac{\partial^2 W_e}{\partial \varepsilon_v^2} = \frac{n_c\langle l^2\rangle k_n}{9}. \tag{2.42}$$

Note that the bulk modulus K, expressing the response of mean stress $\delta p = (\delta\sigma_1+\delta\sigma_2+\delta\sigma_3)/3$ to a volumetric strain $\delta\varepsilon_v = (\delta\varepsilon_1+\delta\varepsilon_2+\delta\varepsilon_3)/3$ as $\delta p = K\delta\varepsilon_v$. From Eq. (2.3) with the assumption that $\delta\varepsilon_1 = \delta\varepsilon_2 = \delta\varepsilon_3 = \delta\varepsilon_v/3$, it is easy to get

$$K = \frac{C_{11}+4C_{12}+2C_{22}+2C_{23}}{9}. \tag{2.43}$$

The relation between K and C_{ij} as shown in Eq. (2.43) is also confirmed by the expression of C_{ij} in EMT shown in Eq. (2.37)

Chapter 3

Rheology and coarse-graining of polyhedral particle flows in rotating drums

Contents

We use particle dynamics simulations to investigate the rheology of granular flows composed of regular octahedral particles in a rotating drum. We focus on the cascading regime and perform an extensive parametric study by varying drum size, particle size, rotation speed, and filling degree. Our simulations indicate that the passive layer undergoes quasistatic shearing and, in contrast to spherical particle flows, no sliding occurs at the drum wall due to the angular particle shape. A scaling parameter combining the Froude number, the ratio of drum to particle size, and the filling degree captures the kinematic and dynamic characteristics of the granular flow such as free surface shape, shear velocity, flow thickness, and inertial number. This scaling suggests simple linear correlations between free surface curvature, flow thickness, and inertial number. We also show that this scaling is fully consistent with the expected effects of increasing particle size.

3.1 Introduction

The flow of granular materials inside a rotating drum is extensively applied in industrial processes such as mixing, grinding, granulation of granular materials. Although it has been studied by means of numerical models and experiments in recent years, there still remain open issues due to the complex and heterogeneous flow combining the upward rigid-body motion of the particles at the drum wall, downward bulk flow, and free surface dynamics [51,65]. Drum flows are commonly classified into six different regimes: slipping, slumping, rolling, cascading, cataracting, and centrifuging [53,54,57]. These regimes are obtained by increasing the *Froude number*, $\mathrm{Fr} = \omega^2 R/g$, where ω is rotation speed, R is drum radius and g is gravity acceleration. The cascading regime provides a suitable particle flow configuration for industrial applications involving convection, mixing, segregation, and milling of particles [57,65,86,94]. This is mainly due to the fact that this regime involves a continuous inertial flow of particles cascading downward due to gravity along a curved free surface and within a thick flowing layer [52,65].

A major issue regarding drum flows is that they depend not only on the Froude number but also on other system parameters such as particle size and filling degree whose effect on the flow has not been fully understood [52, 54, 97]. Several scaling laws that include the system parameters have been proposed. For instance, Félix *et al.* [240] introduced a scaling law linking mean velocity $\langle v \rangle$ and thickness h_a of the active (flowing) layer through a power law $\langle v \rangle \sim h_a^m$, where the exponent m decreases with increasing size ratio D/d, with D and d being the drum and particle diameters, respectively. Pignatel *et al.* [102] found a constant value $m \simeq 1.27$ whereas Govender *et al.* [241] found $m \simeq 0.997$ in their work. By using theoretical and numerical models, Taberlet *et al.* [99] showed that the end walls are responsible for the curvature of the free surface, which is controlled by a dimensionless number including drum width, drum diameter, and rotation speed. In the case of wet granular flows of glass beads in rolling regime, Jarray *et al.* [242] found experimentally that dynamic angle of repose can be scaled by a parameter combining the Froude number and Weber number (ratio of inertial forces to capillary forces). The flow variables in the cascading regime were studied by Orozco *et al.* [65] who proposed a

scaling by a single parameter that combines the Froude number, drum size D, particle size d, and filling degree J.

The above examples show that, although most previous studies have focused on the rolling regime and the flow of spherical particles, there are significant differences between the proposed scaling laws. Furthermore, the cascading regime has received much less attention and has been only recently studied on a systematic basis [51,65]. Another important issue concerns the influence of particle shape on the flow regimes and more specifically on the behavior of the cascading regime [80, 206, 243–245]. With increasing computational power and optimization of contact detection algorithms, aspherical shapes are becoming accessible to large-scale particle dynamics simulations based on the Discrete Element Method (DEM). Examples of particles shapes that have been used in rotating drums for different applications are ellipsoids [68, 246–248], superquadrics [87, 249, 250], arbitrary-shaped clumps of spheres [82, 251, 252], and polyhedra [253–256].

Among these shapes, polyhedral particles are of primary importance since they are common in many applications and in nature, and also because arbitrary particles shapes can in principle be represented as polyhedra by meshing their surface into polygons. A key aspect of polyhedral particles is that they can interact through face-face, face-edge, vertex-face, and edge-edge contacts, which must be taken into account both in the contact detection procedure and for the calculation of forces. The distinction of contact types in drum flows has been addressed by a few recent DEM developments [86,87,256,257].

In this paper, we use DEM simulations to analyze granular flows of octahedral particles in rotating drums in the cascading regime. The simulations are based on an original approach dealing properly with different contact types. We perform extensive simulations for a wide range of values of rotation speed, drum diameter, particle diameter, and filling degree. By a detailed analysis of flow variables such as the average and maximum slopes of free surface, flow thickness, shear rate, and inertia number in the flowing layer we find a dimensionless scaling parameter that accounts for the effect of all system parameters. In particular, we focus on the effect of particle-coarsening and we show that it is consistent with our scaling of flow variables. As we shall see, our scaling works also for spherical particles allowing thereby to highlight the effect of polyhedral particle shape through differences between model parameters.

In the following, we first introduce in Section 3.2 the numerical model and the procedures used to simulate drum flows. In Section 3.3, we describe the particle velocity fields and free surface profiles of drum flows. The scaling law of cascading flows will be proposed in Section 3.4. We also introduce a particle coarsening model in Section 3.5. Finally, we discuss the most salient results of this work in Section 3.6.

3.2 Numerical model and procedures

3.2.1 Simulation of polyhedral particles

The simulations were carried out by means of DEM in which polyhedral particles are treated as rigid bodies while the contacts between them are assumed to be compliant and obeying a viscoelastic behavior [22, 224, 258]. Polyhedral particles are transformed by means of Minkowski sum with a sphere of a small radius R_m [259]. This operation smoothens the polyhedra by replacing all edges by thin cylinders and all vertices by spheres. As a consequence, each polyhedron consists of three sub-elements, namely vertices which are small spheres of radius R_m, edges which are cylinders of radius R_m connecting two vertices, and faces which are planes of thickness $2R_m$ connecting at least three vertices.

The contacts between two polyhedra are represented by the contacts of its sub-elements, leading to six contact types: vertex-face, edge-edge, vertex-edge, vertex-vertex, edge-face, face-face. The unilateral constraint associated with these contact types do not have the same nature. The vertex-face, vertex-edge, vertex-vertex, and edge-edge interactions involve a single contact point, which can be treated in the same way as the contacts between spherical particles. Such simple contacts represent a single unilateral constraint as shown in Figs 3-1a and 3-1b. In contrast, a face-face contact is a plane that needs at least three points for its definition. Therefore, a face-face contact is equivalent to three simple contacts or unilateral constraints [22, 223]. This means that at least three contact points are necessary to represent the contact. Note that, the number of contact points can be larger depending on the number of edges as illustrated in Fig. 3-1d, but the number of independent constraints is always 3 since the particles are rigid. In a similar vein, edge-face interactions need two contact points as shown in Fig 3-1c. For this reason, edge-face and face-face contacts can be described as 'double' and 'triple' contacts, respectively.

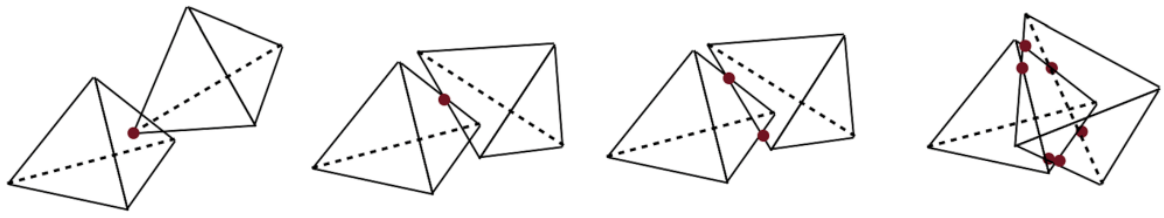

(a) **(b)** **(c)** **(d)**

Fig. 3-1. Different types of contacts between two polyhedra: (a),(b) simple contact, (c) double contact, and (d) triple contact.

At each contact point, either a linear or a nonlinear force law is implemented. For smooth particle surfaces with well-defined curvatures at the contact point, the Hertz law can be used. However, in this paper due to the faceted shape of particles, we used linear elastic law which is equivalent to a linear unilateral spring acting the the contact point. To account for contact inelasticity, a viscous damping term is added to the normal elastic repulsion force. Let $\vec{n}$ and $\vec{t}$

be the normal and tangential unit vectors at a contact point c between particles i and j. The force $\vec{f} = f_n\vec{n} + f_t\vec{t}$ acting by particle j on particle i is expressed as a function of the normal overlap δ_n and cumulative tangential displacement $\vec{\delta}_t$. The normal force law is defined as follows [204, 224]:

$$f_n = \begin{cases} 0, & \tilde{f}_n \leq 0, \\ \tilde{f}_n, & \tilde{f}_n > 0, \end{cases} \tag{3.1}$$

where $\tilde{f}_n = k_n\delta_n - 2a\sqrt{k_n m}\dot{\delta}_n$, k_n is normal stiffness, δ_n is overlap (with sign convention that $\delta_n > 0$ when two particle overlap), $\dot{\delta}_n$ is the relative normal velocity, m is reduced mass of two touching particles, and a is the dimensionless damping parameter which can take a value between 0 and 1. For $a = 0$, the contact is fully elastic whereas for $a = 1$ the contact is fully inelastic. In binary collisions, the normal restitution coefficient is a decreasing function of a [181, 260]. It is noteworthy that energy dissipation in dense granular flows is a collective multicontact process that involves elastic wave propagation across the system. Typically low-frequency vibration modes are damped slowly in DEM calculations. For this reason, in DEM simulations of dense granular flows it is convenient to enhance contact dissipation by setting the restitution coefficient to a value close to zero (i.e. a close to 1). In our simulations, we set the coefficient of restitution to 0.001.

The tangential force f_t is governed by the Coulomb friction law:

$$f_t = min\{|k_t\vec{\delta}_t|,\ \mu_s f_n\}, \tag{3.2}$$

where k_t is tangential stiffness, δ_t is cumulative tangential displacement, and μ_s is the interparticle friction coefficient. The orientation of the tangential force $\vec{t}$ is opposite to either the relative elastic displacement $\vec{\delta}_t$ below the Coulomb threshold or the relative velocity $\vec{v}_t$ at the contact point when the Coulomb threshold is reached.

3.2.2 Sample setup and boundary conditions

We consider horizontal drums of diameter $D = 2R$ and width W filled with monodisperse octahedral particles of diameter d, and subjected to rotation speed ω as illustrated in Fig. 3-2a. We used a monodisperse system to avoid introducing unnecessary parameters. Note also that long-range ordering in monodisperse systems is a pathology of 2D systems. A packing of monodisperse particles in 3D does not develop long-range ordering. Octahedral particle shape was chosen due to its high angularity, distinguishing it from spherical shape [22]. Periodic boundary conditions are imposed along the drum axis y to reduce wall effects. This makes the flow invariant along the y axis. The filling degree is defined by the ratio $J = h_0/D$, where h_0 is the thickness of granular material at the midpoint of the free surface at rest. The friction coefficients between particles and with drum wall are set to $\mu = 0.4$, which is a common value used for smooth drum wall [65, 261].

The simulations were carried out for a broad range of values of ω, D, d, and J as shown in Table 3-1. As we shall see, the selected ranges of these parameters the flow is in the cascading

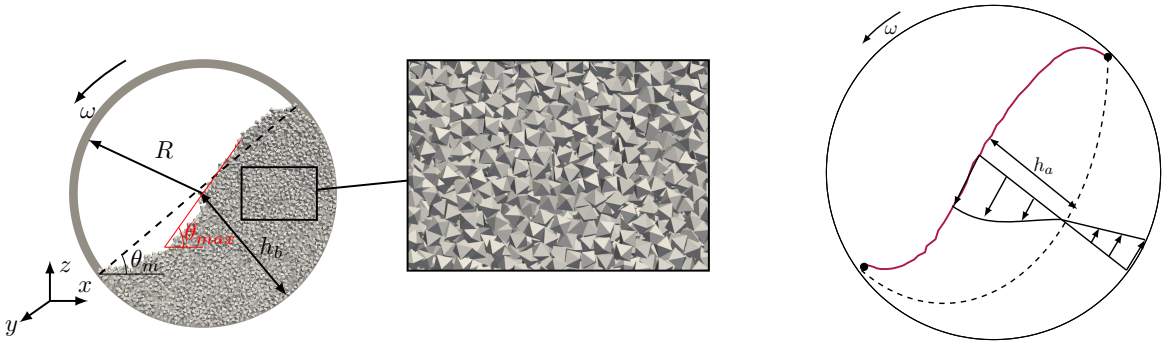

(a) **(b)**

Fig. 3-2. Geometrical parameters of granular flow in rotating drum in the steady state (a), and particle velocity profile along the bed depth direction in the center of the cylinder (b).

regime. In order to isolate the effect of drum size, particle size and filling degree, we performed four sets of simulations. In the first set (set A), drum diameter D was changed for $d = 0.682$ mm and $J = 0.40$. In the second set (set B), d was varied for $D = 40$ mm and $J = 0.40$. In the third set (set C), J was changed for $D = 40$ mm and $d = 0.682$ mm. Furthermore, to verify the accuracy of the scaling law that will be discussed in this paper, we performed more simulations by changing all parameters simultaneously (set D).

The simulations were run for at least 10 drum rotations to allow the system to reach a steady flow state. The data analyzed in this paper, such as the free surface profile, flow thickness, relative particle velocities, flow rate, and inertia number are averaged over time in the steady state.

Parameter	Symbol	Value	Unit
Number of particles	N_p	$[2522; 18392]$	-
Particle density	ρ_s	1.2×10^4	kg/m^3
Normal stiffness	k_n	10^8	N/m
Tangential stiffness	k_t	8×10^7	N/m
Restitution coefficient	e_n^2	0.001	-
Friction coefficient	μ	0.4	-
Gravity acceleration	g	9.81	m/s^2
Mean particle diameter	d	$[0.682; 1.092]$	mm
Rotation speed	ω	$[10; 20]$	rad/s
Drum diameter	D	$[30; 55]$	mm
Drum width	W	6	mm
Froude number	Fr	$[0.12; 0.70]$	-
Filling degree	J	$[0.29; 0.40]$	-

Table 3-1. Simulation parameters of rotating drums.

3.3 Particle velocity fields and free surface profiles

A snapshot of particle velocity vectors in a rotating drum of size ratio $D/d = 81$, and the free surface for different size ratios, but with the same filling degree J and rotation speed ω, are displayed in Fig. 3-3. The largest velocities are located at the center of free surface where particles are cascading down, and they increase in magnitude with drum size despite the constant value of rotation speed ω. We see that for all values of size ratio the flow is in the cascading regime with a free surface curvature that increases with size ratio.

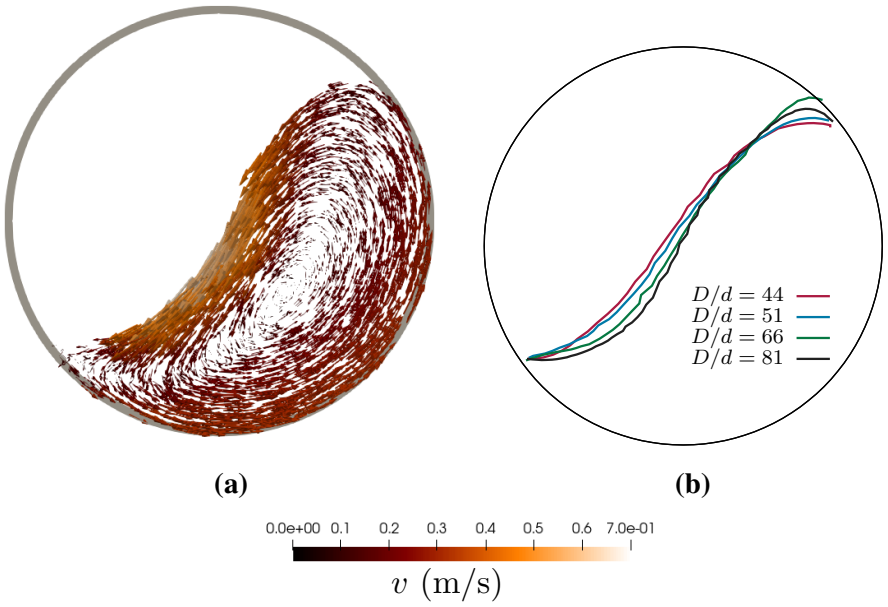

Fig. 3-3. Velocity vector fields in drum of the size ratios $D/d = 81$ (a), the free surface in drums of different size ratios (b). The filling degree ($J = 0.4$), mean particle diameter ($d = 0.682$ mm), and rotation speed ($\omega = 12$ rad/s) are the same in all cases. The arrow length and color are proportional to particle velocity magnitude.

Two examples of averaged particle velocity fields in drums of different size ratios are displayed in Fig. 3-4. The velocity vectors are projected on the secant slope. Positive values correspond to particles flowing downward under the effect of gravity whereas negative values correspond to upward motion of the particles. From the velocity field, we clearly distinguish the active layer (upper) from the passive layer (lower). The passive layer behaves as a solid body undergoing slow deformation against the drum wall. When the particles reach the free surface, they join the active layer at different positions above the borderline between the two layers, flow downward, and eventually rejoin the passive layer. We also see the boundary at the interface between the active and passive layers. The flow thickness h_b is evaluated from the free surface along the line passing by the midpoint of the secant slope and perpendicular to it (see Fig. 3-2a). The secant line is defined by joining the uppermost point of the free surface to its lowermost point. The active layer thickness h_a is part of h_b, and is defined as the distance from the free surface to the interface between the active and passive layers (see Fig. 3-2b). The active

layer thickness h_a is an important parameter for phenomena such as mixing, segregation, and heat transfer in rotating drums [54, 57] and it varies with system parameters in the cascading regime.

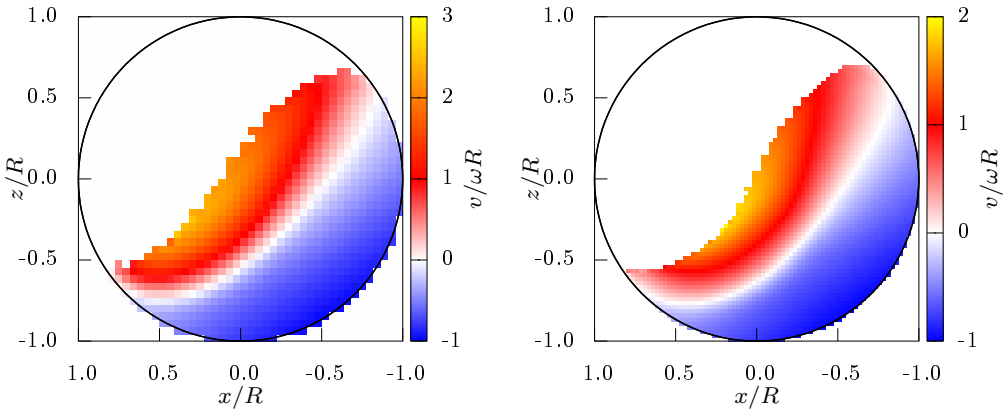

Fig. 3-4. Time-averaged particle velocity field in drums of two different size ratios D/d of 44 (a) and 81 (b) for filling degree $J = 0.4$, mean particle diameter $d = 0.682$ mm, and rotation speed $\omega = 12$ rad/s in all cases. The particle velocity is projected on the secant slope defined by its angle θ_m.

Figure 3-5 displays the velocity profile along the bed depth direction (with depth h measured from the free surface) for our three data sets (set A, set B, and set C). The particle velocity is projected on the secant slope defined by the angle θ_m. The profile in the passive layer is almost linear. From $v \simeq -0.5\omega R$ to $v \simeq 0$, we observe an intermediate region over which the transition to the active layer occurs. For $v > 0$, the particles are in the active layer and the velocity profile is again nearly linear [87, 94, 262]. The transition zone is the locus of convective rolls that accommodate strain fields between the passive and active layers as suggested by the particle velocity vectors shown in Fig 3-3. The thickness of this zone is nearly 5 particle diameters in the center of the drum. In Fig. 3-5(a) we observe that for $D/d = 74$ and $D/d = 81$ the velocity profile tends to turn upward near the free surface, deviating from the linear profile. This is due to the high value of Froude number and small size of the particles, which, as we shall see, lead to larger curvature of the free surface and increasing fluidization in the center of the flow. This deviation is a signature of transition to the cataracting regime in which the particles in the center of flow follow a ballistic motion.

It is noteworthy that the particle velocity of the layer in contact with the drum wall is close to ωR, implying that the particles do not slide along the drum wall. Slippage of particles against drum wall has been observed in the case of spherical particles. We also see that the ratio h_a/h_b, where h_b is the thickness of the flow in the center of the drum during flow, and the free surface curvature increase with increasing drum size [65]. On the other hand, the free surface velocity and the ratio h_a/h_b decrease for larger particle sizes.

To characterize the free surface shape, we define two slope angles: the secant slope θ_m and

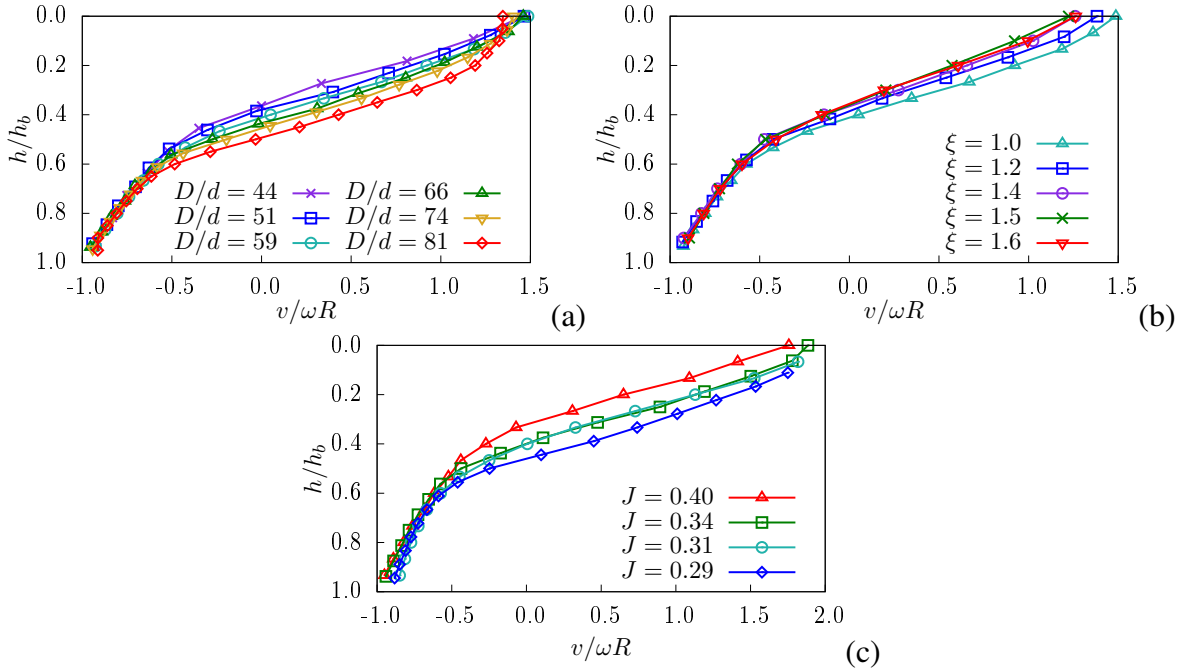

Fig. 3-5. Time-averaged velocity profile in the center of the drum as a function of depth measured from the free surface and normalized by the total bed depth h_b for three data sets: (a) set A (D is varied) with $\omega = 15$ rad/s, $d = 0.682$ mm, (b) set B (d is varied) with $\omega = 15$ rad/s, $\xi = d/d_0$, where $d_0 = 0.682$ mm, and (c) set C (J is varied) with $\omega = 10$ rad/s, $d = 0.682$ mm. The particle velocity is projected on secant slope and normalized by ωR.

the tangent slope θ_{max} of the steepest descent along the free surface, as shown in Fig. 3-2a. The secant slope represents the average slope of the free surface. The angle θ_{max} reflects the kinematics of the free surface flow and the flow rate due to the amount of feeding particles. The rotation speed ω or Froude number Fr are insufficient to capture the evolution of θ_m and θ_{max} [65, 97]. The slope ratio θ_{max}/θ_m represents a measure of the curvature of the slope. Its significance appears through its scaling with system parameters, as we shall see below.

The evolutions of slope ratio θ_{max}/θ_m and thickness ratio h_a/h_b as a function of size ratio D/d are shown in Fig. 3-6 for data set A with four values of ω. We see that both ratios increase with drum size and with rotation speed in agreement with previous studies [65]. Note that all data points shown in Fig. 3-6 are in the cascading regime. The maximum values reached are $\theta_{max}/\theta_m = 1.7$ and $h_a/h_b = 0.5$. Beyond this limit, a crossover is observed from cascading flow to cataracting flow. By definition, in the rolling regime we have $\theta_{max}/\theta_m = 1$. Hence, it is expected that the lowest value of this ratio is 1 and occurs at crossover from rolling regime to cascading regime. However, in Fig. 3-6 we see that the lowest value is ~ 1.3. This point will be discussed in Sec. 3.4.

Let us define v_r as the relative velocity of particles in contact with drum wall:

$$v_r = \omega R - v_w, \tag{3.3}$$

where v_w is the time-averaged velocity of particles in contact with drum wall in the steady state. Figure 3-7 shows v_r as a function of the relative velocity $\dot{\gamma}_p d$, where $\dot{\gamma}_p$ is shear rate in the

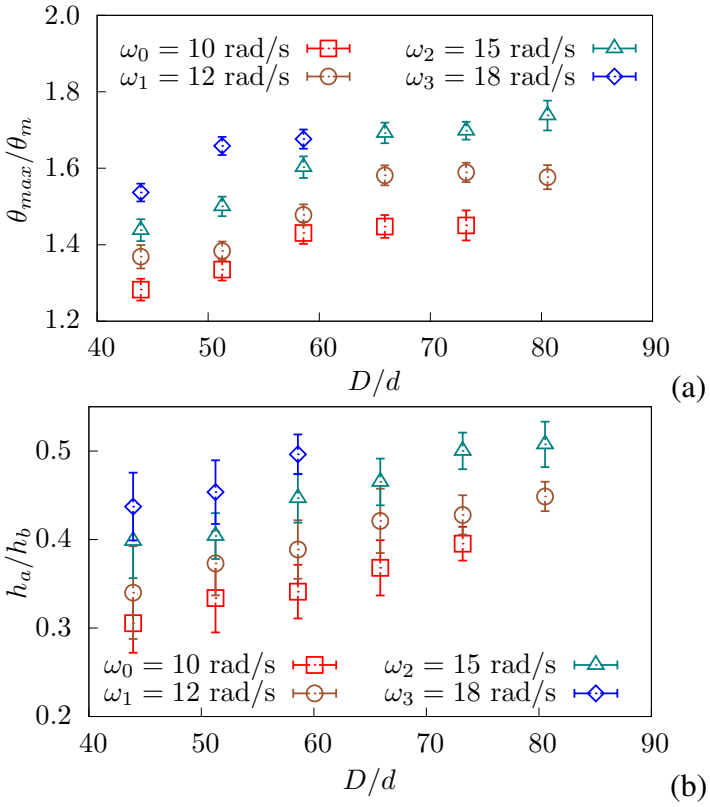

Fig. 3-6. The ratios (a) θ_{max}/θ_m and (b) h_a/h_b as a function of size ratio D/d for different rotating speeds ω for $d = 0.682$ mm and variable drum diameter D. The error bars represent standard deviation in steady flow.

passive layer. We see that v_r increases with and is nearly equal to $\dot{\gamma}_p d$. This means that the value of v_w is mainly controlled by shearing in the passive layer rather than sliding against the drum wall. The absence of sliding at the drum wall can be attributed to the lower mobility of polyhedral particles as compared to spherical particles [65, 99]. In the rolling regime, where wall sliding is often observed, v_r is much higher than $\dot{\gamma}_p d$ [100].

Since there is almost no sliding at the wall, mass conservation implies that the upward flux of particles in the passive layer must be equal to the downward flux in the active layer. Let us consider the flow rate per unit of width $Q = \Phi v h$, where Φ, v, and h are solid fraction, average velocity and thickness of a layer, respectively. In the passive layer, the average flow rate is given by $Q_p \simeq \langle \Phi_p \rangle (h_b - h_a) \langle v_p \rangle$, where $\langle \Phi_p \rangle$ and $\langle v_p \rangle$ are the average solid fraction and velocity, respectively, in the passive layer evaluated for the whole period of flow. In the same way, in the active layer, the average flow rate is $Q_a \simeq \langle \Phi_a \rangle h_a \langle v_a \rangle$, where $\langle \Phi_a \rangle$ and $\langle v_a \rangle$ are the average solid fraction and velocity, respectively, in the active layer. Figure 3-8 shows $Q_a/(d\sqrt{gd})$ as a function of $Q_p/(d\sqrt{gd})$ for all our datasets. We see that all data points collapse well on the $Q_a/(d\sqrt{gd}) = Q_p/(d\sqrt{gd})$ line. This confirms that sliding at the wall is negligible. Deviations are due to the fact that the flow profile is not symmetric around the secant line used to define the average direction of flow and the interface between the passive and active layers fluctuates in time.

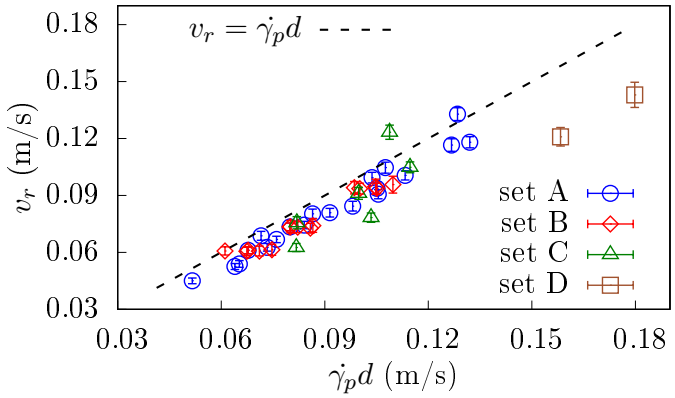

Fig. 3-7. The relative velocity of particles in contact with drum wall as a function of the relative velocity $\dot{\gamma}_p d$ inside the passive layer for a range of different values of drum diameter D and particle diameter d.

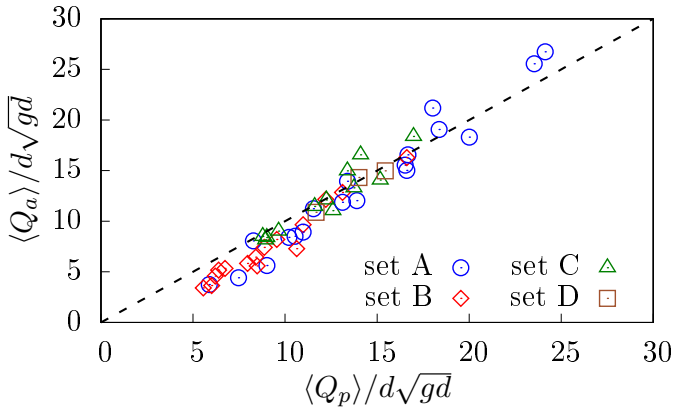

Fig. 3-8. Dimensionless flow rate Q_a in the active layer as a function of dimensionless flow rate Q_p in the passive layer, both normalized by $d\sqrt{gd}$, where g is gravity acceleration. The dashed line represents the line $Q_a/(d\sqrt{gd}) = Q_p/(d\sqrt{gd})$.

3.4 Scaling behavior of cascading flows

Dimensional analysis suggests that the flow behavior depends on three dimensionless numbers: (1) Froude number, which accounts for the dynamics and inertial effects, (2) size ratio D/d accounting for finite-size effects, and (3) filling degree J characterizing the geometry of the flow. As suggested previously for spherical packings [65], we look for a general dimensionless scaling parameter based on a multiplicative combination of the above three parameters:

$$\Gamma = \mathrm{Fr}^{\alpha} \left(\frac{D}{d}\right)^{\beta} J^{\gamma}, \tag{3.4}$$

where the exponents α, β, and γ will be fixed from the simulation data. Since $J = h_0/D$ and $\mathrm{Fr} = \omega^2 R/g$, the scaling parameter Γ is proportional to $\omega^{2\alpha} D^{\alpha+\beta-\gamma} d^{-\beta}$.

To find the values of the three exponents, we can use any dynamical variable of the system as a function of Γ. The value of α can be calculated by plotting the relation between v_r and ω while keeping other system parameters constant. In Fig. 3-9, we plot the normalized velocity

$v_r/\sqrt{gd}$ as a function of ω for different values of drum size D with the same values of d and J. We see that $v_r/\sqrt{gd}$ is proportional to ω so that $\alpha = 1/2$. The value of β can be extracted from the relation of v_r and d while keeping D, J, and ω at constant values. Figure 3-10 shows that v_r is independent of d, meaning that $v_r/\sqrt{gd} \sim d^{-1/2}$, and thus we have $\beta = 1/2$.

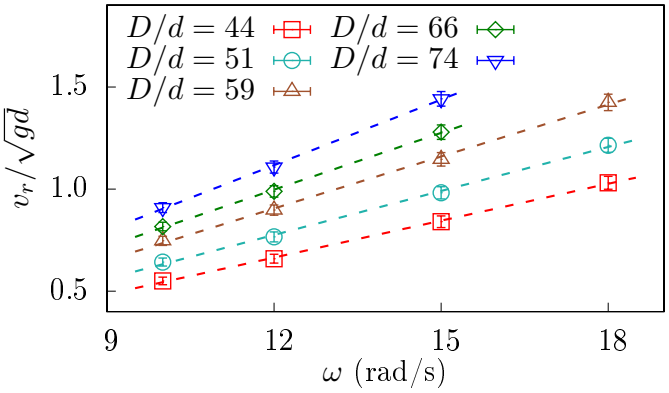

Fig. 3-9. The normalized relative velocity of particles in contact with drum wall as a function of rotation speed ω for different values of drum diameter D and constant mean particle diameter $d = 0.682$ mm and filling rate $J = 0.40$.

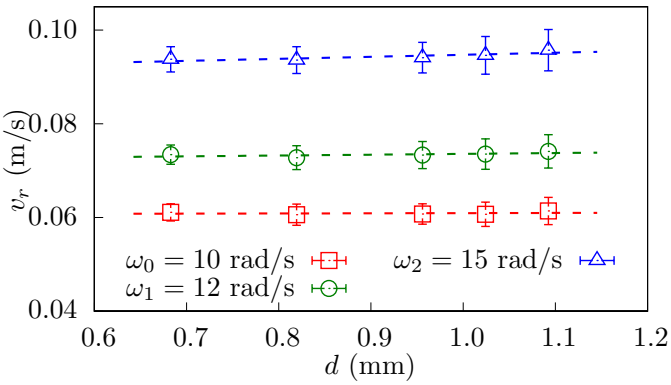

Fig. 3-10. Relative velocity of particles at drum wall as a function of mean particle diameter d for different values of rotation speed ω and constant drum diameter $D = 40$ mm and filling rate $J = 0.40$.

With the values $\alpha = 1/2$ and $\beta = 1/2$, we plotted normalized relative velocity $v_r/\sqrt{gd}$ as a function of Γ for all our simulation data and we found that all the data collapse on a master curve for $\gamma = 1/4$, as shown in Fig. 3-11. Furthermore, this curve is a linear function:

$$\frac{v_r}{\sqrt{gd}} \simeq 0.29\Gamma - 0.05. \tag{3.5}$$

This simple relation suggests that $\Gamma = \mathrm{Fr}^{1/2}(D/d)^{1/2}J^{1/4}$ can be the scaling parameter not only for v_r but for all flow variables of the system. Indeed, as shown in Fig. 3-12, within statistical precision of the simulation data, both the thickness ratio h_a/h_b and slope ratio θ_{max}/θ_m are well fit to linear functions of Γ for all our simulation data:

$$\frac{h_a}{h_b} \simeq 0.07\Gamma + 0.16, \tag{3.6}$$

and

$$\frac{\theta_{max}}{\theta_m} \simeq 0.15\Gamma + 1.00. \tag{3.7}$$

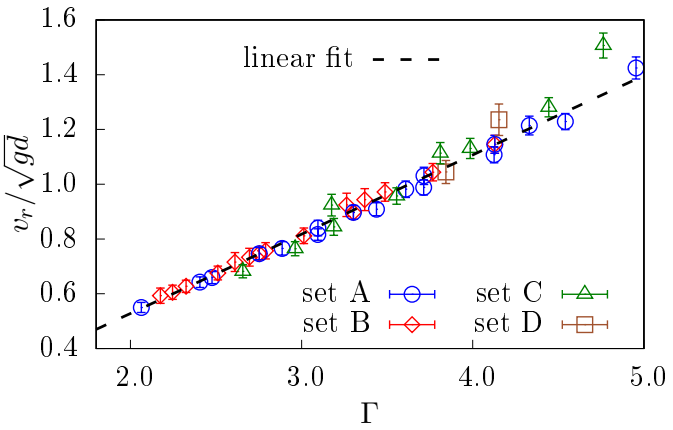

Fig. 3-11. The normalized velocity of particle in contact with drum wall as a function of the scaling parameter Γ defined by Eq. (3.4) with $\alpha = 1/2$, $\beta = 1/2$, $\gamma = 1/4$ for all simulation data.

We also note that in Fig. 3-12 the data points at higher values of Γ seem to deviate from the above general scaling. This observation suggests that these points are at the crossover from cascading regime to cataracting regime. These deviations occur when h_a/h_b approaches 0.5 and θ_{max}/θ_m reaches 1.7, corresponding therefore to the thickest flow layers and highest slopes. It is noteworthy that previous studies of the rolling regime have indicated that the transition from rolling to cascading regime occurs at $h_a/h_b \simeq 0.3$, which corresponds to $\Gamma \simeq 2$ as seen in Fig. 3-12 [57, 263]. Hence, according to our data for octahedral particles, the cascading regime is limited to the range of values of Γ from 2 to 5 independently of the specific values of ω, D, d, and h_0.

The above scaling suggests that all flow variables are connected together through their dependence on Γ. For example, the ratio θ_{max}/θ_m as a kinematic property of drum flow is correlated with the active layer thickness ratio h_a/h_b, which is a dynamic property of the flow. Our scaling predicts the following relation:

$$\frac{h_a}{h_b} \simeq 0.47\frac{\theta_{max}}{\theta_m} - 0.31. \tag{3.8}$$

This relation is in excellent agreement with our data as shown in Fig. 3-13.

Another important flow variable is the average inertia number I in the active layer. It is defined as follows:

$$I = \langle\dot{\gamma}_a\rangle d(\rho_s/p)^{1/2}, \tag{3.9}$$

where $\langle\dot{\gamma}_a\rangle$ is average shear rate in the center of the active layer, ρ_s is particle density, and $p \simeq 0.5\langle\Phi_a\rangle\rho_s g h_a$ is the average pressure in the center of the active layer. Figure 3-14 shows that I is scaled quite well by Γ with the following linear relation:

$$I \simeq 0.45\Gamma + 0.2. \tag{3.10}$$

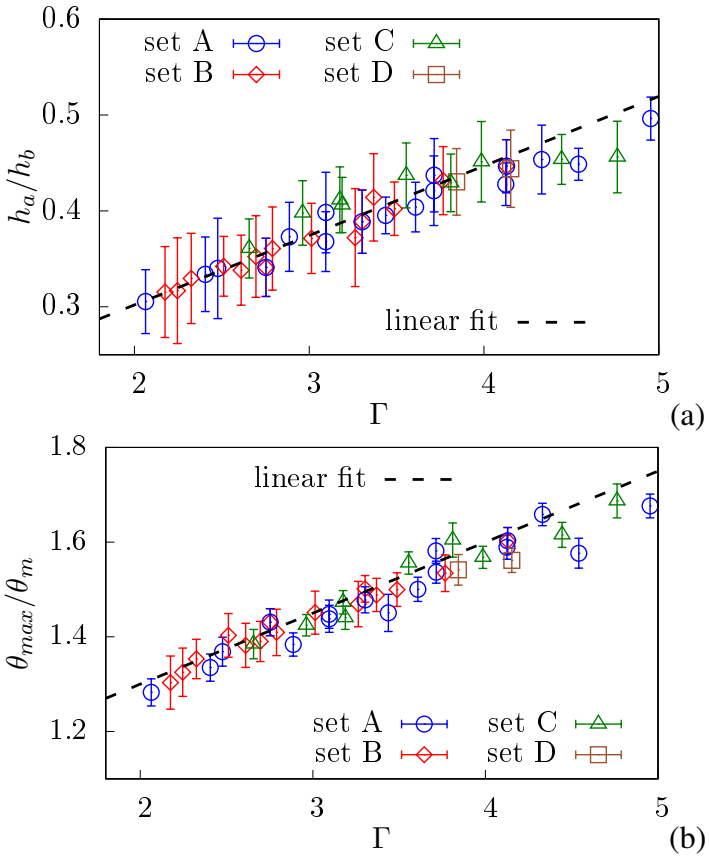

Fig. 3-12. Thickness ratio h_a/h_b (a) and slope ratio θ_{max}/θ_m (b) as a function of the scaling parameter Γ defined by Eq. (3.4) with $\alpha = 1/2$, $\beta = 1/2$, $\gamma = 1/4$ for all simulation data. The dashed lines are fitted lines proposed.

We see that I has generally high values and exceeds 2 at $\Gamma = 4$.

Similar scaling parameters have been proposed by other authors. In particular, Orozco *et al.* [65] found a different scaling parameter for their data obtained from simulations of rotating drums filled with spheres for periodic boundary conditions along drum axis to remove end wall effects. We consider here part of their data as a function of our scaling parameter Γ in order to compare the flows of polyhedra and spheres in the cascading regime. For comparison, we consider the data of Orozco et al. either at a constant value of the filling degree $J = 0.45$ or for changing values of J and ω. Figure 3-15 displays the evolution of slope ratio θ_{max}/θ_m for both octahedral and spherical drum flows versus the scaling parameter Γ in these two cases. We see that the data of spherical particles at $J = 0.45$ coincide well with those of octahedral particles. However, for variable J and ω and a constant size ratio D/d, the slope ratio for spheres increases with Γ but they do not fall on the scaling line of octahedral particles. We have no clear clue as to the origins of this discrepancy, but we believe that a full comparison is necessary to understand the differences for the two particles shapes with respect to all system parameters and the scaling behavior. In particular, the effect of the filling degree seems to be less well accounted for in the simulations of spheres. It is also important to remark that the ranges of values of Γ for which the flow is in the cascading regime is different for octahedral and spherical particle flows.

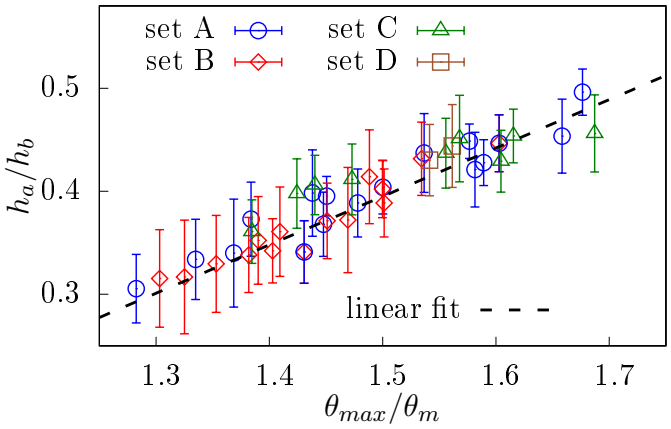

Fig. 3-13. The ratio θ_{max}/θ_m versus the ratio of active layer thickness to total thickness h_a/h_b for all our data points. The dashed line shows the prediction of the scaling relation in Eq. (3.8).

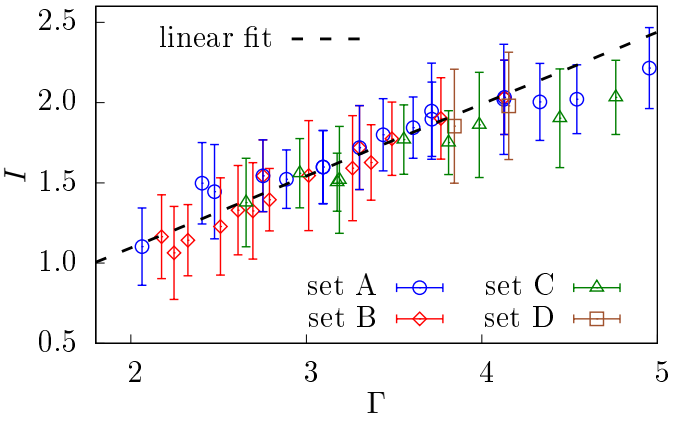

Fig. 3-14. Average inertia number in the center of the active layer I as a function of scaling parameter Γ defined by Eq. (3.4) with $\alpha = 1/2$, $\beta = 1/2$, $\gamma = 1/4$ for all simulation data.

3.5 Particle coarsening approach

The scaling parameter $\Gamma = \mathrm{Fr}^{1/2}(D/d)^{1/2}J^{1/4}$ extracted from our simulation data involves a dependence of cascading flow properties on particle size as $d^{-1/2}$. Here, we would like to show that this size dependence is consistent with the particle coarsening approach. In this approach, particle size is artificially scaled up by a factor ξ, i.e. $d \to d' = \xi d$, while keeping the size of the system, i.e. $D \to D' = \xi^0 D$, so that the total number of particles is reduced by a factor ξ^3 ($N_p \to N_p' = \xi^{-3} N_p$) [264–266]. The scaling of the dimensional quantities of the system depends on the variables that are assumed to be invariant functions of ξ. In general, we require that both macroscopic variables and system-scale quantities (boundary conditions and loading) are invariant by scale change. The physical rationale behind this assumption is that coarse-grained variables must be independent of particle size, which is a microscopic length of the system.

In application to rotating drum, we assume that drum size D, particle density ρ_s, and filling degree J are invariant. This implies that the total mass of the flowing particles is invariant.

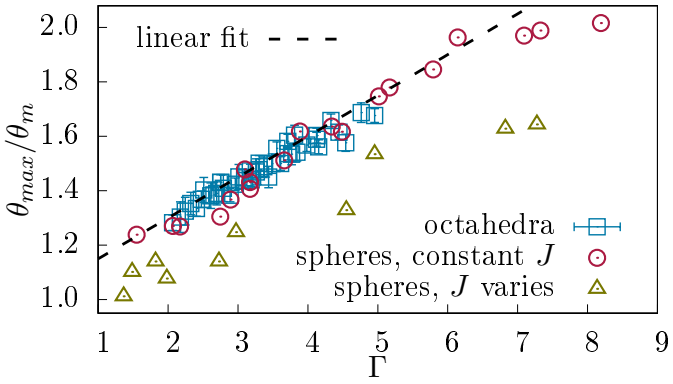

Fig. 3-15. Slope ratio θ_{max}/θ_m as a function of scaling parameter Γ defined by Eq. (3.4) with $\alpha = 1/2$, $\beta = 1/2$, $\gamma = 1/4$ for simulation data of octahedral particles (this work) and spherical particles (data from Orozco *et al.* [65]) in which the filling degree J is kept constant or varies with other parameters kept constant.

In the same way, the rotation speed ω, gravity g, and velocity field $\{\vec{v}^i\}$ are invariants of ξ. Consistently, it is easily seen that the total kinetic energy $E_{tot} = N_p(\langle mv^2/2\rangle + \langle I_o\omega_o^2/2\rangle)$, where I_o is the moment of inertia of the particle around its rotation axis and ω_o is angular speed around the axis, is also invariant since $N_p \to N_p' = \xi^{-3}N_p$, $m \to m' = \xi^3 m$, $v \to v' = \xi^0 v$, $I_o \to I_o' = \xi^5 I_o$, and $\omega_o \to \omega_o' = \xi^{-1}\omega_o$. In our simulations, we have 5 values of d which can be considered as upscaled diameters of the smallest particle size $d_0 = 0.682$ mm by coarsening factors $\xi = d/d_0$, which vary from 1 to 1.6. Figure 3-16 shows the total kinetic energy E_{tot} and relative velocity v_r for three different values of rotation speed as a function of ξ while all other parameters keep their values in set B. We see that both E_{tot} and v_r are invariant as a function of the coarsening factor ξ.

Regarding dynamic variables, since gravity g is invariant, momentum balance implies that particle weights and contact forces scale with ξ^3 while stresses vary as ξ. As a consequence, the inertial number in the active layer $I = \dot{\gamma}_a d\sqrt{\rho_s/p}$ varies as $I' = \xi^{-1/2}I$. This is fully consistent with the linear dependence of I on Γ in Eq. (3.10). Hence, the exponent $\beta \simeq 1/2$ in Eq. (3.4) is a natural consequence of coarse graining. Fig. 3-17 displays $\langle\dot{\gamma}_a\rangle d$ and $\xi^{1/2}(I-0.2)$ as a function of ξ for the data set B for three different values of ω. We see that both variables are independent of ξ. The offset 0.2 in $I-0.2$ has been added here to restrict the analysis to the cascading regime, in which the lowest value of I is 0.2. Note also that the invariance of $\langle\dot{\gamma}_a\rangle d$ simply reflects that of the velocity field. It implies that $\langle\dot{\gamma}_a\rangle$ varies as ξ^{-1} and thus also all times scale as ξ. This property of particle coarsening is well known in granular gases and leads to a decrease of collision rate and dissipation when particles are coarsened [267].

The dependence of inertial number on particle size leads to the variation of the free surface shape. Figure 3-18 shows snapshots of the particles in the drums at steady state with the same rotation speed ω, but different coarsening factors ξ. We see that the free surface becomes less curved as ξ increases. This is in agreement with the scaling law of Eq. (3.7). The proposed scaling law also implies that changing particle size can lead to a change of flow regime. Hence,

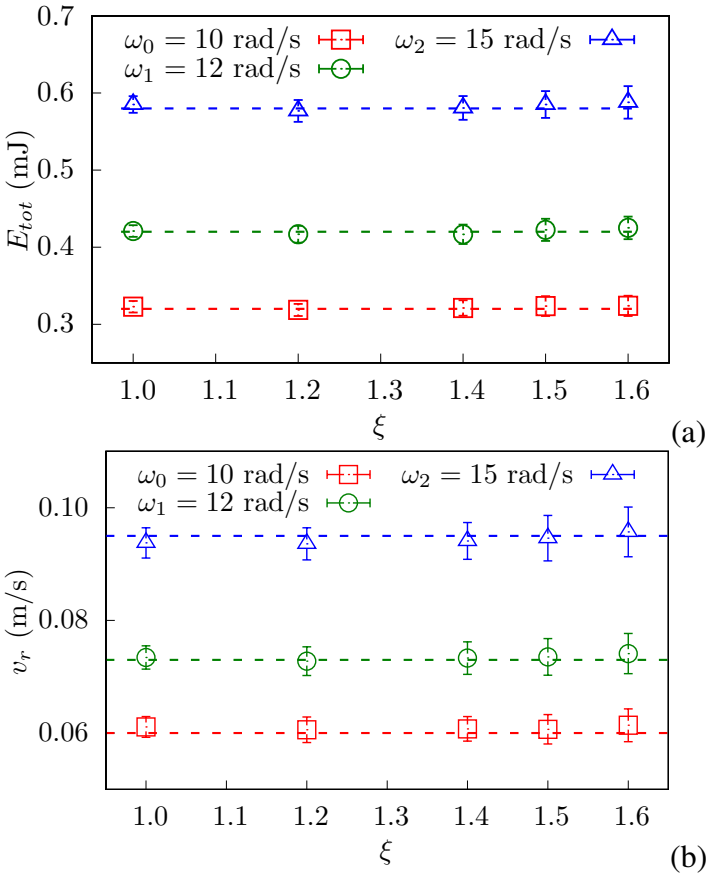

Fig. 3-16. Total kinetic energy of particles E_{tot} and relative velocity of particles near drum wall v_r as a function of coarsening factor ξ. The error bars represent the standard deviation.

the range of values of parameters for which the system is in the cascading regime varies with particle size. This issue and particle size dependence of thickness ratio h_a/h_b and slope ratio θ_{max}/θ_m can be mitigated by applying a scale factor $\xi^{1/2}$ to rotation speed ω which leads to the multiplication of shear rates by a factor $\xi^{1/2}$, making them independent of coarsening factor. This solution can be applied to the simulations of industrial-scale drums with a reduced number of coarser grains for the sake of computational efficiency.

It is also worth noting that the assumption of the invariance of velocity field may seem to contradict the evolution of flow geometry as observed in Fig. 3-4. Indeed, the particle velocities can not be strictly compared between the two configurations. The issue is that the surface shape is a free parameter in drum flow. We showed that the relative velocity v_r near drum wall and the total kinetic energy are indeed invariants of particle coarsening (see Fig. 3-16). This suggest that we may adopt this weaker form of invariance when the geometrical configuration varies with particle coarsening. In other words, the particle coarsening analysis can be applied to the mean flow variables rather than full field variables.

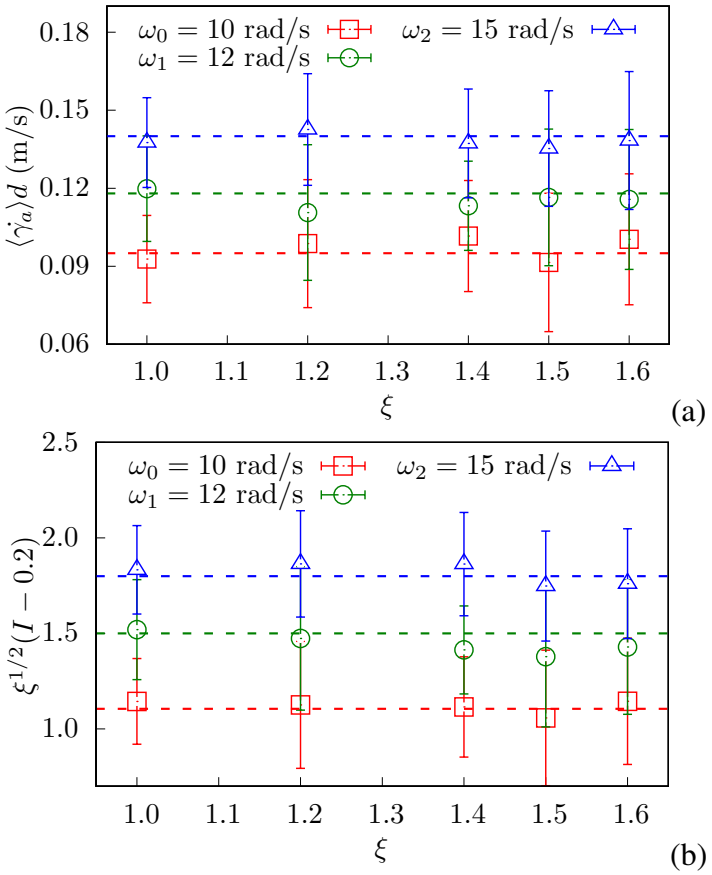

Fig. 3-17. The evolution of relative velocity $\langle\dot{\gamma}_a\rangle d$ and inertial number I inside active layer as a function of coarsening factor ξ. Error bars represent standard deviation.

3.6 Conclusions

In this paper, we used particle dynamics simulations to analyze granular flows composed of octahedral particles in 3D rotating drums for a range of control parameters for which the flow remains in the cascading regime, characterized by dense flows of particles with a curved free surface. A major effect of angular particle shape is the absence of particle slippage at the drum wall, which is commonly observed in drum flows of spherical particles. For this reason, the steady state is characterized by a full balance between flow rates in the passive upward flow and active downward flow layers independently of the values of system parameters such as drum size and rotation speed.

A detailed parametric study was carried out by varying independently drum diameter D, particle diameter d, rotation speed ω, and filling degree J. We showed that the free surface curvature, inertial active flow thickness, and shear velocity are unique linear functions of a scaling parameter $\Gamma = \mathrm{Fr}^{1/2}(D/d)^{1/2}J^{1/4}$, which combines the Froude number $\mathrm{Fr}=D\omega^2/2g$, size ratio D/d, and filling degree J. We argued that this scaling is fully consistent with a particle-coarsening analysis in which the flow scale variables are assumed to be constant and independent of particle size d. We also briefly compared our data with those obtained for flows of spherical particles in a drum.

Further work is necessary to extend the proposed scaling to other particle shapes and to perform a full comparison with drum flows of spherical particles. We are also interested in the effect of both friction coefficient between particles and particle shape angularity on the scaling and crossover from rolling to cascading and from cascading to cataracting regimes. Another important direction of research concerns the effects of size polydispersity and particle breakage on the scaling behavior. While we expect that the general scaling proposed in this paper will not be affected, the numerical parameters involved in the expressions of flow variables as a function of the scaling parameter may well depend on size polydispersity or evolve with particle breakage. Actually, this scaling provides also a general framework for quantifying such effects.

Last but not least, the findings discussed in this paper suggest new experiments. The flow variables such as slope ratio and thickness ratio are easy to measure using particle tracking. The simple relations between these variables suggested by our simulations, such as the relations (3.8) and (3.10), can therefore be checked by experiments using model particles of octahedral shape. By performing experiments with different particle sizes, it is also possible to investigate the effect of particle size through the scaling parameter Γ for different flow variables. For example, relation (3.8) predicts that the surface curvature increases with increasing ratio D/d. Experiments can be used to validate this trend and to determine whether it holds for large values of D/d and evaluate its limits. We believe that the scaling proposed in this paper holds also for other particle shapes such as elongated particles. However, due to the effect of particle shape on the angle of repose, the numerical values of parameters involved in the relations derived in this paper may change with particle shape. The effect of particle shape can be investigated in parallel by both simulations and experiments. We currently develop new experiments in the geometry of rotating drum with the goal of performing a detailed comparison between experiments and the findings of this paper. The uncertainties associated with possible code-level errors or numerical model parameters can also be evaluated within this project.

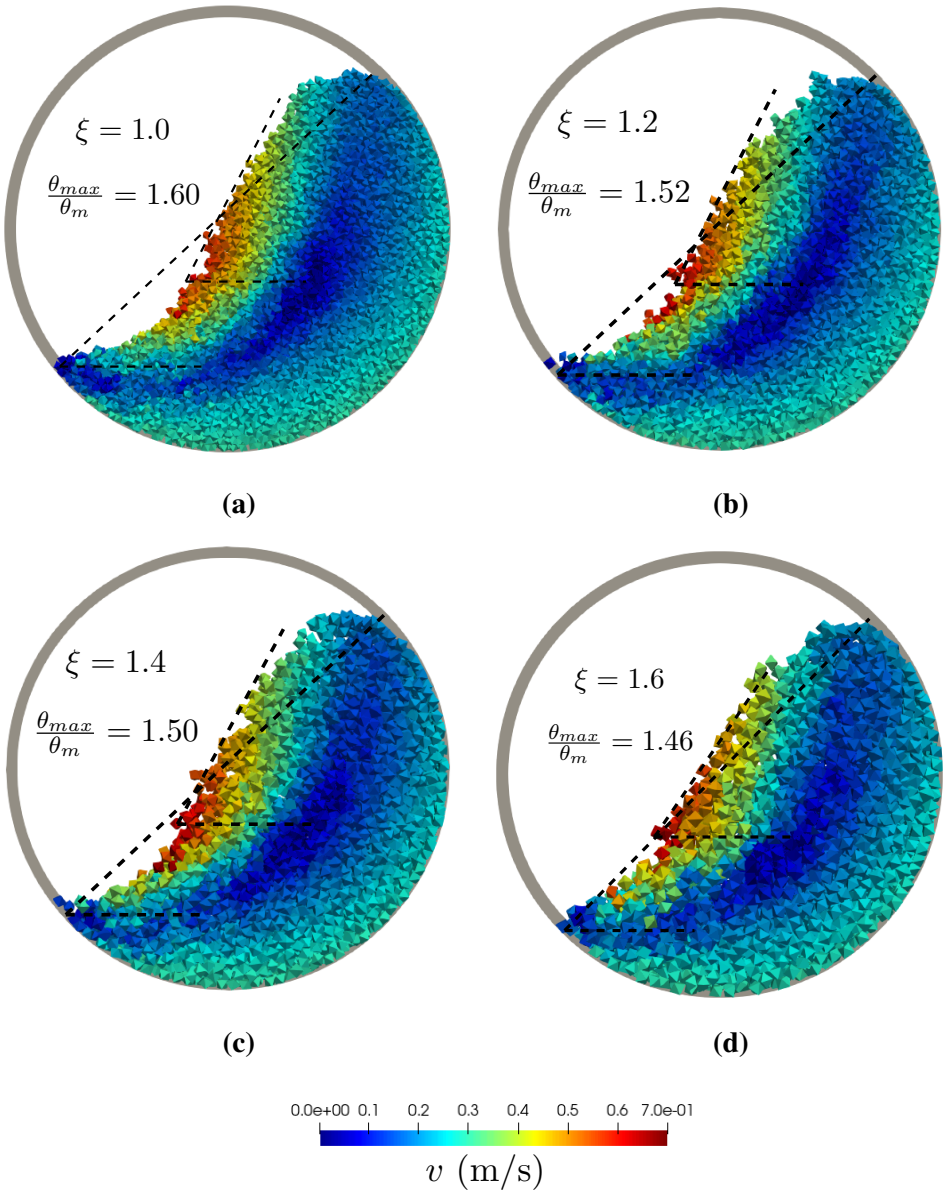

Fig. 3-18. Snapshot of particles and their velocities in rotating drum for different particle coarsening factors ξ for constant filling degree $J = 0.4$, drum diameter $D = 40$ mm, and rotation speed $\omega = 15$ rad/s. Color bar indicates particle velocities. The values of slope ratios are averages in steady flow.

Chapter 4

Scaling law for impact-induced breakage of a single particle

Contents

We introduce a novel approach to particle breakage, wherein the particle is modeled as an aggregate of polyhedral cells with their common surfaces governed by the Griffith criterion of fracture. This model is implemented within a discrete element code to simulate and analyze the breakage behavior of a single particle impacting a rigid plane. We find that fracture dynamics involves three distinct regimes as a function of the normalized impact energy ω. At low values of ω, the particle undergoes elastic rebound, and no cracks occur inside the particle. In the intermediate range, the particle is damaged by nucleation and propagation of cracks, and the effective restitution coefficient declines without breakup of the particle. Finally, for values of ω beyond a well-defined threshold, the particle breaks into fragments, and the restitution coefficient increases with ω due to kinetic energy carried away by the fragments. We show that particle damage, restitution coefficient, and fracture efficiency (the amount of energy input consumed for particle fracture) collapse well as a function of dimensionless scaling parameters. Our data are also sufficiently accurate to scale fragment size and shape distributions. It is found that fragment masses (volumes) follow a power-law distribution with an exponent decreasing with fracture energy. Interestingly, the average elongation and flatness of fragments are very close to those observed in experiments and lunar samples at the optimal fracture efficiency.

4.1 Introduction

Particle breakage is a commonly observed phenomenon in natural flows and industrial processes involving powders and grains [268–272]. Particle breakage is most of time undesirable, but it represents also the goal of milling operations, which are known for their energy intensive nature. Despite extensive past research, particle breakage mechanisms in granular materials remain poorly understood due to their multi-scale nature, involving material sub-particle scales to particle scale and up to the packing and process scales [139, 273–275]. The fragmentation of particles is controlled by the mechanical properties of the particles and their contacts, on the one hand, and the process operational factors, on the other hand [125, 133, 177, 178, 276, 277]. For instance, the distribution of fragment sizes during the grinding process in ball mills is influenced by the cohesive strength of single particles, numbers and sizes of grinding balls, amount of granular material, and other system parameters [121, 178]. The particles can break under various loading modes such as compression, distortion, shear, and impact. Different fracture modes generally take place simultaneously during a comminution process in different parts of the system [51]. To model particle breakage, an important issue is therefore to identify physical mechanisms at different scales: sub-particle processes at the origin the strength and potential weaknesses of particles, single particle fracture by impact or forces exerted by other particles, collective dynamics of particles, and process-scale mechanisms of energy supply to the particles.

Experimental studies of single particle fragmentation have been carried out to analyze the fragment mass and size distributions, crack patterns, and failure modes. The masses in the range of small fragments are often found to follow a power law distribution with exponents that do

not always seem to be universal but depend on the brittle or ductile nature of fracture and dimensionality of the object [139, 278–284]. A general observation is that during impact between two particles plastic deformation develops first around the contact point, then cracks appear and propagate through the particle and eventually split the particle [278, 285]. Part of supplied energy is consumed in producing new fracture surfaces inside the particle while a large amount of the supplied energy is also taken away in the form of the kinetic energy of the fragments after collision and dissipated by plastic deformations and frictional or inelastic collisions. Impact-induced fragmentation was found experimentally to generate elongated shapes characterized by the dimensions a, b, and c of their bounding box. In several reported investigations, the ratios were found to be distributed around the proportions $a : b : c \simeq 2 : \sqrt{2} : 1$ [126, 137, 138, 286].

Due to the inherent complexity of experimental measurement of dynamic fracture of a single particle or the evolution of a collection of particles in real time, particle dynamics simulations based on the Discrete Element Method (DEM) have also been developed as an alternative approach for the investigation of particle breakage in granular materials. For example, experimental findings of fragment size distributions were reproduced by such simulations [114, 140, 287, 288]. Important results were obtained by DEM simulations such as crossover from damaged state to the fragmented state at a well-defined value of impact energy [122, 124–127]. The critical point of this transition was identified as the impact velocity for which the average fragment mass takes a maximum value [127, 132]. The effects of material properties such as interface energy on the fracture pattern were also investigated [129, 130].

The DEM -based model extensively used for particle fragmentation is known as Bonded Particle Method (BPM) that simulates a parent particle as an aggregate of spherical particles [114, 130, 131, 277]. For primary spheres, since the external boundary of the aggregate is used to represent the particle surface and the aggregate is porous, the volume is not conserved during fragmentation. In contrast, the primary polyhedra can fill the volume of a particle with zero porosity and no volume is lost during particle breakage [120, 121, 132, 151]. Furthermore, in a cluster of polyhedra the bonds coincide with the common surfaces between polyhedra, so that the breakage of a bond naturally creates a fracture surface. Particle tessellation into contiguous polyhedra was coined Bonded Cell Method (BCM) [151]. In BCM, each face-face interaction represents a potential crack and the fracture energy is obtained by multiplying the area by surface energy [121, 151]. The cell-meshed particles, when they are randomly distributed, allow for arbitrary fragment shapes if the number of primary polyhedra composing the particle is sufficiently high [151].

Particle fracture by BCM requires a fracture criterion. Numerical studies reported in the literature are generally based on force or stress thresholds which lead to brittle behavior while fracture mechanics requires a model fully based on energy [114, 120, 126, 132, 151, 277]. In their model of thermodynamically consistent breakup model, Orozco *et al.* [121] used a criterion based on the fracture energy in the framework of the Contact Dynamics method (non-smooth DEM), which does not account for elastic deflections at the contact points [223]. For this reason, the debonding criterion was based on the amount of energy absorbed by an interface and it was

postulated that an interface between two adjacent cells breaks if the total amount of energy exceeds the fracture energy. Using this criterion they were able to scale particle breakage as a function of the impact energy in 3D single-particle impact and the evolution of grinding in ball mills [121, 177].

In this paper, we use BCM with a fracture law that is based on the Griffith criterion of crack propagation by accounting for elastic energy release in each interface. In other words, the initial formulation of this criterion in terms of incremental creation of new fracture area, is coarse-grained for application to finite surface creation. Thus a cell-cell interface breaks only if the total elastic energy stored per unit interface area exceeds two times the specific fracture energy. We investigate in detail the breakage of a single particle impacting a rigid plane by means of extensive simulations. We analyze particle damage, fracture efficiency, and restitution coefficient as a function of impact energy. We propose functional forms that capture well the behavior in each fracture regime and transition between different regimes and we compare our data with those of Orozco et al. [121]. We also have enough data to analyze the resulting fragment size distributions and particle shapes. As we shall see, our findings are consistent with previous studies, but they provide a more general picture in the range of weak impact velocities where rebound and damage of the particle occur without particle fragmentation.

In the following, we first introduce in Section 4.2 the fracture model and the boundary conditions of impact test. The scaling of breakage behavior is presented in Section 4.3. In Section 4.4 we analyze the distributions of fragment shapes and sizes. Finally, we discuss the most salient results of this work in Section 4.5.

4.2 Bonded Cell Method and rupture model

4.2.1 Voronoi tessellation

We use the Bonded Cell Method (BCM) based on the division of the particle into polyhedral cells interacting with their neighboring cells via an interface characterized by a fracture energy. Each particle is divided into 1728 cells by Voronoi tessellation using the NEPER software [289]. One possible technique to construct the centroidal Voronoi tessellation is known as the Lloyd's method which simply alternates between constructing Voronoi tessellations and mass centroids [120, 290, 291]. An example of particle model composed of polyhedral cells is shown in Fig. 4-1. For the sake of geometrical consistency between the shape of the parent particle and its constitutive polyhedral cells, we use *truncated pentakis dodecahedron* shape composed of 92 faces involving 12 regular pentagons, 20 regular hexagons, and 60 mirror-symmetric hexagons. The cells (primary particles) have random sizes and shapes but they are always convex and share their faces with their neighboring cells. A key numerical parameter of BCM is the number of cells in the particles (both the parent particle and its progeny) to ensure arbitrary fragment shapes and a meaningful range of fragment sizes. For instance, several phenomena such as particle shattering, surface breakage, and damage without breakage are well captured by the

simulation but the number of cells must be sufficiently high to avoid fragment shapes after shattering that are controlled by initial Voronoi tessellation [151, 178]. It has also been observed that the fracture process is influenced by the number of cells if it is below 100 [120, 121].

Figure 4-2 displays the size and shape distribution of the primary particles generated by Voronoi tessellation. The aspect ratio a cell is defined as the ratio of the longest dimension to the shortest dimension of its bounding box. The diameter of a cell is defined as the diameter of a sphere having the same volume as the polyhedral cell. We see that the aspect ratios of cells range between 1 and 1.3 with a mean value around 1.2. Cell diameters mostly range from 0.16 to 0.17 mm, so that the cell sizes are approximately equal. The sizes of the parent particle and cells are the upper and lower bounds, respectively, of the size distribution of fragments in the debris generated by particle fracture. The statistical representativity of particle size distribution in the process of fragmentation depends therefore on their ratio.

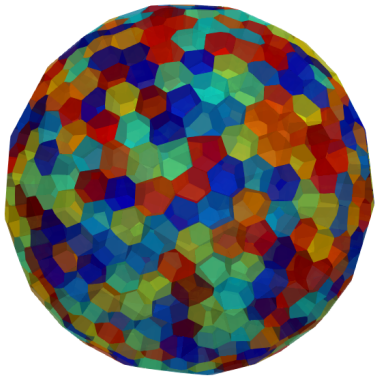

Fig. 4-1. Particle model generated by Voronoi tessellation with 1728 polyhedral cells represented by different colors.

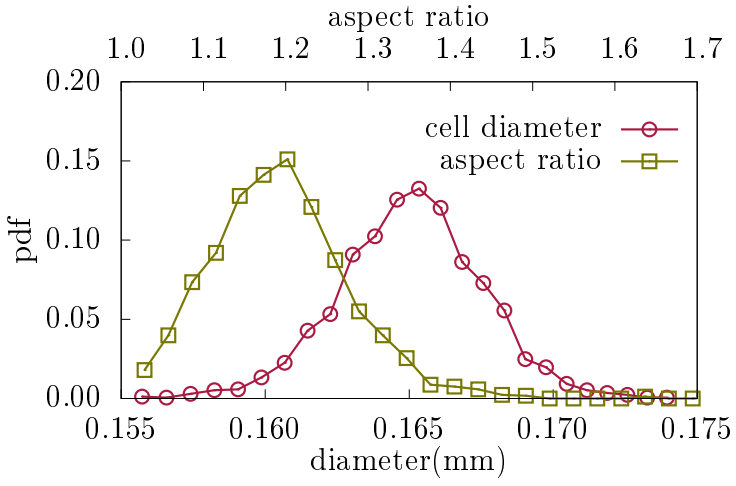

Fig. 4-2. The distribution of the shapes and sizes of primary particles.

4.2.2 Interactions between polyhedra

In our simulation model, primary polyhedral cells are smoothed by means of Minkowski sum with a sphere of desired radius (Minkowski radius). As a consequence, each polyhedron consists of three sub-elements namely vertex which is a small sphere, edge which is a cylinder connecting two vertices, and face which is a plane connecting at least three vertices. The contacts between two polyhedra are represented by the contacts of its sub-elements, leading to six contact types such as vertex-face, edge-edge, vertex-edge, vertex-vertex, edge-face, face-face. The unilateral constraints associated with these contact types do not have the same dimension. The vertex-face, vertex-edge, vertex-vertex, and edge-edge interactions involve a single contact point, which can be handled in the same way as contacts between spherical particles. Such simple contacts represent a single unilateral constraint, see Figs 4-3a, 4-3b. In contrast, a face-face contact is a plane that needs at least three points for its definition. Therefore, a face-face contact is equivalent to three simple contacts or unilateral constraints [22, 223]. This implies that at least three contact points are necessary to represent a face-face contact between two rigid polyhedra. Note that, the number of contact points can be larger than 3 depending on the number of edges, but the number of independent constraints is always 3, see Fig. 4-3d. In a similar vein, full representation of an edge-face interaction needs at least two contact points, see Fig 4-3c. Thus the edge-face and face-face contacts can be described as 'double' and 'triple' contacts, respectively.

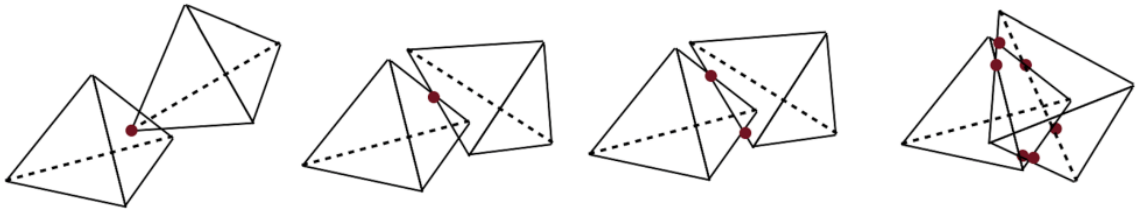

(a) **(b)** **(c)** **(d)**

Fig. 4-3. Different types of contacts between two polyhedra: simple contact (a, b), double (edge-face) contact (c), and triple (face-face) contact (d).

The Voronoi tessellation of the parent particle leads to a configuration of polyhedral cells that have face-face, vertex-vertex and parallel edge-edge contacts. We consider only the face-face contacts to define cohesive interfaces. The edge-edge and vertex-vertex contacts in the cell configurations are assumed to carry no surface energy and neglected since the internal cohesion of the particle is carried by the interfaces. However, as the interfaces break and the generated fragments move during particle fracture, other contact types may appear, but they will be treated as frictional cohesionless contacts due to the irreversible nature of fracture.

At each contact point between cells, either a linear or a nonlinear force law can be implemented. For smooth particle surfaces with well-defined curvatures at the contact point, the Hertz law can be used. However, in this paper due to the faceted shapes of the cells, we use linear elastic law which is equivalent to a linear spring acting the the contact point. This means

that the behavior of the particle as a whole is linear elastic. Let $\vec{n}$ and $\vec{t}$ be the normal and tangential unit vectors at a contact point c between particles i and j. The force $\vec{f} = f_n\vec{n} + f_t\vec{t}$ acting by particle j on particle i at this point of the interface is expressed as a function of the normal relative displacement (overlap) δ_n and cumulative tangential displacement $\vec{\delta}_t$. The normal force law is expressed as

$$f_n = -k_n\delta_n - 2\alpha\sqrt{k_n m}\,\dot{\delta}_n, \tag{4.1}$$

where k_n is normal stiffness of inter-cell bonds, δ_n is normal displacement (with the sign convention that $\delta_n < 0$ is an overlap and $\delta_n > 0$ is a gap), $\dot{\delta}_n$ is the relative normal velocity, m is the reduced mass of the two particles, and the dimensionless damping number α takes a value between 0 and 1. The viscous damping term accounts for normal energy dissipation and α is a function of restitution coefficient e_n:

$$\alpha = \begin{cases} \frac{-\log e_n}{\sqrt{(\log e_n)^2+\pi^2}} & \text{for } 0 < e_n \leq 1, \\ 1 & \text{for } e_n = 0. \end{cases} \tag{4.2}$$

In our simulations, e_n is set to a value close to 1 in order to showcase the effect of particle elasticity on fracture in contrast to previous simulations in which e_n was set to zero. The tangential force is given by:

$$\vec{f}_t = -k_t\vec{\delta}_t - 2\alpha\sqrt{k_n m}\,\vec{v}_t, \tag{4.3}$$

where k_t is the tangential stiffness, and $\vec{v}_t = \dot{\vec{\delta}}_t$ is relative tangential velocity. For internal bonds between cells there is no friction unless the interface fails and transforms into a frictional contact; see below. Hence, as long as an interface between two cells has not failed, the only source of dissipation is viscous damping.

4.2.3 Rupture criterion

Thermodynamically, the creation of cohesionless surface and crack propagation obeys the Griffith criterion. According to this criterion, a crack propagates if the rate of elastic potential energy released by surface creation is above the fracture energy. The Griffith formulation is based on a differential criterion with the assumption that crack growth is a continuous process. Hence, it can not be applied as such to a cell-cell interface of finite area $\mathscr{S}$ in BCM. For this reason, a 'coarse-grained' form of the energy criterion should be applied by considering a finite variation ΔW_p of the elastic energy. This condition for the creation of a surface equal to $\mathscr{S}$ can be expressed as [121, 292]:

$$-\frac{\Delta W_p}{2\mathscr{S}} = G \geq G_c, \tag{4.4}$$

where G_c is fracture energy per unit surface, the so-called toughness, and G is energy release rate.

Since the elastic energy associated with the interface vanishes when the bond fails, ΔW_p is actually the total potential elastic energy of interface. Furthermore, since the compressive

failure threshold is very high compared to the threshold in tension, we set the threshold in compression to infinity. Hence, ΔW_p must involve only the forces in tension:

$$\Delta W_p = \sum_{i \in \mathscr{S}} \left(\frac{f_{ni}^2}{2k_n} H(\delta_{ni}) + \frac{f_{ti}^2}{2k_t} \right), \tag{4.5}$$

where the function $H(\delta_{ni})$ is the Heaviside function defined by:

$$H(\delta_{ni}) = \begin{cases} 0 & \text{if } \delta_{ni} \leq 0, \\ 1 & \text{if } \delta_{ni} > 0. \end{cases} \tag{4.6}$$

This assumption implies that compressive forces do not contribute to fracture. Figure 4-4 shows a strength envelope based on Eqs (4.4) and (4.5). This envelop is simplified by considering a single contact point belonging to the interface. Since the interface involves at least three contact points, the strength envelope should be represented in a six dimensional space.

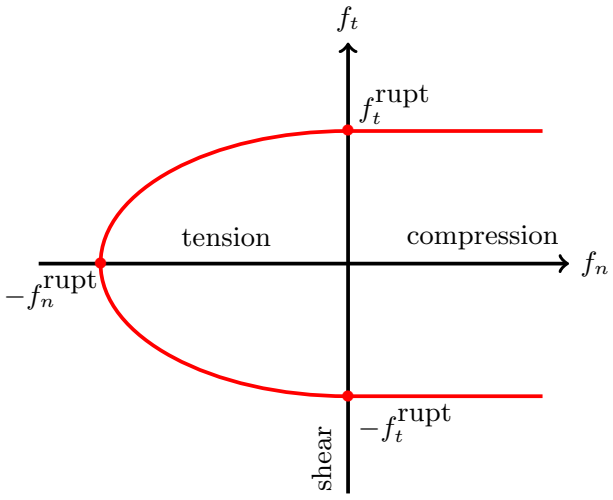

Fig. 4-4. Strength envelope of a single contact point belonging to an interface between polyhedral primary cells.

Once $G \geq G_c$, the cohesive bond fails and all contacts of this interface become frictional without cohesion. If the gap created as a result of interface deformation is nonzero ($\delta_n > 0$), the normal and tangential forces are both zero and the newly created contact is open. Otherwise ($\delta_n \leq 0$) the contact remains active and the relation between the normal force f_n and the overlap δ_n is given by Eq. (4.1). Note that, if the viscous damping term makes f_n negative, we set f_n to zero. This is necessary to avoid negative normal forces at cohesionless contacts [293]. In our simulations, we also set the restitution coefficient e_n for frictional contacts to a value close to zero while the restitution coefficient for internal bonds between cells is high; see Table 4-1.

The tangential force of frictional contacts is governed by the Coulomb friction law:

$$f_t = min\{|k_t \vec{\delta}_t|,\ \mu_s f_n\}, \tag{4.7}$$

Parameter	Symbol	Value	Unit
Number of cells	N_c	1728	-
Particle density	ρ_s	6000	kg/m^3
Gravity acceleration	g	9.81	m/s^2
Impact velocity	v_0	[0.5;10]	m/s
For frictional contacts			
Normal stiffness	k_n	10^8	N/m
Tangential stiffness	k_t	8×10^7	N/m
Restitution coefficient	e_n^2	0.001	-
Friction coefficient	μ_s	0.3	-
For cohesive bonds			
Normal stiffness	k_n	10^7	N/m
Tangential stiffness	k_t	0.8×10^7	N/m
Restitution coefficient	e_n^2	0.999	-
Fracture energy	G_c	[0.2;2.0]	J/m^2

Table 4-1. Simulation parameters for impact test of single particle with a rigid plane.

where k_t is tangential stiffness of frictional contact, and μ_s is the interparticle friction coefficient. The values of normal and tangential stiffnesses and restitution coefficients are given in Table 4-1. The orientation of the tangential force $\vec{t}$ is opposite to either the relative elastic displacement $\vec{\delta}_t$ below the Coulomb threshold or the relative velocity $\vec{v}_t$ at the contact point when the Coulomb threshold is reached.

4.3 Scaling of breakage behavior

We performed 3D impact tests of a single particle with a rigid plane. The particle is placed close to the horizontal plane and given an initial velocity v_0. The impact energy (kinetic energy before collision) is varied by changing the impact velocity in the range given in Table 4-1. The parent particle diameter is 2 mm in all tests. Each impact test was repeated 5 times, each with a different tessellation of the particle into cells. All our data points correspond to average values over the 5 tests with an error bar representing their standard deviation. We note that the point of impact with the plane should be random, so that the particle, which has a polyhedral shape, can fall on a face, edge, or vertex. To avoid systematic errors due to this effect, we rotated the particle in a random direction with a random angle before each impact test. As we shall see below, the error bars are generally small, meaning that particle orientation has little effect on the fragmentation process. For the parametric study, we also changed the fracture energy G_c, as shown in Table 4-1.

During an impact, part of the initial kinetic energy $W_k^- = mv^2/2$ of the particle is transmitted to the fragments. Note that v is pre-collision velocity of particle. Since the particle is placed very

close to the rigid plane, we have $v \simeq v_0$. Let W_k^+ be the total kinetic energy of the fragments after collision. The difference $W_d = W_k^- - W_k^+$ is consumed in fracture and other dissipative interactions, including friction and inelastic collisions between fragments. If $\mathscr{A}$ is the total cohesiveness surface area created during fracture, the total fracture energy is given by

$$W_f = 2\mathscr{A}G_c. \tag{4.8}$$

We also define the total surface energy $W_s = 2\mathscr{A}_0 G_c$ which is the total energy required to break all interfaces of the total initial area $\mathscr{A}_0$. Hence, particle damage D_w can be defined as

$$D_w = \frac{W_f}{W_s} = \frac{\mathscr{A}}{\mathscr{A}_0}. \tag{4.9}$$

By definition, D_w varies from 0 to 1.

Figure 4-5 displays particle damage D_w as a function of impact velocity v, for different values of fracture energy G_c. The damage first increases rapidly with v and then slowly tends to a constant value. The maximum value of damage is below 1, meaning that despite huge initial kinetic energy, the cell-cell interfaces do not break entirely apart. As we shall see, since the number of primary cells is sufficiently high, elongated fragments composed of several cell-cell interfaces are generated. Examples of particle fragmentation are shown in Fig. 4-6 for several values of fracture energy G_c with impact velocity $v = 4.5$ m/s. Obviously, the damage of particle with smaller values of G_c is higher at the same impact velocity v and increases faster than those of larger G_c. We also see that the error bars are small, indicating that the variability of fracture as a result of the variations of impact position is not significant.

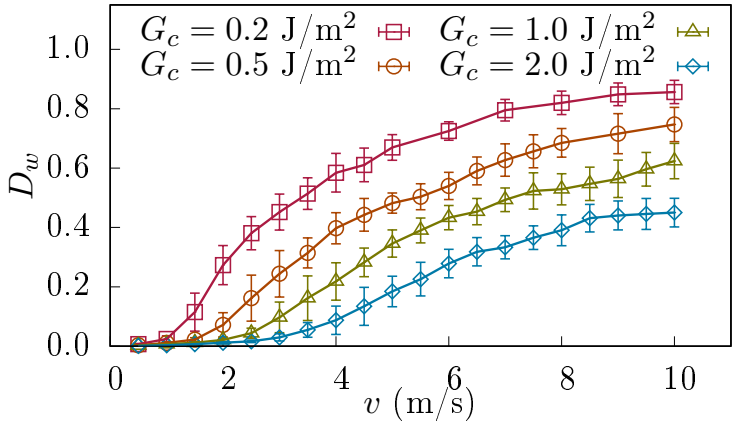

Fig. 4-5. Particle damage D_w versus impact velocity v for different values of fracture energy G_c. For each test, the error bar represents standard deviation over 5 independent tests.

In the comminution process, the amount of energy consumed for fracture as a function of impact energy is one of the most important aspects that must be considered thoroughly. We define the fracture efficiency η as the ratio of the total energy W_f consumed for fracture to the impact energy

$$\eta = \frac{W_f}{W_k^-}. \tag{4.10}$$

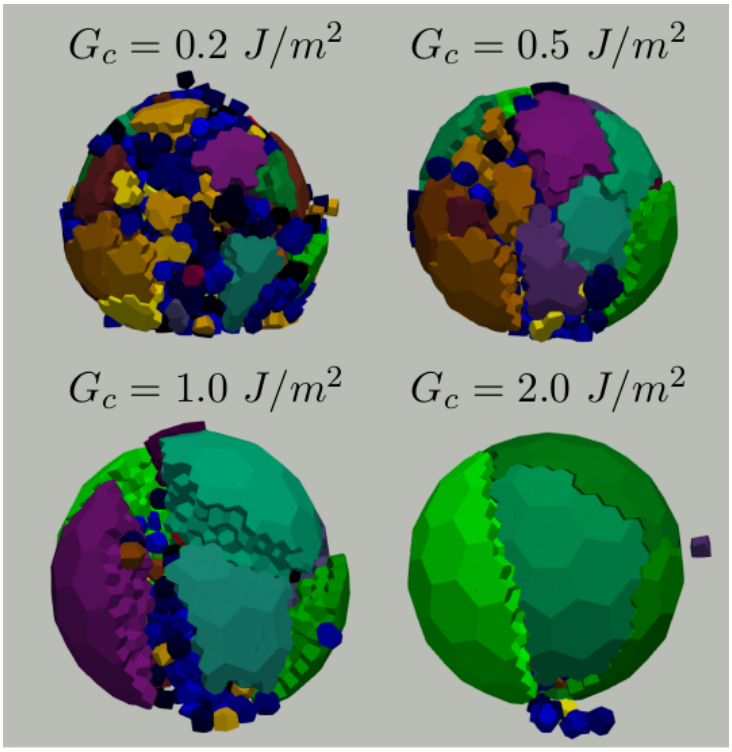

Fig. 4-6. Fragmentation of a particle impacting a rigid wall for different values of fracture energy G_c. The simulation was carried out with an impact velocity of 4.5 m/s.

Comminution is generally not an efficient process in the sense that most of the supplied energy is not consumed in fracture. It is thus interesting to see how the value of η for a single particle depends on the impact parameters.

The evolution of η as a function of impact velocity v for different values of G_c is shown in Fig. 4-7. We see that fracture efficiency first decreases to a minimum value of the order of 0.05 and then it increases rapidly with v up to a peak value of the order of 0.2. After the peak, it slowly declines towards a nonzero asymptotic value depending on G_c. The velocity at which η takes its peak value increases with G_c. The variation of η in our study is consistent with previous studies [121], except for the initial decrease of η at low impact velocity v. This decrease as a function of impact velocity reflects energy loss by inelastic interactions and opening of cracks inside the particle in the vicinity of the impact point. Since cracked interfaces are governed by frictional contact interactions, the loss of energy at the increasing number of such contacts grows with velocity and leads to a lower amount of energy available for fracture. Note also that the velocity at which η reaches its minimum value increases with G_c. The unmonotonic behavior of the evolution of η means that there is a characteristic velocity at which the conversion of kinetic energy to fracture is optimal. As we shall see, below and above the characteristic velocity the supplied energy is, to a large extent, either dissipated by inelastic collisions or taken away by the fragments.

During fragmentation, the kinetic energy of the parent particle can be dissipated by viscous damping between the particle and the rigid plane, plastic deformation, and damage of the par-

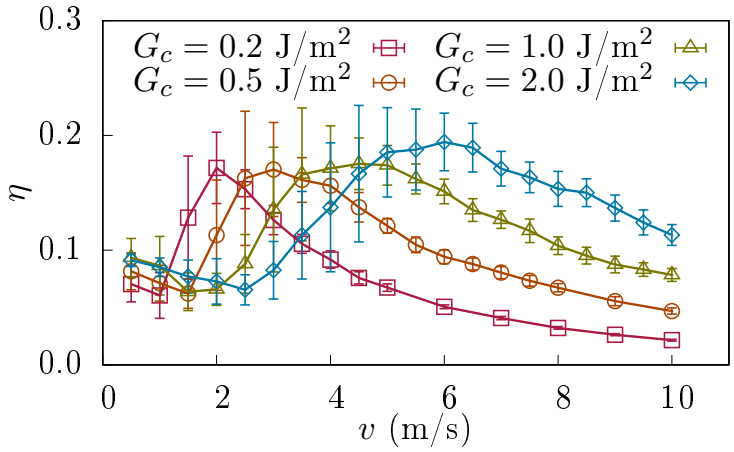

Fig. 4-7. Fracture efficiency η versus impact velocity v for different values of fracture energy G_c.

ticle or transferred to the fragments. We define an effective restitution coefficient e_k from the ratio of the pre-impact and post-impact kinetic energies:

$$e_k^2 = \frac{W_k^+}{W_k^-}. \tag{4.11}$$

The evolution of e_k^2 as a function of impact velocity is shown in Fig. 4-8. Consistently with the initial decrease of η, the squared restitution coefficient e_k^2 decreases from a value close to 1 since the restitution coefficient between primary cells is close to 1. From a value of v at which fracture efficiency η reaches its minimum, e_k^2 starts declining rapidly to a minimal value that decreases with increasing fracture energy G_c and then increases again. The restitution coefficient at high impact velocity is larger for lower values of G_c.

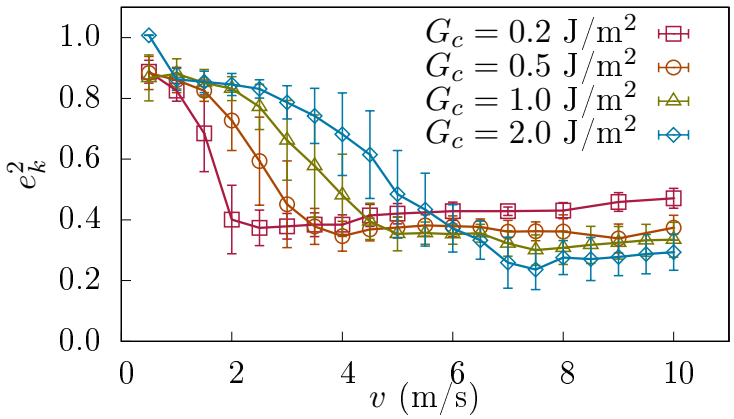

Fig. 4-8. Squared restitution coefficient e_k^2 as a function of impact velocity v for different values of fracture energy G_c.

These results show that the evolutions of D_w, η and e_k^2 as a function of v differ according to the value of the fracture energy G_c. This is an expected behavior since the induced fracture by impact energy W_k^- directly depends on the surface energy. Thus we define a normalized impact

energy ω as the ratio of supplied energy W_k^- normalized by total surface energy W_s:

$$\omega = \frac{W_k^-}{W_s}. \tag{4.12}$$

We naturally expect that the simulation data collapse when expressed as a function of this dimensionless energy ratio ω.

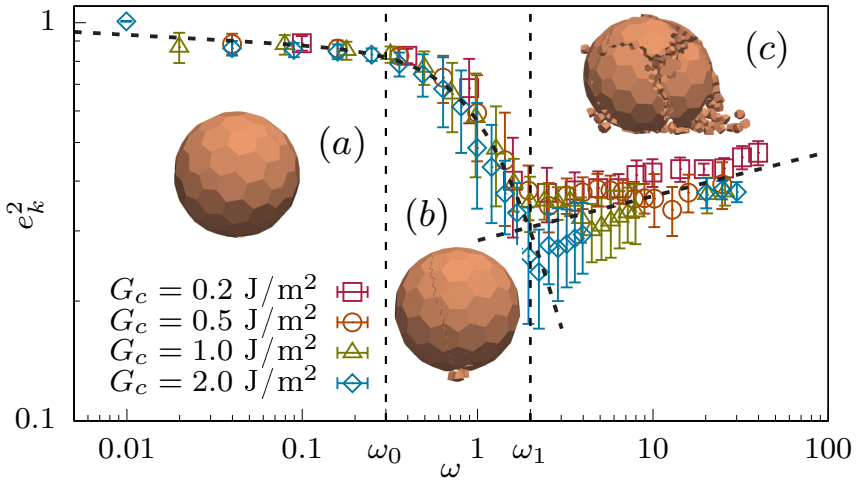

Fig. 4-9. Squared restitution coefficient e_k^2 as a function of normalized impact energy ω on log-log scale for different values of fracture energy G_c. The dotted lines are the fitting forms of Eqs.(4.13) and (4.14).

Figure 4-9 displays the evolution of e_k^2 as a function of ω on the log-log scale. We see that all data points fall into three distinct regimes with two well-defined crossover values ω_0 and ω_1. The data nearly collapse on a master curve in the first two regimes, but differ slightly in the third regime. In the range $\omega < \omega_0 \simeq 0.3$, e_k^2 decreases slowly. In this regime, the particle is not broken and only a small fraction of the supplied energy is used to create cracks close to the impact point. There is otherwise no crack inside particle. In the range of intermediate values $\omega_0 < \omega < \omega_1 \simeq 2.0$, the restitution coefficient declines rapidly with increasing ω due to increasing number of cracks created inside the particle. Finally, in the range $\omega_1 < \omega$, the particle breaks into an increasing number of fragments as a function of ω and the restitution coefficient increases gradually and linearly in log-log scale. It is noteworthy that the first two regimes of Fig. 4-9 were not clearly observed in simulations of Ref. [121] due to the low value of restitution coefficient in those simulations. But the crossover to particle fragmentation occurs at the same value $\omega_1 \simeq 2.0$ as in our simulations despite differences in the numerical methods employed.

Figure 4-9 also shows that the whole range of the first two regimes $\omega < \omega_1$ is well fit to a double power-law function:

$$e_k^2 = \frac{1}{a\left(\frac{\omega}{\omega_0}\right)^m + b\left(\frac{\omega}{\omega_0}\right)^n}, \tag{4.13}$$

with prefactors $a = 0.058$ and $b = 1.165$, and exponents $m = 1.9$ and $n = 0.024$. The data do not exactly collapse as a function of ω in the second and third regimes. Higher values of G_c

lead to lower values of e_k at ω_1. The values of parameters for the above fitting form slightly depend on G_c. We used the highest value of G_c to obtain their values. It is also remarkable that in the third regime, the data seem to tend to an asymptotic power law function as ω increases:

$$e_k^2 = c\left(\frac{\omega}{\omega_1}\right)^k, \tag{4.14}$$

where $c = 0.3$ and $k = 0.11$.

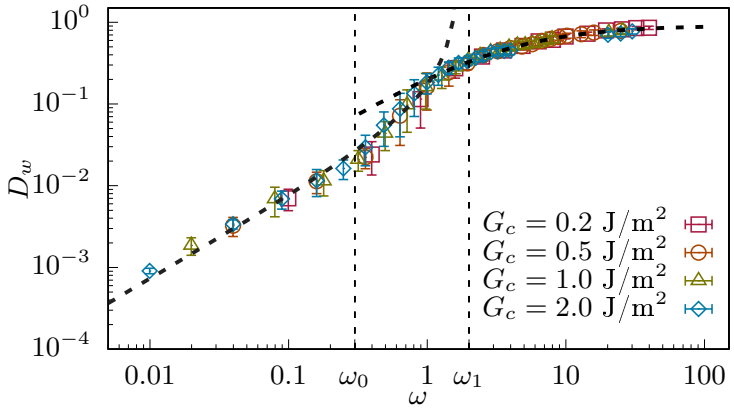

Fig. 4-10. Particle damage D_w as a function of the normalized impact energy ω on log-log scale. The dotted lines are the fitting forms shown in Eqs. (4.15) and (4.16).

Figure 4-10 shows particle damage D_w as a function of ω. Here, all the data nicely collapse on a single increasing function of ω. In the low-energy regime, D_w increases from 10^{-3} to 10^{-2}. In the second regime, it increases faster from 10^{-2} to 0.2. In the third regime, it increases from 0.2 towards 1. For the first two regimes, the following fitting function captures well the data:

$$D_w = \frac{a'(\omega/\omega_0)}{1 + b'(\omega/\omega_0)}, \tag{4.15}$$

with $a' = 0.022$ and $b' = -0.175$. In the high-energy regime, the following form suits well to the data:

$$D_w = \frac{c'(\omega/\omega_1)}{1 + d'(\omega/\omega_1)}, \tag{4.16}$$

where $c' = d' = 0.403$, ensuring that as $\omega \to \infty$, D_w tends to 1.

According to Eqs (4.9) and (4.10), we have $\eta = D_w/\omega$. We may therefore express η as a function of ω from that of D_w. Hence, for the low and intermediate-energy regimes, we have

$$\eta = \frac{a'/\omega_0}{1 + b'(\omega/\omega_0)}. \tag{4.17}$$

For the high-energy regime, we have

$$\eta = \frac{c'/\omega_1}{1 + d'(\omega/\omega_1)}. \tag{4.18}$$

The evolution of fracture efficiency η as a function of ω together with these fitting forms are displayed in Fig. 4-11. In the first regime, η decreases slightly from 0.1. However, in the

second regime at which part of supplied energy contributes to crack nucleation, η increases with ω before reaching the peak value around $\omega = \omega_1$. We see that the fitting form (4.17) does not exactly capture the initial decrease of η but it follows the data points within the available statistical precision. The third regime is excellently captured by the proposed fit. In this regime, η declines although particle damage D_w increases. This means that the amount of energy contributing to particle breakage increases, but it requires an excess energy supply which increases faster, leading thereby to fast reduction of η.

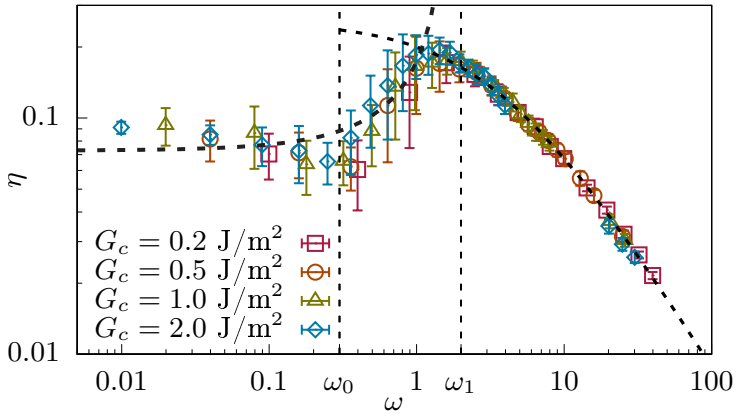

Fig. 4-11. Fracture efficiency η as a function of normalized impact energy ω. The dotted lines are the fitting forms (4.17) and (4.18).

Another variable of interest is the ratio χ of the post-impact kinetic energy to the fracture energy:

$$\chi = \frac{W_k^+}{W_f}. \tag{4.19}$$

This variable quantifies the relative weight of the energy transported by the fragments with respect to that consumed in particle breakage. It can be expressed as a function of e_k and η:

$$\chi = \frac{e_k^2}{\eta}. \tag{4.20}$$

Given the fitting forms of e_k and η as a function of ω, the evolution of χ in the first and second regimes must be captured by the following fitting form:

$$\chi = \frac{\omega_0 + b'\omega}{a'a\left(\frac{\omega}{\omega_0}\right)^m + a'b\left(\frac{\omega}{\omega_0}\right)^n}, \tag{4.21}$$

and for the third regime by

$$\chi = \frac{c}{c'}(\omega_1 + d'\omega)\left(\frac{\omega}{\omega_1}\right)^k, \tag{4.22}$$

The evolution of χ as a function of ω on the log-log scale is shown in Fig. 4-12 for different values of G_c. The fitting form is close to the data points in the first two regimes within statistical precision but does not capture well the trend in the first regime, while in the third regime it follows well the data points. The value of χ increases from 10 to 18 in the first regime, implying

that the kinetic energy of fragments is high compared to the energy consumed for fracture, which should be vanishingly small in the absence of crack generation. Then, it decreases in the second regime at which the energy consumed for crack generation increases faster than kinetic energy. It reaches its minimum value coinciding with the peak of η as shown in Fig. 4-11. At this point, we have $\chi \simeq 1$, which means that the amount of energy consumed at this point for fracture is nearly equal to that carried away by the fragments. In the third regime χ increases again due to the faster increase of the kinetic energy of fragments than the energy consumed by breakage.

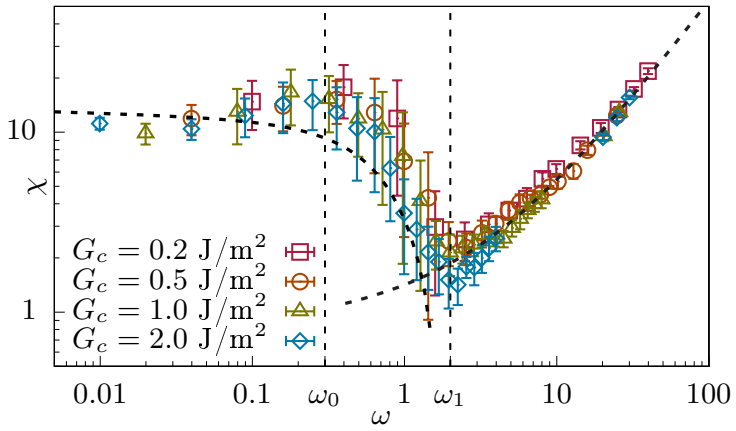

Fig. 4-12. Fragmentation efficiency η as a function of the normalized impact energy ω. The dotted lines are the fitting forms (4.21) and (4.22).

It is also interesting to consider the energy W_c dissipated by inelastic collisions and friction:

$$W_c = W_k^- - W_k^+ - W_f. \tag{4.23}$$

We normalize this energy by the total surface energy W_s and the following expression can be easily established:

$$\frac{W_c}{W_s} = \omega\left(1 - \eta - e_k^2\right). \tag{4.24}$$

The evolution of this ratio as a function of ω is displayed in Fig. 4-13 for $\omega > \omega_1$ where particle breakage occurs. It increases almost linearly with ω with slope $\simeq 1/2$ up to very high values of ω. This implies that approximately half of the supplied kinetic energy is dissipated by contact inelasticity and friction when the particle breaks. The remaining half is either used for fracture or carried away by the fragments.

4.4 Fragment sizes and shapes

The shapes and sizes of fragments reflect the fragmentation process. Several experimental studies have shown that the fragments of rock generated by explosion or impact have an elongated shape and the probability distribution of the fragment masses is a power-law function [114, 137–139]. To define an appropriate shape descriptor, we construct the bounding box of

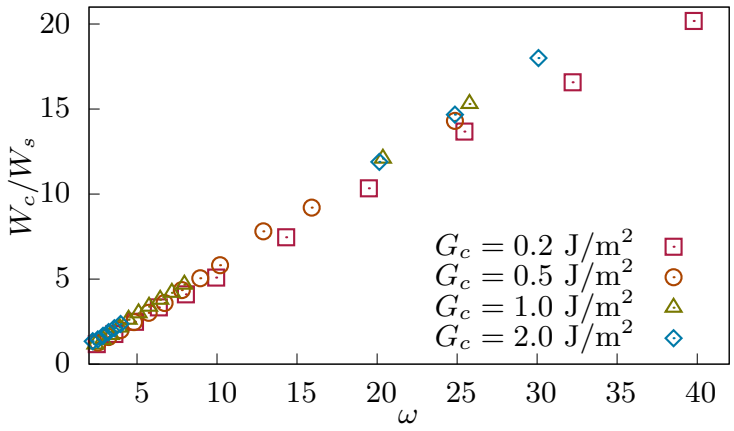

Fig. 4-13. Normalized energy dissipated by inelastic collisions and friction W_c/W_s versus normalized impact energy ω for $\omega > \omega_1$.

each fragment with principal axis $c \leq b \leq a$ as shown in Fig. 4-14. The length a of the bounding box is the longest dimension of the fragment, b is the largest distance perpendicular to the direction of a, and c is defined as the largest distance perpendicular to the plane determined by a and b. The shapes of fragments can be described in terms of the elongation ratio b/a and flatness ratio c/b. The inverse values a/b and b/c represent the two aspect ratios.

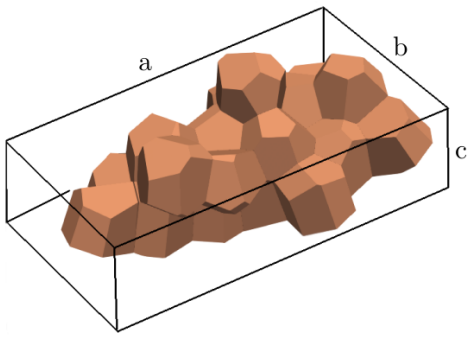

Fig. 4-14. The space dimensions of a fragment according to its bounding box in three mutually orthogonal planes ($a \geq b \geq c$).

We consider the average value of elongation ratio and flatness ratio calculated over all fragments generated as a result of particle breakage. We neglect the fragments composed of a single primary cell in order to remove the effect of Voronoi tessellation. The values of $\langle c/b \rangle$ and $\langle b/a \rangle$ are shown in Fig. 4-15 as a function of ω for $\omega > \omega_1$. The minimum values of elongation ratio $\langle b/a \rangle$ and flatness ratio $\langle c/b \rangle$ are $\simeq 0.69$ and $\simeq 0.77$, respectively. Interestingly, these values are close to the data obtained from particle size and shape distributions in lunar samples [137, 138, 294]. The ratio c/b increases and tends to a constant value $\simeq 0.88$ while b/a slightly decreases and remains constant and equal to 0.69. It has been argued that this ratio represents a *self-similar shape*: once broken into two equal fragments, each fragment has the same elongation ratio as the parent particle [138]. Mathematically, the ratio of self-similar shape by this operation is $\sqrt{2}/2 \simeq 0.7$.

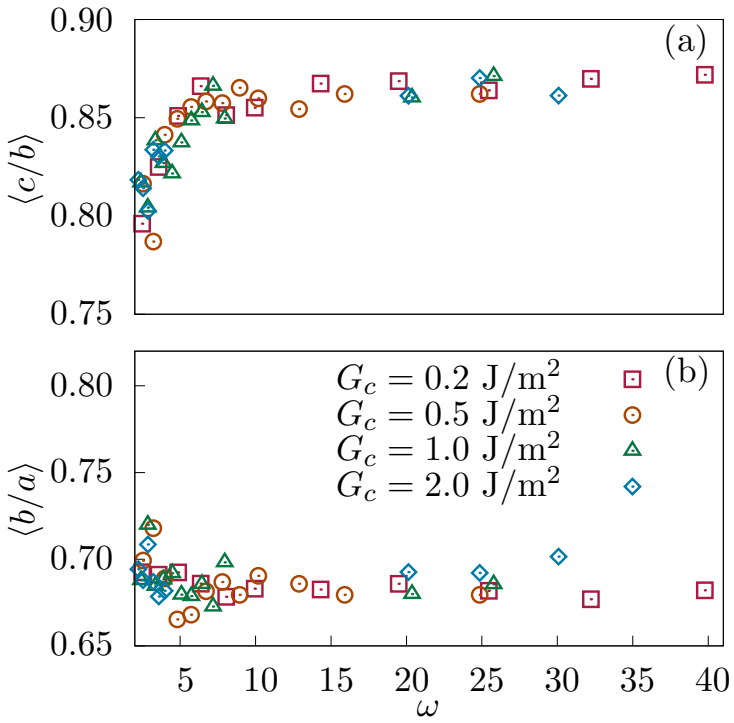

Fig. 4-15. The average shape descriptors as a function of normalized impact energy ω for all values of fracture energy G_c, (a) the flatness ratio $\langle c/b \rangle$ and (b) the elongation ratio $\langle b/a \rangle$.

Another quantity that has been used for the characterization of particle shape is the shape factor S_f defined as [139]:

$$S_f = (1/a + 1/b + 1/c)\sqrt{a^2 + b^2 + c^2}/\sqrt{3}. \tag{4.25}$$

This parameter reaches its lowest value $S_f = 3$ for nearly spherical fragments with $a \simeq b \simeq c$, while elongated shapes have larger values $S_f > 3$. To quantify the statistics of occurrence of different shapes of fragments, we determined the probability distribution $p(S_f)$ of the shape factor. Note that we gather data of fragment shapes for different impact velocities v together to gain large enough data sets for calculating distribution function. Figure 4-16 shows that the simulation data for all values of G_c collapse on a curve which has a decreasing exponential form for $S_f > 3.2$. This is in remarkable agreement with the experimental results of Ref. [139] although the fragments in our simulations result from single-particle fracture rather than a multi-particle granular process. The mean value of S_f is about 3.3 for all cases in our simulations.

We also investigated the probability distribution $p(m)$ of fragment masses. Several previous studies suggest that the distribution is generically a power-law function:

$$p(m) \sim m^{-\tau}. \tag{4.26}$$

It seems that the value of the exponent τ is not universal but depends on the material or the amount of energy consumed for fragmentation [123, 139, 142, 274, 287, 295]. Figure 4-17 presents the fragment mass distributions $p(m)$ for different values of fracture energy G_c on the log-log scale. The masses of fragments m are normalized by the maximum mass $m_{\max}$. We observe here a power-law behavior for all values of G_c. The value of exponent at $G_c = 0.2$ J/m^2 is

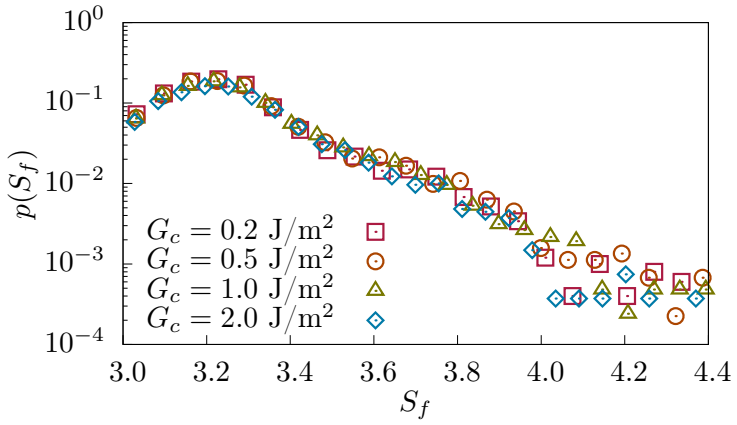

Fig. 4-16. Probability distribution of the shape factor S_f on semilogarithmic plot for all values of fracture energy G_c and impact velocity v.

$\tau = 3.0$, but decreases as G_c increases. For $G_c = 2.0$ J/m^2, we find $\tau = 2.1$. The value of τ in our study is higher than the value $\tau = 5/3$ proposed for three-dimensional solids [114,139,287,296]. It is important to recall here again that particle size distribution resulting from the comminution of a granular material is a consequence of the combined effects of stress distribution inside the material and single-particle fragmentation process. For this reason, the size and shape distributions of single-particle impact may differ from those of a granular process involving multicontact stress transmission.

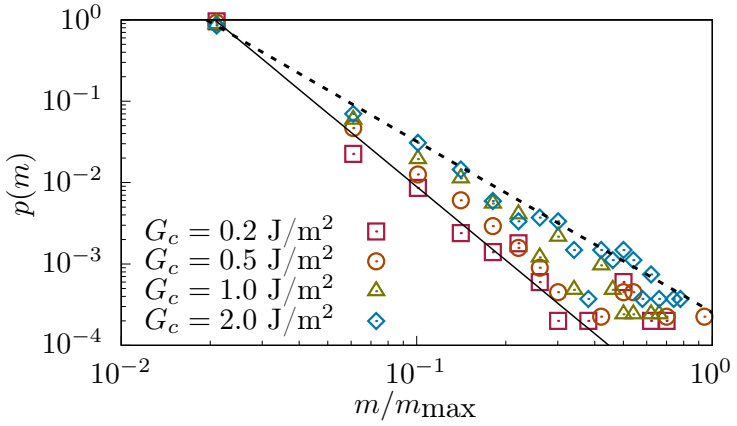

Fig. 4-17. Fragment mass distributions $p(m)$ for different values of the fracture energy G_c. The solid line shows the power function (4.26) with $\tau = 3.0$ for $G_c = 0.2$ J/m^2 and the dotted line with $\tau = 2.1$ for $G_c = 2.0$ J/m^2.

4.5 Conclusions

In this paper, a fracture law based on the Griffith criterion was used with the Bonded Cell Method implemented in a 3D DEM code for the simulation of the fracture behavior of a single particle impacting a rigid plane. The particle is discretized by means of Voronoi tessellation

into polyhedral cells whose interfaces represent potential cracks while the cells and their combinations represent potential fragments. The fracture law implies that a cell-cell interface fails if the energy release rate is above the fracture energy. Our results of single-particle fracture compare well with both past simulations of the same process and recent experimental data.

Our simulations show that the behavior of the impacting particle involves three distinct regimes depending on the ratio ω of the impact energy to the fracture energy of the particles. Our results are consistent with previous experimental and numerical findings, in which our two first regimes correspond to damaged state and high-energy regime is coincident with fragmented state. This behavior makes appear two critical energy ratios which determine whether the particle breaks or it simply rebounds with or without being damaged. For different values of fracture energy, we showed that several physical variables such as particle damage, restitution coefficient, fracture efficiency, and the amount of energy dissipated by inelastic collisions and friction are well scaled by ω. The fracture efficiency is an unmonotonic function of impact energy with its optimal value at crossover to the third regime where particles break into several pieces. We found that In the third regime, nearly half of the input energy is dissipated by contact inelasticity and friction, the other half being either consumed for fracture or carried away by the fragments generated as a result of particle breakage.

We also found that the distribution of fragment masses is a power-law function with an exponent slightly decreasing with fracture energy. It is remarkable that the shape descriptors of the fragments such as flatness ratio and elongation ratio have generic values previously observed in real samples of granular materials. In particular, we found that the fragments in the whole range of values of ω have an average aspect ratio which is nearly equal to $\sqrt{2}$, a value that hints at a self-similar shape. This self-similarity is consistent with the existence of a power-law size distribution, which is a consequence of the absence of characteristic lengths (between cell size and initial particle size) in the system.

It will be important to extend this work to a broader parametric study to assess the generality of the scaling behavior evidenced in this work. For example, the initial particle used in our simulations is undamaged and its total surface energy W_s is constant. It will be interesting to consider damaged initial particles (containing pre-cracks) to study the effect of varying W_s on the dependence of restitution coefficient and damage on ω. Furthermore, the restitution coefficient can be set to lower values to study its effect on the two first regimes and the crossover values of ω. In longer terms, we would like to use our results to predict the fracture of particles in rotating drums and during quasi-static deformation of granular materials. Extensive simulations will be performed in both configurations for the scaling of particle breakage as a function of system parameters to obtain clues for the scale-up of comminution from particle scale to a collection of particles.

Chapter 5

General conclusions and perspectives

5.1 Summary

The main objective of this PhD work was to apply advanced particle simulations based on Discrete Element Method (DEM) to investigate quasistatic and dynamic granular flows of polyhedral-shaped particles and modeling particle breakage for the simulation of the comminution process in rotating drums. Our numerical developments and simulations were carried out by means of the simulation code Rockable. We did new developments during this doctoral work to optimize contact detection between cylindrical walls of the rotating drum and polyhedra, and to implement fully periodic boundary conditions with the possibility of controlling either displacement or pressure in every space direction. Periodic boundary conditions were also used along the rotating drum axis. The code was parallelized and efficiently used for all simulations on multiple processors.

We focussed on 1) the elasto-plastic behavior of samples composed of polyhedral and spherical particles under tri-periodic boundary conditions and its relation with the microstructure, 2) the scaling behavior of cascading flows of polyhedral particles in a rotating drum, and 3) the breakage dynamics of a single polyhedral particle. The methodology developed for the simulation and the micromechanical and scaling analysis of these different configurations lays the foundations for realistic 3D simulations and analysis of the grinding process in rotating drums with potential application to the fabrication process of nuclear fuel. The ultimate aim is to provide a generic and reliable framework combining discrete mechanical simulations with physical analysis to optimize the properties of multi-component powders while minimizing the energy cost.

For elastic behavior of granular packings, we found that the orthotropic elastic moduli under triaxial boundary conditions can be expressed as a function of contact network variables such as connectivity and contact orientation anisotropy. The proposed expression does not depend on particle shape, but involves coefficients that depend on particle shape. We argued that accurate determination of these coefficients makes it possible to predict the evolution of elastic moduli with strain. This expression therefore reveals three different origins of elastic moduli, namely a stress scale, an isotropic part, and an anisotropic part. The stress scale depends on the force

model, and its value is simply given by the ratio of contact stiffness and particle diameter. We compared the elastic moduli with the predictions of the effective medium theory (EMT) and discussed important differences and similarities between them. We showed that the particle shape affects the elastic moduli through our model parameters which do not depend on friction coefficient, but relate to nonaffine displacement field and through its impact on the contact network which depend on friction coefficient. We also showed that the level of nonaffinity is the same for the simulated shapes during compression, underlying the constant values of the model parameters. This expression also reveals how the face-face and face-edge contacts enhance the elastic moduli compared to spherical particle packings.

For the influence of polyhedral particle shapes on the cascading flow regime in rotating drums, extensive simulations were performed for a broad range of values of rotation speed, drum diameter, particle diameter, and filling degree. By a detailed analysis of flow variables such as the average and maximum slopes of free surface, flow thickness, shear rate, and inertia number in the active layer, we found a unique dimensionless scaling parameter combining Froude number, ratio of drum to particle diameter, and filling degree. We showed that this scaling parameter works also for spherical particles thereby highlighting the effect of polyhedral particle shape through differences between model parameters. We also analyzed on the effect of particle coarsening and we showed that it is consistent with our scaling of flow variables.

For impact-induced breakage of single particle, we introduced a breakage model fully based on the fracture energy. In this bonded-cell model, the cell-cell interface breaks only if the elastic energy stored in the whole interface exceeds the fracture energy. We found that the impact process involves three distinct regimes: 1) low-energy regime, 2) intermediate-energy regime, and 3) high-energy regime. The critical transition impact energies between these regimes was identified by a detailed analysis of breakage variables. We proposed fitting forms that correctly adjust the evolution of breakage variables as a function of impact energy. We also found that the distribution of fragment masses is a power-law function with an exponent depending on the fracture energy.

5.2 Extensions and outlook

The 3D simulation of granular flows of breakable particles in rotating drums with and without grinding balls is a natural extension of this PhD work. Several key issues can be investigated by means of parametric simulations:

1. How does particle breakage influence the flow behavior in the cascading regime?
2. How does particle breakage scale with system parameters?
3. How does the microstructure evolve during comminution?
4. What is the optimal number of grinding balls for efficient milling with regard to energy consumption and grinding time?

5. How does grinding rate scale with drum size?

6. How do the breakage index and particle size distribution evolve with time?

These issues already been considered in previous 2D simulations in a rotating drum [65, 177]. But similar simulations in 3D requires much higher computational power and algorithmic developments some of which have been done during this thesis.

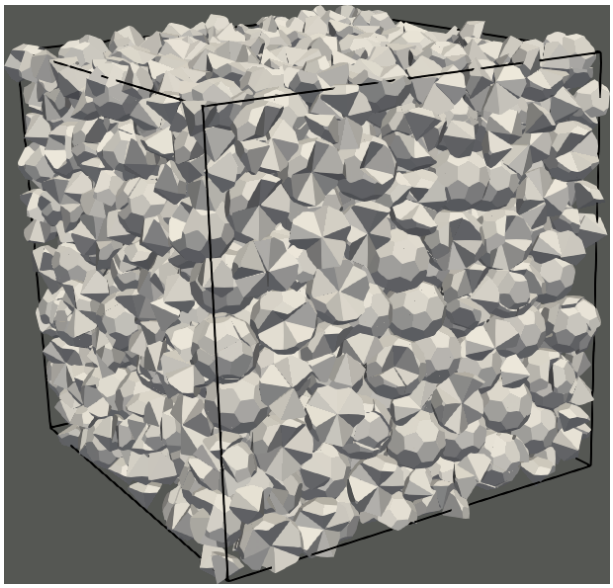

Fig. 5-1. Fragmentation of particles in a cubic box as a representative volume element with fully periodic boundary conditions.

Another issue that was considered in the context of the scaling of cascading flows is particle coarsening. We found that particle coarsening with the rules that were used in this work was consistent with our data. These rules need, however, to be re-examined in the case of breakable particles. This is because in the framework of the bonded cell method the energy needed for the fracture of an interface depends on its area and varies as the square of particle size while the kinetic energy depends on the particle size to power three.

Apart from particle breakage, the flow behavior in the cascading regime can be further investigated by considering the effects of rough drum walls. We found that the sliding of particles at the walls is negligible for polyhedral particles. However, the effect of wall roughness on the flow of spherical particles needs to be investigated to validate the comparison made with polyhedral particles. In the same way, we assumed periodic conditions along the drum axis. However, there are reports indicating that the friction with end walls plays a role in the characteristics of flow. A systematic analysis of the effect of friction coefficient with the end walls and the distance between the two end walls for polyhedral and spherical particles. It is also obvious that more simulations with polyhedra of irregular numbers of faces must also be performed in the future to analyze in a systematic way the effect of particle shape angularity on the nature of the flows.

Another important challenge will be to validate and/or calibrate simulations by direct comparison with experiments. Such experiments require model breakable particles, the possibility of modifying particle size and drum size, and measurement of particle size distributions during the milling process. These comparisons can be made by comparing the evolution of particle size distribution between simulations and experiments. Furthermore, the particle shapes and sizes in experiments can also be extracted from tomographic images. This technique has already been applied to investigate particle breakage under quasi-static conditions [297].

Regarding elastic moduli, as far as we know, they have never been measured for polyhedral particles. Moreover, most DEM simulations of polyhedral particles are based on contact forces calculated using the penalty method based on the overlap volume between particles. This approach is clearly not physically well founded because it does not differentiate different types of contacts between polyhedra. This is most crucial for face-face contacts that involves three geometrical constraints between two particles. It would be therefore interesting to compare the elastic moduli measured from our simulations with those obtained from the volume-overlap approach. They both must also be compared with experiments with well-calibrated particle shapes. Another very important extension of this work consists in simulating triaxial compression of other particle shapes (elongated, platy, nonconvex) and applying strain probes to measure the evolution of elastic moduli in order to calculate the coefficients of the linear model as a function of constraint number and fabric anisotropy proposed in chapter 2. This will allow generalizing our model to arbitrary particle shapes or to determine its limitations.

Appendices

Appendix A

Polyhedral particle packings under triaxial compression

We prepared three different packings of octohedral, dodecahedral, and icosahedral shapes, each of them composed of 8000 monodisperse particles enclosed in a triperiodic cubic cell such that either force or displacement can be controlled in each direction [188,226,298]. We prepared one more spherical particle packing with exactly the same number of particles, values of parameters, and boundary conditions. We started with a gas of particles that undergoes isotropic compression by the application of a constant isotropic stress p. The gravity g and interparticle friction coefficient μ_s are set to zero. For this reason, we obtained dense isotropic samples corresponding to a Random Closed Packing (RCP) of solid fraction $\Phi \simeq 0.611$ for octahedral particles, $\Phi \simeq 0.648$ for dodecahedral particles, $\Phi \simeq 0.632$ for icosahedral particles, and $\Phi \simeq 0.637$ for spherical particles. Figure A-1 displays three snapshots of the polyhedral particle packings at the end of isotropic compaction.

The isotropic packings prepared without friction were sheared by triaxial compression for four value of friction coefficient $\mu_s = 0.1$, 0.2, 0.3, and 0.4 between particles. The compression was applied along the z axis by imposing a small constant strain rate $\dot{\varepsilon}_z$ while keeping the same stress p in lateral directions x and y. Since we are interested in quasistatic behavior, the shear rate should be such that the kinetic energy supplied by shearing is negligible compared to the applied lateral pressure. This can be formulated in terms of an inertia number I defined by [11]

$$I = \dot{\varepsilon}_z d \sqrt{\frac{\rho}{p}}, \tag{A.1}$$

where ρ is particle density and d is mean particle diameter. The quasi-static limit is characterized by the condition $I < 10^{-3}$, which is remained during shearing [179, 299].

A.1 Strength and dilatancy

In this section, we consider the stress-strain and volume change behaviors as a function of the particle shape and friction coefficient μ_s. To evaluate stress tensor, we start with the tensorial

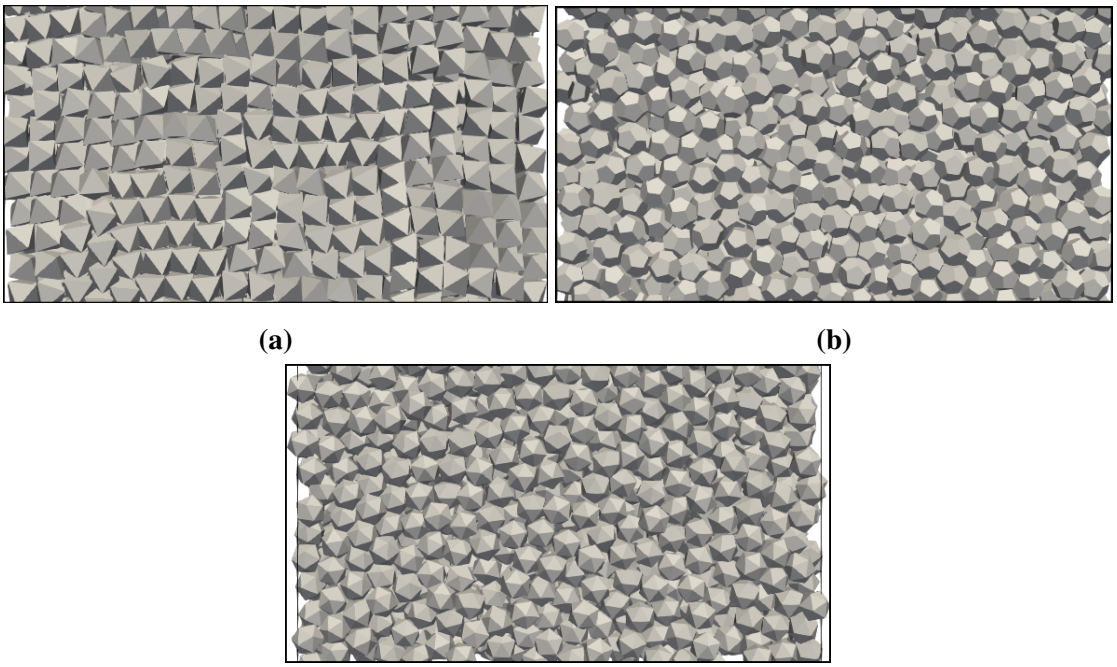

Fig. A-1. A snapshot of the octohedral (a), dodecahedral (b), and icosahedral (c) particle packing.

moment $\boldsymbol{M}^i$ of each particle i which is defined by [186, 300]

$$M^i_{\alpha\beta} = \sum_{c\in i} f^c_\alpha r^c_\beta, \tag{A.2}$$

where f^c_α is the α component of the force exerted on particle i at the contact c, r^c_β is the β component of the position vector of the same contact c, and the summation runs over all contact neighbors of particle i (noted briefly by $c \in i$). The average stress tensor $\boldsymbol{\sigma}$ in the volume V of the granular assembly is given by the sum of the tensorial moments of individual particles divided by the volume [23, 258]

$$\sigma_{\alpha\beta} = \frac{1}{V}\sum_{i\in V} M^i_{\alpha\beta} = \frac{1}{V}\sum_{c\in V} f^c_\alpha \ell^c_\beta, \tag{A.3}$$

where ℓ^c_β is the β component of the branch vector joining the centers of the two touching particles at the contact c. Note that, the first summation runs over all particles whereas the second summation involves the contacts, each contact appearing only once.

Under triaxial conditions, the principal stresses and strain rates coincide with the three space directions with σ_1 and ε_1 along the z direction, $\sigma_2 = \sigma_3$, and $\varepsilon_2 \simeq \varepsilon_3$. The mean stress p, and stress deviator q are defined by:

$$\begin{aligned} p &= (\sigma_1 + 2\sigma_3)/3, \\ q &= (\sigma_1 - \sigma_3)/3, \end{aligned} \tag{A.4}$$

and cumulative volumetric strain ε_p, cumulative shear strain ε_q are given by:

$$\begin{aligned} \varepsilon_p &= \varepsilon_1 + 2\varepsilon_3, \\ \varepsilon_q &= \varepsilon_1 - \varepsilon_3. \end{aligned} \tag{A.5}$$

For our system, the stress state is characterized by the mean stress p and the stress ratio q/p. Figure A-2a displays the stress ratio q/p versus shear strain ε_q of dodecahedral and spherical particle packings with different friction coefficient μ_s. Due to initially high value of solid fraction Φ, q/p quickly reaches the peak value and then decreases before approaching toward a stress plateau corresponding to the so-called critical state at $\sim 60\%$ of shear strain. Note that, due to three-periodic boundary conditions, no shear band develops in our systems. We also see that the peak value of q/p increases with μ_s. Cumulative volumetric strain ε_p as a function of shear strain ε_q is shown in Fig. A-2b. Starting with initially dense state, shear strain-volumetric strain curves first decrease from zero to negative values at very small value of ε_q and this means that the packings are compressed. Then, they increase to positive values corresponding to dilation of all packings and there exits a linear relation between the volume change and the change of the shear strain. The variation of q/p and ε_p of octahedral and icosahedral particle packings follow a similar evolution with shear strain.

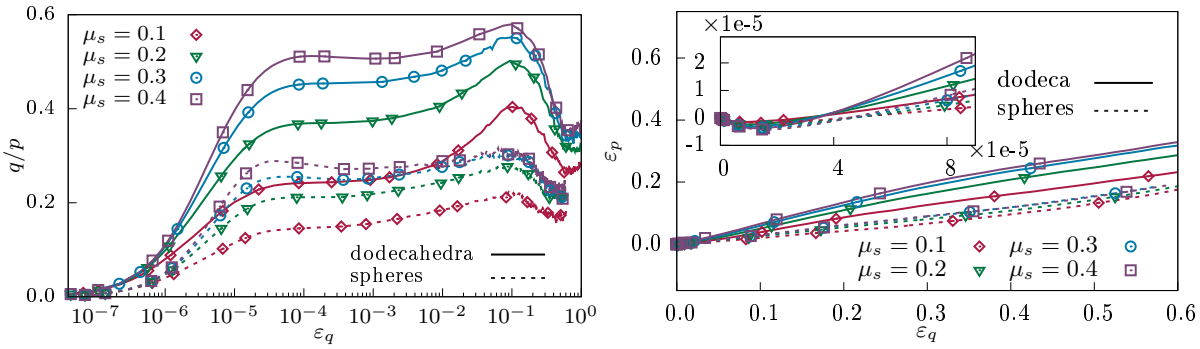

Fig. A-2. (a) Stress ratio q/p versus shear strain ε_q in log-linear scale, (b) cumulative volumetric strain ε_p versus shear strain ε_q in linear scale for packings of dodecahedral and spherical particles with four values of friction coefficient μ_s. The inset shows the same plot in the range $\varepsilon_p < 10^{-4}$. The dashed and solid lines are for spheres and dodecahedra, respectively. Only few data points are shown for the sake of clarity.

We also consider the angle of friction φ expressing the ratio of a shear stress to a normal stress, and can be defined in terms of principal stresses. Combining with Eq. (A.4), we have

$$\sin\varphi = \frac{\sigma_1 - \sigma_3}{\sigma_1 + \sigma_3} = \frac{3q}{2p+q}. \tag{A.6}$$

It is important to note that the definition of the angle of friction remains unchanged for different stress conditions (e.g. triaxial compression, plane strain). The dilation angle, ψ commonly used to represent the dilation characteristic of soil, is defined clearly for plane strain conditions.

However, the extension of the definition of ψ to other than plane strain conditions need to be treated with more care. Although several definition of ψ have been used [301–303] under axi-symmetric loading conditions, the usual definition employed is [301, 304]:

$$\sin\psi = \frac{-(\dot{\varepsilon}_1 + \dot{\varepsilon}_2 + \dot{\varepsilon}_3)}{\dot{\varepsilon}_1 - \dot{\varepsilon}_3} = \frac{-\dot{\varepsilon}_p}{\dot{\varepsilon}_q}. \tag{A.7}$$

The minus sign in Eq. (A.7) arises simply from the convention that compressive stresses and strains ae taken as positive, and is introduced so that the angle of dilation is positive when the sample expands. The superposed dots to indicate the strain rates used in plasticity theory, in which the time increment is artificial. The equation could just as well be expressed in terms of strain increments $\delta\varepsilon$ rather than strain rate $\dot{\varepsilon}$.

The angle of dilation should strictly be defined in terms of the plastic components of the strain rates, not the total strain rates. If the strain rate $\dot{\varepsilon}$ is divided into elastic and plastic components $\dot{\varepsilon} = \dot{\varepsilon}^e + \dot{\varepsilon}^p$ then Eq. (A.7) should be modified to:

$$\sin\psi = \frac{-(\dot{\varepsilon}_1^p + \dot{\varepsilon}_2^p + \dot{\varepsilon}_3^p)}{\dot{\varepsilon}_1^p - \dot{\varepsilon}_3^p}. \tag{A.8}$$

In theory this important distinction means that the determination of the angle of dilation from a test becomes much more difficult, since it depends on the estimate of elastic strains. In practice the distinction is less important since the elastic strains ae much smaller than the plastic strains and the difference between Eqs. (A.7) and (A.8) is small. After stress peak, we assume that elastic strain rates are sufficiently small that Eq. (A.7) can be used with adequate accuracy [301].

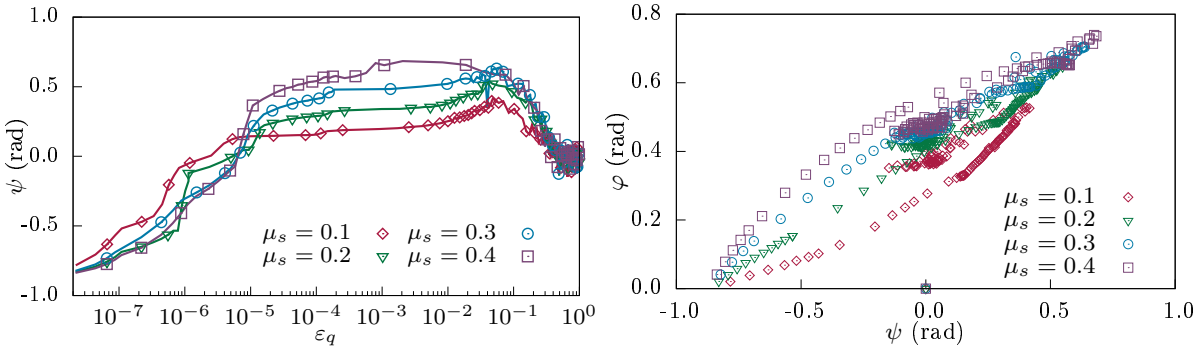

(a) **(b)**

Fig. A-3. (a) The evolution of dilation angle ψ versus shear strain ε_q of dodecahedral particle packings with different values of μ_s. Only few data points are shown for the sake of clarity. (b) The stress-dilatancy diagram representing the relation between the internal angle of friction φ and the dilation angle ψ of dodecahedral particle packings.

The evolution of ψ as a function of shear strain ε_q is shown in Fig. A-3a for the dodecahedral particle packings. We see that ψ increases from a negative value corresponding to a contraction of the packings. It reaches zero at $\varepsilon_q \simeq 5 \times 10^{-6}$, which is a yield of characteristic state of packings. In the first paper, we showed that if $\varepsilon_q \simeq 5 \times 10^{-6}$ the packings undergo elastic

behavior and this means that the strain rate $\dot{\varepsilon}$ is elastic. From Eq. (A.8), ψ in this range should be zero. Then, ψ takes positive values meaning the packings are expanding. It reaches the peak at stress peak and then decreases gradually to zero at residual state of triaxial compression.

The relationship between φ and ψ is illustrated in Fig. A-3b. It is well known that this relation is linear function as following, so called a flow rule [301, 304]:

$$\varphi = m\psi + \varphi_{cv}, \tag{A.9}$$

where φ_{cv} is the critical state friction angle. The subscript "cv" is to indicate that in this case the shearing takes place at constant volume, (e.g. no dilation occurs). The prefactor m is found always smaller than 1. We see that the value of m depends on the friction coefficient and particle shapes. From initial state to characteristic state, we do not consider such relation since the strain tensor are almost elastic as discussed previously. We pay more attention to the stress-dilatancy diagram in post-peak state where plastic strain rate exceeds significantly elastic strain rate. The values of m and φ_{cv} for different μ_s, and particle shapes are shown in Table. A-1.

μ_s	m	φ_{cv}(rad)	φ_{max}(rad)	ψ_{max}(rad)
dodecahedra				
0.1	0.400	0.370	0.528	0.415
0.2	0.388	0.433	0.646	0.549
0.3	0.387	0.461	0.706	0.638
0.4	0.380	0.479	0.740	0.684
icosahedra				
0.1	0.423	0.360	0.519	0.414
0.2	0.414	0.436	0.647	0.529
0.3	0.415	0.470	0.721	0.642
0.4	0.387	0.489	0.751	0.737
octahedra				
0.1	0.861	0.315	0.784	0.648
0.2	0.635	0.415	0.907	0.860
0.3	0.489	0.486	0.950	1.070
0.4	0.403	0.518	0.970	1.528
spheres				
0.1	0.418	0.237	0.305	0.179
0.2	0.382	0.286	0.379	0.375
0.3	0.361	0.305	0.410	0.389
0.4	0.350	0.312	0.415	0.391

Table A-1. The values of parameters in Eq. (A.9) for different particle shapes, friction coefficients for post-peak state of triaxial compression.

Appendix B

Relation between fabric and constraint number

In the presence of steric exclusions, the granular microstructure is highly disordered at the particle scale [305]. For quasi-static state, since the mechanical interactions are governed by contact and friction, the granular microstructure is basically encoded in the force-bearing contact network. At the lowest order, the contact network is characterized by the coordination number Z, which is average number of contacts per particle [24, 306]. While the definition of Z is straightforward in the case of spherical particles, we need to consider the contact types for polyhedral particles. As discussed in Section 2.5, we define a constraint number by

$$Z_c = \frac{2(N_s + 2N_d + 3N_t)}{N_p}, \tag{B.1}$$

where N_s, N_d, N_t are the number of simple, double, and triple contacts, respectively, and N_p is number of particles.

At initial state of triaxial compression meaning in the end of isotropic compaction with zero friction, we see that Z_c jumps from ~ 6 for spherical particle packing to ~ 12 for polyhedral particle packings ($Z_c = 12.07$ for octahedra, $Z_c = 12.05$ for dodecahedra, $Z_c = 12.04$ for icosahedra). This observation is in full agreement with the isostatic nature of our initial packings, in which we expect that $Z_c = 6$ for spheres and $Z_c = 12$ for polyhedra. This is due to the fact that for frictionless polyhedral particles the rotations should be considered as effective degrees of freedom. The values of Z_c in our samples are slightly above the expected values due to the finite confining pressure and overlaps between particles.

Figure B-1 displays the evolution of Z_c during triaxial compression of spherical and dodecahedral particle packings. We see that Z_c is constant and independent of μ_s when shear strains are small ($< 10^{-5}$), due to the stability of the contact network. When particle rearrangement begin to occur, Z_c decreases and tends to a constant value at critical state of compression where the rate of loosing contact equalizes the rate of creating contacts. The variation of Z_c in octahedral and icosahedral particle packings follow the similar evolution.

Granular structure is generically anisotropic due to the relative motions of particles, leading to contacts are gained along the directions of compression and lost along the directions of ex-

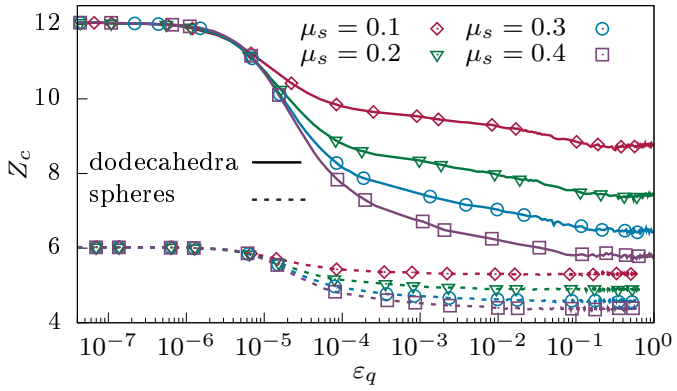

Fig. B-1. Constraint number Z_c versus shear strain ε_q for packings of spherical and dodecahedral particles for different values of friction coefficient μ_s. The dashed and solid lines are for packings of spheres and dodecahedra, respectively. Only few data points are shown for the sake of clarity.

tension. In order to gain further information about the angular positions of contact neighbors, one can rely on the *fabric tensor* $\boldsymbol{F}$ constructed from contact normals $\vec{n}$, or resort to the contact probability density function $P(\vec{n})$ defined as the probability that a contact normal is oriented along $\vec{n}$ [307]. For polyhedral particles, contact normals can be defined at contact points in *contact frame* $(\vec{n}, \vec{t}, \vec{s})$, and also in the frame associated with the branch vector ℓ in *branch vector frame* $(\vec{n}', \vec{t}', \vec{s}')$, as shown in Fig. B-2. These frames are exactly coincident for spherical particles. They are also parallel on average in the case of two convex particles. Indeed, we checked that in our samples, we have $\langle \vec{n} \cdot \vec{n}' \rangle \simeq 1$. Since the anisotropies expressed in the branch frame are simpler, we restrict here our analysis to the branch vector partition.

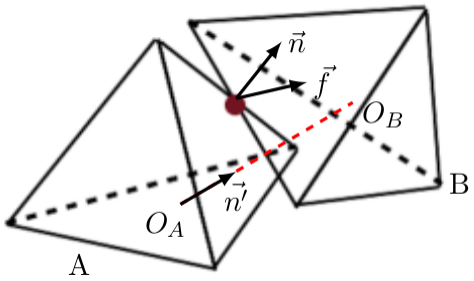

Fig. B-2. Geometry of a contact between two polyhedra. $\vec{n}$ is unit normal vector of contact point, $\vec{n}'$ is unit normal vector of branch length.

In spherical coordinates, unit vector in branch vector frame can be parameterized by the azimuth ϕ and the latitude θ. In general, we have

$$\begin{cases} \vec{n}' = (\cos\theta, \sin\theta\cos\phi, \sin\theta\sin\phi), \\ \vec{t}' = (-\sin\theta, \cos\theta\cos\phi, \cos\theta\sin\phi), \\ \vec{s}' = (0, -\sin\phi, \cos\phi), \end{cases} \tag{B.2}$$

where the angle $\theta \in [0;\pi]$ and $\phi \in [0;2\pi]$. Under axi-symmetric conditions, the probability

density function $P(\vec{n'})$ is independent of the angle ϕ. So within a second-order harmonic approximation, we have

$$P(\vec{n'}) = P(\Omega) = P(\theta) = \frac{1}{4\pi}\left[1 + a_c(3\cos^2\theta - 1)\right], \tag{B.3}$$

where Ω is the solid angle that defines the orientation of $\vec{n'}$, with $d\Omega = \sin\theta d\theta d\phi$, and a_c is contact orientation anisotropy.

In practice, the values of a_c can be more conveniently extracted from the fabric tensor $\boldsymbol{F}$, with

$$F_{ij} = \int_\Omega n'_i n'_j P(\Omega) d\Omega = \frac{1}{N_c}\sum_{c\in V} n'^c_i n'^c_j, \tag{B.4}$$

where i and j design the components in a reference frame, and N_c is the total number of contacts in the control volume V. From Eqs. (B.2), (B.3), and (B.4) the eigenvalues of the fabric tensor are given by

$$\begin{cases} F_1 = \int_\Omega n'^2_1 P(\Omega) d\Omega = \dfrac{5+4a_c}{15}, \\ F_2 = F_3 = \int_\Omega n'^2_2 P(\Omega) d\Omega = \dfrac{5-2a_c}{15}. \end{cases} \tag{B.5}$$

From Eqs. (B.2), (B.3), and (B.5) we have

$$a_c = \frac{5}{4}\langle 3\cos^2\theta - 1\rangle. \tag{B.6}$$

The average $\langle 3\cos^2\theta - 1\rangle$ represents the anisotropy and it may be evaluated either from $P(\Omega)$ or directly from the numerical data. However, the fabric anisotropy easier calculated by using Eq. (B.5) [232, 308]:

$$a_c = 5(F_1 - F_2)/2. \tag{B.7}$$

The largest eigenvalue F_1 occurs along the compression axis, the two other eigenvalues are $F_2 = F_3 = (1 - F_1)/2$. Figure B-3 displays the evolution of a_c during compression. The fabric anisotropy initially increases as a result of the loss of contacts perpendicular to the compression axis. It reaches the peak at stress peak and then decreases gradually to a constant value at critical state of compression. It is larger in packings of polyhedral particles compared to spheres, and its peak value increases with μ_s.

The constraint number Z_c and the fabric tensor can be combined in a single enriched tensor defined by [24]:

$$G_{ij} = \frac{Z_c}{2}F_{ij} = \frac{Z_c}{2}\int_\Omega n'_i n'_j P(\Omega) d\Omega. \tag{B.8}$$

By definition, since $\mathrm{tr}(\boldsymbol{F}) = 1$ we have $\mathrm{tr}(\boldsymbol{G}) = Z_c/2$. We define the following invariant of $\boldsymbol{G}$:

$$\begin{cases} p_G = \dfrac{G_1 + G_2 + G_3}{3} = \dfrac{Z_c}{6}, \\ q_G = \dfrac{G_1 - G_2}{3} = \dfrac{Z_c a_c}{15} \end{cases} \tag{B.9}$$

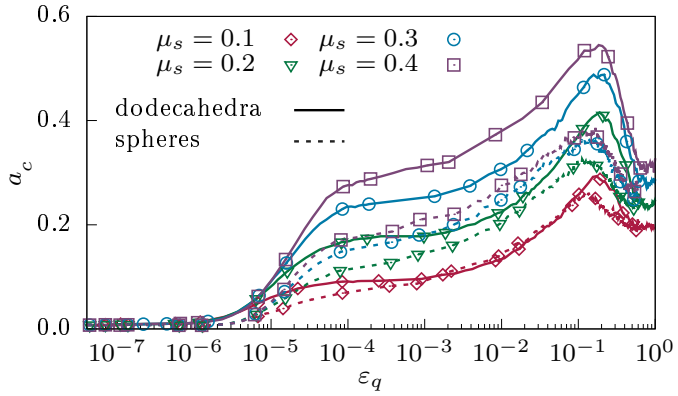

Fig. B-3. Fabric anisotropy a_c versus shear strain ε_q for packings of spherical and dodecahedral particles for different values of friction coefficient μ_s. The dashed and solid lines are for packings of spheres and dodecahedra, respectively. Only few data points are shown for the sake of clarity.

Given its invariant, the enriched fabric tensor $\boldsymbol{G}$ may be represented by a Mohr circle in the space of its normal and tangential projections $G_n(\vec{m}) = \boldsymbol{G}\vec{m}\cdot\vec{m}$ and $G_t(\vec{m}) = \boldsymbol{G}\vec{m}\cdot\vec{t}$, respectively, along arbitrary space direction $\vec{m}$ parameterized by the angle θ. Simple algebra yields

$$\begin{cases} G_n(\theta) = p_G + q_G(3\cos^2\theta - 1), \\ G_t(\theta) = \dfrac{3}{2} q_G \sin 2\theta. \end{cases} \tag{B.10}$$

We assume that Z_c is bounded between two limits $Z_c^{\min}$ and $Z_c^{\max}$. The upper bound $Z_c^{\max}$ is dictated by steric exclusions. The lower bound $Z_c^{\min}$ reflects the condition of mechanical equilibrium. For instance, stable particles often involve more than four contacts in 3D. We define two limit states: (1) the *loosest isotropic state*, characterized by $G_t = 0$ and $G_n^{\min} = Z_c^{\min}/6$, and (2) the *densest isotropic state*, characterized by $G_t = 0$ and $G_n^{\max} = Z_c^{\max}/6$. All accessible fabric states are enclosed between these two limit states, so that $G_1 \leq G_n^{\max}$ and $G_2 \geq G_n^{\min}$. Within this range a_c and Z_c are independent parameters unless one of the two equalities $G_2 = G_n^{\min}$ or $G_1 = G_n^{\max}$ occurs, in which case p_G and q_G may no more evolve independently.

The condition $G_2 = G_n^{\min}$ implies $p_G - q_G = Z_c^{\min}/6$, which together with Eq. (B.9) yields

$$a_c = \frac{5}{2}\left(1 - \frac{Z_c^{\min}}{Z_c}\right). \tag{B.11}$$

This limit corresponds to a *loss saturation* limit where the mechanical equilibrium implies that no contacts may be lost along the direction of extension. In the same way, the condition $G_1 = G_n^{\max}$ implies $p_G + 2q_G = Z_c^{\max}/6$, which together with Eq. (B.9) yields

$$a_c = \frac{5}{4}\left(\frac{Z_c^{\max}}{Z_c} - 1\right). \tag{B.12}$$

This is the *gain saturation* limit where no contacts may be gained along the direction of contraction. Hence, all accessible fabric states in the space (a_c, Z_c) belong to a domain defined

by

$$a_c^{\max}(Z_c) = \min\left[\frac{5}{2}\left(1 - \frac{Z_c^{\min}}{Z_c}\right), \frac{5}{4}\left(\frac{Z_c^{\max}}{Z_c} - 1\right)\right]. \tag{B.13}$$

The largest anisotropy a_c^* occurs when both conditions $G_2 = G_n^{\min}$ and $G_1 = G_n^{\max}$ are satisfied simultaneously. Hence,

$$a_c^* = a_c^{\max}(Z_c^*) = \frac{5}{2}\left(\frac{Z_c^{\max} - Z_c^{\min}}{Z_c^{\max} + 2Z_c^{\min}}\right) \tag{B.14}$$

with

$$Z_c^* = \frac{Z_c^{\max} + 2Z_c^{\min}}{3} \tag{B.15}$$

Figure B-4 shows the joint evolution of a_c and Z_c of dodecahedral particle packings with different values of μ_s during triaxial compression. The solid lines represent the limit states predicted by Eq. (B.13) whose parameters are shown in Table. B-1. The data follow different gain-saturation limit lines with $Z_c^{\max}$ varying between 8.32 and 10.82 for dodecahedral particles.

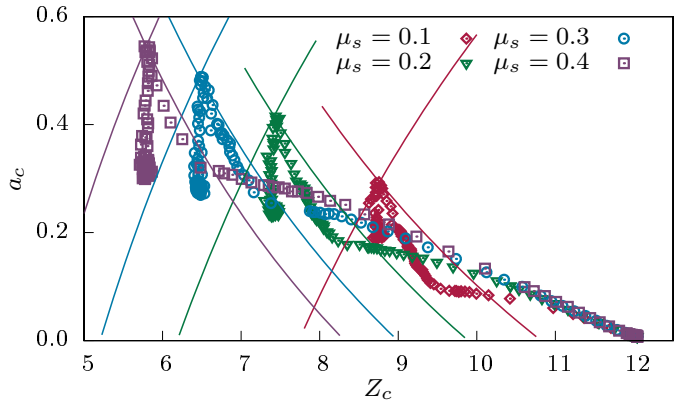

Fig. B-4. Fabric evolution in the (Z_c, a_c) space for dedocahedral particle packings with different values of friction coefficient μ_s. The solid lines represent the limits states predicted by Eq. (B.13).

Figure B-5 shows $Z_c a_c$ as a function of Z_c for dodecahedral particle packings with different values of μ_s. We see that Z_c^* decreases as μ_s increases whereas a_c^* increases nearly as $1/Z_c^*$. We also see that the value of $Z_c a_c$ at critical state seems to be constant.

μ_s	Z_c^*	a_c^*	$Z_c^{\max}$	$Z_c^{\min}$
dodecahedra				
0.1	8.76	0.29	10.82	7.73
0.2	7.42	0.42	9.89	6.19
0.3	6.47	0.49	8.99	5.20
0.4	5.79	0.54	8.32	4.53
icosahedra				
0.1	8.71	0.28	10.68	7.73
0.2	7.40	0.41	9.82	6.18
0.3	6.43	0.49	8.97	5.16
0.4	5.72	0.55	8.22	4.47
octahedra				
0.1	8.93	0.33	11.29	7.74
0.2	7.66	0.53	10.93	6.03
0.3	6.73	0.64	10.19	5.00
0.4	6.01	0.72	9.47	4.28
spheres				
0.1	5.31	0.26	6.42	4.76
0.2	4.90	0.33	6.18	4.26
0.3	4.59	0.36	5.92	3.92
0.4	4.38	0.39	5.73	3.70

Table B-1. The values of parameters in Eq. (B.13) for different particle shapes, friction coefficients.

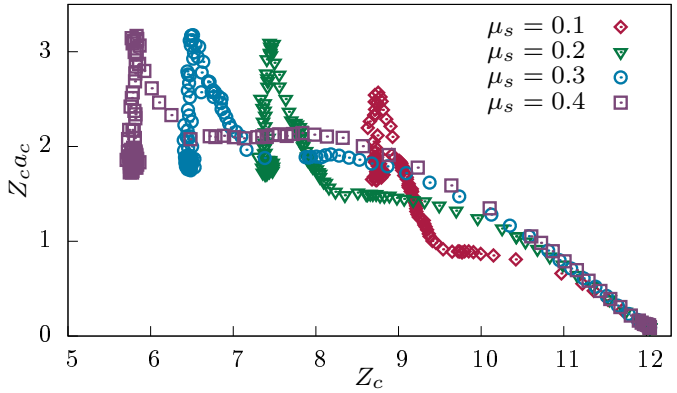

Fig. B-5. Fabric evolution in the (Z_c, a_c) space for dedocahedral particle packings with different values of friction coefficient μ_s.

Appendix C

Weak and strong force networks

As we show in Eq. (A.3), the stress tensor is expressed as an average involving branch vectors and contact forces, so that partial summations allow one to define partial stress tensors that can be used to investigate the scale up of local quantities. For instance, the subset of contacts carrying a force below a threshold reveals the respective roles of weak and strong force chains with respect to the overall shear strength of granular material [232, 309]. In this section, this methodology is applied to analyze the stress and anisotropy parameters in view of elucidating the effect of faceted particle shapes.

We consider various fabric and force parameters for the ξ networks defined as the subsets $\mathscr{S}(\xi)$ of contacts which carry a force below a cutoff force ξ normalized by the mean force ($f_n/\langle f_n \rangle \in [0,\xi]$), where ξ is varied from 0 to the maximal force in the system. The weak network corresponds to $\mathscr{S}(1)$ whereas the strong network is its complement.

In Eq. (B.3), we define the probability distribution of the contact normal $P(\vec{n'})$ as a function of angle θ. In a similar vein, the distribution of the contact normal in a subset $\mathscr{S}(\xi)$ also can be defined by

$$P(\theta,\xi) = \frac{1}{4\pi}\left[1 + a_c(\xi)(3\cos^2\theta - 1)\right], \tag{C.1}$$

where $a_c(\xi)$ is the amplitude of contact anisotropy in the ξ network. The fabric tensor of subset $\mathscr{S}(\xi)$ is given by

$$F_{ij}(\xi) = \int_\Omega n'_i n'_j P(\theta,\xi) d\Omega. \tag{C.2}$$

As a result, the contact anisotropy in the ξ network is given by

$$a_c(\xi) = 5(F_1(\xi) - F_2(\xi))/2. \tag{C.3}$$

Figure C-1 displays the amplitude of contact anisotropy a_c in the ξ network as a function of ξ for different values of friction coefficient for dodecahedral and spherical particle packings. In polyhedral particle packings when the values of μ_s is small, the anisotropy of weak contacts is negative but increases in absolute value and reaches its peak value at $\xi \simeq 0.5$, see Fig. C-1a, which is different compared to $\xi \simeq 1$ in 2D spherical particle packings [232, 309]. This negative value indicated that in low friction coefficient packings the weak contacts are oriented preferentially perpendicular to the major principal stress direction. As more contacts come

into play with increasing ξ, the partial anisotropy $a_c(\xi)$ becomes less negative and finally get the positive value. This means that the strong contacts are mainly oriented along the major principal stress direction. We also see that this bimodal behavior of stress transmission holds in the packing of spherical particles, see Fig. C-1b.

Interestingly, for bigger values of μ_s in polyhedral particle packings the partial anisotropies of weak networks become positive, as observed in Fig. C-1a. This means that the weak and strong contacts in polyhedral particle packings of high μ_s cannot be differentiated on the basis of their roles in the ξ networks. Physically, this behavior can be interpreted by the fact that the static equilibrium of the networks of polyhedral particles does not require the stabilizing effect of the weak contacts. However, for spherical particle packings the friction coefficient plays no significant role in the evolution of partial anisotropy of weak networks. The value of $a_c(\xi)$ is always negative if $\xi < 1$, as shown in Fig. C-1b. This means that the networks of spheres always require the stabilizing effect of the weak contacts.

The effects of friction coefficient are more pronounced in polyhedral particle packings than those in spherical particle packings due to the appearance of face-face contacts. The friction affects not only on magnitude of the fabric anisotropy in whole networks ($\xi = \infty$), but also on partial anisotropy of weak networks ($\xi < 1$). On the one hand the face-face contacts, which is strong networks, in polyhedral particle packings are more stable. On the other hand if friction coefficient is sufficient high, the strong networks can stand along compression axis without the weak contacts along lateral axis.

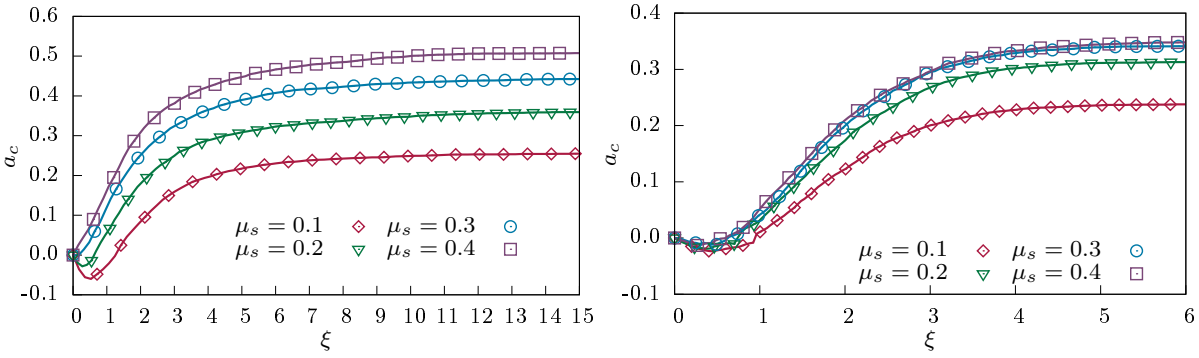

Fig. C-1. Partial fabric anisotropy a_c as a function of force cutoff ξ normalized by the mean force for different values of friction coefficient μ_s of dodecahedral particle packings (a), and spherical particle packings (b) in configuration before stress peak.

The partial force anisotropies can be defined by considering the angle average normal and tangential forces, $\langle f_n\rangle(\theta,\xi)$ and $\langle f_t\rangle(\theta,\xi)$, in the ξ network. A second-order Fourier expansion provides an adequate representation of these distributions for all values of ξ.

$$\begin{cases} \langle f_n\rangle(\theta,\xi) = \langle f_n\rangle(\xi)\left[1 + a_n(\xi)(3\cos^2\theta - 1)\right], \\ \langle f_t\rangle(\theta,\xi) = \langle f_t\rangle(\xi) a_t(\xi)\sin 2\theta, \end{cases} \tag{C.4}$$

where $a_n(\xi)$ and $a_t(\xi)$ are the amplitude of normal and tangential force anisotropies in the ξ

network. In practice, the anisotropy parameters can be calculated by means of the following force tensors

$$\begin{cases} \chi_{ij}^{f_n}(\xi) = \int_\Omega \langle f_n \rangle(\theta,\xi) n_i' n_j' P(\theta,\xi) d\Omega, \\ \chi_{ij}^{f_t}(\xi) = \int_\Omega \langle f_t \rangle(\theta,\xi) n_i' t_j' P(\theta,\xi) d\Omega. \end{cases} \tag{C.5}$$

With these definitions, the following relationship can be established

$$\begin{cases} a_n(\xi) = 2.5(\chi_1^{f_n}(\xi) - \chi_2^{f_n}(\xi)) - a_c(\xi), \\ a_t(\xi) = 2.5(\chi_1^{f}(\xi) - \chi_2^{f}(\xi)) - a_c(\xi) - a_n(\xi), \end{cases} \tag{C.6}$$

where $\chi_{ij}^{f}(\xi) = \chi_{ij}^{f_n}(\xi) + \chi_{ij}^{f_t}(\xi)$ and the indices 1, 2, and 3 refer to the principal values of each tensor.

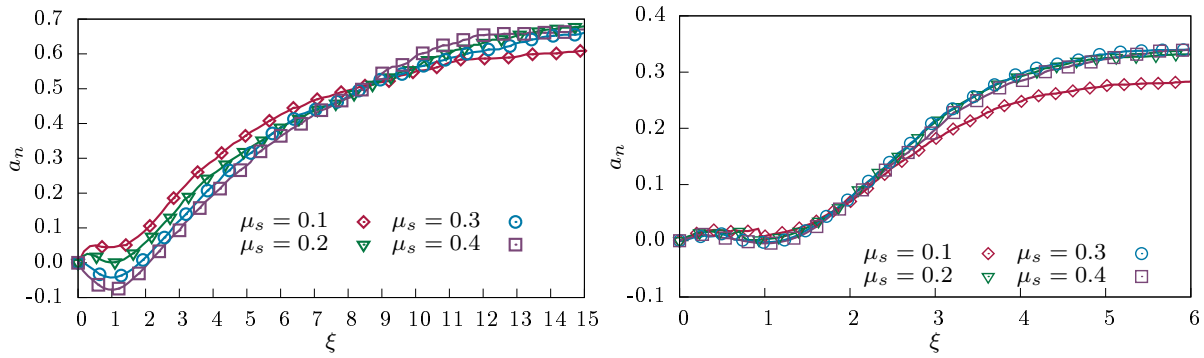

(a) **(b)**

Fig. C-2. Partial normal force anisotropies as functions of force cutoff ξ normalized by the mean force for different value of friction coefficient μ_s in dodecahedral particle packings (a), and spherical particle packings (b) in configuration before stress peak.

Figure C-2 illustrates the normal and tangential force anisotropies as functions of ξ for all value of μ_s in dodecahedral particle packings. A remarkable feature of $a_n(\xi)$ is that its value is negative in the weak network for packing with high value of μ_s, and is positive for those of small value of μ_s. Hence, the weak forces in a packing with high μ_s occur at contacts preferentially oriented orthogonally to the principal stress direction, whereas in a packing of small μ_s they are parallel. As we see before, an inverse behavior take places for the contact anisotropies. The weak contacts in the packings with high μ_s are parallel to the principal stress direction and orthogonal for packings of small μ_s. In the assemblies of high μ_s, $a_n(\xi)$ reaches the negative peak at $\xi \simeq 1$, then increases as more contacts from the strong network with a positive contribution to the anisotropy are included in the ξ network. $a_n(\xi)$ becomes positive value at $\xi \simeq 2$ as the strong forces tend to parallel to the principal stress direction. The tangential force anisotropy $a_t(\xi)$ is always positive and increasing for both ξ and μ_s.

The branch vector $\vec{\ell} = \ell\vec{n}'$ in $(\vec{n}', \vec{t}', \vec{s}')$ frame. We introduce here its truncated expansion on a Fourier basis:

$$\langle \ell \rangle(\theta,\xi) = \langle \ell \rangle(\xi) \left[1 + a_y(\xi)(3\cos^2\theta - 1)\right], \tag{C.7}$$

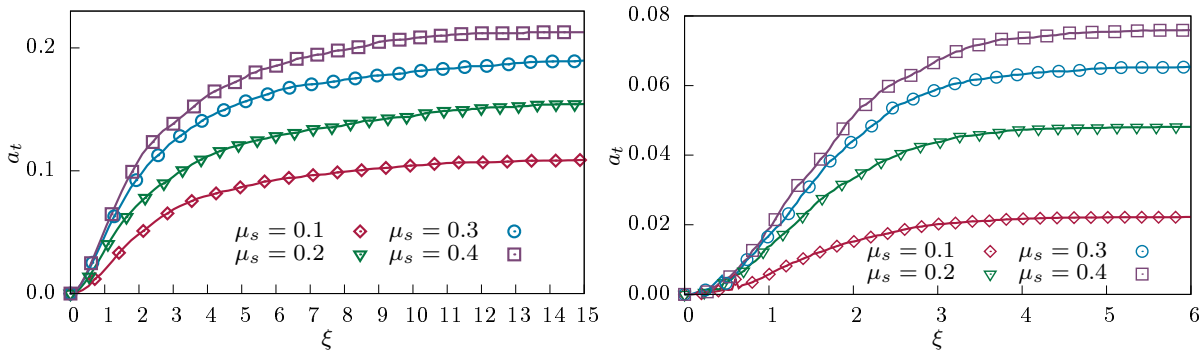

(a) **(b)**

Fig. C-3. Partial tangential force anisotropies as functions of force cutoff ξ normalized by the mean force for different value of friction coefficient μ_s in dodecahedral particle packings (a), and spherical particle packings (b) in configuration before stress peak.

where $a_y(\xi)$ is the branch anisotropy in the ξ networks. For calculation of $a_y(\xi)$, we introduce the following branch tensor:

$$\chi^{\ell}_{ij}(\xi) = \int_{\Omega} \langle \ell \rangle(\theta,\xi) n'_i n'_j P(\theta,\xi) d\Omega, \tag{C.8}$$

The following relations are then easily obtained:

$$a_y(\xi) = 2.5(\chi^{\ell}_1(\xi) - \chi^{\ell}_2(\xi)) - a_c(\xi), \tag{C.9}$$

Figure C-4 shows the branch vector anisotropy as a function of ξ in dodecahedral particle packings with different values of μ_s. From weak to strong networks, $a_y(\xi)$ is always negative although its absolute value is much smaller than the fabric or force anisotropies. Note that for spherical particle packings, the value of $a_y(\xi)$ is even smaller and close to zero.

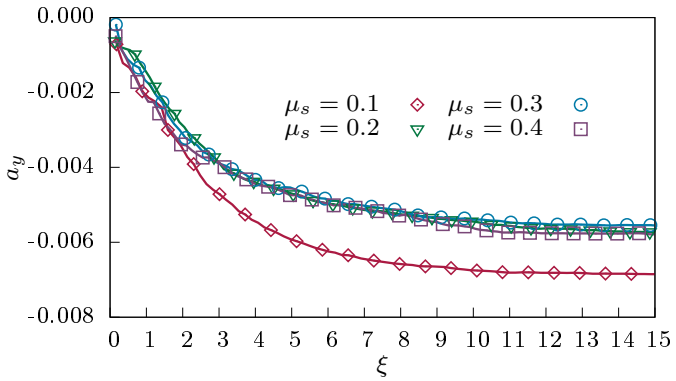

Fig. C-4. Partial branch anisotropy as a function of ξ for all value of friction coefficient μ_s in dodecahedral particle packings in configuration before stress peak.

Since the stress tensor is a function of forces and branch vectors, as shown in Eq. (A.3). We also can define the partial stress tensor of ξ network by restricting the summation to the corresponding contacts

$$\sigma_{ij}(\xi) = \frac{1}{V} \sum_{c \in V} f^c_i(\xi) \ell^c_j(\xi). \tag{C.10}$$

From Eq. (C.10), we define deviatoric stress in the ξ network

$$q(\xi) = (\sigma_1(\xi) - \sigma_3(\xi))/3. \tag{C.11}$$

The partial stress ratio $q(\xi)/p$ as a function of ξ is displayed in Fig. C-5. We see that $q(\xi < 1)/p$ is zero for the packing of $\mu_s = 0.1$, implying that strong forces carry the whole deviatoric load. The partial stress ratio $q(\xi = 1)/p$ in the weak network increases slightly with μ_s but remains small value, below 0.05, in all cases. The weak value of $q(\xi)/p$ in the weak network is a consequence of the opposite sign of $a_c(\xi = 1)$ and $a_n(\xi = 1)$, together with small value of $a_t(\xi = 1)$.

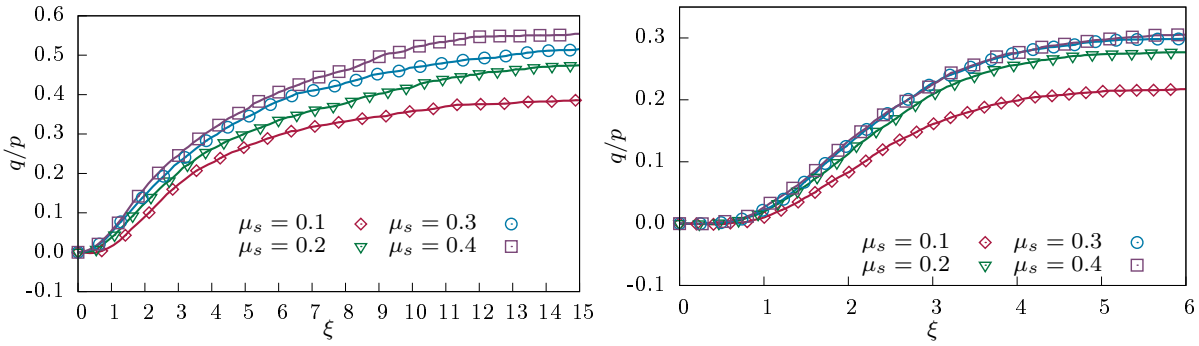

(a) **(b)**

Fig. C-5. Partial stress ratio as a function of ξ for all value of friction coefficient μ_s in dodecahedral particle packings (a), and spherical particle packings (b) in configuration before stress peak.

Appendix D

Different definitions of fabric anisotropy

As discussed previously, the contacts between polyhedra are divided into three types: simple, double and triple contacts. From Eqs. (B.4) and (B.1), we define a fabric tensor that takes into account contact types in branch vector frame:

$$F'_{ij} = \frac{1}{N_s + 2N_d + 3N_t} \sum_{c \in V} h n'^c_i n'^c_j, \tag{D.1}$$

where $h = 1$, 2, and 3 for simple, double, and triple contacts, respectively. By definition, we also have $\mathrm{tr}(\boldsymbol{F'}) = 1$, and due to axi-symmetry the principal values $F'_2 = F'_3 = (1 - F'_1)/2$. As a result, the contact orientation anisotropy calculated by tensor $\boldsymbol{F'}$ is defined by:

$$a'_c = 5(F'_1 - F'_2)/2. \tag{D.2}$$

Since most triple contacts are strong networks and oriented along compression axis, we expect that $a'_c > a_c$.

Another fabric tensor should be considered in the contact normal frame $(\vec{n}, \vec{t}, \vec{s})$, as shown in Fig. B-2. From Eq. (B.4), we define a fabric tensor by:

$$F^*_{ij} = \frac{1}{N_c} \sum_{c \in V} n^c_i n^c_j, \tag{D.3}$$

By definition and under axi-symmetry conditions, we also have $F^*_2 = F^*_3 = (1 - F^*_1)/2$. As a consequence, the contact orientation anisotropy corresponding to $\boldsymbol{F}^*$ is given by

$$a^*_c = 5(F^*_1 - F^*_2)/2. \tag{D.4}$$

Each contact between two polyhedra may involve several contact points as discussed previously. The normal and tangential vectors at each contact point are parallel with the frame $(\vec{n}, \vec{t}, \vec{s})$. We define a fabric tensor calculated from all contact points

$$\tilde{F}_{ij} = \frac{1}{N_{cp}} \sum_{cp \in V} n^{cp}_i n^{cp}_j, \tag{D.5}$$

where N_{cp} is number of contact points, the superscript "cp" is to indicate contact points. We also have the relation $\tilde{F}_2 = \tilde{F}_3 = (1 - \tilde{F}_1)/2$, and the contact anisotropy in this case is given by

$$\tilde{a}_c = 5(\tilde{F}_1 - \tilde{F}_2)/2. \tag{D.6}$$

Corresponding to each definition of fabric tensor, we define also normal, tangential force, and branch tensors in the same way. Note that we keep $\boldsymbol{\chi}'^{f_n} = \boldsymbol{\chi}^{f_n}$, $\boldsymbol{\chi}'^{f_t} = \boldsymbol{\chi}^{f_t}$, and $\boldsymbol{\chi}'^{\ell} = \boldsymbol{\chi}^{\ell}$ due to the fact that the effect of contact types is already involved in the magnitude of the forces and the branch vector length. In the same vein, we define normal force, tangential force, and branch anisotropy as following

$$\begin{cases} \hat{a}_n = 2.5(\hat{\chi}_1^{f_n} - \hat{\chi}_2^{f_n}) - \hat{a}_c, \\ \hat{a}_t = 2.5(\hat{\chi}_1^{f} - \hat{\chi}_2^{f}) - \hat{a}_c - \hat{a}_n, \\ \hat{a}_y = 2.5(\hat{\chi}_1^{\ell} - \hat{\chi}_2^{\ell}) - \hat{a}_c, \end{cases} \tag{D.7}$$

where $\hat{a}_c$ represents for a'_c, a^*_c, $\tilde{a}_c$; $\hat{a}_n$ represents for a'_n, a^*_n, $\tilde{a}_n$; $\hat{a}_t$ represents for a'_t, a^*_t, $\tilde{a}_t$, and $\hat{a}_y$ represents for a'_y, a^*_y, $\tilde{a}_y$ in its context.

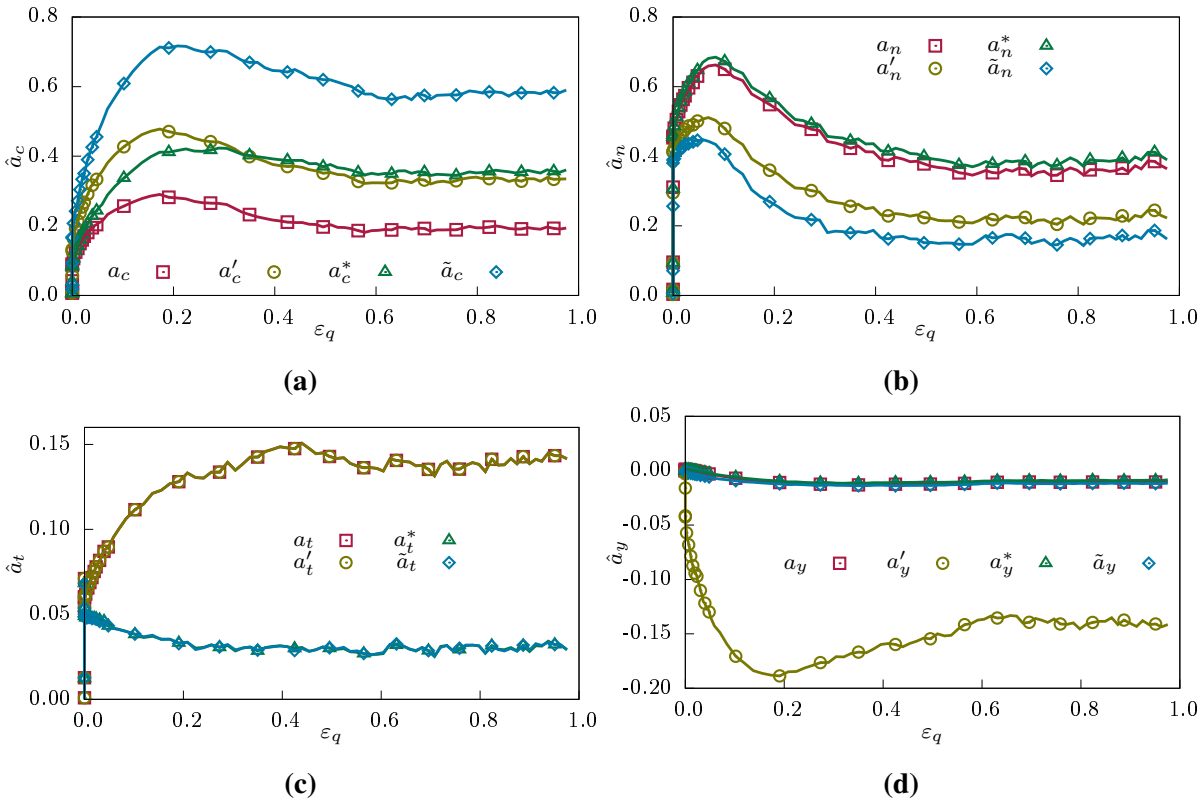

Fig. D-1. Different definition of anisotropy in dodecahedral particle packings as a function of shear strain ε_q with friction coefficient $\mu_s = 0.1$.

Figure D-1 describes the evolution of different anisotropy as a function of shear strain ε_q in dodecahedral particle packings with $\mu_s = 0.1$. The evolution of anisotropies in the packings of other particle shapes and other values of friction coefficient is similar.

Neglecting cross products between all anisotropies, we get the following relation [22, 310, 311]:

$$\frac{q}{p} = \frac{2}{5}(\hat{a}_c + \hat{a}_n + \hat{a}_t + \hat{a}_y). \tag{D.8}$$

As shown in Fig. D-2 this relation is held only for combination of a_c, a_n, a_t, and a_y. As a result,

the anisotropies should be calculated in the branch vector frame and without accounting contact types.

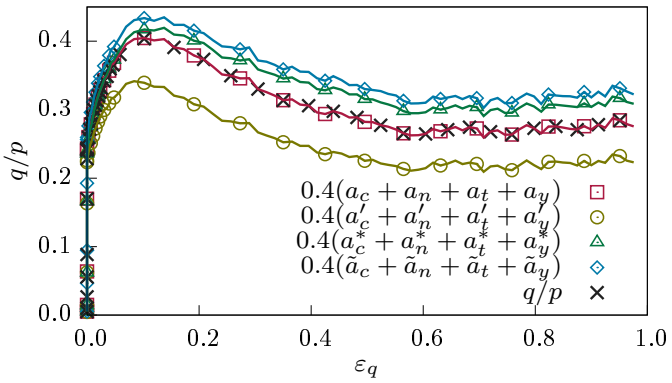

Fig. D-2. Relationship between stress ratio q/p and anisotropy in dodecahedral particle packings as a function of shear strain ε_q with friction coefficient $\mu_s = 0.1$.

Summary in French

Contexte général de la thèse

Afin d'améliorer les performances des poudres broyées tout en minimisant les coûts énergétiques il est nécessaire de se pencher sur le procédé de broyage qui devient aujourd'hui un sujet majeur de recherche. La complexité des phénomènes mis en jeux dans les tambours rotatifs à deux origines principales. La première réside dans la nature dynamique et inhomogène des flux résultant de la géométrie de tambour. Ces flux de particules dépendent de nombreux paramètres procédés comme la vitesse de rotation, le degré de remplissage, la taille des particules, la taille du tambour, ainsi que le nombre et la taille de boulets. Le second facteur est la complexité du matériau composé de particules de formes et de tailles diverses interagissant par le biais d'interactions cohésives et frictionnelles. Les travaux antérieurs dans le domaine sont en général largement empiriques et les phénomènes d'écoulement à l'intérieur de tambours rotatifs et à fortiori les phénomènes de commutation restent mal compris. Ces travaux ne permettent pas, par exemple, un changement d'échelle ou une augmentation du taux de fragmentation en s'appuyant sur l'optimisation des paramètres de ces études. Cependant, les contraintes de sécurité sur la mise en œuvre des matières nucléaires ne cessent de croître et il devient très difficile de multiplier les expériences. Par exemple seuls de petites quantités de matière peuvent être conservées dans des conditions contrôlées, nécessitant un environnement confiné et un équipement dédié pour éviter toute forme de contamination.

Dans ces conditions, les simulations dynamique de particules basées sur la méthode des éléments discrets (DEM) constituent un outil précieux pour l'étude détaillée des mécanismes physiques impliqués dans le processus de broyage. Néanmoins, cette étude nécessite des modèles physique précis du matériau et des calculs haute performance permettant une représentation significative du matériau granulaire. Dans des études numériques antérieures (thèse L. Orozco 2016-2019 [7]), une approche a été développée pour modéliser la fragmentation dynamique des particules en 3D et la fracture d'une seule particule a été étudiée. La méthode numérique utilisée alors appelée Dynamique des Contacts, est basée sur la modélisation non régulière des contacts frictionnels avec une intégration implicite des équations de mouvement. Son utilisation pour les simulations de broyage dans des tambours rotatifs a été limitée par les difficultés d'une parallélisation efficace. Il a toutefois été montré que la méthode des cellules liées (Bonded Cell Method) avec un critère de rupture basé sur l'énergie de rupture permet d'obtenir une rupture de particules réaliste et évolutive. Les études 3D ont été limitées aux particules sphériques dans

des tambours rotatifs pour la mise à l'échelle des flux en cascade. Le processus de broyage a également été étudié en 2D avec des particules polygonales cassables. Plusieurs relations entre le profil de la surface, l'épaisseur de la couche active, le glissement sur les parois et la variabilité des forces ont été identifiées, et un nouveau paramètre d'échelle a été proposé pour le taux de rupture et les caractéristiques de l'écoulement. Ces résultats mettent déjà en perspective certaines observations expérimentales qui étaient mal comprises jusqu'ici et montrent que les simulations d'écoulements granulaires avec rupture dans des tambours rotatifs constituent un moyen puissant d'étude des processus de broyage.

Organisation générale de la thèse

Ce travail de thèse, qui représente une extension du travail précédent, a pour but de développer un modèle DEM pour l'étude des écoulements granulaires quasistatiques et dynamiques de particules de formes polyédriques tout en intégrant une rupture potentielle de ces particules pour la simulation du processus de broyage en tambours rotatifs. Pour améliorer les performances de calcul, et permettre des simulations massivement parallèles, une approche alternative à celle introduite dans la thèse de L. Orozco à été mise en oeuvre. De nouveaux développements numériques ont été nécessaires dans le but de reformuler le modèle de fragmentation des particules en tenant compte de leur forme et de l'énergie de rupture dans ce nouveau cadre. Pour cela nous nous sommes appuyés sur le code de calcul *Rockable*, développé par V. Richefeu à Grenoble et mis à disposition dans le cadre d'un projet collaboratif impliquant quatre institutions (CNRS, CEA, INRAE et Université de Montpellier). Les éléments clés de ce code sont 1) la représentation de particules de formes arbitraires sous forme de sphéro-polyèdres, 2) un algorithme de détection des contacts efficace, et 3) la différenciation explicite des différents types de contacts (face-face, face-arête) entre polyèdres. Pour réduire encore plus le temps de calcul, de nouveaux développements ont été nécessaires au cours de ce travail de doctorat comme par exemple : l'optimisation de la procédure de détection des contacts (entre les parois cylindriques du tambour rotatif et les polyèdres, par exemple) ou, la mise en œuvre de conditions aux limites tri-périodiques avec possibilité de contrôler le déplacement ou la pression dans chaque direction de l'espace. Des conditions limites périodiques ont également été implémentées le long de l'axe du tambour rotatif.

Dans la continuité de la thèse de L. Orozco, des simulations paramétriques détaillées ont été réalisées pour mettre à l'échelle des caractéristiques essentielles de l'écoulement dans la géométrie de tambour. Ces caractéristiques sont l'épaisseur de l'écoulement dans la couche active, la forme de la surface libre et le nombre inertiel dans la couche en écoulement. Comme les particules polyédriques sont utilisées pour la première fois pour cette analyse, nous avons comparé la loi d'échelle avec les données de L. Orozco obtenues pour des particules sphériques dans le régime de cascade. On pourra noter que comme notre méthode de simulation diffère de celle utilisée par L. Orozco, la comparaison porte également sur les méthodes numériques. Enfin, une autre nouveauté de notre étude est l'inclusion d'un argument du type "particle-coarsening"

pour expliquer la dérivation de la loi d'échelle.

Une partie de ce travail de thèse est consacré aux déformations quasi-statiques de matériaux granulaires composés de particules polyédriques. Nous utilisons des conditions aux limites tri-périodiques pour étudier le comportement quasi-statique de plusieurs formes de particules polyédriques (octaèdres, dodécaèdres, icosaèdres) ainsi que des particules sphériques. Pour la première fois, les cinq modules élastiques orthotropes sont évalués en cours de compression triaxiale en appliquant des sondes en petites déformations sur des intervalles réguliers d'évolution des échantillons. Pour quatre valeurs de coefficient de frottement entre particules, nous analysons l'évolution de la microstructure et ses corrélations avec les différents modules élastiques. Nos résultats mettent clairement en évidence le rôle du nombre de coordination et de l'anisotropie de fabrique ainsi que l'effet de la forme des particules à travers plusieurs paramètres impliqués dans la corrélation linéaire entre les modules élastiques et la microstructure. Ces résultats sont comparés aux prédictions de la théorie des milieux effectifs (effective medium theory) que nous appliquons à notre configuration triaxiale. Bien que l'étude des conditions quasi-statiques ne soient pas directement liées à la problématique du broyage en tambours tournant, celle-ci fournit un cadre l'analyse, dans l'étape suivante, de la fragmentation des particules et ses conséquences sur la rhéologie dans des conditions limites périodiques. De plus, l'état passif dans le tambour se fait à déformation quasi-statique et un aspect important du broyage concerne précisément la fragmentation autogène des particules dans cette zone. Enfin, la fragmentation quasi-statique des particules est également impliquée dans certains procédés et a un intérêt particulier pour la comparaison entre des simulations et des expériences tomographiques nécessairement lentes, en vue de la validation et/ou à l'étalonnage du modèle de rupture.

Pour la fragmentation des particules, nous avons développé un nouveau modèle qui s'inscrit dans le cadre des méthodes de type "cellules liées" (Bonded Cell Method). Dans cette méthode, les particules sont décomposées en cellules irrégulières convexes obtenues sur la base d'une tessellation irrégulière. Dans cette méthode une décohésion peut apparaitre aux niveaux des interfaces entre cellules selon les conditions dictées par un modèle de rupture. Si un avantage de la méthode des cellules liées est de prendre en compte la distribution des contraintes à l'intérieur de chaque particule, son succès réside essentiellement dans la versatilité avec laquelle peut être implémenté le modèle de rupture. Dans cette thèse, ce dernier est basé sur l'énergie de rupture et est équivalent au critère de Griffith pour la propagation des fissures. Les liaisons face à face entre cellules sont modélisées comme des points de contact multiples au niveau desquels des liaisons linéaires (ressorts) sont implémentés. L'énergie élastique totale de traction stockée dans ces ressorts est comparée à l'énergie de rupture de l'interface et celle-ci est rompue si l'énergie élastique dépasse l'énergie de rupture. Une étude paramétrique détaillée de la rupture de particules uniques a été réalisée et comparée avec des résultats issus des travaux de L. Orozco. La mise à l'échelle du coefficient de restitution effectif et de l'énergie totale dissipée par la rupture en fonction de la vitesse d'impact et de l'énergie de rupture est au centre de ce travail.

Cette thèse de doctorat est organisée en plusieurs chapitres. Une revue de la littérature sur

les matériaux granulaires ainsi que des éléments concernant la méthodologie numérique sont présentées dans le chapitre 1. Les propriétés physiques et mécaniques des écoulements granulaires sont abordés pour des conditions aux limites de type volume élémentaire représentatif (VER) et tambours rotatifs. Nous présentons également plusieurs résultats importants, issus d'études antérieurs, concernant le processus de fragmentation des particules.

Dans le chapitre 2, l'effet de la forme de particule facetisées sur le comportement élastique d'assemblages granulaires est étudiée. Cette étude s'appuie sur des simulations dynamique basées sur la méthode des éléments discrets (DEM). En comparant les données de simulation avec la théorie des milieux effectifs, nous proposons une expression analytique générale qui prédit avec précision les modules élastiques en fonction de deux paramètres microstructuraux : 1) un nombre de contrainte ou "constraint number" qui tient compte des types de contact (contacts face-face et face-arête entre polyèdres) et qui est réduit à un nombre de coordination pour les particules sphériques, et 2) l'anisotropie de l'orientation des contacts. Cette expression quantifie à la fois l'effet direct de la forme des particules à travers les paramètres de notre modèle et l'effet indirect à travers la microstructure.

Dans le chapitre 3, nous étudierons la rhéologie et la mise à l'échelle des écoulements granulaires dans un tambour tournant partiellement rempli de particules polyédriques. La méthode utilisée est la même que celle présentée au chapitre 2 et qui a servi de base à une étude paramétrique détaillée sur une large gamme de valeurs de diamètre de tambours, de diamètre de particules, de vitesse de rotation et de degré de remplissage. Le régime de cascade sera étudié en détail en raison de son rôle important dans les processus industriels et de l'absence d'analyse systématique de ses variables d'influence. Un paramètre d'échelle sans dimension, qui tient compte de l'effet de tous les paramètres du système, sera proposé. Il résulte d'une analyse détaillée des variables d'écoulement telles que les pentes moyennes et maximales de la surface libre, l'épaisseur de la zone d'écoulement, le taux de cisaillement et le nombre d'inertie dans la couche d'écoulement. Enfin, ce chapitre présente la méthode de particle-coarsening et sa pertinence dans la mise à l'échelle des variables d'écoulement.

Dans le chapitre 4, en s'appuyant sur la méthode des cellules liées, nous analyserons la fragmentation sous impact de particules uniques. Un modèle de rupture entièrement basé sur l'énergie de fracture est introduit. Dans ce modèle les interfaces cellule-cellule se rompent si l'énergie élastique stockée à l'échelle de l'interface dépasse son énergie spécifique de fracture. Nous analysons le processus de fragmentation ainsi que les régimes distincts de rupture. La transition entre ces régimes sera étudiée en fonction des variables impliquées dans la rupture telles que le coefficient de restitution, l'endommagement des particules et l'efficacité de la fragmentation. Nous proposons également des modèles analytiques prédisant les tendances de l'évolution des variables de rupture en fonction de l'énergie d'impact. Enfin, nous étudions la distribution des masses de ces fragments en fonction de l'énergie de rupture.

Enfin, dans le dernier chapitre qui conclu cette thèse, les principaux résultats sont rappelés et quelques perspectives de ce travail de doctorat sont évoquées.

Principales conclusions

L'objectif principal de la thèse a été de mettre en oeuvre une approche DEM avancée pour l'étude des écoulements granulaires de particules de forme polyédrique (en situation quasistatiques et dynamiques) et pour modéliser le processus de broyage en considérant la rupture des particules dans une géométrie de tambours tournant. L'ensemble des développements et des simulations numériques ont été réalisés sur la base du code Rockable développé en collaboration avec Vincent Richefeu à l'Université Grenoble Alpes. Parmi les améliorations remarquable, on peu citer l'optimisation de la détection de contacts au niveau des parois cylindriques du tambour rotatif, l'implémentation de conditions aux limites tripériodiques (avec possibilité de contrôler le déplacement ou la pression dans chaque direction de l'espace), l'ajout de conditions périodiques selon l'axe du tambour. Enfin, la parallélisation du code de calcul s'est montrée particulièrement efficace permettant des simulations sur un nombre important de processeurs et des études paramétriques de grande ampleur.

Nous nous sommes concentrés en particulier sur 1) le comportement élasto-plastique et sa relation avec l'évolution de la microstructure dans le cas d'échantillons composés de particules sphériques ou polyédriques en conditions aux limites tri-périodiques; 2) la mise à l'échelle, dans le régime de cascade, des écoulements de particules polyédriques en tambour rotatif; 3) la dynamique de rupture d'une seule particule polyédrique. La méthodologie développée pour la simulation, l'analyse micromécanique et le changement d'échelle, jette les bases d'une approche de simulations 3D dynamique réaliste permettant l'analyse détaillée des processus de broyage avec de nombreuses applications potentielles aux technologies des poudres en général et aux procédés de fabrication du combustible nucléaire en particulier. L'objectif final est de fournir un cadre générique combinant simulations mécaniques discrètes et analyse physique afin d'optimiser les propriétés de poudres de compositions complexes tout en minimisant les coûts énergétiques.

Dans l'analyse du comportement élastique des assemblage de particules sollicités en conditions triaxiales, nous avons constaté que les modules élastiques orthotropes peuvent être exprimés comme une fonction des variables associées au réseau de contact telles que la connectivité et l'anisotropie de l'orientation des contacts. L'expression générale proposée ne dépend pas directement de la forme des particules, mais implique des coefficients qui eux en dépendent. Leur détermination permet une prédire de l'évolution des modules élastiques en fonction de la déformation. En outre, cette expression révèle trois origines différentes du comportement élastique dépendants : d'une partie isotrope, d'une partie anisotrope et d'une échelle de contrainte. Cette dernière est associée au modèle de force, et sa valeur est simplement donnée par le rapport entre la rigidité de contact et le diamètre des particules. Nous avons comparé les modules élastiques avec les prédictions de la théorie des milieux effectifs et discuté des différences et similitudes entre ces modèles. Par exemple, la forme des particules influence les modules élastiques à travers des paramètres de notre modèle ne dépendant pas directement du coefficient de frottement mais qui sont liés au champ de déplacement non affine et à ses conséquences sur

le réseau de contact (qui lui dépend du coefficient de frottement). Nous avons également montré que le niveau de non-affinité est le même pour toutes les formes simulées pendant la compression, ce qui vient étayer des valeurs constantes des paramètres pour le modèle. Cette expression révèle également la façon dont les contacts face-face et face-arête renforcent le module élastique par rapport au cas de particules sphériques.

L'influence de la forme des particules sur le régime d'écoulement en cascade dans les tambours tournants a été étudiée en détail. Un étude paramétrique a été réalisée pour une large gamme de valeurs de vitesse de rotation, diamètre du tambour, diamètre des particules et de degré de remplissage. Grâce à une analyse détaillée des variables d'écoulement telles que les pentes moyennes et maximales de la surface libre, l'épaisseur de l'écoulement, le taux de cisaillement et le nombre d'inertie dans la couche active, nous avons trouvé un paramètre d'échelle sans dimension unique combinant le nombre de Froude, le rapport entre le diamètre du tambour et celui de la particule et le degré de remplissage. Nous avons montré que ce paramètre d'échelle fonctionne également pour les particules sphériques, mettant ainsi en évidence l'effet de la forme polyédrique des particules. Nous avons également analysé l'effet de "particle-coarsening" des particules et nous avons montré qu'il est cohérent avec notre mise à l'échelle des différentes variables d'écoulement.

Enfin, pour la rupture induite par l'impact d'une particule unique, nous avons introduit un modèle de rupture entièrement basé sur l'énergie de rupture. Dans ce modèle de cellule liée, l'interface cellule-cellule ne se rompt que si l'énergie élastique emmagasinée au niveau de l'interface dépasse l'énergie de rupture. Nous avons constaté que le processus de fragmentation implique trois régimes distincts : 1) le régime de basse énergie, 2) le régime d'énergie intermédiaire et 3) le régime de haute énergie. La transition critique des énergies d'impact entre ces régimes a été identifiée par une analyse détaillée des variables de rupture. Nous avons proposé des modèles analytiques qui ajustent correctement l'évolution des variables de rupture en fonction de l'énergie d'impact. Nous avons également constaté que la distribution des masses des fragments est une fonction en loi de puissance dont l'exposant dépend de l'énergie de rupture.

List of Tables

List of Figures

Bibliography

[1] Yannick Guérin, Daniel Parrat, Jean Noirot, Christine Struzik, Victor Blanc, Antoine Bouloré, Lionel Desgranges, Christian Colin, and Christelle Duguay. Nuclear fuels for light water reactors and fast reactors. *CEA Cadarache*, 2019. (Cited on pages vi and 132.)

[2] LG Austin and P Bagga. An analysis of fine dry grinding in ball mills. *Powder Technology*, 28(1):83–90, 1981. (Cited on page vii.)

[3] Rodolfo J Brandao, Rondinelli M Lima, Raphael L Santos, Claudio R Duarte, and Marcos AS Barrozo. Experimental study and dem analysis of granular segregation in a rotating drum. *Powder Technology*, 364:1–12, 2020. (Cited on page vii.)

[4] MJ Mankosa, GT Adel, and RH Yoon. Effect of media size in stirred ball mill grinding of coal. *Powder technology*, 49(1):75–82, 1986. (Cited on page vii.)

[5] Amlan Datta and Raj K Rajamani. A direct approach of modeling batch grinding in ball mills using population balance principles and impact energy distribution. *International Journal of Mineral Processing*, 64(4):181–200, 2002. (Cited on page vii.)

[6] M Capece, E Bilgili, and R Davé. Insight into first-order breakage kinetics using a particle-scale breakage rate constant. *Chemical Engineering Science*, 117:318–330, 2014. (Cited on page vii.)

[7] Luisa Orozco. *Numerical modeling and rheology of crushable granular flows: application to ball mills*. PhD thesis, Université de Montpellier, 2019. (Cited on pages vii, 29, and 125.)

[8] Jean-Noël Roux and Gaël Combe. Quasistatic rheology and the origins of strain. *Comptes Rendus Physique*, 3(2):131–140, 2002. (Cited on pages 2, 3, 4, and 132.)

[9] Isaac Goldhirsch. Rapid granular flows. *Annual review of fluid mechanics*, 35:267, 2003. (Cited on page 2.)

[10] Yoël Forterre and Olivier Pouliquen. Flows of dense granular media. *Annual Review of Fluid Mechanics*, 40(1):1–24, 2008. (Cited on pages 2 and 40.)

[11] GDR MiDi gdrmidi@ polytech. univ-mrs. fr http://www. lmgc. univ-montp2. fr/MIDI/. On dense granular flows. *The European Physical Journal E*, 14:341–365, 2004. (Cited on pages 2, 11, 40, and 106.)

[12] Stuart B Savage. The mechanics of rapid granular flows. *Advances in applied mechanics*, 24:289–366, 1984. (Cited on page 2.)

[13] Christophe Ancey, Philippe Coussot, and Pierre Evesque. A theoretical framework for granular suspensions in a steady simple shear flow. *Journal of Rheology*, 43(6):1673–1699, 1999. (Cited on page 2.)

[14] Lassaad Hazzar, Mathieu Nuth, and Mohamed Chekired. Dem simulation of drained triaxial tests for glass-beads. *Powder Technology*, 364:123–134, 2020. (Cited on page 3.)

[15] Kai Wu, Patrick Pizette, Frederic Becquart, Sebastien Remond, NorEdine Abriak, Weiya Xu, and Songyu Liu. Experimental and numerical study of cylindrical triaxial test on mono-sized glass beads under quasi-static loading condition. *Advanced Powder Technology*, 28(1):155–166, 2017. (Cited on page 3.)

[16] N Belheine, J-P Plassiard, F-V Donzé, F Darve, and A Seridi. Numerical simulation of drained triaxial test using 3d discrete element modeling. *Computers and Geotechnics*, 36(1-2):320–331, 2009. (Cited on page 3.)

[17] Jose E Andrade, CF Avila, Stephen A Hall, Nicolas Lenoir, and Gioacchino Viggiani. Multiscale modeling and characterization of granular matter: from grain kinematics to continuum mechanics. *Journal of the Mechanics and Physics of Solids*, 59(2):237–250, 2011. (Cited on page 3.)

[18] L Rothenburg and Nicolaas P Kruyt. Critical state and evolution of coordination number in simulated granular materials. *International Journal of Solids and Structures*, 41(21):5763–5774, 2004. (Cited on pages 4 and 46.)

[19] Yang Li, Masahide Otsubo, and Reiko Kuwano. Dem analysis on the stress wave response of spherical particle assemblies under triaxial compression. *Computers and Geotechnics*, 133:104043, 2021. (Cited on page 4.)

[20] Daniel Barreto and Catherine O'Sullivan. The influence of inter-particle friction and the intermediate stress ratio on soil response under generalised stress conditions. *Granular Matter*, 14(4):505–521, 2012. (Cited on page 4.)

[21] Emilien Azéma, Farhang Radjai, and Gilles Saussine. Quasistatic rheology, force transmission and fabric properties of a packing of irregular polyhedral particles. *Mechanics of Materials*, 41(6):729–741, 2009. (Cited on pages 4, 37, and 46.)

[22] Emilien Azéma, Farhang Radjai, and Frédéric Dubois. Packings of irregular polyhedral particles: Strength, structure, and effects of angularity. *Phys. Rev. E*, 87(6):062203, June 2013. (Cited on pages 4, 37, 44, 45, 64, 65, 86, and 123.)

[23] Emilien Azéma and Farhang Radjaï. Stress-strain behavior and geometrical properties of packings of elongated particles. *Physical Review E*, 81(5):051304, 2010. (Cited on pages 4, 37, and 107.)

[24] Farhang Radjai, J-Y Delenne, Emilien Azéma, and Stéphane Roux. Fabric evolution and accessible geometrical states in granular materials. *Granular Matter*, 14(2):259–264, 2012. (Cited on pages 4, 44, 111, and 113.)

[25] S Joseph Antony, William Hoyle, and Yulong Ding. *Granular materials: fundamentals and applications*. Royal Society of Chemistry, 2004. (Cited on page 4.)

[26] Nicolaas P Kruyt and L Rothenburg. Kinematic and static assumptions for homogenization in micromechanics of granular materials. *Mechanics of Materials*, 36(12):1157–1173, 2004. (Cited on pages 4 and 6.)

[27] Matteo Baggioli, Michael Landry, and Alessio Zaccone. Deformations, relaxation, and broken symmetries in liquids, solids, and glasses: A unified topological field theory. *Physical Review E*, 105(2):024602, 2022. (Cited on pages 4, 5, 6, and 132.)

[28] Farhang Radjai and Stéphane Roux. Turbulentlike fluctuations in quasistatic flow of granular media. *Physical review letters*, 89(6):064302, 2002. (Cited on page 5.)

[29] Farhang Radjai, Jean-Noël Roux, and Ali Daouadji. Modeling granular materials: Century-long research across scales. *J. Eng. Mech.*, 143:04017002, January 2017. (Cited on pages 5, 37, and 132.)

[30] John F Peters and Laura E Walizer. Patterned nonaffine motion in granular media. *Journal of Engineering Mechanics*, 139(10):1479–1490, 2013. (Cited on page 5.)

[31] I Agnolin and Nicolaas P Kruyt. On the elastic moduli of two-dimensional assemblies of disks: Relevance and modeling of fluctuations in particle displacements and rotations. *Computers & Mathematics with Applications*, 55(2):245–256, 2008. (Cited on pages 6, 38, 43, 46, 50, and 51.)

[32] Ivana Agnolin and Jean-Noël Roux. Internal states of model isotropic granular packings. iii. elastic properties. *Physical Review E*, 76(6):061304, 2007. (Cited on pages 6, 7, 38, 54, and 55.)

[33] K Walton. The effective elastic moduli of a random packing of spheres. *Journal of the Mechanics and Physics of Solids*, 35(2):213–226, 1987. (Cited on page 6.)

[34] Yang Li, Masahide Otsubo, and Reiko Kuwano. Interpretation of static and dynamic young's moduli and poisson's ratio of granular assemblies under shearing. *Computers and Geotechnics*, 142:104560, 2022. (Cited on page 6.)

[35] Mohamed Hassan Khalili, Jean-Noël Roux, Jean-Michel Pereira, Sébastien Brisard, and Michel Bornert. Numerical study of one-dimensional compression of granular materials. ii. elastic moduli, stresses, and microstructure. *Physical Review E*, 95(3):032908, 2017. (Cited on pages 6, 7, 38, 44, 46, 50, and 54.)

[36] Hernán A Makse, Nicolas Gland, David L Johnson, and Lawrence M Schwartz. Why effective medium theory fails in granular materials. *Physical Review Letters*, 83(24):5070, 1999. (Cited on pages 6, 38, and 46.)

[37] Corey S O'hern, Leonardo E Silbert, Andrea J Liu, and Sidney R Nagel. Jamming at zero temperature and zero applied stress: The epitome of disorder. *Physical Review E*, 68(1):011306, 2003. (Cited on page 6.)

[38] Wouter G Ellenbroek, Zorana Zeravcic, Wim van Saarloos, and Martin van Hecke. Non-affine response: Jammed packings vs. spring networks. *EPL (Europhysics Letters)*, 87(3):34004, 2009. (Cited on page 6.)

[39] M Schlegel, J Brujic, EM Terentjev, and A Zaccone. Local structure controls the non-affine shear and bulk moduli of disordered solids. *Scientific reports*, 6(1):1–8, 2016. (Cited on page 6.)

[40] M Ostoja-Starzewski and C Wang. Linear elasticity of planar delaunay networks. part ii: Voigt and reuss bounds, and modification for centroids. *Acta mechanica*, 84(1):47–61, 1990. (Cited on page 6.)

[41] Nicolaas P Kruyt and L Rothenburg. Micromechanical bounds for the effective elastic moduli of granular materials. *International Journal of Solids and Structures*, 39(2):311–324, 2002. (Cited on pages 6, 7, 43, and 46.)

[42] Alessio Zaccone and Enzo Scossa-Romano. Approximate analytical description of the nonaffine response of amorphous solids. *Physical Review B*, 83(18):184205, 2011. (Cited on pages 6 and 38.)

[43] Matthieu Wyart. On the rigidity of amorphous solids. price fluctuations, conventions and microstructure of financial markets, 2005. (Cited on page 7.)

[44] Hernán A Makse, Nicolas Gland, David L Johnson, and Lawrence Schwartz. Granular packings: Nonlinear elasticity, sound propagation, and collective relaxation dynamics. *Physical Review E*, 70(6):061302, 2004. (Cited on pages 7, 38, and 54.)

[45] Pierre-Emmanuel Peyneau and Jean-Noël Roux. Solidlike behavior and anisotropy in rigid frictionless bead assemblies. *Physical Review E*, 78(4):041307, 2008. (Cited on pages 7 and 40.)

[46] B Velickỳ and C Caroli. Pressure dependence of the sound velocity in a two-dimensional lattice of hertz-mindlin balls: Mean-field description. *Physical Review E*, 65(2):021307, 2002. (Cited on page 7.)

[47] Vanessa Magnanimo, Luigi La Ragione, James T Jenkins, P Wang, and Hernán A Makse. Characterizing the shear and bulk moduli of an idealized granular material. *Europhysics Letters*, 81(3):34006, 2008. (Cited on page 7.)

[48] Marco A Cacciuttolo and Alahari Arunakumari. Scale-up considerations for biotechnology-derived products. In *Pharmaceutical Process Scale-Up*, pages 163–194. CRC Press, 2005. (Cited on page 8.)

[49] Luís Marcelo Tavares. A review of advanced ball mill modelling. *KONA Powder and Particle Journal*, page 2017015, 2017. (Cited on page 8.)

[50] A Brunaugh and HDC Smyth. Process optimization and particle engineering of micronized drug powders via milling. *Drug Delivery and Translational Research*, 8(6):1740–1750, 2018. (Cited on page 8.)

[51] Indresan Govender. Granular flows in rotating drums: A rheological perspective. *Minerals Engineering*, 92:168–175, June 2016. (Cited on pages 8, 62, 63, and 82.)

[52] R. Y. Yang, A. B. Yu, L. McElroy, and J. Bao. Numerical simulation of particle dynamics in different flow regimes in a rotating drum. *Powder Technology*, 188(2):170–177, December 2008. (Cited on pages 8, 9, and 62.)

[53] J. Mellmann. The transverse motion of solids in rotating cylinders–forms of motion and transition behavior. *Powder Technology*, 118(3):251–270, August 2001. (Cited on pages 8, 9, and 62.)

[54] Yulong Ding, J. P. K. Seville, R. Forster, and D. Parker. Solids motion in rolling mode rotating drums operated at low to medium rotational speeds. *Chemical Engineering Science*, 56:1769–1780, March 2001. (Cited on pages 8, 62, and 68.)

[55] H Henein, JK Brimacombe, and AP Watkinson. Experimental study of transverse bed motion in rotary kilns. *Metallurgical transactions B*, 14(2):191–205, 1983. (Cited on page 8.)

[56] H Henein, JK Brimacombe, and AP Watkinson. The modeling of transverse solids motion in rotary kilns. *Metallurgical Transactions B*, 14(2):207–220, 1983. (Cited on pages 8 and 9.)

[57] Amara Aissa, Carl Duchesne, and Denis Rodrigue. Transverse mixing of polymer powders in a rotary cylinder part i: Active layer characterization. *Powder Technology*, 219:193–201, March 2012. (Cited on pages 8, 62, 68, and 73.)

[58] Troy Shinbrot, Albert Alexander, Maher Moakher, and Fernando J Muzzio. Chaotic granular mixing. *Chaos: An Interdisciplinary Journal of Nonlinear Science*, 9(3):611–620, 1999. (Cited on page 9.)

[59] Manogna Adepu, Brandon Boepple, Bradley Fox, and Heather Emady. Experimental investigation of conduction heat transfer in a rotary drum using infrared thermography. *Chemical Engineering Science*, 230:116145, 2021. (Cited on page 9.)

[60] Clive E Davies, A Williams, SJ Tallon, K Fenton, and N Brown. A new approach to monitoring the movement of particulate material in rotating drums. *Developments in Chemical Engineering and Mineral Processing*, 12(3-4):263–275, 2004. (Cited on page 9.)

[61] Amara Aït Aissa, Carl Duchesne, and Denis Rodrigue. Effect of friction coefficient and density on mixing particles in the rolling regime. *Powder technology*, 212(2):340–347, 2011. (Cited on page 9.)

[62] J Lehmberg, M Hehl, and K Schügerl. Transverse mixing and heat transfer in horizontal rotary drum reactors. *Powder Technology*, 18(2):149–163, 1977. (Cited on page 9.)

[63] Dennis R Van Puyvelde, Michael A Wilson, Brent R Young, and S James Schmidt. Modelling transverse mixing in a rolling drum. *The Canadian Journal of Chemical Engineering*, 78(4):635–642, 2000. (Cited on page 9.)

[64] PV Barr, JK Brimacombe, and AP Watkinson. A heat-transfer model for the rotary kiln: Part ii. development of the cross-section model. *Metallurgical and Materials Transactions B*, 20(3):403–419, 1989. (Cited on page 9.)

[65] Luisa Fernanda Orozco, Jean-Yves Delenne, Philippe Sornay, and Farhang Radjai. Rheology and scaling behavior of cascading granular flows in rotating drums. *Journal of Rheology*, 64(4):915–931, 2020. (Cited on pages 9, 10, 12, 18, 62, 63, 65, 68, 69, 70, 71, 74, 76, 103, and 136.)

[66] SY He, JQ Gan, David Pinson, AB Yu, and ZY Zhou. Flow regimes of cohesionless ellipsoidal particles in a rotating drum. *Powder Technology*, 354:174–187, 2019. (Cited on page 9.)

[67] QJ Zheng and AB Yu. Modelling the granular flow in a rotating drum by the eulerian finite element method. *Powder technology*, 286:361–370, 2015. (Cited on page 9.)

[68] Huaqing Ma and Yongzhi Zhao. Modelling of the flow of ellipsoidal particles in a horizontal rotating drum based on dem simulation. *Chemical Engineering Science*, 172:636–651, November 2017. (Cited on pages 9, 10, and 63.)

[69] MMHD Arntz, HH Beeftink, Wouter K den Otter, Willem J Briels, and RM Boom. Segregation of granular particles by mass, radius, and density in a horizontal rotating drum. *AIChE journal*, 60(1):50–59, 2014. (Cited on page 9.)

[70] A Santomaso, M Olivi, and P Canu. Mixing kinetics of granular materials in drums operated in rolling and cataracting regime. *Powder Technology*, 152(1-3):41–51, 2005. (Cited on page 9.)

[71] Christine Beaulieu, David Vidal, Carine Niyonkuru, Anthony Wachs, Jamal Chaouki, and François Bertrand. Effect of particle angularity on flow regime transitions and segregation of bidisperse blends in a rotating drum. *Computational Particle Mechanics*, 9(3):443–463, 2022. (Cited on page 9.)

[72] DA Santos, R Scatena, CR Duarte, and MAS Barrozo. Transition phenomenon investigation between different flow regimes in a rotary drum. *Brazilian Journal of Chemical Engineering*, 33:491–501, 2016. (Cited on page 9.)

[73] Wanessa M Benedito, Claudio R Duarte, Marcos AS Barrozo, and Dyrney A Santos. Cataracting-centrifuging transition investigation using nonspherical and spherical particles in a rotary drum through cfd simulations. *Particuology*, 60:48–60, 2022. (Cited on page 9.)

[74] Gabriel Juarez, Pengfei Chen, and Richard M Lueptow. Transition to centrifuging granular flow in rotating tumblers: A modified froude number. *New Journal of Physics*, 13(5):053055, 2011. (Cited on page 9.)

[75] DA Santos, IJ Petri, CR Duarte, and MAS Barrozo. Experimental and cfd study of the hydrodynamic behavior in a rotating drum. *Powder technology*, 250:52–62, 2013. (Cited on page 9.)

[76] Gwenaëlle Félix. *Ecoulements de milieux granulaires en tambour tournant. Étude de quelques transitions de régime. Application à la ségrégation.* PhD thesis, Institut National Polytechnique de Lorraine-INPL, 2002. (Cited on page 9.)

[77] YL Ding, Robin Forster, JPK Seville, and DJ Parker. Granular motion in rotating drums: bed turnover time and slumping–rolling transition. *Powder Technology*, 124(1-2):18–27, 2002. (Cited on page 9.)

[78] Gary W Delaney and Paul W Cleary. The packing properties of superellipsoids. *EPL (Europhysics Letters)*, 89(3):34002, 2010. (Cited on pages 10 and 23.)

[79] Guang Lu, James R Third, and Christoph R Müller. Effect of wall rougheners on cross-sectional flow characteristics for non-spherical particles in a horizontal rotating cylinder. *Particuology*, 12:44–53, 2014. (Cited on page 10.)

[80] G. Lu, J. R. Third, and C. R. Müller. Discrete element models for non-spherical particle systems: From theoretical developments to applications. *Chemical Engineering Science*, 127:425–465, May 2015. (Cited on pages 10 and 63.)

[81] Christian Wellmann, Claudia Lillie, and Peter Wriggers. A contact detection algorithm for superellipsoids based on the common-normal concept. *Engineering Computations*, 2008. (Cited on page 10.)

[82] Andriarimina Daniel Rakotonirina, Jean-Yves Delenne, Farhang Radjai, and Anthony Wachs. Grains3d, a flexible dem approach for particles of arbitrary convex shape–part iii: extension to non-convex particles modelled as glued convex particles. *Computational Particle Mechanics*, 6(1):55–84, January 2019. (Cited on pages 10, 23, and 63.)

[83] CJ Coetzee. Calibration of the discrete element method. *Powder Technology*, 310:104–142, 2017. (Cited on page 10.)

[84] JF Favier, MH Abbaspour-Fard, and M Kremmer. Modeling nonspherical particles using multisphere discrete elements. *Journal of Engineering Mechanics*, 127(10):971–977, 2001. (Cited on page 10.)

[85] D Höhner, S Wirtz, and V Scherer. A study on the influence of particle shape and shape approximation on particle mechanics in a rotating drum using the discrete element method. *Powder Technology*, 253:256–265, 2014. (Cited on page 10.)

[86] Nicolin Govender. A dem study on the thermal conduction of granular material in a rotating drum using polyhedral particles on gpus. *Chemical Engineering Science*, 252:117491, April 2022. (Cited on pages 10, 62, and 63.)

[87] Olivier Dubé, Ebrahim Alizadeh, Jamal Chaouki, and François Bertrand. Dynamics of non-spherical particles in a rotating drum. *Chemical Engineering Science*, 101:486–502, September 2013. (Cited on pages 10, 63, and 68.)

[88] Nan Gui, Xingtuan Yang, Jiyuan Tu, and Shengyao Jiang. Numerical simulation and analysis of mixing of polygonal particles in 2d rotating drums by siphpm method. *Powder Technology*, 318:248–262, 2017. (Cited on page 10.)

[89] G Félix and N Thomas. Evidence of two effects in the size segregation process in dry granular media. *Physical Review E*, 70(5):051307, 2004. (Cited on page 10.)

[90] Nitin Jain, Julio M Ottino, and Richard M Lueptow. Regimes of segregation and mixing in combined size and density granular systems: an experimental study. *Granular Matter*, 7:69–81, 2005. (Cited on page 10.)

[91] Ram Chand, Murad Ali Khaskheli, Abdul Qadir, Baoliang Ge, and Qingfan Shi. Discrete particle simulation of radial segregation in horizontally rotating drum: Effects of

drum-length and non-rotating end-plates. *Physica A: Statistical Mechanics and its Applications*, 391(20):4590–4596, 2012. (Cited on page 10.)

[92] DC Rapaport. Radial and axial segregation of granular matter in a rotating cylinder: a simulation study. *Physical Review E*, 75(3):031301, 2007. (Cited on page 10.)

[93] Christian M Dury and Gerald H Ristow. Competition of mixing and segregation in rotating cylinders. *Physics of fluids*, 11(6):1387–1394, 1999. (Cited on page 10.)

[94] Ebrahim Alizadeh, François Bertrand, and Jamal Chaouki. Characterization of mixing and size segregation in a rotating drum by a particle tracking method. *AIChE Journal*, 59, June 2013. (Cited on pages 10, 62, and 68.)

[95] Edgar Buckingham. On physically similar systems; illustrations of the use of dimensional equations. *Physical review*, 4(4):345, 1914. (Cited on page 11.)

[96] Michael Levin. *Pharmaceutical process scale-up*. CRC Press, 2001. (Cited on page 11.)

[97] Ashish V. Orpe and D. V. Khakhar. Scaling relations for granular flow in quasi-two-dimensional rotating cylinders. *Phys. Rev. E*, 64(3):031302, August 2001. (Cited on pages 11, 62, and 69.)

[98] Christian M Dury, Gerald H Ristow, Jamie L Moss, and Masami Nakagawa. Boundary effects on the angle of repose in rotating cylinders. *Physical Review E*, 57(4):4491, 1998. (Cited on page 11.)

[99] Nicolas Taberlet, Patrick Richard, and E. John Hinch. S shape of a granular pile in a rotating drum. *Phys. Rev. E*, 73(5):050301, May 2006. (Cited on pages 11, 62, and 70.)

[100] Hsien-Ter Chou and Ching-Fang Lee. Cross-sectional and axial flow characteristics of dry granular material in rotating drums. *Granular Matter*, 11(1):13–32, January 2009. (Cited on pages 11 and 70.)

[101] Albert Alexander, Troy Shinbrot, and Fernando J Muzzio. Scaling surface velocities in rotating cylinders as a function of vessel radius, rotation rate, and particle size. *Powder Technology*, 126(2):174–190, 2002. (Cited on page 11.)

[102] Florent Pignatel, Caroline Asselin, Lucas Krieger, Ivan C. Christov, Julio M. Ottino, and Richard M. Lueptow. Parameters and scalings for dry and immersed granular flowing layers in rotating tumblers. *Phys. Rev. E*, 86(1):011304, July 2012. (Cited on pages 11, 12, and 62.)

[103] Tomohiro Iwasaki, Tomoya Yabuuchi, Haruki Nakagawa, and Satoru Watano. Scale-up methodology for tumbling ball mill based on impact energy of grinding balls using discrete element analysis. *Advanced Powder Technology*, 21(6):623–629, 2010. (Cited on pages 11 and 18.)

[104] MR Coop, KK Sorensen, T Bodas Freitas, and G Georgoutsos. Particle breakage during shearing of a carbonate sand. *Géotechnique*, 54(3):157–163, 2004. (Cited on pages 13 and 17.)

[105] Haydar Arslan, Gokhan Baykal, and Stein Sture. Analysis of the influence of crushing on the behavior of granular materials under shear. *Granular Matter*, 11(2):87–97, 2009. (Cited on pages 13 and 16.)

[106] Bernd Imre, Jan Laue, and Sarah Marcella Springman. Fractal fragmentation of rocks within sturzstroms: insight derived from physical experiments within the eth geotechnical drum centrifuge. *Granular matter*, 12:267–285, 2010. (Cited on pages 13 and 16.)

[107] A Ezaoui, Thibaut Lecompte, H Di Benedetto, and E Garcia. Effects of various loading stress paths on the stress-strain properties and on crushability of an industrial soft granular material. *Granular Matter*, 13(4):283–301, 2011. (Cited on pages 13 and 16.)

[108] Francesca Casini, Giulia MB Viggiani, and Sarah M Springman. Breakage of an artificial crushable material under loading. *Granular matter*, 15:661–673, 2013. (Cited on pages 13 and 16.)

[109] HY Liu, SQ Kou, and P-A Lindqvist. Numerical studies on the inter-particle breakage of a confined particle assembly in rock crushing. *Mechanics of materials*, 37(9):935–954, 2005. (Cited on page 13.)

[110] Ann Bäckström, Juha Antikainen, Tobias Backers, Xiating Feng, Lanru Jing, Akira Kobayashi, Tomofumi Koyama, Pengzhi Pan, Mikael Rinne, Baotang Shen, et al. Numerical modelling of uniaxial compressive failure of granite with and without saline porewater. *International Journal of Rock Mechanics and Mining Sciences*, 45(7):1126–1142, 2008. (Cited on page 13.)

[111] Gang Ma, Wei Zhou, Xiao-Lin Chang, and Ming-Xiang Chen. A hybrid approach for modeling of breakable granular materials using combined finite-discrete element method. *Granular Matter*, 18(1):1–17, 2016. (Cited on pages 13, 29, and 133.)

[112] Duc-Hanh Nguyen, Emilien Azéma, Philippe Sornay, and Farhang Radjai. Bonded-cell model for particle fracture. *Physical Review E*, 91(2):022203, 2015. (Cited on pages 13, 14, and 30.)

[113] N al Cho, CD Martin, and DC Sego. A clumped particle model for rock. *International journal of rock mechanics and mining sciences*, 44(7):997–1010, 2007. (Cited on page 13.)

[114] G. Timár, J. Blömer, F. Kun, and H. J. Herrmann. New universality class for the fragmentation of plastic materials. *Phys. Rev. Lett.*, 104(9):095502, March 2010. (Cited on pages 13, 15, 16, 29, 30, 83, 96, 99, and 133.)

[115] Matthew J Metzger and Benjamin J Glasser. Numerical investigation of the breakage of bonded agglomerates during impact. *Powder Technology*, 217:304–314, 2012. (Cited on page 13.)

[116] Takao Ueda, Takashi Matsushima, and Yasuo Yamada. Dem simulation on the one-dimensional compression behavior of various shaped crushable granular materials. *Granular Matter*, 15:675–684, 2013. (Cited on pages 13 and 16.)

[117] Jianfeng Wang and Haibin Yan. Dem analysis of energy dissipation in crushable soils. *Soils and Foundations*, 52(4):644–657, 2012. (Cited on pages 13 and 18.)

[118] Gian Antonio D'Addetta, F Kun, and Ekkehard Ramm. On the application of a discrete model to the fracture process of cohesive granular materials. *Granular matter*, 4(2):77–90, 2002. (Cited on pages 13 and 30.)

[119] Sergio Andres Galindo-Torres, DM Pedroso, DJ Williams, and Ling Li. Breaking processes in three-dimensional bonded granular materials with general shapes. *Computer Physics Communications*, 183(2):266–277, 2012. (Cited on pages 13 and 30.)

[120] D. Cantor, E. Azéma, P. Sornay, and F. Radjai. Three-dimensional bonded-cell model for grain fragmentation. *Computational Particle Mechanics*, 4(4):441–450, October 2017. (Cited on pages 13, 29, 30, 33, 83, 84, 85, and 133.)

[121] Luisa Fernanda Orozco, Jean-Yves Delenne, Philippe Sornay, and Farhang Radjai. Discrete-element model for dynamic fracture of a single particle. *International Journal of Solids and Structures*, 166:47–56, July 2019. (Cited on pages 13, 29, 30, 82, 83, 84, 85, 87, 91, 93, and 133.)

[122] C. Thornton, K. K. Yin, and M. J. Adams. Numerical simulation of the impact fracture and fragmentation of agglomerates. *Journal of Physics D: Applied Physics*, 29(2):424, February 1996. (Cited on pages 14, 29, and 83.)

[123] Ferenc Kun and Hans J. Herrmann. Transition from damage to fragmentation in collision of solids. *Phys. Rev. E*, 59(3):2623–2632, March 1999. (Cited on pages 14 and 98.)

[124] Bhupalendra Behera, Ferenc Kun, Sean McNamara, and Hans J. Herrmann. Fragmentation of a circular disc by impact on a frictionless plate. *Journal of Physics: Condensed Matter*, 17(24):S2439, June 2005. (Cited on pages 14, 15, and 83.)

[125] H. A. Carmona, F. K. Wittel, F. Kun, and H. J. Herrmann. Fragmentation processes in impact of spheres. *Phys. Rev. E*, 77(5):051302, May 2008. (Cited on pages 14, 82, and 83.)

[126] Gang Ma, Wei Zhou, Yida Zhang, Qiao Wang, and Xiaolin Chang. Fractal behavior and shape characteristics of fragments produced by the impact of quasi-brittle spheres. *Powder Technology*, 325:498–509, February 2018. (Cited on pages 14, 15, 83, and 132.)

[127] G. Timár, F. Kun, H. A. Carmona, and H. J. Herrmann. Scaling laws for impact fragmentation of spherical solids. *Phys. Rev. E*, 86(1):016113, July 2012. (Cited on pages 14, 15, 83, and 132.)

[128] R. Moreno, M. Ghadiri, and S. J. Antony. Effect of the impact angle on the breakage of agglomerates: a numerical study using dem. *Powder Technology*, 130(1):132–137, February 2003. (Cited on page 15.)

[129] K. D. Kafui and C. Thornton. Numerical simulations of impact breakage of a spherical crystalline agglomerate. *Powder Technology*, 109(1):113–132, April 2000. (Cited on pages 15 and 83.)

[130] R. Moreno-Atanasio and M. Ghadiri. Mechanistic analysis and computer simulation of impact breakage of agglomerates: Effect of surface energy. *Chemical Engineering Science*, 61(8):2476–2481, April 2006. (Cited on pages 15 and 83.)

[131] B. K. Mishra and C. Thornton. Impact breakage of particle agglomerates. *International Journal of Mineral Processing*, 61(4):225–239, April 2001. (Cited on pages 15, 29, and 83.)

[132] H. A. Carmona, A. V. Guimarães, J. S. Andrade, I. Nikolakopoulos, F. K. Wittel, and H. J. Herrmann. Fragmentation processes in two-phase materials. *Phys. Rev. E*, 91(1):012402, January 2015. (Cited on pages 15 and 83.)

[133] L. Liu, K. D. Kafui, and C. Thornton. Impact breakage of spherical, cuboidal and cylindrical agglomerates. *Powder Technology*, 199(2):189–196, April 2010. (Cited on pages 15 and 82.)

[134] Kehong Zheng, Changlong Du, Jianping Li, Bingjing Qiu, Lin Fu, and Jiawei Dong. Numerical simulation of the impact-breakage behavior of non-spherical agglomerates. *Powder Technology*, 286:582–591, December 2015. (Cited on page 15.)

[135] Akira Fujiwara, Goro Kamimoto, and Akisama Tsukamoto. Expected shape distribution of asteroids obtained from laboratory impact experiments. *Nature*, 272(5654):602–603, 1978. (Cited on page 15.)

[136] Daniel D Durda, Adriano Campo Bagatin, Rafael A Alemañ, George J Flynn, Melissa M Strait, Angela N Clayton, and Emma B Patmore. The shapes of fragments from catastrophic disruption events: effects of target shape and impact speed. *Planetary and Space Science*, 107:77–83, 2015. (Cited on page 15.)

[137] Tatsuhiro Michikami, Axel Hagermann, Tokiyuki Kadokawa, Akifumi Yoshida, Akira Shimada, Sunao Hasegawa, and Akira Tsuchiyama. Fragment shapes in impact experiments ranging from cratering to catastrophic disruption. *Icarus*, 264:316–330, January 2016. (Cited on pages 15, 16, 83, 96, 97, and 132.)

[138] Matsushima Takashi, Katagiri Jun, Uesugi Kentaro, Tsuchiyama Akira, and Nakano Tsukaka. 3d shape characterization and image-based dem simulation of the lunar soil simulant fjs-1. *Journal of Aerospace Engineering*, 22(1):15–23, January 2009. (Cited on pages 15, 17, 83, 96, 97, and 132.)

[139] Gábor Domokos, Ferenc Kun, András Arpád Sipos, and Tímea Szabó. Universality of fragment shapes. *Scientific Reports*, 5(1):9147, March 2015. (Cited on pages 15, 16, 82, 83, 96, 98, and 99.)

[140] J. A. Åström, F. Ouchterlony, R. P. Linna, and J. Timonen. Universal dynamic fragmentation in d dimensions. *Phys. Rev. Lett.*, 92(24):245506, June 2004. (Cited on pages 16 and 83.)

[141] J. R. Gladden, N. Z. Handzy, A. Belmonte, and E. Villermaux. Dynamic buckling and fragmentation in brittle rods. *Phys. Rev. Lett.*, 94(3):035503, January 2005. (Cited on page 16.)

[142] Hiroaki Katsuragi, Satoshi Ihara, and Haruo Honjo. Explosive fragmentation of a thin ceramic tube using pulsed power. *Phys. Rev. Lett.*, 95(9):095503, August 2005. (Cited on pages 16 and 98.)

[143] Itai Einav. Breakage mechanics—part i: theory. *Journal of the Mechanics and Physics of Solids*, 55(6):1274–1297, 2007. (Cited on page 16.)

[144] Itai Einav and Julio R Valdes. On comminution and yield in brittle granular mixtures. *Journal of the Mechanics and Physics of Solids*, 56(6):2136–2148, 2008. (Cited on page 16.)

[145] Poul V Lade, Jerry A Yamamuro, and Paul A Bopp. Significance of particle crushing in granular materials. *Journal of Geotechnical Engineering*, 122(4):309–316, 1996. (Cited on page 16.)

[146] GR McDowell, MD Bolton, and D Robertson. The fractal crushing of granular materials. *Journal of the Mechanics and Physics of Solids*, 44(12):2079–2101, 1996. (Cited on page 16.)

[147] Fawad A Chuhan, Arild Kjeldstad, Knut Bjørlykke, and Kaare Høeg. Porosity loss in sand by grain crushing—experimental evidence and relevance to reservoir quality. *Marine and Petroleum Geology*, 19(1):39–53, 2002. (Cited on page 16.)

[148] Wenbo Zheng, Suyanne Costa Silva, and Dwayne D Tannant. Crushing characteristics of four different proppants and implications for fracture conductivity. *Journal of Natural Gas Science and Engineering*, 53:125–138, 2018. (Cited on page 16.)

[149] YP Cheng, MD Bolton, and Y Nakata. Crushing and plastic deformation of soils simulated using dem. *Geotechnique*, 54(2):131–141, 2004. (Cited on page 16.)

[150] VPB Esnault and J-N Roux. 3d numerical simulation study of quasistatic grinding process on a model granular material. *Mechanics of Materials*, 66:88–109, 2013. (Cited on page 16.)

[151] Duc-Hanh Nguyen, Émilien Azéma, Philippe Sornay, and Farhang Radjaï. Rheology of granular materials composed of crushable particles. *The European Physical Journal E*, 41(4):50, April 2018. (Cited on pages 16, 17, 83, 85, and 132.)

[152] DD Shi, D Cao, YB Deng, and JF Xue. Dem investigations of the effects of intermediate principal stress ratio and particle breakage on the critical state behaviors of granular soils. *Powder Technology*, 379:547–559, 2021. (Cited on page 16.)

[153] John P de Bono and Glenn R McDowell. On the packing and crushing of granular materials. *International Journal of Solids and Structures*, 187:133–140, 2020. (Cited on page 16.)

[154] Luis E Vallejo, Sebastian Lobo-Guerrero, and Kevin Hammer. Degradation of a granular base under a flexible pavement: Dem simulation. *International Journal of geomechanics*, 6(6):435–439, 2006. (Cited on page 17.)

[155] Junyu Huang, Songlin Xu, and Shisheng Hu. Influence of particle breakage on the dynamic compression responses of brittle granular materials. *Mechanics of materials*, 68:15–28, 2014. (Cited on page 17.)

[156] Wei Zhou, Di Wang, Gang Ma, Xuexin Cao, Chao Hu, and Wei Wu. Discrete element modeling of particle breakage considering different fragment replacement modes. *Powder Technology*, 360:312–323, 2020. (Cited on page 18.)

[157] Ru Fu, Xinli Hu, and Bo Zhou. Discrete element modeling of crushable sands considering realistic particle shape effect. *Computers and Geotechnics*, 91:179–191, 2017. (Cited on page 18.)

[158] Fan Zhu and Jidong Zhao. Modeling continuous grain crushing in granular media: a hybrid peridynamics and physics engine approach. *Computer Methods in Applied Mechanics and Engineering*, 348:334–355, 2019. (Cited on pages 18 and 132.)

[159] Mehmet B Cil and Khalid A Alshibli. Modeling the influence of particle morphology on the fracture behavior of silica sand using a 3d discrete element method. *Comptes Rendus Mécanique*, 343(2):133–142, 2015. (Cited on page 18.)

[160] Danda Shi, Dong Cao, Jianfeng Xue, Yibing Deng, and Yonghui Liang. Dem studies on the effect of particle breakage on the critical state behaviours of granular soils under undrained shear conditions. *Acta Geotechnica*, 17(11):4865–4885, 2022. (Cited on page 18.)

[161] Zhaonan Wang, Gang Wang, and Qinguo Ye. A constitutive model for crushable sands involving compression and shear induced particle breakage. *Computers and Geotechnics*, 126:103757, 2020. (Cited on page 18.)

[162] Tabassom Afshar, Mahdi M Disfani, Arul Arulrajah, Guillermo A Narsilio, and Sacha Emam. Impact of particle shape on breakage of recycled construction and demolition aggregates. *Powder technology*, 308:1–12, 2017. (Cited on page 18.)

[163] VK Gupta. Effect of size distribution of the particulate material on the specific breakage rate of particles in dry ball milling. *Powder Technology*, 305:714–722, 2017. (Cited on page 18.)

[164] A Seyfi Erdem and Ş Levent Ergün. The effect of ball size on breakage rate parameter in a pilot scale ball mill. *Minerals Engineering*, 22(7-8):660–664, 2009. (Cited on pages 18 and 20.)

[165] John A Herbst and Alexander V Potapov. Making a discrete grain breakage model practical for comminution equipment performance simulation. *Powder Technology*, 143:144–150, 2004. (Cited on page 18.)

[166] Matthew J Metzger and Benjamin J Glasser. Simulation of the breakage of bonded agglomerates in a ball mill. *Powder Technology*, 237:286–302, 2013. (Cited on page 18.)

[167] Michele Marigo and Edmund Hugh Stitt. Discrete element method (dem) for industrial applications: comments on calibration and validation for the modelling of cylindrical pellets. *KONA Powder and Particle Journal*, 32:236–252, 2015. (Cited on page 18.)

[168] Rodrigo M de Carvalho and Luís Marcelo Tavares. Predicting the effect of operating and design variables on breakage rates using the mechanistic ball mill model. *Minerals Engineering*, 43:91–101, 2013. (Cited on page 18.)

[169] M Capece, RN Davé, and E Bilgili. A pseudo-coupled dem–non-linear pbm approach for simulating the evolution of particle size during dry milling. *Powder Technology*, 323:374–384, 2018. (Cited on page 18.)

[170] JD Litster and AG Waters. Influence of the material properties of iron ore sinter feed on granulation effectiveness. *Powder Technology*, 55(2):141–151, 1988. (Cited on page 19.)

[171] BK Mishra, C Thornton, and Daksha Bhimji. A preliminary numerical investigation of agglomeration in a rotary drum. *Minerals Engineering*, 15(1-2):27–33, 2002. (Cited on page 19.)

[172] J Detyna. Stochastic models of particle distribution in separation processes. *Archives of Civil and Mechanical Engineering*, 10(1):15–26, 2010. (Cited on page 19.)

[173] Luís Marcelo Tavares and Rodrigo M de Carvalho. Modeling breakage rates of coarse particles in ball mills. *Minerals Engineering*, 22(7-8):650–659, 2009. (Cited on page 19.)

[174] Vivien PB Esnault, H Zhou, and Daniel Heitzmann. New population balance model for predicting particle size evolution in compression grinding. *Minerals Engineering*, 73:7–15, 2015. (Cited on page 19.)

[175] DW Fuerstenau and A-ZM Abouzeid. The energy efficiency of ball milling in comminution. *International Journal of Mineral Processing*, 67(1-4):161–185, 2002. (Cited on page 19.)

[176] VK Gupta and Shivani Sharma. Analysis of ball mill grinding operation using mill power specific kinetic parameters. *Advanced Powder Technology*, 25(2):625–634, 2014. (Cited on page 19.)

[177] Luisa Fernanda Orozco, Duc-Hanh Nguyen, Jean-Yves Delenne, Philippe Sornay, and Farhang Radjai. Discrete-element simulations of comminution in rotating drums: Effects of grinding media. *Powder Technology*, 362:157–167, February 2020. (Cited on pages 19, 20, 82, 84, 103, and 133.)

[178] Luisa Fernanda Orozco, Jean-Yves Delenne, Philippe Sornay, and Farhang Radjai. Scaling behavior of particle breakage in granular flows inside rotating drums. *Phys. Rev. E*, 101(5):052904, May 2020. (Cited on pages 19, 82, and 85.)

[179] Farhang Radjai and Frédéric Dubois. *Discrete-element modeling of granular materials*. Wiley-Iste, 2011. (Cited on pages 21, 23, 39, 40, and 106.)

[180] B Garcia, P Villard, V Richefeu, and D Daudon. Comparison of full-scale rockfall tests with 3d complex-shaped discrete element simulations. *Engineering Geology*, 310:106855, 2022. (Cited on page 22.)

[181] Nikolai V. Brilliantov, Frank Spahn, Jan-Martin Hertzsch, and Thorsten Pöschel. Model for collisions in granular gases. *Phys. Rev. E*, 53(5):5382–5392, May 1996. (Cited on pages 22 and 65.)

[182] Vincent Richefeu and Pascal Villard. *Modeling gravity hazards from rockfalls to landslides*. Elsevier, 2016. (Cited on pages 23, 38, and 39.)

[183] Guilhem Mollon, Vincent Richefeu, Pascal Villard, and Dominique Daudon. Numerical simulation of rock avalanches: Influence of a local dissipative contact model on the collective behavior of granular flows. *Journal of Geophysical Research: Earth Surface*, 117(F2), 2012. (Cited on pages 24 and 133.)

[184] Eun Hyun Park, Volodymyr Kindratenko, and Youssef MA Hashash. Shared memory parallelization for high-fidelity large-scale 3d polyhedral particle simulations. *Computers and Geotechnics*, 137:104008, 2021. (Cited on pages 24, 25, 26, and 133.)

[185] F Alonso-Marroquın. An efficient algorithm for computing conservative interactions be-tween two-dimensional, complex-shaped rigid bodies. (Cited on pages 25 and 26.)

[186] Bruno Andreotti, Yoël Forterre, and Olivier Pouliquen. *Granular media: between fluid and solid*. Cambridge University Press, 2013. (Cited on pages 26 and 107.)

[187] Shane J Burns and Kevin J Hanley. Establishing stable time-steps for dem simulations of non-collinear planar collisions with linear contact laws. *International Journal for Numerical Methods in Engineering*, 110(2):186–200, 2017. (Cited on page 26.)

[188] Farhang Radjai. Multi-periodic boundary conditions and the contact dynamics method. *Comptes Rendus Mécanique*, 346(3):263–277, 2018. (Cited on pages 27, 40, and 106.)

[189] MP Allen. Dj tildesley 'computer simulation of liquids' clarendon, 1987. (Cited on page 27.)

[190] Farhang Radjai and Charles Voivret. Periodic boundary conditions. *Discrete Numerical Modeling of Granular Materials*, pages 181–198, 2011. (Cited on page 28.)

[191] J Subero, Z Ning, M Ghadiri, and C Thornton. Effect of interface energy on the impact strength of agglomerates. *Powder Technology*, 105(1-3):66–73, 1999. (Cited on page 29.)

[192] GR McDowell and O Harireche. Discrete element modelling of soil particle fracture. *Géotechnique*, 52(2):131–135, 2002. (Cited on page 29.)

[193] R Moreno-Atanasio and M Ghadiri. Mechanistic analysis and computer simulation of impact breakage of agglomerates: effect of surface energy. *Chemical engineering science*, 61(8):2476–2481, 2006. (Cited on page 29.)

[194] Ferenc Kun and Hans J Herrmann. A study of fragmentation processes using a discrete element method. *Computer Methods in Applied Mechanics and Engineering*, 138(1-4):3–18, 1996. (Cited on page 30.)

[195] Bart Van de Steen, André Vervoort, and JAL Napier. Numerical modelling of fracture initiation and propagation in biaxial tests on rock samples. *International Journal of Fracture*, 108(2):165–191, 2001. (Cited on page 30.)

[196] Atsuyuki Okabe, Barry Boots, Kokichi Sugihara, and Sung Nok Chiu. Spatial tessellations: concepts and applications of voronoi diagrams. 2009. (Cited on page 31.)

[197] David Cantor Garcia. *Compaction des matériaux granulaires fragmentables en 3D*. PhD thesis, Université Montpellier, 2017. (Cited on pages 31 and 133.)

[198] Qiang Du, Vance Faber, and Max Gunzburger. Centroidal voronoi tessellations: Applications and algorithms. *SIAM review*, 41(4):637–676, 1999. (Cited on pages 32 and 133.)

[199] Stuart Lloyd. Least squares quantization in pcm. *IEEE transactions on information theory*, 28(2):129–137, 1982. (Cited on page 32.)

[200] Hadrien Hyacinthe Laubie. *Elastic properties and failure behavior of disordered porous solids: a potential-of-mean-force-based lattice element approach*. PhD thesis, Massachusetts Institute of Technology, 2017. (Cited on page 33.)

[201] Grzegorz Ludwik Golewski. Generalized fracture toughness and compressive strength of sustainable concrete including low calcium fly ash. *Materials*, 10(12):1393, 2017. (Cited on page 33.)

[202] GR Irwin. Linear fracture mechanics, fracture transition, and fracture control. *Engineering fracture mechanics*, 1(2):241–257, 1968. (Cited on page 34.)

[203] Heinrich M. Jaeger, Sidney R. Nagel, and Robert P. Behringer. The physics of granular materials. *Physics Today*, 49(4):32–38, April 1996. (Cited on page 37.)

[204] Hans J Herrmann, J-P Hovi, and Stefan Luding. *Physics of dry granular media*, volume 350. Springer Science & Business Media, 2013. (Cited on pages 37, 39, and 65.)

[205] Aleksandar Donev, Ibrahim Cisse, David Sachs, Evan A. Variano, Frank H. Stillinger, Robert Connelly, Salvatore Torquato, and P. M. Chaikin. Improving the density of jammed disordered packings using ellipsoids. *Science*, 303(5660):990–993, February 2004. (Cited on page 37.)

[206] Paul Cleary. The effect of particle shape on simple shear flows. *Powder Technology*, 179:144–163, January 2008. (Cited on pages 37 and 63.)

[207] B. Saint-Cyr, J.-Y. Delenne, C. Voivret, F. Radjai, and P. Sornay. Rheology of granular materials composed of nonconvex particles. *Phys. Rev. E*, 84(4):041302, October 2011. (Cited on page 37.)

[208] CEGEO, B. Saint-Cyr, K. Szarf, C. Voivret, E. Azéma, V. Richefeu, J.-Y. Delenne, G. Combe, C. Nouguier-Lehon, P. Villard, P. Sornay, M. Chaze, and F. Radjai. Particle shape dependence in 2d granular media. *Europhysics Letters*, 98(4):44008, May 2012. (Cited on page 37.)

[209] Athanasios G. Athanassiadis, Marc Z. Miskin, Paul Kaplan, Nicholas Rodenberg, Seung Hwan Lee, Jason Merritt, Eric Brown, John Amend, Hod Lipson, and Heinrich M. Jaeger. Particle shape effects on the stress response of granular packings. *Soft Matter*, 10(1):48–59, 2014. (Cited on page 37.)

[210] Sandra Wegner, Ralf Stannarius, Axel Boese, Georg Rose, Balázs Szabó, Ellák Somfai, and Tamás Börzsönyi. Effects of grain shape on packing and dilatancy of sheared granular materials. *Soft Matter*, 10(28):5157–5167, 2014. (Cited on page 37.)

[211] Duc-Hanh Nguyen, Émilien Azéma, Farhang Radjai, and Philippe Sornay. Effect of size polydispersity versus particle shape in dense granular media. *Physical Review E*, 90(1):012202, 2014. (Cited on page 37.)

[212] Duc-Hanh Nguyen, Emilien Azéma, Philippe Sornay, and Farhang Radjai. Effects of shape and size polydispersity on strength properties of granular materials. *Physical Review E*, 91(3):032203, 2015. (Cited on page 37.)

[213] Shiwei Zhao and Xiaowen Zhou. Effects of particle asphericity on the macro- and micro-mechanical behaviors of granular assemblies. *Granular Matter*, 19(2):38, April 2017. (Cited on page 37.)

[214] Reid Kawamoto, Edward Andò, Gioacchino Viggiani, and Jose Andrade. All you need is shape: Predicting shear banding in sand with ls-dem. *Journal of the Mechanics and Physics of Solids*, 111, November 2017. (Cited on page 37.)

[215] Shiwei Zhao and Jidong Zhao. A poly-superellipsoid-based approach on particle morphology for dem modeling of granular media. *International Journal for Numerical and Analytical Methods in Geomechanics*, 43(13):2147–2169, 2019. (Cited on page 37.)

[216] Eloïse Marteau and José E. Andrade. An experimental study of the effect of particle shape on force transmission and mobilized strength of granular materials. *J. Appl. Mech*, 88(11), August 2021. (Cited on page 37.)

[217] Nicolaas P Kruyt, I Agnolin, Stefan Luding, and L Rothenburg. Micromechanical study of elastic moduli of loose granular materials. *Journal of the Mechanics and Physics of Solids*, 58(9):1286–1301, 2010. (Cited on pages 38, 43, and 51.)

[218] Luigi La Ragione and Vanessa Magnanimo. Evolution of the effective moduli of an anisotropic, dense, granular material. *Granular Matter*, 14(6):749–757, 2012. (Cited on page 38.)

[219] Ivana Agnolin, James T Jenkins, and Luigi La Ragione. A continuum theory for a random array of identical, elastic, frictional disks. *Mechanics of Materials*, 38(8-10):687–701, 2006. (Cited on page 38.)

[220] HJ Herrmann and Stefan Luding. Modeling granular media on the computer. *Continuum Mechanics and Thermodynamics*, 10(4):189–231, 1998. (Cited on page 38.)

[221] C Thornton and SJ Antony. Quasi-static shear deformation of a soft particle system. *Powder technology*, 109(1-3):179–191, 2000. (Cited on page 38.)

[222] Jean Jacques Moreau. Sorne numerical methods in multibody dynamics: application to granular materials. *European Journal of Mechanics-A/Solids*, 13(4-suppl):93–114, 1994. (Cited on page 39.)

[223] Farhang Radjai and Vincent Richefeu. Contact dynamics as a nonsmooth discrete element method. *Advances in the Dynamics of Granular Materials*, 41(6):715–728, June 2009. (Cited on pages 39, 64, 83, and 86.)

[224] Vincent Richefeu, Moulay Saïd El Youssoufi, and Farhang Radjaï. Shear strength properties of wet granular materials. *Phys. Rev. E*, 73(5):051304, May 2006. (Cited on pages 39, 64, and 65.)

[225] S Dippel, GG Batrouni, and DE Wolf. How transversal fluctuations affect the friction of a particle on a rough incline. *Physical Review E*, 56(3):3645, 1997. (Cited on page 39.)

[226] Michael P Allen and Dominic J Tildesley. *Computer simulation of liquids*. Oxford university press, 2017. (Cited on pages 40 and 106.)

[227] Lars Fast, JM Wills, Börje Johansson, and O Eriksson. Elastic constants of hexagonal transition metals: Theory. *Physical Review B*, 51(24):17431, 1995. (Cited on page 42.)

[228] Vlado Lubarda and Michelle Chen. On the elastic moduli and compliances of transversely isotropic and orthotropic materials. *Journal of Mechanics of Materials and Structures*, 3(1):153–171, 2008. (Cited on page 42.)

[229] A Ezaoui and H Di Benedetto. Experimental measurements of the global anisotropic elastic behaviour of dry hostun sand during triaxial tests, and effect of sample preparation. *Géotechnique*, 59(7):621–635, 2009. (Cited on page 44.)

[230] Richard J Bathurst and Leo Rothenburg. Observations on stress-force-fabric relationships in idealized granular materials. *Mechanics of materials*, 9(1):65–80, 1990. (Cited on pages 44 and 45.)

[231] Chao-Fa Zhao and Niels P Kruyt. An evolution law for fabric anisotropy and its application in micromechanical modelling of granular materials. *International journal of solids and structures*, 196:53–66, 2020. (Cited on page 44.)

[232] Farhang Radjai, Dietrich E. Wolf, Michel Jean, and Jean-Jacques Moreau. Bimodal character of stress transmission in granular packings. *Phys. Rev. Lett.*, 80(1):61–64, January 1998. (Cited on pages 44, 46, 113, and 117.)

[233] Masanobu Oda. Initial fabrics and their relations to mechanical properties of granular material. *Soils and foundations*, 12(1):17–36, 1972. (Cited on page 45.)

[234] M Satake. Constitution of mechanics of granular materials through graph representation. *Theoretical and applied mechanics*, 26:257–266, 1978. (Cited on page 45.)

[235] Chase P Broedersz, Xiaoming Mao, Tom C Lubensky, and Frederick C MacKintosh. Criticality and isostaticity in fibre networks. *Nature Physics*, 7(12):983–988, 2011. (Cited on page 53.)

[236] CP Broedersz, M Sheinman, and FC MacKintosh. Filament-length-controlled elasticity in 3d fiber networks. *Physical review letters*, 108(7):078102, 2012. (Cited on page 53.)

[237] David A Head, Alex J Levine, and FC MacKintosh. Deformation of cross-linked semiflexible polymer networks. *Physical review letters*, 91(10):108102, 2003. (Cited on page 53.)

[238] Santhosh Mathesan, Madhusmita Tripathy, Anand Srivastava, and Pijush Ghosh. Non-affine deformation of free volume during strain dependent diffusion in polymer thin films. *Polymer*, 155:177–186, 2018. (Cited on page 53.)

[239] TCT Ting and Tungyang Chen. Poisson's ratio for anisotropic elastic materials can have no bounds. *The quarterly journal of mechanics and applied mathematics*, 58(1):73–82, 2005. (Cited on page 55.)

[240] G. Félix, V. Falk, and U. D'Ortona. Granular flows in a rotating drum: the scaling law between velocity and thickness of the flow. *The European Physical Journal E*, 22(1):25–31, January 2007. (Cited on page 62.)

[241] Indresan Govender, Max C. Richter, Aubrey N. Mainza, and David N. De Klerk. A positron emission particle tracking investigation of the scaling law governing free surface flows in tumbling mills. *AIChE J.*, 63(3):903–913, March 2017. (Cited on page 62.)

[242] Ahmed Jarray, Vanessa Magnanimo, and Stefan Luding. Wet granular flow control through liquid induced cohesion. *Continuous Manufacturing/Processing*, 341:126–139, January 2019. (Cited on page 62.)

[243] Paul W. Cleary, Guy Metcalfe, and Kurt Liffman. How well do discrete element granular flow models capture the essentials of mixing processes? *Applied Mathematical Modelling*, 22(12):995–1008, December 1998. (Cited on page 63.)

[244] Paul W. Cleary. Dem simulation of industrial particle flows: case studies of dragline excavators, mixing in tumblers and centrifugal mills. *Powder Technology*, 109(1):83–104, April 2000. (Cited on page 63.)

[245] Nicolin Govender, Daniel N. Wilke, Chuan-Yu Wu, Raj Rajamani, Johannes Khinast, and Benjamin J. Glasser. Large-scale gpu based dem modeling of mixing using irregularly shaped particles. *Advanced Powder Technology*, 29(10):2476–2490, October 2018. (Cited on page 63.)

[246] S. Y. He, J. Q. Gan, D. Pinson, and Z. Y. Zhou. Particle shape-induced radial segregation of binary mixtures in a rotating drum. *Continuous Manufacturing/Processing*, 341:157–166, January 2019. (Cited on page 63.)

[247] S. Y. He, J. Q. Gan, D. Pinson, A. B. Yu, and Z. Y. Zhou. Particle shape-induced axial segregation of binary mixtures of spheres and ellipsoids in a rotating drum. *Chemical Engineering Science*, 235:116491, May 2021. (Cited on page 63.)

[248] Yuki Mori and Mikio Sakai. Advanced dem simulation on powder mixing for ellipsoidal particles in an industrial mixer. *Chemical Engineering Journal*, 429:132415, February 2022. (Cited on page 63.)

[249] G. G. Pereira and P. W. Cleary. Segregation due to particle shape of a granular mixture in a slowly rotating tumbler. *Granular Matter*, 19(2):23, March 2017. (Cited on page 63.)

[250] Shunying Ji, Siqiang Wang, and Zongyan Zhou. Influence of particle shape on mixing rate in rotating drums based on super-quadric dem simulations. *Advanced Powder Technology*, 31(8):3540–3550, August 2020. (Cited on page 63.)

[251] M. H. Abbaspour-Fard. Theoretical validation of a multi-sphere, discrete element model suitable for biomaterials handling simulation. *Biosystems Engineering*, 88(2):153–161, June 2004. (Cited on page 63.)

[252] Jakub Hlosta, Lucie Jezerská, Jiří Rozbroj, David Žurovec, Jan Nečas, and Jiří Zegzulka. Dem investigation of the influence of particulate properties and operating conditions on the mixing process in rotary drums: Part 1–determination of the dem parameters and calibration process, 2020. (Cited on page 63.)

[253] D. Höhner, S. Wirtz, and V. Scherer. A study on the influence of particle shape and shape approximation on particle mechanics in a rotating drum using the discrete element method. *Powder Technology*, 253:256–265, February 2014. (Cited on page 63.)

[254] Nan Gui, Xingtuan Yang, Jiyuan Tu, Shengyao Jiang, and Zhen Zhang. Numerical simulation of tetrahedral particle mixing and motion in rotating drums. *Particuology*, 39:1–11, August 2018. (Cited on page 63.)

[255] Nicolin Govender, Paul W. Cleary, Daniel N. Wilke, and Johannes Khinast. The influence of faceted particle shapes on material dynamics in screw conveying. *Chemical Engineering Science*, 243:116654, November 2021. (Cited on page 63.)

[256] Nicolin Govender, Rafał Kobyłka, and Johannes Khinast. The influence of cohesion on polyhedral shapes during mixing in a drum. *Chemical Engineering Science*, 270:118499, April 2023. (Cited on page 63.)

[257] Alejandro López, Vincenzino Vivacqua, Robert Hammond, and Mojtaba Ghadiri. Analysis of screw feeding of faceted particles by discrete element method. *Powder Technology*, 367:474–486, May 2020. (Cited on page 63.)

[258] Ivana Agnolin and Jean-Noël Roux. Internal states of model isotropic granular packings. i. assembling process, geometry, and contact networks. *Physical Review E*, 76(6):061302, 2007. (Cited on pages 64 and 107.)

[259] Lu Liu and Shunying Ji. Bond and fracture model in dilated polyhedral dem and its application to simulate breakage of brittle materials. *Granular Matter*, 21(3):41, 2019. (Cited on page 64.)

[260] Michel Y. Louge. Computer simulations of rapid granular flows of spheres interacting with a flat, frictional boundary. *Physics of Fluids*, 6(7):2253–2269, July 1994. (Cited on page 65.)

[261] Hongxiang Tang, Rui Song, Yan Dong, and Xiaoyu Song. Measurement of restitution and friction coefficients for granular particles and discrete element simulation for the tests of glass beads, 2019. (Cited on page 65.)

[262] J. A. I. N. Nitin and R. M. Ottino, J. M. andLueptow. Effect of interstitial fluid on a granular flowing layer. *Journal of Fluid Mechanics*, 508:23–44, 2004. (Cited on page 68.)

[263] Graham Weir, Donal Krouse, and Peter McGavin. The maximum thickness of upper shear layers of granular materials in rotating cylinders. *Chemical Engineering Science*, 60(7):2027–2035, April 2005. (Cited on page 73.)

[264] Daniel Schiochet Nasato, Christoph Goniva, Stefan Pirker, and Christoph Kloss. Coarse graining for large-scale dem simulations of particle flow - an investigation on contact and cohesion models. *New Paradigm of Particle Science and Technology Proceedings of The 7th World Congress on Particle Technology*, 102:1484–1490, January 2015. (Cited on page 75.)

[265] Mikio Sakai and Seiichi Koshizuka. Large-scale discrete element modeling in pneumatic conveying. *Chemical Engineering Science*, 64(3):533–539, February 2009. (Cited on page 75.)

[266] Ruihuan Cai and Yongzhi Zhao. An experimentally validated coarse-grain dem study of monodisperse granular mixing. *Powder Technology*, 361:99–111, February 2020. (Cited on page 75.)

[267] Yann Dufresne, Micaël Boulet, and Stéphane Moreau. Energy dissipation and onset of instabilities in coarse-grained discrete element method on homogeneous cooling systems. *Physics of Fluids*, 34(3):033306, March 2022. (Cited on page 76.)

[268] N. L. Johnson, P. H. Krisko, J.-C. Liou, and P. D. Anz-Meador. Nasa's new breakup model of evolve 4.0. *Advances in Space Research*, 28(9):1377–1384, January 2001. (Cited on page 82.)

[269] S. Michaux and N. Djordjevic. Influence of explosive energy on the strength of the rock fragments and sag mill throughput. *Minerals Engineering*, 18(4):439–448, April 2005. (Cited on page 82.)

[270] Philip J. Hajduk and Jonathan Greer. A decade of fragment-based drug design: strategic advances and lessons learned. *Nature Reviews Drug Discovery*, 6(3):211–219, March 2007. (Cited on page 82.)

[271] Parra Galvez and Hector Ivan. Analysis of the state of the art of blast-induced fragment conditioning. *Minerals Engineering*, 24(14):1638–1640, November 2011. (Cited on page 82.)

[272] José A. Sanchidrián, Finn Ouchterlony, Pablo Segarra, and Peter Moser. Size distribution functions for rock fragments. *International Journal of Rock Mechanics and Mining Sciences*, 71:381–394, October 2014. (Cited on page 82.)

[273] D. Touil, S. Belaadi, and C. Frances. Energy efficiency of cement finish grinding in a dry batch ball mill. *Cement and Concrete Research*, 36(3):416–421, March 2006. (Cited on page 82.)

[274] J. A. Aström. Statistical models of brittle fragmentation. *Advances in Physics*, 55(3-4):247–278, May 2006. (Cited on pages 82 and 98.)

[275] Ian Bailon-Poujol, Jean-Paul Bailon, and Gilles L'Espérance. Ball-mill grinding kinetics of master alloys for steel powder metallurgy applications. *Powder Technology*, 210(3):267–272, July 2011. (Cited on page 82.)

[276] C. Hosten and H. Cimilli. The effects of feed size distribution on confined-bed comminution of quartz and calcite in piston-die press. *International Journal of Mineral Processing*, 91(3):81–87, May 2009. (Cited on page 82.)

[277] Falk K. Wittel. Single particle fragmentation in ultrasound assisted impact comminution. *Granular Matter*, 12(4):447–455, July 2010. (Cited on pages 82 and 83.)

[278] Rania Majzoub and M. Munawar Chaudhri. High-speed photography of low-velocity impact cracking of solid spheres. *Philosophical Magazine Letters*, 80(6):387–393, June 2000. (Cited on page 83.)

[279] Y. S. Cheong, A. D. Salman, and M. J. Hounslow. Effect of impact angle and velocity on the fragment size distribution of glass spheres. *Powder Technology*, 138(2):189–200, December 2003. (Cited on page 83.)

[280] Hiroaki Katsuragi, Daisuke Sugino, and Haruo Honjo. Scaling of impact fragmentation near the critical point. *Phys. Rev. E*, 68(4):046105, October 2003. (Cited on page 83.)

[281] Hiroaki Katsuragi, Daisuke Sugino, and Haruo Honjo. Crossover of weighted mean fragment mass scaling in two-dimensional brittle fragmentation. *Phys. Rev. E*, 70(6):065103, December 2004. (Cited on page 83.)

[282] Manoj Khanal, Wolfgang Schubert, and Jürgen Tomas. Ball impact and crack propagation - simulations of particle compound material. *Granular Matter*, 5(4):177–184, February 2004. (Cited on page 83.)

[283] W. Schubert, M. Khanal, and J. Tomas. Impact crushing of particle-particle compounds–experiment and simulation. *International Journal of Mineral Processing*, 75(1):41–52, January 2005. (Cited on page 83.)

[284] S. Z. Wu, K. T. Chau, and T. X. Yu. Crushing and fragmentation of brittle spheres under double impact test. *Particle Breakage*, 143-144:41–55, June 2004. (Cited on page 83.)

[285] Jürgen Tomas, Matthias Schreier, Torsten Gröger, and Sabine Ehlers. Impact crushing of concrete for liberation and recycling. *Powder Technology*, 105(1):39–51, November 1999. (Cited on page 83.)

[286] Giuseppe Buscarnera and Itai Einav. The mechanics of brittle granular materials with co-evolving grain size and shape. *Proceedings of the Royal Society A: Mathematical, Physical and Engineering Sciences*, 477(2249):20201005, May 2021. (Cited on page 83.)

[287] F. Wittel, F. Kun, H. J. Herrmann, and B. H. Kröplin. Fragmentation of shells. *Phys. Rev. Lett.*, 93(3):035504, July 2004. (Cited on pages 83, 98, and 99.)

[288] F. Kun, F. K. Wittel, H. J. Herrmann, B. H. Kröplin, and K. J. Måløy. Scaling behavior of fragment shapes. *Phys. Rev. Lett.*, 96(2):025504, January 2006. (Cited on page 83.)

[289] R. Quey, P. R. Dawson, and F. Barbe. Large-scale 3d random polycrystals for the finite element method: Generation, meshing and remeshing. *Computer Methods in Applied Mechanics and Engineering*, 200(17):1729–1745, April 2011. (Cited on page 84.)

[290] Qiang Du, Maria Emelianenko, and Lili Ju. Convergence of the lloyd algorithm for computing centroidal voronoi tessellations. *SIAM J. Numer. Anal.*, 44(1):102–119, January 2006. (Cited on page 84.)

[291] Chuanfeng Fang, Zhihong Nie, Jian Gong, Bo Li, Wei Hu, and Ashiru Mohammed. Discrete element simulation of effects of multicontact loading on single particle crushing. *Particuology*, 69:49–60, October 2022. (Cited on page 84.)

[292] Dominique Leguillon. Strength or toughness? a criterion for crack onset at a notch. *European Journal of Mechanics - A/Solids*, 21(1):61–72, January 2002. (Cited on page 87.)

[293] Thomas Schwager and Thorsten Pöschel. Coefficient of restitution and linear-dashpot model revisited. *Granular Matter*, 9(6):465–469, 2007. (Cited on page 88.)

[294] Le Pen, M. L., W. Powrie, A. Zervos, S. Ahmed, and S. Aingaran. Dependence of shape on particle size for a crushed rock railway ballast. *Granular Matter*, 15(6):849–861, December 2013. (Cited on page 97.)

[295] P. Kekäläinen, J. A. Åström, and J. Timonen. Solution for the fragment-size distribution in a crack-branching model of fragmentation. *Phys. Rev. E*, 76(2):026112, August 2007. (Cited on page 98.)

[296] A. Bershadskii. Some classification of fragmentation processes related to fracture. *Journal of Physics A: Mathematical and General*, 33(11):2179, March 2000. (Cited on page 99.)

[297] Zeynep Karatza, Edward Andò, Stefanos-Aldo Papanicolopulos, Gioacchino Viggiani, and Jin Y. Ooi. Effect of particle morphology and contacts on particle breakage in a granular assembly studied using x-ray tomography. *Granular Matter*, 21(3):44, May 2019. (Cited on page 104.)

[298] Pierre-Emmanuel Peyneau and Jean-Noël Roux. Solidlike behavior and anisotropy in rigid frictionless bead assemblies. *Phys. Rev. E*, 78(4):041307, October 2008. (Cited on page 106.)

[299] Yoël Forterre and Olivier Pouliquen. Flows of dense granular media. *Annu. Rev. Fluid Mech.*, 40(1):1–24, January 2008. (Cited on page 106.)

[300] Lydie Staron and Farhang Radjai. Friction versus texture at the approach of a granular avalanche. *Phys. Rev. E*, 72(4):041308, October 2005. (Cited on page 107.)

[301] Guy Houlsby. How the dilatancy of soils affects their behavior. *Soil Mechanics Report*, 121/91, January 1991. (Cited on pages 109 and 110.)

[302] T Schanz and PA Vermeer. Angles of friction and dilatancy of sand. *Géotechnique*, 46(1):145–151, 1996. (Cited on page 109.)

[303] Yogi Vaid and S. Sasitharan. The strength and dilatancy of sand. *Canadian Geotechnical Journal*, 29:522–526, January 2011. (Cited on page 109.)

[304] Sam Frydman, Mark Talesnick, Hana Nawatha, and Keren Schwartz. Stress-dilation of undisturbed sand samples in drained and undrained triaxial shear. *Soils and foundations*, 47(1):27–32, 2007. (Cited on pages 109 and 110.)

[305] H. Troadec, F. Radjai, S. Roux, and J. C. Charmet. Model for granular texture with steric exclusion. *Phys. Rev. E*, 66(4):041305, October 2002. (Cited on page 111.)

[306] Richard J. Bathurst and Leo Rothenburg. Observations on stress-force-fabric relationships in idealized granular materials. *Mechanics of Materials*, 9(1):65–80, May 1990. (Cited on page 111.)

[307] F Radjaï, H Troadec, and S Roux. Key features of granular plasticity. *Granular materials: Fundamentals and applications*, page 157, 2004. (Cited on page 112.)

[308] Chao-Fa Zhao and Niels P. Kruyt. An evolution law for fabric anisotropy and its application in micromechanical modelling of granular materials. *International Journal of Solids and Structures*, 196-197:53–66, July 2020. (Cited on page 113.)

[309] Emilien Azéma and Farhang Radjaï. Force chains and contact network topology in sheared packings of elongated particles. *Phys. Rev. E*, 85(3):031303, March 2012. (Cited on page 117.)

[310] L. Rothenburg and R. J. Bathurst. Analytical study of induced anisotropy in idealized granular materials. *Géotechnique*, 39(4):601–614, December 1989. (Cited on page 123.)

[311] H. Ouadfel and L. Rothenburg. 'stress-force-fabric' relationship for assemblies of ellipsoids. *Mechanics of Materials*, 33(4):201–221, April 2001. (Cited on page 123.)

QUASI-STATIC AND DYNAMIC GRANULAR FLOWS: SCALING BEHAVIOR, MICROSTRUCTURE, AND PARTICLE SHAPE EFFECTS

Abstract: Granular processes in nature and industry often involve complex quasistatic or dynamic flows of various particle shapes and frictional properties. Although empirical approaches have been developed for such flows, advanced particle dynamics simulations can be used for detailed sensitivity analysis of their scaling behavior as a function of system parameters or to connect their behavior to the microstructure. In this work, extensive simulations are used in 3D to study the effects of polyhedral particle shape on quasi-static granular flows under fully periodic boundary conditions and dynamic cascading flows in rotating drums. Orthotropic elastic moduli under triaxial compression are expressed as a function of the contact network anisotropy and a constraint number accounting for different types of contacts between polyhedra. In rotating drums, the cascading flow regime is investigated for a broad range of parameter values and shown to be governed by a unique dimensionless scaling parameter that combines all system parameters. Finally, the impact-induced breakage of a single particle is modeled by means of a novel fracture model based exclusively on fracture energy. The fragment shapes and sizes are studied systematically and the distribution of fragment masses is found to be a power-law function with an exponent depending on the fracture energy.
Keywords: Granular Materials, Discrete Element Method, Microstructure, Scaling

ECOULEMENTS GRANULAIRES QUASI-STATIQUES ET DYNAMIQUES: MISE À L'ÉCHELLE, MICROSTRUCTURE ET EFFETS DE LA FORME DES PARTICULES

Resumé: Les processus granulaires naturels et industriels impliquent souvent des écoulements quasi-statiques ou dynamiques complexes de diverses formes de particules. Même si des modèles empiriques de tels écoulements existent, les simulations avancées de dynamique granulaire permettent aujourd'hui de réaliser des analyses de sensibilité détaillée de leur comportement en fonction des paramètres de l'écoulement ou relier leur comportement à la microstructure. Dans ce travail de thèse, des vastes campagnes de simulation ont été menées dans le but d'étudier les effets de la forme polyédrique des particules sur les écoulements granulaires quasi-statiques sous conditions tri-périodiques et sur les écoulements dynamiques dans le régime de cascade dans des tambours rotatifs. Les modules élastiques orthotropes sous compression triaxiale ont été exprimés en fonction de l'anisotropie du réseau de contacts et un nombre de contrainte prenant en compte différents types de contacts entre polyèdres. Dans les tambours rotatifs, le régime d'écoulement en cascade a été étudié pour un large spectre de valeurs des paramètres et il a été montré qu'il est régi par un paramètre d'échelle sans dimension qui combine tous les paramètres du système. Il a été également démontré que la mise à l'échelle proposée est cohérente avec une méthode de coarse-graining. Enfin, la rupture d'une seule particule sous l'effet d'impact avec un plan a été simulée par un nouveau modèle de fracture basé exclusivement sur l'énergie de rupture. Les simulations révèlent une distribution des masses des fragments en loi de puissance avec un exposant qui dépend de l'énergie de rupture.
Mots Clés: Matériaux granulaires, Discrete Element Method, Microstructure, Scaling